nanomaterials

Special Issue Reprint

Functional Graphene-Based Nanodevices

Edited by
Qijin Cheng and Jian Zhou

mdpi.com/journal/nanomaterials

MDPI

Functional Graphene-Based Nanodevices

Functional Graphene-Based Nanodevices

Guest Editors

Qijin Cheng
Jian Zhou

MDPI

Basel • Beijing • Wuhan • Barcelona • Belgrade • Novi Sad • Cluj • Manchester

Guest Editors

Qijin Cheng
School of Electronic Science and Engineering
Xiamen University
Xiamen
China

Jian Zhou
College of Mechanical and Vehicle Engineering
Hunan University
Changsha
China

Editorial Office
MDPI AG
Grosspeteranlage 5
4052 Basel, Switzerland

This is a reprint of the Special Issue, published open access by the journal *Nanomaterials* (ISSN 2079-4991), freely accessible at: https://www.mdpi.com/journal/nanomaterials/special_issues/graphene_nanodevices.

For citation purposes, cite each article independently as indicated on the article page online and as indicated below:

Lastname, A.A.; Lastname, B.B. Article Title. *Journal Name* **Year**, *Volume Number*, Page Range.

ISBN 978-3-7258-4503-3 (Hbk)
ISBN 978-3-7258-4504-0 (PDF)
https://doi.org/10.3390/books978-3-7258-4504-0

Contents

About the Editors

Qijin Cheng

Qijin Cheng, associate professor at the School of Electronic Science and Engineering, Xiamen University, China. He obtained his Ph.D. in Physics from Nanyang Technological University, Singapore in 2008. His research interests include wide bandgap materials, two-dimensional semiconductor nanomaterials, photodetectors, solar cells, power devices, etc. He has published more than 100 SCI papers in *Advanced Optical Materials*, *Journal of Materials Chemistry A*, *Journal of Materials Chemistry C*, *Acta Materialia*, *Nanoscale*, *ACS Applied Materials & Interfaces*, *Applied Physics Letters*, etc.

Jian Zhou

Jian Zhou received his B.Eng. in Electronic Science and Technology from Hunan University in 2010 and Ph.D. in Physical Electronics from Zhejiang University in 2015. Currently serving as a Professor at the College of Mechanical and Vehicle Engineering, Hunan University, his research focuses on graphene-based nanomaterials and devices, MEMS sensors, flexible electronics, and AI-enhanced sensing technologies. Dr. Zhou has authored over 100 SCI-indexed publications in leading journals including *Advanced Functional Materials*, *npj Flexible Electronics*, *Applied Physics Reviews*, *ACS Sensors*, and *Microsystems & Nanoengineering*.

nanomaterials

MDPI

Editorial

Editorial for Special Issue "Functional Graphene-Based Nanodevices"

Qijin Cheng [1,*] and Jian Zhou [2]

[1] School of Electronic Science and Engineering, Xiamen University, Xiamen 361005, China
[2] College of Mechanical and Vehicle Engineering, Hunan University, Changsha 410082, China; jianzhou@hnu.edu.cn
* Correspondence: qijin.cheng@xmu.edu.cn

As a typical ultra-thin two-dimensional nanomaterial, graphene has many excellent properties, including, but not limited to, mechanical, optical, thermal and electrical properties. For example, it possesses a high Young's modulus of 1 TPa, a high transmittance of 97.7%, a high thermal conductivity of 5×10^3 W/m.K, and a high carrier mobility of 2×10^5 cm^2/V.s [1–5]. In particular, owing to its distinct electronic properties, graphene exhibits several electron transport phenomena, including the single-electron tunneling effect, the electron coherence effect, and the anomalous quantum Hall effect [6–9]. These unique properties endow graphene with a broad range of potential applications in transistors, sensors, photodetectors, energy storage devices, solar cells, transparent conductive electrodes, biomedicine, etc. [10–20].

This Special Issue, entitled "Functional Graphene-Based Nanodevices", focuses on the synthesis, modification and functionalization of graphene-based nanomaterials and their applications in nanodevices. It contains ten articles, as outlined below.

Graphene-based transistors are considered in contribution 1,2. In contribution 1, the integrated structure of a graphene single-electron transistor and nanostrip electrometer is prepared using the semiconductor fabrication process; the transistor is able to deplete the electrons in the quantum dot structure at low temperatures, while the nanostrip electrometer coupled with the quantum dot can be used to detect the quantum dot signal. In contribution 2, the use of trilayer graphene scrolls in the channel material of field effect transistors for a self-powered tribotronics and mechanosensation matrix is reported; the fabricated transistor is extremely stretchable, has excellent temperature sensitivity and is highly transparent, while the fabricated mechanosensation matrix possesses the tactile sensing properties of high sensitivity (1.125 mm^{-1}), a rapid response time (~16 ms), and a durable operation over thousands of cycles.

Graphene synthesis and its application in heterojunction photodetectors are considered in contribution 3,4. In contribution 3, a remote plasma-enhanced chemical vapor deposition is proposed to directly grow graphene nanowalls (GNWs) at a low radio-frequency power, effectively enhancing the growth rate and reducing the number of structural defects; the fabricated GNWs/HfO_2/Si photodetector features a low dark current of 3.85×10^{-10} A, with a responsivity of 0.19 AW^{-1}, a specific detectivity of 1.38×10^{12} Jones and an external quantum efficiency of 47.1% at zero bias. Contribution 4 reports a facile approach to the selective synthesis of MoS_2 on graphene via the application of laser-based photothermal treatment, enabling the direct formation of graphene/MoS_2 heterostructures; the fabricated graphene/MoS_2 photodetector is highly responsive to the incident pulsed light, with excellent stability and reproducibility over multiple cycles.

Graphene-based energy storage devices are considered in contribution 5,6. In contribution 5, a novel structure of lithium-ion capacitors (LICs), using LiBETI as the electrolyte and a self-synthesized graphene/single-walled carbon nanotube composite as the cathode, is successfully assembled; the fabricated LIC has excellent performance, with a specific

capacitance of up to 85 F g^{-1}, a capacity retention of up to 72% after 10,000 cycles, and a maximum energy density of 182.6 Wh kg^{-1} at a power density of 2678.0 W kg^{-1}. In contribution 6, high-performance graphene-based solid-state hydrogen storage devices are created through the mechanical exfoliation of expanded graphite and functionalization with palladium nanoparticles, revealing that the nanoparticle size and dispersion play a crucial role in the uptake and release of hydrogen.

The applications of graphene in sensors are considered in contribution 7,8. Contribution 7 reports a novel crossbeam structure with a graphene varistor protected by Si_3N_4 for nano/micro–electro–mechanical system (N/MEMS) mechanical sensors; this structure substantially overcomes the poor reliability of previous sensors with suspended graphene. The fabricated sensor displays excellent performance, with a gauge factor, sensitivity, hysteresis error, nonlinear error, and repeatability error of ~1.35, 33.13 mV/V/MPa, 2.0119%, 3.3622%, and 4.0271%, respectively. In contribution 8, a sensitive and rapid electrochemical method for the detection of paraquat in environmental water samples using a glassy carbon electrode modified with vertically ordered mesoporous silica films and a nanocarbon composite is proposed; the proposed sensor has a superior analytical sensitivity and anti-fouling ability compared with that based on the bare glassy carbon electrode.

The synthesis and relevant applications of graphene derivatives are considered in contribution 9,10. In contribution 9, the optical characteristics (optical transitions, optical bandgap, absorption coefficient, and absorbance spectrum width) of graphene oxide (GO) and reduced graphene oxide (rGO) are investigated by tailoring the drying time and reduction time at two different temperatures; importantly, the absorption coefficients of the synthesized GO and rGO surpass those reported for exfoliated graphene dispersions by two to three times. In contribution 10, a seeded emulsion polymerization is firstly employed to synthesize polystyrene microspheres, and the uniform monolayer of the polystyrene microspheres is prepared on the substrate via the dipping method; moreover, a single-electron transistor is successfully fabricated based on self-assembled gold nanoparticles and using the polystyrene microsphere template as a mask.

Overall, this volume provides a collection of selected papers addressing the synthesis and relevant applications of graphene-based nanomaterials, and we hope that the readers find this useful.

Conflicts of Interest: The author declares no conflicts of interest.

List of Contributions:

1. Li, X.; Sui, J.; Fang, J. Single-Electron Transport and Detection of Graphene Quantum Dots. *Nanomaterials* **2023**, *13*, 889.
2. Meng, Y. Highly Stretchable Graphene Scrolls Transistors for Self-Powered Tribotronic Non-Mechanosensation Application. *Nanomaterials* **2023**, *13*, 528.
3. Shen, Y.; Li, Y; Chen, W.; Jiang, S.; Li, C.; Cheng, Q. High-Performance Graphene Nanowalls/Si Self-Powered Photodetectors with HfO_2 as an Interfacial Layer. *Nanomaterials* **2023**, *13*, 1681.
4. Jeon, M. J.; Hyeong, S.-K.; Jang, H. Y.; Mun, J.; Kim, T.-W.; Bae, S.; Lee, S.-K. Selective Laser-Assisted Direct Synthesis of MoS_2 for Graphene/MoS_2 Schottky Junction. *Nanomaterials* **2023**, *13*, 2937.
5. Yin, H.; Tang, J.; Zhang, K.; Lin, S.; Xu, G.; Qin, L.-C. Achieving High-Energy-Density Graphene/Single-Walled Carbon Nanotube Lithium-Ion Capacitors from Organic-Based Electrolytes. *Nanomaterials* **2024**, *14*, 45.
6. Chow, D.; Burns, N.; Boateng, E.; Zalm, J. V. D.; Kycia, S.; Chen, A. Mechanical Exfoliation of Expanded Graphite to Graphene-Based Materials and Modification with Palladium Nanoparticles for Hydrogen Storage. *Nanomaterials* **2023**, *13*, 2588.
7. Wang, J.; Zhu, Z.; Qi, Y.; Li, M. A Novel Crossbeam Structure with Graphene Sensing Element for N/MEMS Mechanical Sensors. *Nanomaterials* **2022**, *12*, 2101.
8. Zheng, W.; Su, R.; Yu, G.; Liu, L.; Yan, F. Highly Sensitive Electrochemical Detection of Paraquat in Environmental Water Samples Using a Vertically Ordered Mesoporous Silica Film and a Nanocarbon Composite. *Nanomaterials* **2022**, *12*, 3632.

9. Tene, T.; Naranjo, P. G. V.; Cevallos, Y.; Arias, F. A.; Pietra, M. L.; Scarcello, A.; Salazar, Y. C.; Polanco, M. A.; Straface, S.; Gomez, C. V.; Caputi, L. S.; Bellucci, S. Temperature-Dependent Optical Properties of Oxidized Graphenes, *Nanomaterials*. **2023**, *13*, 2263.
10. Fang, J.; Li, X.; Xie W.; Sun, K. A Novel Fabrication of Single Electron Transistor from Patterned Gold Nanoparticle Array Template-Prepared by Polystyrene Nanospheres. *Nanomaterials* **2022**, *12*, 3102.

References

1. Lee, C.; Wei, X.; Kysar, J.W.; Hone, J. Measurement of the Elastic Properties and Intrinsic Strength of Monolayer Graphene. *Science* **2008**, *321*, 385–388. [CrossRef] [PubMed]
2. Balandin, A.A.; Ghosh, S.; Bao, W.; Calizo, I.; Teweldebrhan, D.; Miao, F.; Lau, C.N. Superior Thermal Conductivity of Single-Layer Graphene. *Nano Lett.* **2008**, *8*, 902–907. [CrossRef] [PubMed]
3. Nair, R.R.; Blake, P.; Grigorenko, A.N.; Novoselov, K.S.; Booth, T.J.; Stauber, T.; Peres, N.M.R.; Geim, A.K. Fine Structure Constant Defines Visual Transparency of Graphene. *Science* **2008**, *320*, 1308. [CrossRef] [PubMed]
4. Du, X.; Skachko, I.; Barker, A.; Andrei, E.Y. Approaching Ballistic Transport in Suspended Graphene. *Nat. Nanotechnol.* **2008**, *3*, 491–495. [CrossRef] [PubMed]
5. Geim, A.K. Graphene: Status and Prospects. *Science* **2009**, *324*, 1530–1534. [CrossRef] [PubMed]
6. Efimkin, D.K.; Burg, G.W.; Tutuc, E.; MacDonald, A.H. Tunneling and Fluctuating Electron-hole Cooper Pairs in Double Bilayer Graphene. *Phys. Rev. B* **2015**, *101*, 035413. [CrossRef]
7. Wang, L.; Guo, L.; Zhang, Q. A Light-controllable Topological Transistor Based on Quantum Tunneling of Anomalous Topological Edge States. *Appl. Phys. Express* **2022**, *15*, 115003. [CrossRef]
8. McIver, J.; Schulte, B.; Stein, F.-U.; Matsuyama, T.; Jotzu, G.; Meier, G.; Cavalleri, A. Light-induced Anomalous Hall Effect in Graphene. *Nat. Phys.* **2020**, *16*, 38–41. [CrossRef] [PubMed]
9. De Laissardière, G.T.; Mayou, D. Conductivity of Graphene with Resonant and Nonresonant Adsorbates. *Phys. Rev. Lett.* **2013**, *111*, 146601. [CrossRef] [PubMed]
10. Jia, Y.; Zhang, J.; Kong, D.; Zhang, C.; Han, D.; Han, J.; Tao, Y.; Lv, W.; Yang, Q.H. Practical Graphene Technologies for Electrochemical Energy Storage. *Adv. Funct. Mater.* **2022**, *32*, 2204272. [CrossRef]
11. Kaczmarek-Szczepańska, B.; Michalska-Sionkowska, M.; Binkowski, P.; Lukaszewicz, J.P.; Kamedulski, P. 3D-Structured and Blood-Contact-Safe Graphene Materials. *Int. J. Mol. Sci.* **2023**, *24*, 3576. [CrossRef] [PubMed]
12. Li, X.; Zhu, H.; Wang, K.; Cao, A.; Wei, J.; Li, C.; Jia, Y.; Li, Z.; Li, X.; Wu, D. Graphene-On-Silicon Schottky Junction Solar Cells. *Adv. Mater.* **2010**, *22*, 2743–2748. [CrossRef] [PubMed]
13. Kim, J.M.; Kim, S.; Shin, D.H.; Seo, S.W.; Lee, H.S.; Kim, J.H.; Jang, C.W.; Kang, S.S.; Choi, S.-H.; Kwak, G.Y.; et al. Si-Quantum-Dot Heterojunction Solar Cells with 16.2% Efficiency Achieved by Employing Doped-Graphene Transparent Conductive Electrodes. *Nano Energy* **2018**, *43*, 124–129. [CrossRef]
14. Wang, Z.; Yu, X.; Qiu, X.; Fu, J.; Yang, D. High-Responsivity Graphene/Hyperdoped-Silicon Heterostructure Infrared Photodetectors. *Opt. Laser Technol.* **2022**, *153*, 108291. [CrossRef]
15. Xia, F.; Mueller, T.; Lin, Y.-M.; Valdes-Garcia, A.; Avouris, P. Ultrafast Graphene Photodetector. *Nat. Nanotechnol.* **2009**, *4*, 839–843. [CrossRef] [PubMed]
16. Lin, H.; Sturmberg, B.C.P.; Lin, K.-T.; Yang, Y.; Zheng, X.; Chong, T.K.; De Sterke, C.M.; Jia, B. A 90-nm-thick Graphene Metamaterial for Strong and Extremely Broadband Absorption of Unpolarized Light. *Nat. Photonics* **2019**, *13*, 270–276. [CrossRef]
17. Casalino, M.; Sassi, U.; Goykhman, I.; Eiden, A.; Lidorikis, E.; Milana, S.; De Fazio, D.; Tomarchio, F.; Iodice, M.; Coppola, G.; et al. Vertically Illuminated, Resonant Cavity Enhanced, Graphene–Silicon Schottky Photodetectors. *ACS Nano* **2017**, *11*, 10955–10963. [CrossRef] [PubMed]
18. Lee, J.H.; Shin, W.H.; Lim, S.Y.; Kim, B.G.; Choi, J.W. Modified Graphite and Graphene Electrodes for High-performance Lithium Ion Hybrid Capacitors. *Mater. Renew. Sustain. Energy* **2014**, *3*, 22. [CrossRef]
19. Yeh, P.-C.; Ohkatsu, G.; Toyama, R.; Tue, P.T.; Ostrikov, K.; Majima, Y.; Chiang, W.-H. Towards Single Electron Transistor-based Photon Detection with Microplasma-enabled Graphene Quantum Dots. *Nanotechnology* **2021**, *32*, 50LT01. [CrossRef] [PubMed]
20. Lin, G.; Wang, H.; Zhang, L.; Cheng, Q.; Gong, Z.; Ostrikov, K.K. Graphene Nanowalls Conformally Coated with Amorphous/Nanocrystalline Si as High-Performance Binder-Free Nanocomposite Anode for Lithium-Ion Batteries. *J. Power Sources* **2019**, *437*, 226909. [CrossRef]

nanomaterials

MDPI

Article

Achieving High-Energy-Density Graphene/Single-Walled Carbon Nanotube Lithium-Ion Capacitors from Organic-Based Electrolytes

Hang Yin [1,2], Jie Tang [1,2,*], Kun Zhang [1], Shiqi Lin [1], Guangxu Xu [1,2] and Lu-Chang Qin [3]

[1] National Institute for Materials Science, 1-2-1 Sengen, Tsukuba 305-0047, Ibaraki, Japan; yin.hang@nims.go.jp (H.Y.); zhang.kun@nims.go.jp (K.Z.); lin.shiqi@nims.go.jp (S.L.); xu.guangxu@nims.go.jp (G.X.)
[2] Graduate School of Pure and Applied Sciences, University of Tsukuba, 1-1-1 Tennodai, Tsukuba 305-0006, Ibaraki, Japan
[3] Department of Physics and Astronomy, University of North Carolina at Chapel Hill, Chapel Hill, NC 27599-3255, USA; lcqin@email.unc.edu
* Correspondence: tang.jie@nims.go.jp; Tel.: +81-02-98592728

Abstract: Developing electrode materials with high voltage and high specific capacity has always been an important strategy for increasing the energy density of lithium-ion capacitors (LICs). However, organic-based electrolytes with lithium salts limit their potential for application in LICs to voltages below 3.8 V in terms of polarization reactions. In this work, we introduce Li[$N(C_2F_5SO_2)_2$] (lithium Bis (pentafluoroethanesulfonyl)imide or LiBETI), an electrolyte with high conductivity and superior electrochemical and mechanical stability, to construct a three-electrode LIC system. After graphite anode pre-lithiation, the anode potential was stabilized in the three-electrode LIC system, and a stable solid electrolyte interface (SEI) film formed on the anode surface as expected. Meanwhile, the LIC device using LiBETI as the electrolyte, and a self-synthesized graphene/single-walled carbon nanotube (SWCNT) composite as the cathode, showed a high voltage window, allowing the LIC to achieve an operating voltage of 4.5 V. As a result, the LIC device has a high energy density of up to 182 Wh kg^{-1} and a 2678 W kg^{-1} power density at 4.5 V. At a current density of 2 A g^{-1}, the capacity retention rate is 72.7% after 10,000 cycles.

Keywords: lithium-ion capacitor; graphene; asymmetric capacitor; LiBETI; three-dimensional structure

1. Introduction

Electrochemical energy storage devices, such as lithium-ion batteries (LIBs) and electric double-layer capacitors (EDLCs), have made great strides in the past decade [1–3]. Commercial LIBs can store energy densities of 150–200 Wh kg^{-1} [4,5]. However, their power output (<1 kW kg^{1}) and lifetime (<10^{-3} times) are not as satisfactory as expected [6,7]. Conversely, EDLCs can achieve power densities and lifetimes of >5000 W kg^{-1} and >100,000 cycles, respectively [8,9]. However, the energy densities in EDLC with organic electrolytes are less than 10 Wh kg^{-1} [10–12]. Therefore, combining the high energy density of batteries and the high power density and cycle life of EDLCs, hybrid lithium-ion capacitors (LIC) have received great attention in recent years [13–15].

In recent years, many efforts have been made to obtain higher energy-density LIC devices for fabrication, cathode and anode electrode material synthesis and electrolyte synthesis. Capacitor-type cathode materials are mainly composed of carbon-based materials such as activated carbon [16], template carbon [17], graphene [18], and their composites. Graphene-based carbon materials are widely used in LIC cathodes due to their unique two-dimensional structure, porous structure, superior electrical conductivity, and much larger specific capacitance. However, Graphene sheets can severely aggregate and reaccumulate, decreasing capacity after several charge/discharge cycles. There have been many efforts to

solve this issue, and one effective method is to form 3D nanostructures by using carbon nanotubes as spacers in the graphene sheet layers. This structure can provide enough space for charge storage and numerous paths for ion transport [19,20]. For example, Xiao and co-workers prepared graphene/CNT 3D composite structural materials using microwave irradiation. When used as the cathode and anode of LIC, graphene/CNT showed a high energy density of 232.6 Wh kg^{-1} at 226.0 W kg^{-1} [21].

The other factor that affects energy density and power density is the mismatch in kinetics between the cathode and anode. Generally, the anode kinetics based on Li-ion intercalation/ deintercalation is much slower than the cathode based on the EDLC model, leading to lower energy densities at relatively high power densities [22]. This means that when the power density is high, the energy density is low. Therefore, finding an electrolyte that matches the kinetics of the cathode and anode is vital to address the high energy and power density demands of LICs. $Li[N(C_2F_5SO_2)_2]$ (LiBETI) has superior ionic conductivity and capacity retention compared to conventional $LiPF_6$ used in lithium-ion batteries [23]. In an LIC, superior ionic conductivity provides the reaction kinetics, and LiBETI can also maintain the stability of the anode after pre-lithiation. So far, few reports have investigated using LiBETI as an electrolyte for lithium-ion capacitors.

In this work, a 3D porous structure is achieved using SWCNTs as spacers inserted into the graphene sheets. It can effectively prevent the stacking of graphene sheets. The synthesized graphene/SWCNT composite is used as the LIC cathode, and the pre-lithiated graphite is used as the anode to assemble a three-electrode system LIC device. The results show that using LiBETI as the electrolyte, the LIC devices have better conductivity and higher specific capacity than the general lithium salt electrolyte, such as lithium hexafluorophosphate ($LiPF_6$) and lithium difluorosulfimide ($F_2LiNO_4S_2$ or LiFSI). Analyzing the anode potential in the three-electrode system shows that the anode potential remains almost constant at all charge and discharge voltages (at 3.8–4.5 V). It indicates that LiBETI can make the anode form a stable SEI film. As will be described in detail in this report, the hybrid LIC device has a high energy density of up to 182 Wh kg^{-1} and a 2678 W kg^{-1} power density at 4.5 V. At a current density of 2A g^{-1}, the capacity retention rate is 72.7% after 10,000 cycles.

2. Materials and Methods

2.1. Materials

2.1.1. Reagents

Graphite flakes with a size of about 10 μm were purchased from NSC, Japan. Hydrazine hydrate was purchased from Wako Pure Chemical Industries, Tokyo, Japan. The single-walled carbon nanotube was purchased from Nippon Zeon Co., Ltd. (Tokyo, Japan). The anode electrode material P_5B was purchased from Nippon Carbon Co., Ltd. (Tokyo, Japan) The electrode film conductive agent, Ketjen Black, was purchased from Nippon Ketjen Co., Ltd. (Tokyo, Japan) The electrode film binders polyvinylidene difluoride (PVDF) and the electrolytes lithium salt used lithium hexafluorophosphate ($LiPF_6$), lithium difluorosulfimide (LiFSI), and LiBETI from Tokyo Chemical Industry Co., Ltd. (Tokyo, Japan) The solvent ethylene carbonate (EC) and diethyl carbonate (DEC) were from Tokyo Chemical Industry Co., Ltd.

2.1.2. Synthesis of the Graphene/CNT Composite

Graphene oxide (GO) was synthesized from graphite flakes using a modified Hummers method. Details of the method have been reported in our previous publications [24]. 5 g of natural graphite, 3.75 g of $NaNO_3$, and 310.5 g of H_2SO_4 were placed in a beaker and stirred in an ice bath at 0 °C for 30 min. Under stirring, 22.5 g of $KMnO_4$ was slowly added to the above solution, and the temperature was kept below 10 °C. The resulting mixture was then stirred at room temperature for 2 days, after which 1 L of concentrated H_2SO_4 was added dropwise over a 1 h period. The mixture was stirred until it cooled down. After that, 150 g of H_2O_2 (30%, Aldrich, Tokyo, Japan) was added to the mixture to change the

color of the suspension from reddish brown to yellow. Specifically, after obtaining the GO solution, the GO suspension was diluted with 0.1 mol L^{-1} HCl, centrifuged five times, diluted with deionized water, and continuously centrifuged (30,000 rpm/min) until the pH of the supernatant reached 7 to remove impurities. Graphene/SWCNT composites were prepared by mixing SWCNT and GO in the ultrasonic rod. The SWCNT was well dispersed in GO suspension and reduced by adding hydrazine hydrate for 24 h. The mixture was then filtered to obtain graphene/SWCNT slurry. The mixture suspension was then filtered to obtain an SG slurry. Subsequently, the slurry was washed with distilled water and vacuum-dried to obtain the SG composite as dry powder. Pure graphene without adding carbon tubes was also produced using the same method.

2.2. Material Characterization

The morphology and structure of the synthesized graphene/SWCNT were characterized using scanning electron microscopy (SEM, JSM-7001F, JEOL, Tokyo, Japan) and transmission electron microscopy (TEM, JEM-2100, JEOL, Tokyo, Japan). In addition, the structure was investigated with powder X-ray diffraction (XRD, Rigaku SmartLab (Kyoto, Japan), Cu-Kα radiation, λ = 1.5418 Å). The functional groups on GO and graphene were characterized by X-ray photoelectron spectroscopy (XPS, ULVAC-PHI Quantera SXM, Kanagawa, Japan) and Fourier transform infrared spectroscopy (FTIR, Shimadzu, IRTracer-100, Kyoto, Japan). Raman spectroscopy (RAMAN-11 with a 532 nm laser source, Nanophoton) was used to analyze the D-band and G-band peaks associated with the graphite structure in the composites. Nitrogen adsorption–desorption data (Quantachrome Autosorb iQ) were collected to calculate the specific surface area using the Brunauer–Emmett–Taylor (BET) method and density Functional Theory (DFT) calculations to obtain the pore size distribution.

2.3. Electrochemical Measurement

The three-electrode system's working electrode (cathode) is graphene/SWCNT, the counter electrode (anode) is graphite, and the reference electrode is lithium foil. All the electrodes were prepared using the traditional slurry electrode fabrication route and dried in a vacuum. The cathode and anode were made with 85 wt% active materials, 10 wt% of PVDF, and 5% Ketjen Black. The anode electrode material was coated on a porous copper foil and the cathode electrode material was coated on an aluminum foil. The lithium foil was fixed to the copper foil as a reference electrode by pressing it with a roller. Next, 1 mol/L electrolyte was prepared with $LiPF_6$/LiFSI/LiBETI as lithium salt solute and EC and DEC (EC/DEC 1:1, *v/v*) mixed solution as solvent. To explore the cathode capacity, a symmetrical EDLC pouch cell was assembled using the above electrolyte and a 25-micron cellulose separator. Pre-lithiated graphite anode: the graphite electrode was connected to the lithium electrode to form a half cell, which was discharged to 0.08 V at 20 mA g^{-1} and then kept at the potential for 30 h to reach the lithiated state. To prevent over-discharge of the anode, the LIC was tested at a potential of 2.2~4.5 V. Electrochemical impedance spectroscopy (EIS) measurement was also performed over a frequency range from 20 kHz to 0.2 Hz. All electrochemical tests were performed using an electrochemical workstation (Biologic VSP-300).

The specific capacitance, energy density, and power density of the material were calculated from the constant current charge/discharge curve at different current densities. Electrode mass calculates the total mass of the cathode and anode. The calculation formula is as follows:

$$C = \frac{I \times t}{m \times \Delta V} \quad (1)$$

where I is the discharge current, m is the cathode's and anode's total active mass, t is the discharge time, and ΔV is the voltage difference between charge and discharge.

The formula for calculating energy density (E Wh kg^{-1}) and power density (W kg^{-1}) is as follows:

$$E = \int_{t1}^{t2} IVdt = \frac{1}{2}C(V_{max} + V_{min})(V_{max} - V_{min}) \quad (2)$$

$$P = \frac{E}{t} \quad (3)$$

where V_{max} and V_{min} are the values of voltage at the end and the start of the discharge process.

3. Results and Discussion

To investigate the morphology of the synthesized graphene/SWCNT and whether the SWCNTs were efficiently inserted into the graphene sheets, TEM and SEM of graphene oxide, graphene, and graphene/SWCNT was carried out, respectively. Figure 1a shows that the graphene oxide microstructure is relatively flat. After chemical reduction, graphene (Figure 1b) exhibits multiple wrinkles and stacking, making it disadvantageous for ion transport in electrochemical reactions. With the addition of single-walled carbon tubes (Figure 1c), it is observed that the graphene state is re-flattened. Moreover, the single-walled carbon tubes, which are very difficult to disperse as nanostructures, are also uniformly distributed among the graphene sheets (Figure 1c,d). This phenomenon occurs because the three-dimensional (3D) network-structured graphene/SWCNT composites reduce the re-stacking.

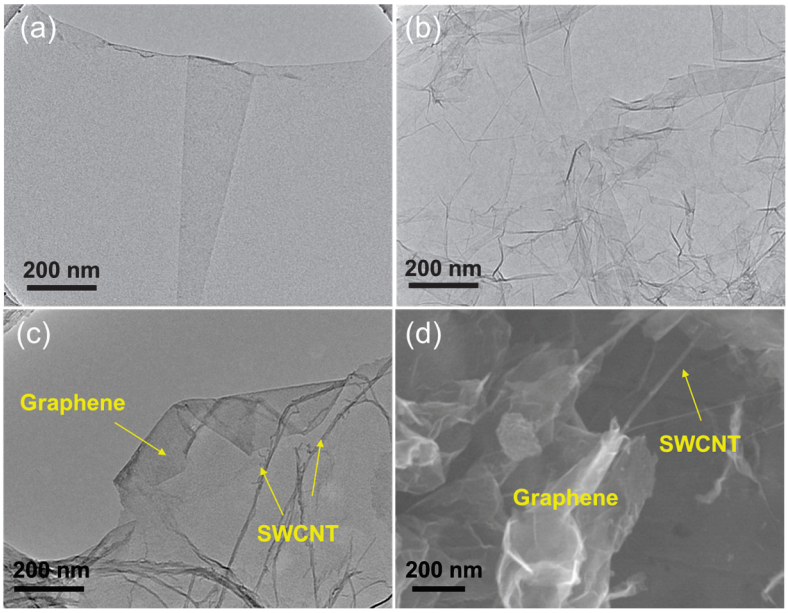

Figure 1. TEM image of (**a**) graphene oxide, (**b**) graphene, (**c**) graphene/SWCNT, and SEM image of (**d**) graphene/SWCNT.

To further explore the microstructure of graphene/SWCNT composites, the XRD results are shown in Figure 2a. Graphene oxide (GO) has the smallest diffraction angle and the smallest half-peak width, and is inferred to have the largest layer spacing. This is due to the preparation of GO using the oxidation method, which has functional groups such as hydroxyl and carboxyl on the surface of graphene oxide. The (002) diffraction peak of graphene/SWCNT is centered at 2θ = 24.2°, which is slightly shifted to a lower angle compared to graphene (2θ = 23.9°), suggesting that the addition of SWCNT slightly increases the layer spacing of graphene. FT-IR spectra (Figure 2b) show that graphene oxide has more functional groups than graphene, such as C-O, C=O, and -OH, on the surface, which is consistent with the XRD results. After co-reduction, there are almost no functional groups on graphene/SWCNT composites, indicating that graphene is sufficiently reduced.

In Raman spectroscopy, the G peak at ~1580 cm^{-1} represents the material's carbonization degree, and the D peak at ~1350 cm^{-1} represents the defects and disordered structure in the hexagonal lattice of graphene. The D and G peaks' intensity ratio (ID/IG) can usually be used to assess the degree of defects in carbon materials [25]. Figure 2c shows the Raman spectra of GO and graphene/SWCNT. Due to the removal of oxygen-containing functional groups, graphene restores the structure of the hexagonal lattice [26]. Thus, the G peak moves from 1592 cm^{-1} for GO to 1573 cm^{-1} for graphene/SWCNT. Compared to the I_D/I_G value of 1.03 for GO, the I_D/I_G ratio of reduced graphene/SWCNT increases to 1.31, indicating that more lattice defects are introduced during the reduction process. Although the reduced graphene restores the conjugated sp^2 carbon structure, some vacancies are left at the positions bound to the carbon atoms with the removal of oxygen-containing functional groups. These defects eventually lead to an increase in the I_D/I_G value [27].

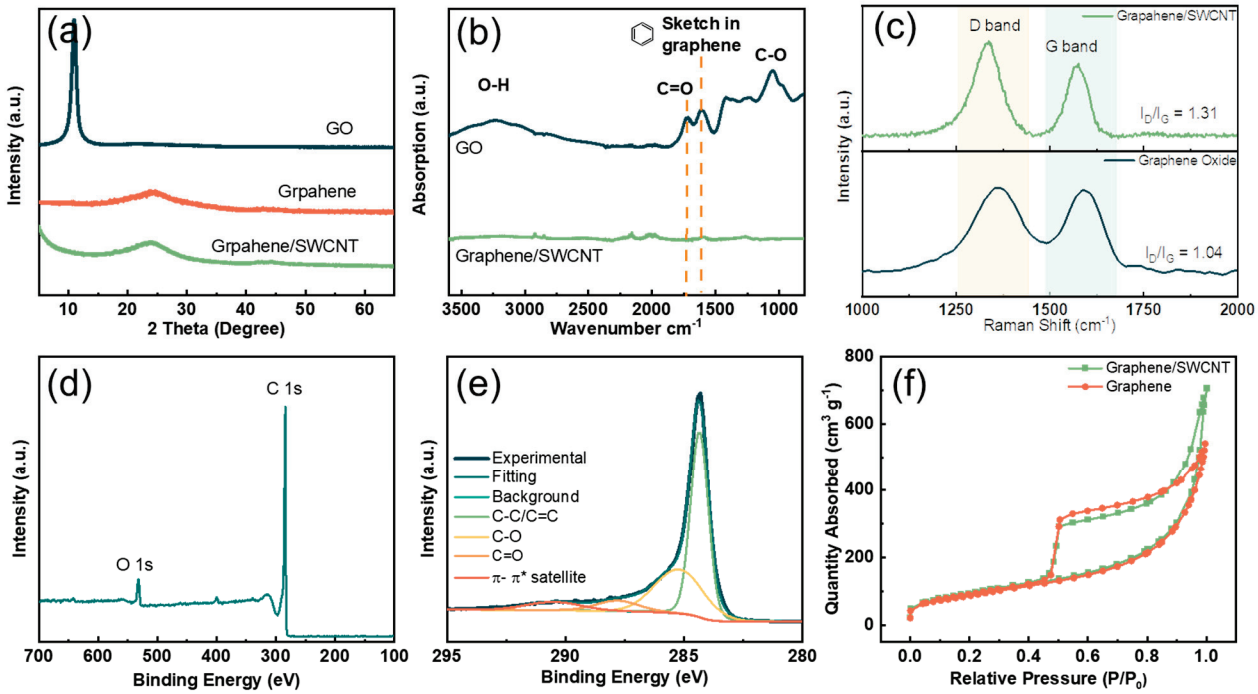

Figure 2. (**a**) XRD patterns of GO, graphene, and graphene/SWCNT; (**b**) FT-IR spectra of GO and graphene/SWCNT; (**c**) Raman spectra of GO and graphene/SWCNT showing the D-band and G-band; (**d**) XPS spectra of graphene/SWCNT. (**e**) analysis of C1s XPS of graphene/SWCNT. (**f**) Nitrogen adsorption/desorption isotherms of graphene and graphene/SWCNT.

XPS (Figure 2d) experiments were carried out to verify the functional group content of the graphene/SWCNT surface. The C1s peak was split, and the fitted curve is shown in Figure 2e. At 284.4 eV, significantly firm peaks were attributed to the graphite carbon (C-C/C=C bond). The weak peaks at 285.2 eV and 288.0 eV, 290.7 eV are due to C-O and C=O, π-π satellite bonds, respectively [28–30]. The π-π satellite bonds were caused by the shake-up process of the pi electrons of graphene and CNTs. The specific relative contents of each chemical bond are shown in Figure S1. The relative content of C-C/C=C bonds is as high as 94.01%. The other carbon–oxygen bonding contents were calculated to be 4.43% C-O and 1.56% C=O. The high content of carbon-carbon bonds implies that hydrazine effectively reduces GO to graphene. To characterize the variation in the specific surface area after SWCNT incorporation, nitrogen adsorption/desorption isotherms were obtained, and the results are shown in Figure 2f. According to the IUPAC classification, all the curves showed typical type IV isotherms [31], indicating the presence of micropores and mesopores. The surface areas of graphene/CNT and graphene were 512 $m^2\ g^{-1}$ and 467 $m^2\ g^{-1}$, respectively. It is evident from the shape of the hysteresis loop that under high pressure, graphene/SWCNT has a more mesoporous structure compared to graphene,

indicating that the carbon nanotubes are effectively incorporated between the graphene sheets, preventing the graphene sheets from re-stacking. The graphene/SWCNT composite exhibits a larger specific surface area, which is more beneficial for absorbing electrolytes and obtaining high-capacity cathode materials.

LICs, as asymmetric electrochemical devices, have different charging and discharging mechanisms for the cathode and anode. LICs' full cell capacity is related to cathode and anode capacity by the following equation, where C is the capacity.

$$\frac{1}{Ccell} = \frac{1}{\text{Ccathode}} + \frac{1}{Canode} \tag{4}$$

Since the anode is pre-lithiated and has a capacity much larger than the cathode, the capacity of the LIC full cell depends on the cathode [32]. Therefore, we first investigated the non-Faradaic process of the cathode, which works similarly to EDLC.

To evaluate the electrochemical behavior of graphene/SWCNT composites as cathodes with the LiBETI, LiFSI, and $LiPF_6$ electrolyte, symmetric capacitor cells were assembled (Figure S2). The cyclic voltammograms (CV) of the LiBETI capacitor within the potential window of 0 to 2.0, 2.5, 3.0, 3.2, and 3.5 V are shown in Figure 3a. The CV curves are nearly rectangular. The galvanostatic current charge/discharge curve is shown in Figure 3b, and the specific capacitance at each voltage is calculated from the discharge curve, as shown in Figure 3c. With increasing voltage, the specific capacitance of graphene/SWCNT can reach 123 F/g at 3.5 V. At a high voltage of 3.5 V, the charge/discharge curves remain parallel to those at low potentials, indicating that the electrolyte exhibits stable electrochemical performance at high voltages. In addition, the EIS (Figure 3d) was tested after charging and discharging at various voltages. The series resistance (Rs), defined as the internal resistance of the electrode in the electrolyte, is typically taken from the high-frequency region of the Nyquist plot. The charge transfer resistance (Rct), measured between the electrode and electrolyte, is taken from the diameter in the Nyquist plot [33,34] with the voltage increasing from 2.0 V to 3.5 V, The Rs is 6.6 Ω, 6.6 Ω, 6.7 Ω, 6.8 Ω, 7.3 Ω. To explore the difference in electrochemical behavior between LiBETI and the commonly used LIC electrolyte $LiPF_6$, LiFSI, the CV curves with scan rate 10 mV/s at 3.5 V are shown in Figure 3e. At a high voltage of 3.5 V, the CV curves of both $LiPF_6$ and LiFSI cannot maintain a parallelogram, attributed to the polarization reaction of the electrolyte [35]. Therefore, LiBETI electrolytes can be used at higher voltages compared to $LiPF_6$ and LiFSI. Compared to the rate performance of the three electrolytes shown in Figure 3f, it is proven that LiBETI has a larger specific capacitance and better rate performance.

In addition, the outstanding capacity (compared with the commercial active carbon capacity of 100 F/g at 3.0 V) of graphene/SWCNT composites in EDLC is attributed to their unique three-dimensional network structure. The main advantages of the composites are as follows: (1) the graphene/SWCNT composites have a large specific surface area and a rich mesoporous structure that can effectively absorb the electrolyte; (2) the use of single-walled carbon nanotubes as spacers prevents graphene from re-stacking; and (3) the integration of carbon tubes enhances the electrical and thermal conductivity of the composites. As discussed by Yuan et al., the electrical conductivity of SWCNT in its axial direction is very high, which makes SWCNT an excellent conductive binder in composites [19,36,37].

A three-electrode LIC full cell was assembled to characterize the electrochemical performance. The cell structure was shown in Figure 4a. The mass ratio between the cathode and anode is 7:3. Lithium foil was used as the reference electrode, graphene/SWCNT as the cathode, and graphite (type P5B, pitch coated graphite) as the anode. The discharge curves for anode pre-lithiation are shown in Figure 4b. The graphite anode exhibits a higher capacity in LiBETI at the same pre-lithiation current and voltage ($LiPF_6$: 452 mAh/g, LiFSI: 668 mAh/g, LiBETI: 700 mAh/g). In the LiBETI electrolyte, the electrode color change before and after pre-lithiation is shown in the illustration, and the electrode changes from black to brownish-yellow, which indicates that after pre-lithiation, the solid electrolyte interface (SEI) film is generated, and the Li ions are intercalated in the graphite [38,39]. To

prevent anode over-discharge [40], the LIC has a discharge cutoff potential of 2.2 V. We also set up experiments at different measurement potential with 2.2~3.8 V (commercial LICs potential 2.2~3.8 V), 2.2~4.2 V, 2.2~4.5 V. First, in LiBETI, the shape of the CV curves (Figure 4c) is well maintained at different voltages for the LIC full cell, indicating the superior reversible property. As shown by the charge and discharge curves in Figure 4d, the specific capacitance of LIC full cell with 3.8 V, 4.2 V, and 4.5 V at 0.1 A g^{-1} current density is calculated to 58 F g^{-1}, 61 F g^{-1}, and 85 F g^{-1}, respectively. The cathode-specific capacitance was calculated using the full cell, (Equation (4)), and it was found that the cathode-specific capacitance was 83 F/g, 88 F/g, 121 F/g, at 4.5 V in $LiPF_6$, LiFSI, and LiBETI, respectively. This is consistent with its EDLC specific capacitance at 3.5 V. The rate performance is shown in Figure 4e. The specific values are shown in Table S1. It was found that in LIC full-cell devices, LiBETI electrolytes show the highest specific capacitance and better rate performance.

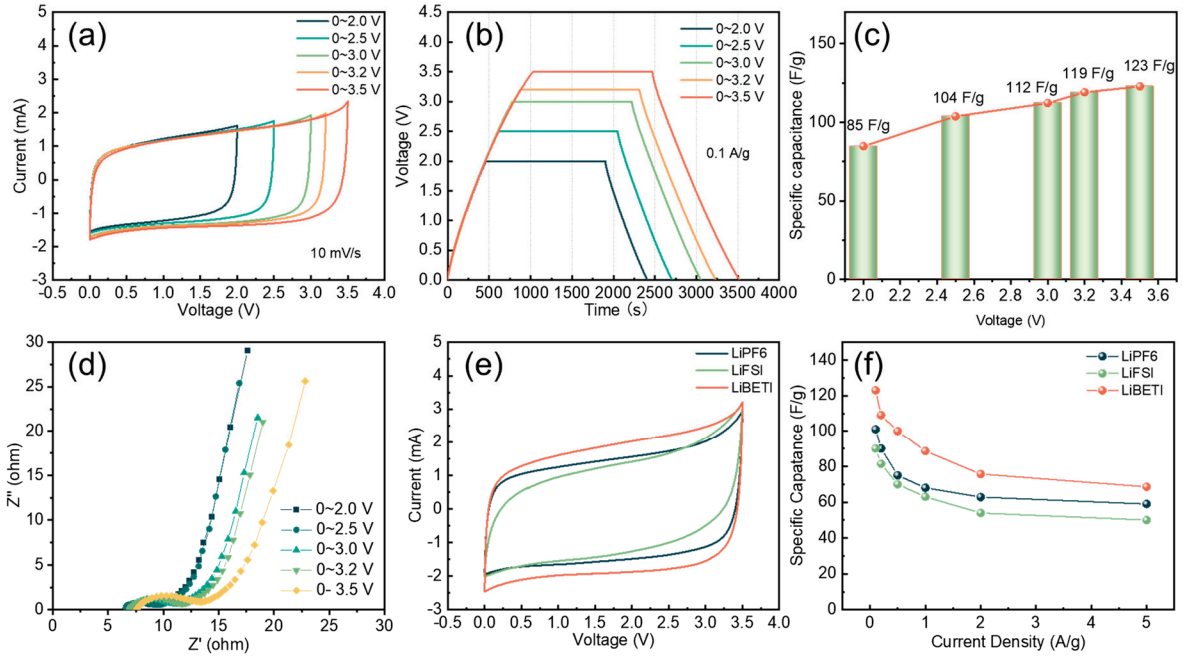

Figure 3. Cathode electrochemical EDLC performance of graphene/SWCNT materials in different electrolytes: (**a**) cyclic voltammograms (CV) curves in LiBETI with scanning rate 10 mV/s, (**b**) galvanostatic charge–discharge curves under different voltages in LiBETI, with 0.1 A/g (**c**) specific capacitance of graphene/SWCNT in LiBETI with different voltage, (**d**) EIS performance of the Nyquist plot under different voltage in LiBETI, (**e**) CV curves, and (**f**) rate performance in $LiPF_6$, LiBETI, and LiFSI at 3.5 V.

To investigate the resistance of LIC full cells in $LiPF_6$, LiFSI, and LiBETI, Figure 4f compares Nyquist curves. The slope LiBETI > $LiPF_6$ > LiFSI in the low-frequency region indicates that LiBETI has the fastest ion diffusion rate and more optimal capacitive behavior. In the high-frequency part, the arc radius in high-frequency area LiBETI < LiPF6 < LiFSI, indicating that the electrode has lower charge transfer resistance and a faster ion transfer rate in the LiBETI electrolyte. The equivalent circuit was fitted using EC-Lab; the included circuit is shown in the inset of Figure 4f, and the fitting result is shown in Figure S3.

To investigate the electrochemical behavior of the cathode and anode further, a three-electrode system was used to explore the potential changes in the cathode and anode. As shown in Figure 5, the potential of the anode remained constant as the charging voltage increased during the charging and discharging process. When the voltage was increased to 4.5 V, the anode potential was close to that achieved when charging to 3.8 V, with a drop of only 0.01 V. From this phenomenon, it can be inferred that the generation of an anode SEI film was sufficiently stable.

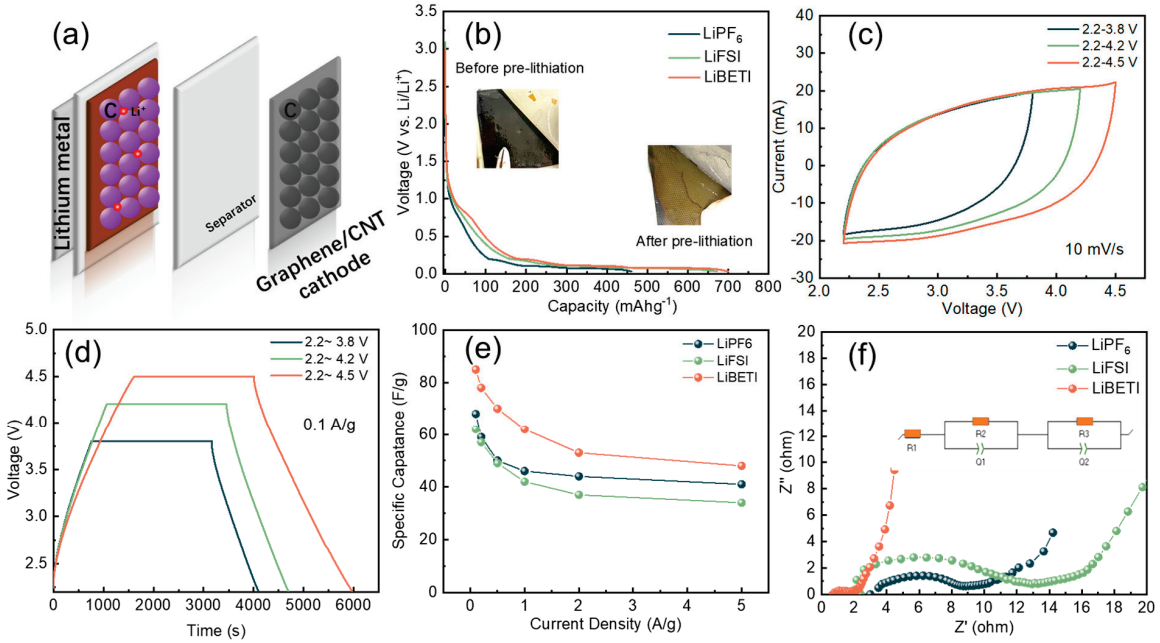

Figure 4. (**a**) Schematic diagram of LIC full cell structure. (**b**) Anode pre-lithiation discharge curves in different electrolytes to 0.08 V at 20 mA g^{-1}. The inset shows the anode comparison before and after pre-lithiation in LiBETI electrolyte. The LIC full cell electrochemical performance: (**c**) CV curves in LiBETI with scanning rate 10 mV/s, (**d**) galvanostatic charge–discharge curves under different voltage in LiBETI, with 0.1 A/g. (**e**) Rate performance in $LiPF_6$, LiBETI, and LiFSI at 2.2~4.5 V. (**f**) EIS performance of Nyquist curves in $LiPF_6$, LiBETI, and LiFSI, and the inset shows the fitted circuit in LiBETI.

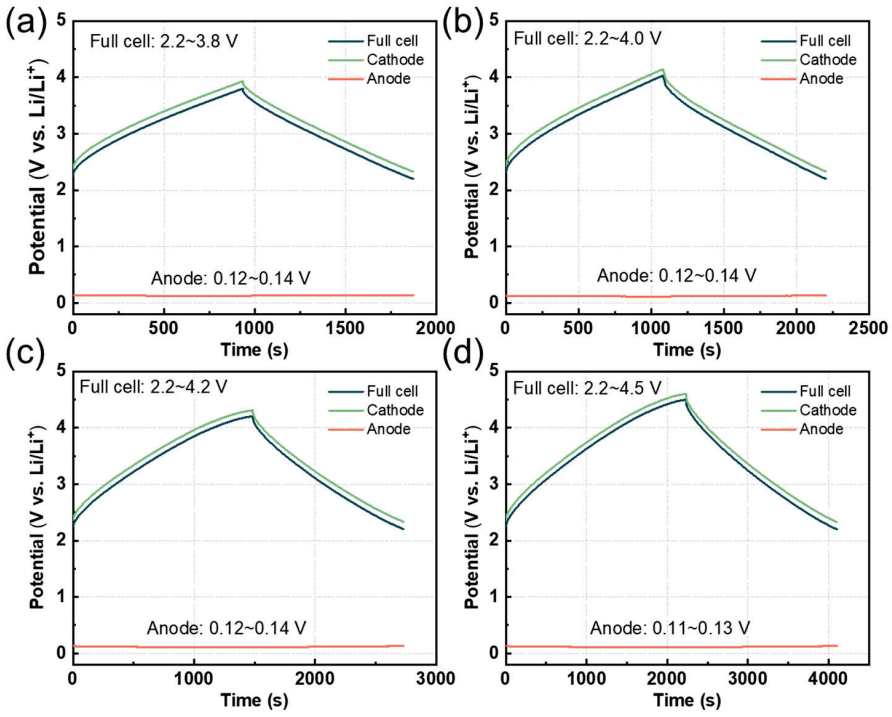

Figure 5. Three-electrode LIC charge/discharge curve with lithium as a reference electrode. Cathode, anode, and LIC full-cell potential at a current density of 0.1 A g^{-1} with different voltages (**a**) 3.8 V; (**b**) 4.0 V; (**c**) 4.2 V; and (**d**) 4.5 V.

To confirm whether the anode SEI film was stable, after 50 charging and discharging cycles at 2.2–4.5 V voltage, we performed an SEM test on the anode electrode film to confirm the surface morphology of the electrode film. The anode in the $LiPF_6$ electrolyte (Figure 6a) was arranged evenly and the graphite block with the size about 3–6 µm. However, compared with the graphite anode in $LiPF_6$, in LiFSI, the surface of the anode graphite material was not flat, and cracks were observed in Figure 6b) [41]; the size of the block did not change significantly, indicating that the anode deteriorated in the LiFSI electrolyte as a result of high voltage cycling. Significantly, a dense SEI film was generated on the anode surface in the LiBETI electrolyte, which can be observed in Figure 6c. It was also verified that the LiBETI electrolyte can help to form a stable SEI film during the anode prelithiation process. As shown in Figure 6d, the LIC full cell presents a typical hybrid charging and discharging mechanism that combines battery and capacitor energy storage. During charging, anions ($BETI^-$) in the electrolyte are adsorbed to the cathode due to electrostatic interaction, and Li^+ intercalates into the anode. When the cell is discharged from the maximum voltage, the $BETI^-$ ions desorb from the cathode and the Li^+ ions de-intercalate from the anode into the electrolyte. In LIC, lithium storage in graphite is achieved through intercalation between graphite layers, and the LiC_x structure is shown in Figure 6e.

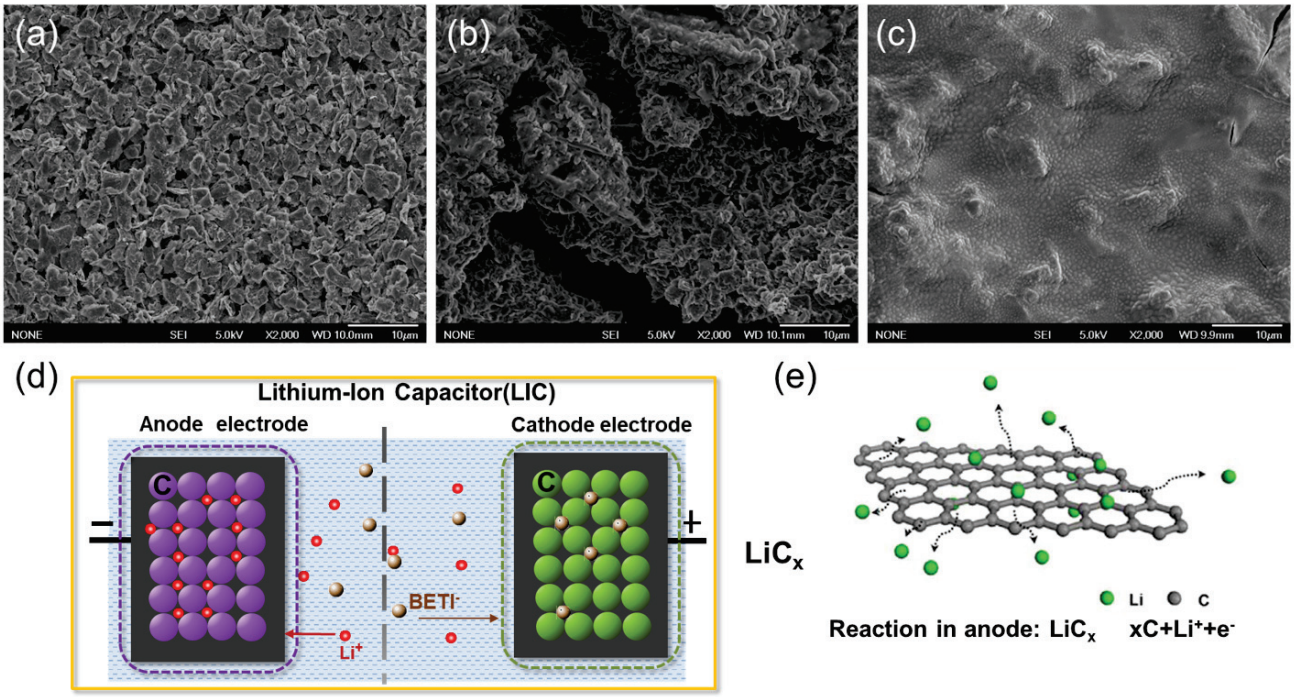

Figure 6. SEM images of graphite anode film after 50 cycles (**a**) with $LiPF_6$, (**b**) with LiFSI, (**c**) with LiBETI, (**d**) charge and discharge mechanism schematic in LIC, and (**e**) schematic diagram of graphite anode structure after pre-lithiation.

The power density and energy density of the graphene/SWCNT LIC are shown in Figure 7a in comparison with the previously reported LICs. With the potential of 2.2–4.5 V, it can be revealed that the graphene/SWCNT LIC achieves a high energy density of 182.6 Wh kg^{-1} at a power density of 2678.0 W kg^{-1}. Even at a high-power density of 23,437.1 W kg^{-1}, the graphene/SWCNT LIC maintains a high energy density of 102.7 Wh kg^{-1}, which exhibits excellent rate performance. Compared with others' work, for example, the previous work Graphene || Graphene/SnO_2 LIC shows a density of 186.0 Wh kg^{-1} at a power density of 146.3 W kg^{-1}. It offers a similar energy density to us, but the power density is much lower. The specific energy density and power density values of other works are in Table S2 [42–45]. Moreover, the cycling performance of the

assembled graphene/SWCNT LIC was also investigated (Figure 7b). It showed excellent cycling stability at high voltage from 2.2 to 4.5 V with a current density of 2 A g^{-1} and exhibited a high-capacity ratio of 72.7% after 10,000 cycles, which was attributed to the stabilized anode SEI film that kept the anode potential constant and stabilized the LIC voltage window at high potential. The assembled high-voltage, high-energy-density LICs show broad prospects for practical applications.

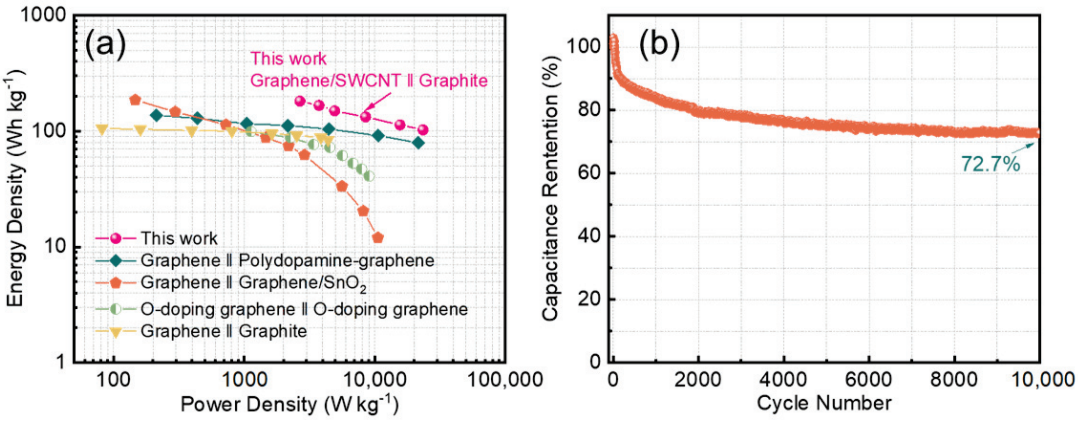

Figure 7. (**a**) Ragone plot of graphene/SWCNT LIC with LiBETI in comparison with previously reported LICs, (**b**) cycle performance of graphene/SWCNT LIC with LiBETI in 2.2~4.5 V.

4. Conclusions

In conclusion, we synthesized graphene/SWCNT 3D structure nanocomposites, in which SWCNT effectively prevents graphene re-stacking and provides a large specific surface area, which offers additional active sites for ion adsorption. The three-electrode system was explored to investigate LiBETI as an electrolyte with high conductivity and excellent electrochemical and mechanical stability. As a result, the asymmetric LIC device assembled using graphene/SWCNT as the cathode and pre-lithiated graphite as the anode has a specific capacitance of up to 85 F g^{-1} and maintains a capacity retention of up to 72% after 10,000 cycles. In addition, it exhibits a maximum energy density of 182.6 Wh kg^{-1} at a power density of 2678.0 W kg^{-1}. Significantly, this work opens up a new avenue for the practical application of low-cost, advanced carbon materials for next-generation energy-storage technologies.

Supplementary Materials: The following supporting information can be downloaded at https://www.mdpi.com/article/10.3390/nano14010045/s1, Figure S1: The specific relative contents of each chemical bond of graphene/SWCNT. Figure S2: Schematic diagram of symmetrical capacitor structure. Table S1: Specific capacitance of LIC in different electrolytes with different current densities. Figure S3: LIC fitting equivalent circuit in LiBETI electrolyte. Table S2: The performance of the previously reported LICs comparison to Graphene/SWCNT LIC.

Author Contributions: H.Y.: conceptualization, investigation, formal analysis, visualization, writing—original draft. J.T.: conceptualization, formal analysis, writing—review and editing, supervision, project administration, funding acquisition. K.Z.: visualization, validation, writing—review and editing. S.L.: formal analysis, visualization. G.X.: visualization. L.-C.Q.: formal analysis, visualization, writing—review and editing. All authors have read and agreed to the published version of the manuscript.

Funding: A part of this work was supported by the NIMS Electron Microscopy Analysis Station, the Nanostructural Characterization Group, and by the NIMS Microstructural Characterization Platform as a program of the "Nanotechnology Platform" of the Ministry of Education, Culture, Sports, Science and Technology (MEXT), Japan.

Data Availability Statement: Data are contained within the article or Supplementary Materials.

Conflicts of Interest: The authors declare no conflicts of interest.

References

1. Choi, N.S.; Chen, Z.; Freunberger, S.A.; Ji, X.; Sun, Y.K.; Amine, K.; Yushin, G.; Nazar, L.F.; Cho, J.; Bruce, P.G. Challenges facing lithium batteries and electrical double-layer capacitors. *Angew. Chem. Int. Ed.* **2012**, *51*, 9994–10024. [CrossRef] [PubMed]
2. Wang, Y.; Song, Y.; Xia, Y. Electrochemical capacitors: Mechanism, materials, systems, characterization and applications. *Chem. Soc. Rev.* **2016**, *45*, 5925–5950. [CrossRef] [PubMed]
3. Zhou, L.; Zhang, K.; Hu, Z.; Tao, Z.; Mai, L.; Kang, Y.M.; Chou, S.L.; Chen, J. Recent developments on and prospects for electrode materials with hierarchical structures for lithium-ion batteries. *Adv. Energy Mater.* **2018**, *8*, 1701415. [CrossRef]
4. Manthiram, A. An outlook on lithium ion battery technology. *ACS Cent. Sci.* **2017**, *3*, 1063–1069. [CrossRef] [PubMed]
5. Xin, S.; You, Y.; Wang, S.; Gao, H.-C.; Yin, Y.-X.; Guo, Y.-G. Solid-state lithium metal batteries promoted by nanotechnology: Progress and prospects. *ACS Energy Lett.* **2017**, *2*, 1385–1394. [CrossRef]
6. Choi, J.W.; Aurbach, D. Promise and reality of post-lithium-ion batteries with high energy densities. *Nat. Rev. Mater.* **2016**, *1*, 16013. [CrossRef]
7. Ruiz, V.; Pfrang, A.; Kriston, A.; Omar, N.; Van den Bossche, P.; Boon-Brett, L. A review of international abuse testing standards and regulations for lithium ion batteries in electric and hybrid electric vehicles. *Renew. Sustain. Energy Rev.* **2018**, *81*, 1427–1452. [CrossRef]
8. Han, P.; Xu, G.; Han, X.; Zhao, J.; Zhou, X.; Cui, G. Lithium ion capacitors in organic electrolyte system: Scientific problems, material development, and key technologies. *Adv. Energy Mater.* **2018**, *8*, 1801243. [CrossRef]
9. Muzaffar, A.; Ahamed, M.B.; Deshmukh, K.; Thirumalai, J. A review on recent advances in hybrid supercapacitors: Design, fabrication and applications. *Renew. Sustain. Energy Rev.* **2019**, *101*, 123–145. [CrossRef]
10. Zhai, Y.; Dou, Y.; Zhao, D.; Fulvio, P.F.; Mayes, R.T.; Dai, S. Carbon materials for chemical capacitive energy storage. *Adv. Mater.* **2011**, *23*, 4828–4850. [CrossRef]
11. Salunkhe, R.R.; Lee, Y.H.; Chang, K.H.; Li, J.M.; Simon, P.; Tang, J.; Torad, N.L.; Hu, C.C.; Yamauchi, Y. Nanoarchitectured graphene-based supercapacitors for next-generation energy-storage applications. *Chem.—A Eur. J.* **2014**, *20*, 13838–13852. [CrossRef] [PubMed]
12. Liu, W.; Zhang, X.; Xu, Y.; Wang, L.; Li, Z.; Li, C.; Wang, K.; Sun, X.; An, Y.; Wu, Z.S. 2D Graphene/MnO Heterostructure with Strongly Stable Interface Enabling High-Performance Flexible Solid-State Lithium-Ion Capacitors. *Adv. Funct. Mater.* **2022**, *32*, 2202342. [CrossRef]
13. Sun, Y.; Tang, J.; Qin, F.; Yuan, J.; Zhang, K.; Li, J.; Zhu, D.-M.; Qin, L.-C. Hybrid lithium-ion capacitors with asymmetric graphene electrodes. *J. Mater. Chem. A* **2017**, *5*, 13601–13609. [CrossRef]
14. Li, X.; Sun, M.; Xu, C.; Zhang, X.; Wang, G.; Tian, Y.; Zhu, G. Fast Kinetic Carbon Anode Inherited and Developed from Architectural Designed Porous Aromatic Framework for Flexible Lithium Ion Micro Capacitors. *Adv. Funct. Mater.* **2023**, *33*, 2300460. [CrossRef]
15. Wang, J.; Meng, Q.; Zhou, X.; Li, X.; Yang, J.; Tang, J.; Zhang, Y. Bamboo-derived flake-layer hierarchically porous carbon coupling nano-Si@ porous carbon for advanced high-performance Li-ion capacitor. *J. Energy Storage* **2023**, *63*, 107044. [CrossRef]
16. Wang, Q.; Liu, F.; Jin, Z.; Qiao, X.; Huang, H.; Chu, X.; Xiong, D.; Zhang, H.; Liu, Y.; Yang, W. Hierarchically divacancy defect building dual-activated porous carbon fibers for high-performance energy-storage devices. *Adv. Funct. Mater.* **2020**, *30*, 2002580. [CrossRef]
17. Banerjee, A.; Upadhyay, K.K.; Puthusseri, D.; Aravindan, V.; Madhavi, S.; Ogale, S. MOF-derived crumpled-sheet-assembled perforated carbon cuboids as highly effective cathode active materials for ultra-high energy density Li-ion hybrid electrochemical capacitors (Li-HECs). *Nanoscale* **2014**, *6*, 4387–4394. [CrossRef]
18. Lee, J.H.; Shin, W.H.; Lim, S.Y.; Kim, B.G.; Choi, J.W. Modified graphite and graphene electrodes for high-performance lithium ion hybrid capacitors. *Mater. Renew. Sustain. Energy* **2014**, *3*, 22. [CrossRef]
19. Yuan, W.; Zhang, Y.; Cheng, L.; Wu, H.; Zheng, L.; Zhao, D. The applications of carbon nanotubes and graphene in advanced rechargeable lithium batteries. *J. Mater. Chem. A* **2016**, *4*, 8932–8951. [CrossRef]
20. Kim, Y.; Woo, S.C.; Lee, C.S.; Park, J.S.; Seo, H.; Kim, J.-H.; Song, J.H. Electrochemical investigation on high-rate properties of graphene nanoplatelet-carbon nanotube hybrids for Li-ion capacitors. *J. Electroanal. Chem.* **2020**, *863*, 114060. [CrossRef]
21. Xiao, Y.; Liu, J.; He, D.; Chen, S.; Peng, W.; Hu, X.; Liu, T.; Zhu, Z.; Bai, Y. Facile synthesis of graphene with fast ion/electron channels for high-performance symmetric lithium-ion capacitors. *ACS Appl. Mater. Interfaces* **2021**, *13*, 38266–38277. [CrossRef] [PubMed]
22. Li, C.; Wu, W.; Zhang, S.; He, L.; Zhu, Y.; Wang, J.; Fu, L.; Chen, Y.; Wu, Y.; Huang, W. A high-voltage aqueous lithium ion capacitor with high energy density from an alkaline–neutral electrolyte. *J. Mater. Chem. A* **2019**, *7*, 4110–4118. [CrossRef]
23. Péter, L.; Arai, J. Anodic dissolution of aluminium in organic electrolytes containing perfluoroalkylsulfonyl imides. *J. Appl. Electrochem.* **1999**, *29*, 1053–1061. [CrossRef]
24. Zhang, F.; Tang, J.; Shinya, N.; Qin, L.-C. Hybrid graphene electrodes for supercapacitors of high energy density. *Chem. Phys. Lett.* **2013**, *584*, 124–129. [CrossRef]
25. Li, W.; Yang, X.; Chen, Z.; Lv, T.; Wang, X.; Qiu, J. Synthesis and structure regulation of armor-wearing biomass-based porous carbon: Suppression the leakage current and self-discharge of supercapacitors. *Carbon* **2022**, *196*, 136–145. [CrossRef]
26. Stoller, M.D.; Park, S.; Zhu, Y.; An, J.; Ruoff, R.S. Graphene-based ultracapacitors. *Nano Lett.* **2008**, *8*, 3498–3502. [CrossRef]

27. Lin, S.; Tang, J.; Zhang, K.; Chen, Y.; Gao, R.; Yin, H.; Qin, L.-C. Tuning oxygen-containing functional groups of graphene for supercapacitors with high stability. *Nanoscale Adv.* **2023**, *5*, 1163–1171. [CrossRef]
28. Kuang, B.; Song, W.; Ning, M.; Li, J.; Zhao, Z.; Guo, D.; Cao, M.; Jin, H. Chemical reduction dependent dielectric properties and dielectric loss mechanism of reduced graphene oxide. *Carbon* **2018**, *127*, 209–217. [CrossRef]
29. Chen, S.; Gao, W.; Chao, Y.; Ma, Y.; Zhang, Y.; Ren, N.; Chen, H.; Jin, L.; Li, J.; Bai, Y. Low temperature preparation of pore structure controllable graphene for high volumetric performance supercapacitors. *Electrochim. Acta* **2018**, *273*, 181–190. [CrossRef]
30. Al-Gaashani, R.; Najjar, A.; Zakaria, Y.; Mansour, S.; Atieh, M. XPS and structural studies of high quality graphene oxide and reduced graphene oxide prepared by different chemical oxidation methods. *Ceram. Int.* **2019**, *45*, 14439–14448. [CrossRef]
31. Guan, T.; Zhao, J.; Zhang, G.; Wang, J.; Zhang, D.; Li, K. Template-free synthesis of honeycomblike porous carbon rich in specific 2–5 nm mesopores from a pitch-based polymer for a high-performance supercapacitor. *ACS Sustain. Chem. Eng.* **2018**, *7*, 2116–2126. [CrossRef]
32. Naderi, R.; Shellikeri, A.; Hagen, M.; Cao, W.; Zheng, J. The influence of anode/cathode capacity ratio on cycle life and potential variations of lithium-ion capacitors. *J. Electrochem. Soc.* **2019**, *166*, A2610. [CrossRef]
33. Guo, N.; Luo, W.; Guo, R.; Qiu, D.; Zhao, Z.; Wang, L.; Jia, D.; Guo, J. Interconnected and hierarchical porous carbon derived from soybean root for ultrahigh rate supercapacitors. *J. Alloys Compd.* **2020**, *834*, 155115. [CrossRef]
34. Li, Y.; Liu, Y.; Wang, M.; Xu, X.; Lu, T.; Sun, C.Q.; Pan, L. Phosphorus-doped 3D carbon nanofiber aerogels derived from bacterial-cellulose for highly-efficient capacitive deionization. *Carbon* **2018**, *130*, 377–383. [CrossRef]
35. Aida, T.; Murayama, I.; Yamada, K.; Morita, M. Analyses of capacity loss and improvement of cycle performance for a high-voltage hybrid electrochemical capacitor. *J. Electrochem. Soc.* **2007**, *154*, A798. [CrossRef]
36. Paulson, S.; Helser, A.; Nardelli, M.B.; Taylor, R.; Falvo, M.; Superfine, R.; Washburn, S. Tunable resistance of a carbon nanotube-graphite interface. *Science* **2000**, *290*, 1742–1744. [CrossRef]
37. Yu, D.; Dai, L. Self-assembled graphene/carbon nanotube hybrid films for supercapacitors. *J. Phys. Chem. Lett.* **2010**, *1*, 467–470. [CrossRef]
38. Forney, M.W.; Ganter, M.J.; Staub, J.W.; Ridgley, R.D.; Landi, B.J. Prelithiation of silicon–carbon nanotube anodes for lithium ion batteries by stabilized lithium metal powder (SLMP). *Nano Lett.* **2013**, *13*, 4158–4163. [CrossRef]
39. Gourdin, G.; Smith, P.H.; Jiang, T.; Tran, T.N.; Qu, D. Lithiation of amorphous carbon negative electrode for Li ion capacitor. *J. Electroanal. Chem.* **2013**, *688*, 103–112. [CrossRef]
40. Ouyang, D.; Chen, M.; Liu, J.; Wei, R.; Weng, J.; Wang, J. Investigation of a commercial lithium-ion battery under overcharge/over-discharge failure conditions. *RSC Adv.* **2018**, *8*, 33414–33424. [CrossRef]
41. Scandurra, A.; Ruffino, F.; Censabella, M.; Terrasi, A.; Grimaldi, M.G. Dewetted gold nanostructures onto exfoliated graphene paper as high efficient glucose sensor. *Nanomaterials* **2019**, *9*, 1794. [CrossRef] [PubMed]
42. Lee, J.H.; Shin, W.H.; Ryou, M.-H.; Jin, J.K.; Kim, J.; Choi, J.W. Functionalized Graphene for High Performance Lithium Ion Capacitors. *ChemSusChem* **2012**, *5*, 2328–2333. [CrossRef] [PubMed]
43. Yang, Y.; Lin, Q.; Ding, B.; Wang, J.; Malgras, V.; Jiang, J.; Li, Z.; Chen, S.; Dou, H.; Alshehri, S.M. Lithium-ion capacitor based on nanoarchitectured polydopamine/graphene composite anode and porous graphene cathode. *Carbon* **2020**, *167*, 627–633. [CrossRef]
44. Xiao, Z.; Zhao, L.; Yu, Z.; Zhang, M.; Li, S.; Zhang, R.; Ayub, M.; Ma, X.; Ning, G.; Xu, C. Multilayered graphene endowing superior dispersibility for excellent low temperature performance in lithium-ion capacitor as both anode and cathode. *Chem. Eng. J.* **2022**, *429*, 132358. [CrossRef]
45. Ajuria, J.; Arnaiz, M.; Botas, C.; Carriazo, D.; Mysyk, R.; Rojo, T.; Talyzin, A.V.; Goikolea, E. Graphene-based lithium ion capacitor with high gravimetric energy and power densities. *J. Power Sources* **2017**, *363*, 422–427. [CrossRef]

nanomaterials

MDPI

Article

Selective Laser-Assisted Direct Synthesis of MoS_2 for Graphene/MoS_2 Schottky Junction

Min Ji Jeon [1], Seok-Ki Hyeong [2], Hee Yoon Jang [1], Jihun Mun [3], Tae-Wook Kim [4,5], Sukang Bae [2,5,*] and Seoung-Ki Lee [1,*]

[1] School of Material Science and Engineering, Pusan National University, Busan 46241, Republic of Korea; minji@pusan.ac.kr (M.J.J.)
[2] Institute of Advanced Composite Materials, Korea Institute of Science and Technology, Wanju 55324, Republic of Korea
[3] Advanced Instrumentation Institute, Korea Research Institute of Standards and Science, Daejeon 34113, Republic of Korea
[4] Department of Flexible and Printable Electronics, Jeonbuk National University, Jeonju-si 54896, Republic of Korea
[5] Department of JBNU-KIST Industry-Academia Convergence Research, Jeonbuk National University, Jeonju-si 54896, Republic of Korea
* Correspondence: sbae@kist.re.kr (S.B.); ifriend@pusan.ac.kr (S.-K.L.); Tel.: +82-63-219-8158 (S.B.); +82-51-510-2999 (S.-K.L.)

Abstract: Implementing a heterostructure by vertically stacking two-dimensional semiconductors is necessary for responding to various requirements in the future of semiconductor technology. However, the chemical-vapor deposition method, which is an existing two-dimensional (2D) material-processing method, inevitably causes heat damage to surrounding materials essential for functionality because of its high synthesis temperature. Therefore, the heterojunction of a 2D material that directly synthesized MoS_2 on graphene using a laser-based photothermal reaction at room temperature was studied. The key to the photothermal-reaction mechanism is the difference in the photothermal absorption coefficients of the materials. The device in which graphene and MoS_2 were vertically stacked using a laser-based photothermal reaction demonstrated its potential application as a photodetector that responds to light and its stability against cycling. The laser-based photothermal-reaction method for 2D materials will be further applied to various fields, such as transparent display electrodes, photodetectors, and solar cells, in the future.

Keywords: selective laser annealing; graphene; molybdenum disulfide (MoS_2); photothermal reaction; heterostructure; photodetector

1. Introduction

With the development of next-generation devices and the introduction of new functionalities, the primary objective for semiconductor technology is to increase integration density while achieving various form factors through downscaling and ultra-thinning techniques [1–3]. Pioneering research has highlighted the potential of thinning traditional materials such as silicon and oxide semiconductors to improve mechanical flexibility without compromising their quality; however, the innate three-dimensional (3D) crystalline structures of class materials imply inevitable limits to continuous downscaling strategies owing to several challenges such as increased surface energy, quantum effect-induced property changes, and thermal instability. In contrast, 2D crystalline materials, characterized by atomic interconnections in a 2D lattice, inherently retain their electrical, mechanical, and physical properties, even at the atomic scale [4,5]. For these reasons, they have attracted considerable attention as potential core materials for future electronic devices [6]. Notably, these 2D materials are highly compatible [7] with traditional Si-based complementary

metal-oxide semiconductor (CMOS) manufacturing processes, leading to promising results in devices with hybrid structures [8,9].

Methods such as metal-organic chemical-vapor deposition (MOCVD), molecular-beam epitaxy, and atomic layer deposition have led to significant progress in the synthesis of transition-metal dichalcogenides, which are representative 2D semiconductors, on various substrates [10–13]. Even though these methods achieve high-quality materials capable of synthesizing single crystals or controlling the number of layers at the wafer scale, they rely on high synthesis temperatures (>700 °C) [14,15], post-thermal treatments, or specific substrates. Such dependence inevitably necessitates a transfer to the target substrate post-synthesis. Unfortunately, this transfer process typically results in unforeseen chemical contamination, physical wrinkles, and damage, making the prediction of the post-transfer quality and uniformity of the synthesized materials [16,17] increasingly challenging. To this end, laser-assisted synthesis methodologies have been proposed as potential solutions to overcome the limitations of conventional techniques [18–22]. Because of the monochromatic, coherent, and collimated nature of laser sources, photothermal reactions on materials can be systemically controlled by selectively [23–26] inducing lattice vibrations. This allows targeted thermal annealing even when the device chip comprises thermally fragile parts. In this context, the effectiveness of laser-assisted synthesis has been proven through research on the selective synthesis of 2D materials using lasers or the partial modulation of the interface properties of electronics [20–22]. Moreover, significant findings are emerging, demonstrating the direct synthesis of 2D heterostructures beyond the scope of individual materials [27–31]: This is accomplished by integrating distinct 2D materials, particularly n-type MoS_2 with p-type WS_2, eliminating the need for a transfer process. Therefore, various heterojunction structures based on 2D materials need to be implemented and validated by exploiting the universal applicability of selective-laser photothermal reactions.

Herein, we implement a graphene/MoS_2 heterojunction structure by integrating n-type MoS_2 on semi-metallic graphene via a laser-assisted selective photothermal-reaction method by optimizing the photothermal and laser parameters. For the synthesis of MoS_2, a thermally decomposable $(NH_4)_2MoS_4$ precursor was mixed with an organic solvent, and a fiber laser ($\lambda = 1.06$ μm) with a high absorption rate for the MoS_2 precursor was selected to prevent damage to the underlying graphene and substrate. Unlike the traditional CVD synthesis method, controlling the thermal-spreading range using the laser parameters suppressed damage to the surrounding layers, such as the underlying graphene and SiO_2/Si wafer, which provided a means to implement a graphene/MoS_2-based photodetector with a robust interface.

2. Experimental Section

2.1. Materials

Poly(methylmethacrylate) ($(C_5O_2H_8)_n$; PMMA), ammonium tetrathiomolybdate ($(NH_4)_2MoS_4$), CAS No. 15060-55-6), and hexamethyldisilazane($(CH_3)_3SiNHSi(CH_3)_3$, CAS No. 999-97-3) were purchased from Sigma-Aldrich (St. Louis, MI, USA). A photoresist (AZ 5214-E; PR, LOT NO. USAW417063) and Developer (AZ 300 MIF developer, LOT NO. KR387425) were purchased from Merck (Rahway, NJ, USA). Dimethyl sulfoxide ($(CH_3)_2SO$, CAS No. 67-68-5) and ammonium persulfate($(NH_4)_2S_2O_8$, CAS No. 7727-54-0) were purchased from Daejung Chemicals (Siheung, Republic of Korea).

2.2. Graphene Synthesis and Transfer

Monolayer graphene was grown via CVD on 25 μm-thick copper foils [32] at temperatures close to 1000 °C using CH_4 (125 sccm) as a carbon source and H_2 (100 sccm) as a reactant gas [33]. The PMMA solution was spin-coated onto the graphene at 3000 rpm for 30 s to serve as a supporting layer. the specimen was annealed on a hot plate at 100 °C for 1 min. The surface of the graphene/copper foils was treated with an O_2 plasma process (power 150 W, time 30 s) to improve the copper foils' wettability. Subsequently, graphene was separated by etching the Cu foil in an ammonium persulfate solution (2 g ammonium

persulfate in 100 mL deionized (DI) water) for 4 h. Once all of the copper was etched away, only the PMMA/graphene film remained, which was lifted using a glass slide and rinsed twice in DI water. The PMMA/graphene layer was then transferred to a 300 nm SiO_2/P+ Si substrate. Finally, to remove PMMA from the graphene, it was immersed in acetone in two steps: first for 30 min and then for an additional 90 min.

2.3. Graphene Patterning, Thermal Cleaning, and Doping

The formation of the graphene-patterned array was achieved using typical photolithography and oxygen plasma etching methods. The graphene was uniformly covered by the PR solution, spinning at 3000 rpm for 30 s, and then baked at 95 °C for 2 min. Subsequently, the sample was exposed to aligner UV light for 15 s, creating a graphene-pattern array with a size of 100 μm × 300 μm. The samples were rinsed with a developer, followed by a rinse with deionized water, and then dried using nitrogen. The exposed graphene regions, not protected by PR, were etched through a reactive ion etching process. The sample was then soaked in acetone for about 30 min to remove the PR from the graphene. As a result, a graphene-pattern array was obtained. To thoroughly remove the PMMA and PR residues that remained after the acetone treatment, the patterned graphene underwent hydrogen annealing (H_2) at 300 °C for 20 min, ensuring a clean surface [34–36]. Then, the patterned graphene was doped for 12 h to be completely submerged in a hexamethyldisilazane (HMDS) solution. Additionally, the doped specimen was dried with nitrogen gas.

2.4. MoS_2 Synthesis on Graphene

To create a vertically stacked MoS_2 heterostructure on patterned graphene, a 0.633 M solution was formulated by mixing 1.0 g of $(NH_4)_2MoS_4$ precursor with 6 mL of dimethyl sulfoxide (DMSO). A multistep coating technique ensured uniform coverage of the precursor solution on the graphene. SiO_2/Si wafers (with a 300-nm-thick SiO_2 layer) underwent two spin-coating stages: an initial 10 s spin at 500 rpm, followed by a 30 s spin at 2500 rpm. Subsequently, the specimen was annealed on a hot plate at 150 °C for 3 min to evaporate any remaining solvent. A fiber laser with a 1.06 μm wavelength and 20 W output was employed to selectively anneal the precursor layer, thereby synthesizing MoS_2. The parameters for optimizing MoS_2 synthesis via the laser were as follows: (i) laser power (from 1 W to 20 W), (ii) scan speed (from 10 mm/s to 500 mm/s), and (iii) frequency (from 20 kHz to 200 kHz). After the selective synthesis of MoS_2, the untreated parts were washed away by immersion in DMSO solvent.

2.5. Device Characterization

The I–V characteristics of the device were measured under low-vacuum conditions (5×10^{-3} Torr) using a probe station connected to a parameter analyzer (4200, Keithley, Cleveland, OH, USA). To confirm the optoelectronic characteristics, the devices were illuminated using a white-light halogen lamp, and the light intensities were measured using a power meter (PM 100d, Thorlabs, Newton, NJ, USA).

3. Results and Discussion

Figure 1a,b illustrates a schematic of the graphene/MoS_2-heterostructure fabrication through laser-based photothermal synthesis, complemented by the corresponding optical-microscopy images for each step. Initially, graphene was synthesized using the conventional CVD method [33,37], which enabled the uniform production of monolayer graphene over a large area. The graphene was then transferred to a SiO_2/Si wafer using a PMMA supporting layer. Following the removal of the supporting layer, a rectangular graphene pattern (100 μm × 300 μm) was defined using photolithography and reactive ion etching with O_2 plasma [38]. During these transfer and patterning stages, water molecules may be trapped between the graphene and substrate, or contamination from organic compounds may occur. Therefore, the patterned graphene was annealed via a thermal-cleaning process at 300 °C in a hydrogen atmosphere for 20 min. Furthermore, a

self-assembled monolayer (SAM) of HMDS was applied as a buffer layer to the graphene via a dipping process. This layer mitigated unintended doping effects on the graphene and protected the graphene from the subsequent laser-synthesis step. Subsequently, an ammonium tetrathiomolybdate ($(NH_4)_2MoS_4$; ATM) precursor solution was spin-coated onto the patterned graphene. Considering the contrasting nature of the graphene pattern (hydrophobic) and SiO_2 surface (hydrophilic), achieving a uniform precursor coating on this nonuniform surface is challenging. The optimization strategies for these coatings are discussed in Figure 2. After forming a uniform precursor film, we employed a fiber laser (λ = 1.06 μm) to synthesize the MoS_2 pattern on the preformed graphene pattern. We chose a fiber laser among the laser sources with various wavelengths because of its low optical absorption in the surrounding materials, such as graphene, SiO_2, and Si; however, it has high optical absorption only in the $(NH_4)_2MoS_2$ precursor. Therefore, only the precursor layer could be selectively heated and thermally decomposed into MoS_2 [39]. In addition, the fiber laser had a low absorption rate in MoS_2, even if MoS_2 was synthesized after the precursor was thermally decomposed; therefore, the laser penetrated the MoS_2 [23] without thermal damage. This was the key principle for realizing the graphene/MoS_2 heterostructure by synthesizing MoS_2 without damaging graphene in the lower layer. More importantly, this direct-synthesis method can realize a vertically stacked layer structure without using a conventional transfer method, thereby fundamentally avoiding problems such as wrinkles or contamination traps at the interface. The optimized laser conditions on the SiO_2/Si substrate were as follows: a laser power of 10.8 W, scan speed of 100 mm/s, and frequency of 20 kHz. Finally, the source and drain were affixed using shadow masks to analyze the electrical properties of the graphene/MoS_2 heterojunction. Figure 1c shows Raman spectra obtained from each region of the material at an excitation wavelength of 532 nm. The G and 2D peaks were observed at ~1599 cm^{-1} and ~2700 cm^{-1}, respectively (marked in red). The 2D peak exhibited a sharp, single Lorentzian line shape and was considerably more intense than the G peak, which is a characteristic feature of monolayer graphene. Additionally, the D peak (~1360 cm^{-1}), which indicates defects and imperfections within the graphene crystal, was barely discernible. The Raman spectra of MoS_2 synthesized via the laser-based photothermal reaction are shown in blue. Two prominent MoS_2 peaks, E_{2g} and A_{1g}, could be distinctly observed at 383 cm^{-1} and 409 cm^{-1}, respectively. A Raman characteristic of MoS_2 is the narrowing of the gap between these two peaks as it transitions from the bulk state to that of a single layer [40,41]. This allowed the determination of the number of MoS_2 layers present. The gap between these peaks was approximately 26 cm^{-1}, confirming the few-layered nature of MoS_2. Atomic force microscopy (AFM) analysis has substantiated that the synthesized molybdenum disulfide (MoS_2) exhibits a consistent and uniform film-like structure with a measured thickness of 10 nm. The thickness control of the MoS_2 film can be achieved through the regulation of solvent concentration and the adjustment of spin-coating velocity. The critical aspect to consider is that to achieve uniform synthesis of MoS_2 in film form, it is necessary to adjust the laser scanning speed in accordance with changes in the thickness of the precursor film (Supplementary Material Figure S2). Specifically, thicker precursor layers demand a greater amount of photothermal energy for complete thermal decomposition into MoS_2, thereby necessitating a reduction in the laser scanning speed. According to previous research results that analyzed the surface of MoS_2 synthesized using this method, the MoS_2 yields a root mean square (RMS) surface roughness of 1.15 nm [23]. Interestingly, these major peaks were also maintained in the heterojunction where graphene and Mos_2 overlapped (green dot in Figure 1b), as evidenced by the green colored Raman spectra. The strength of the D peak was also similar to that of graphene at its initial intensity. For comparison, we prepared a graphene/MoS_2 control sample in which MoS_2 was thermally decomposed from the $(NH_4)_2MoS_4$ precursor using thermal CVD, and we analyzed its Raman characteristics. A comparison between the Raman peak of the graphene/MoS_2 structure synthesized by laser irradiation (marked in green) and that of the graphene/MoS_2 structure created by thermal chemical vapor deposition (T-CVD) (marked in black) showed that the Raman characteristics of MoS_2

were similar, whereas those for graphene exhibited a pronounced difference. When MoS_2 was directly synthesized using general T-CVD, the underlying graphene sustained thermal damage, leading to an amplified D peak and diminished 2D peak. Therefore, our research demonstrates that the laser-based selective thermal-treatment method can be used to directly synthesize MoS_2 layers on a graphene monolayer without causing damage. This mechanism, when paired with other 2D materials that are amenable to thermal decomposition, holds promise for the assembly of diverse heterojunction structures.

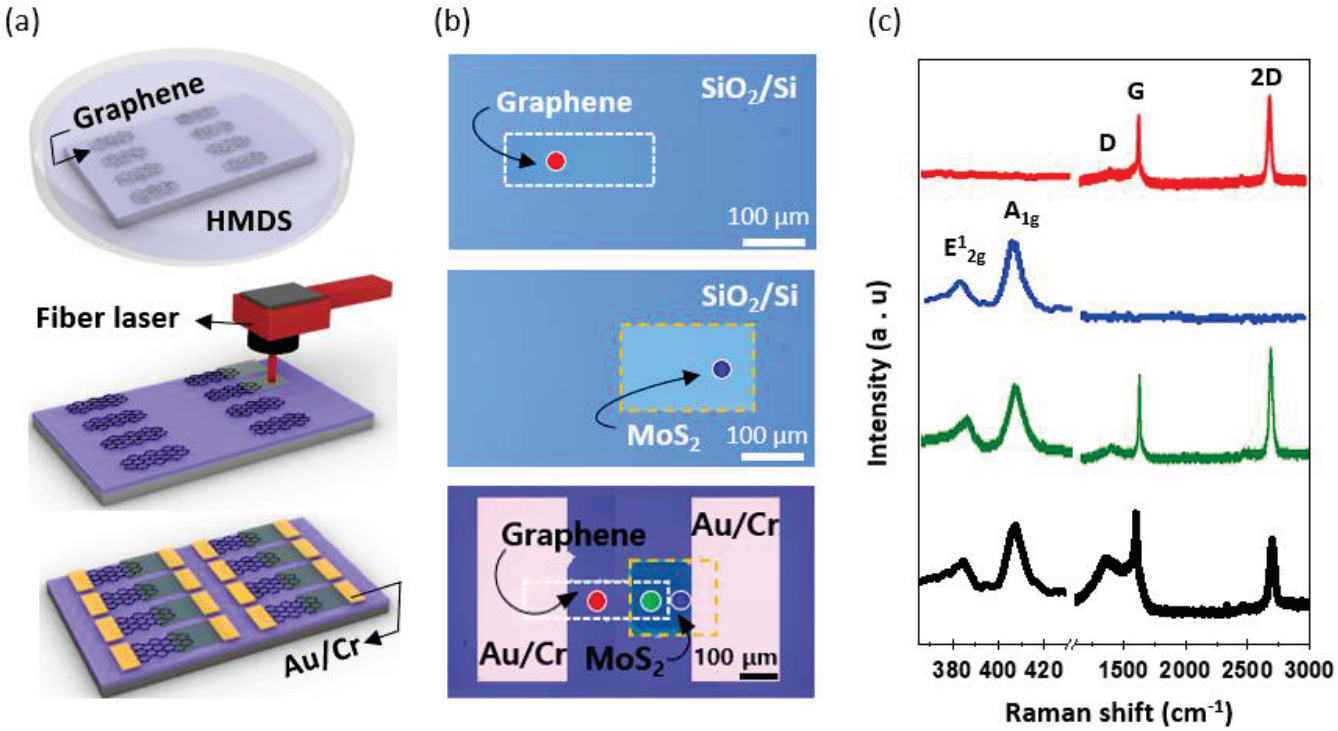

Figure 1. (**a**) Schematic diagram of the device manufacturing process, showing the stacking of MoS_2 on graphene; (**b**) OM image of patterned graphene, MoS_2, and a device made by a graphene/MoS_2 heterostructure; (**c**) Raman spectra for CVD graphene (red), MoS_2 synthesized with a laser (blue), vertically stacked MoS_2 (synthesized with a laser) on graphene (green), and vertically stacked MoS_2 (synthesized with CVD) on graphene (black).

The uniform deposition of the $(NH_4)_2MoS_4$ precursor layer on graphene is essential to demonstrate a MoS_2/graphene-heterojunction structure. In addition, a uniform and continuous pinhole-free thin film with a large area enabled the fabrication of a device array with a high yield. However, because graphene has a hydrophobic-surface characteristic owing to its unique atomic-crystal [42] structure, a difference was observed in the surface homogeneity between the spin coating of the ATM solution on the SiO_2 substrate and the graphene-transferred SiO_2 substrate, as shown in Figure 2a. To enhance the surface uniformity of the ATM film on graphene, three different solvents—dimethylformamide (DMF) mixed with 2-aminoethanol, a Triton X-100 mixture, and DMSO—were studied. In the case of the SiO_2/Si substrate, the surface of the wafer was treated with an O_2 plasma process (power 150 W, time 30 s) prior to spin-coating the ATM solution to improve the surface wettability. As shown in the optical-microscopy images in Figure 2b–d, a monotonous and uniform color indicated that the ATM solvent was evenly distributed in all types of samples. However, plasma treatment is not preferred for graphene surfaces because activated oxygen ions can severely damage the graphene, degrading its electrical performance. Therefore, we attempted to overcome this problem by adjusting the interactions between graphene and the solvent. In dissolved ATM solutions, balancing the viscosity and surface tension of the precursor is important. Initially, DMF and 2-aminoethanol were employed as the

solvent and additive [43], respectively. DMF has been used as a common organic solvent to dissolve ATM precursors [39], and amine group-based additive molecules have been used to stabilize ionic thiomolybdate (MoS_4^{2-}) clusters. However, as a result of numerous mixing control experiments between solutions, when DMF + 2-aminoethanol-based solvent was used, obtaining stable coating conditions was difficult as most of the graphene layers rolled after peeling from the substrate as indicated by the arrow in Figure 2e. Although we attempted to use another amine-based additive (*n*-butylamine), a similar phenomenon occurred when the solvent penetrated the substrate and graphene, resulting in delamination. As an alternative, the surface tension of the solution was controlled by adding Triton X-100 surfactant to the ATM solution. As a non-ionic surfactant, the hydrophobic group of Triton-X-100 engaged in interactions with the carbonaceous surface, leading to its adsorption onto the graphene surface. This adsorptive phenomenon enhanced the wettability of the graphene substrate, thereby facilitating a more uniform dispersion of the solvents on its surface [44]. Figure 2f appears to show improved homogeneity; however, complete homogeneity across the graphene surface was not achieved. As a result, the graphene was partially peeled off from the substrate as indicated by arrow. Interestingly, although DMSO is a polar organic solvent similar to DMF, experimental observations indicated that the ATM solution uniformly coated the graphene without causing any damage when DMSO was used as the solvent [45]. Based on previous experimental procedures, it is speculated that the balance between the surface tension of DMSO, the ionic thiomolybdate cluster, and the van der Waals forces [46] between the graphene and SiO_2 interface may allow for an even coating of the ATM precursor without peeling off the graphene (Figure 2g). Finally, when the ATM solution was spin-coated onto the SiO_2 substrate, it was confirmed that the DMF, Triton X-100 mixture, and DMSO were homogeneously coated on the surface. However, to spin-coat the graphene-transferred SiO_2 substrate, it was confirmed that the surface could be coated homogeneously using the DMSO solvent.

The electrical-junction properties of the fabricated graphene/MoS_2 were investigated. First, an HMDS layer was deposited on the graphene surface to minimize the unintentional doping effect caused by the Cu etchant and supporting polymer during the transfer process of the CVD graphene. That is, the hydrophobic SAM including HMDS suppressed the charge-impurity scattering effect caused by the impurity and simultaneously improved overall uniformity [47,48]. In addition, the HMDS buffer layer prevented damage to graphene from additional processes such as metal deposition [49] and laser annealing. Figure 3a illustrates the HMDS-doped graphene-based back-gate transistor on the Si/SiO_2 substrate. The HMDS treatment was conducted for 12 h on the graphene transferred onto the SiO_2/Si substrate prior to the deposition of the contact electrodes. The Raman spectra of graphene before and after HMDS doping are shown in Figure 3b. The Raman-frequency values of the G and 2D modes were sensitive to charge impurities and strains in graphene, enabling us to confirm the influence of HMDS. The G and 2D peak positions of pure graphene were 1600 cm^{-1} and 2695 cm^{-1}, respectively (marked in black); however, after HMDS formation, both peaks shifted down to 1595 cm^{-1} and 2686 cm^{-1}, respectively (marked in red). The Raman shift indicated that although the surface of graphene had hydrophobic characteristics, the entire surface was covered well with HMDS because some existing defects or oxidized species in graphene played a role in nucleating the SAM [49]. Moreover, the extracted value of $\Delta 2D/\Delta G$ was less than 2 [50], which indicates that no effective stress was applied to graphene after HMDS deposition. A comparative assessment of the Fermi energy and carrier mobility of pristine and HMDS-doped graphene is shown in Figure 3c. For the bare graphene, a gate voltage (Dirac point) was observed at 33.1 V. However, after the HMDS-doping process, a pronounced Dirac-point shift to lower gate voltages was repeatedly observed (V_G: 22.2 V) [48,51–53]. Based on the electronic structure of graphene, the Dirac-point shift may be associated with the change in Fermi energy.

Because of the linear band structure of graphene, the shift in Fermi energy caused by the HMDS dipole can be described as follows [54]:

$$\Delta E = \hbar v_F \sqrt{\pi n (V_2 - V_1)},$$

where v_F is the Fermi velocity previously reported as 1.1×10^6 m/s, n is the intrinsic carrier density per volt with a typical value of approximately 7.2×10^{10} cm^{-2} V^{-1}, and V_1 (V_2) is the Dirac point of devices without (with) HMDS treatment. The calculation confirmed that the HMDS treatment shifted the Fermi-energy level of graphene by 0.11 eV closer to the vacuum level. The field-effect carrier mobility of graphene was additionally calculated from the maximum slope near the charge-neutrality point, as follows:

$$\mu_{FET} = \frac{L_{ch} g_m}{W_{ch} C_{ox} V_D}$$

where L_{ch} and W_{ch} are the channel length and width, respectively, g_m is dI_D/dV_G, C_{ox} is the gate oxide capacitance per area, and V_D is the applied drain-source voltage. As plotted in Figure 3c, the hole and electron carrier mobilities of HMDS-treated graphene showed values of ~450.8 cm^2/Vs and ~297.9 cm^2/Vs, respectively. This represents a significant enhancement in mobility compared to bare graphene (μ_{hole}: ~86.5 cm^2/Vs and μ_{elec}: ~95.4 cm^2/Vs). The electrical properties of MoS_2, interfaced with graphene, were also analyzed via transfer characteristics (Supplementary Materials, Figure S3). The MoS_2 synthesized via laser based photothermal processing demonstrated comparatively lower electron mobility, ranging from 1 to 5 cm^2/Vs, than that synthesized through chemical vapor deposition (CVD) methods, with an observed on/off ratio of 10^3. These moderate properties can be attributed to the fine-grained structure of the laser-synthesized MoS_2. Determining the electronic band structure of the synthesized graphene/MoS_2 heterostructure is necessary for analyzing its electrical characteristics and understanding its charge-transfer dynamics. The work function of each material was experimentally measured using ultraviolet photoelectron spectroscopy. The work function was calculated as follows [33]:

$$\Phi = h\nu - (E_{SECO} - E_{VB}),$$

where $h\nu$ is the energy of the incident UV photons (He I line = 21.21 eV), E_{SECO} is the secondary electron-cutoff energy, and E_{VB} is the onset of the valence band. As expected, bare graphene exhibited significant fluctuations in the analysis value, ranging from 4.3 eV to 5.2 eV depending on the measurement position, whereas HMDS-doped graphene exhibited a stable value of approximately 4.5 eV. Furthermore, MoS_2 synthesized by laser treatment exhibited a uniform work function of approximately 4.2 eV, which was in good agreement with that of the few-layered MoS_2 [21]. Figure 3f illustrates the band alignment of the graphene/MoS_2 heterojunction, delineated according to the positions of the respective band structures. In a thermal-equilibrium state, the band structure bends at the interface due to the difference in work functions between graphene and MoS_2, creating a Schottky barrier (Φ_B) and built-in potential (V_{bi}) on the semiconductor side. For an applied external bias, the Fermi level of graphene shifted downward during the application of a reverse bias owing to the decrease in negative charges moving toward the graphene, whereas the Fermi level of the n-type MoS_2 shifted upward, as illustrated in Figure 3g. This upward shift of the MoS_2 Fermi level relieved the band bending, leading to a decrease in the built-in potential. Conversely, when a forward bias was applied to the graphene/MoS_2 Schottky junction, the Fermi level of graphene shifted upward, whereas that of the MoS_2 shifted downward. This occurred because more positive charges were localized in the MoS_2 and more negative charges were transported to the graphene, as depicted in Figure 3h. Unlike the scenario under reverse bias, the value of the built-in potential increased during the application of a forward bias. When a reverse bias was applied, the majority carriers of MoS_2 and graphene easily overcame the lowered built-in potential and transferred to

the counter materials beyond the junction. However, in the case of a forward bias, the barrier at the junction was high; therefore, the charges were greatly restricted when moving toward each other. Therefore, owing to the aforementioned charge-transfer dynamics, the graphene/MoS_2 junction, which was MoS_2 directly synthesized on graphene using a laser-assisted methodology, exhibited rectification characteristics that depended on the applied forward-to-reverse bias. However, when MoS_2 was grown via the thermal CVD process on the graphene, the underlying graphene experienced pronounced thermal degradation. These harsh synthesis conditions led to a substantial decline in conductivity, or in certain instances, a failure to establish a Schottky barrier, thereby inhibiting any rectifying behavior, as shown in Figure 3e.

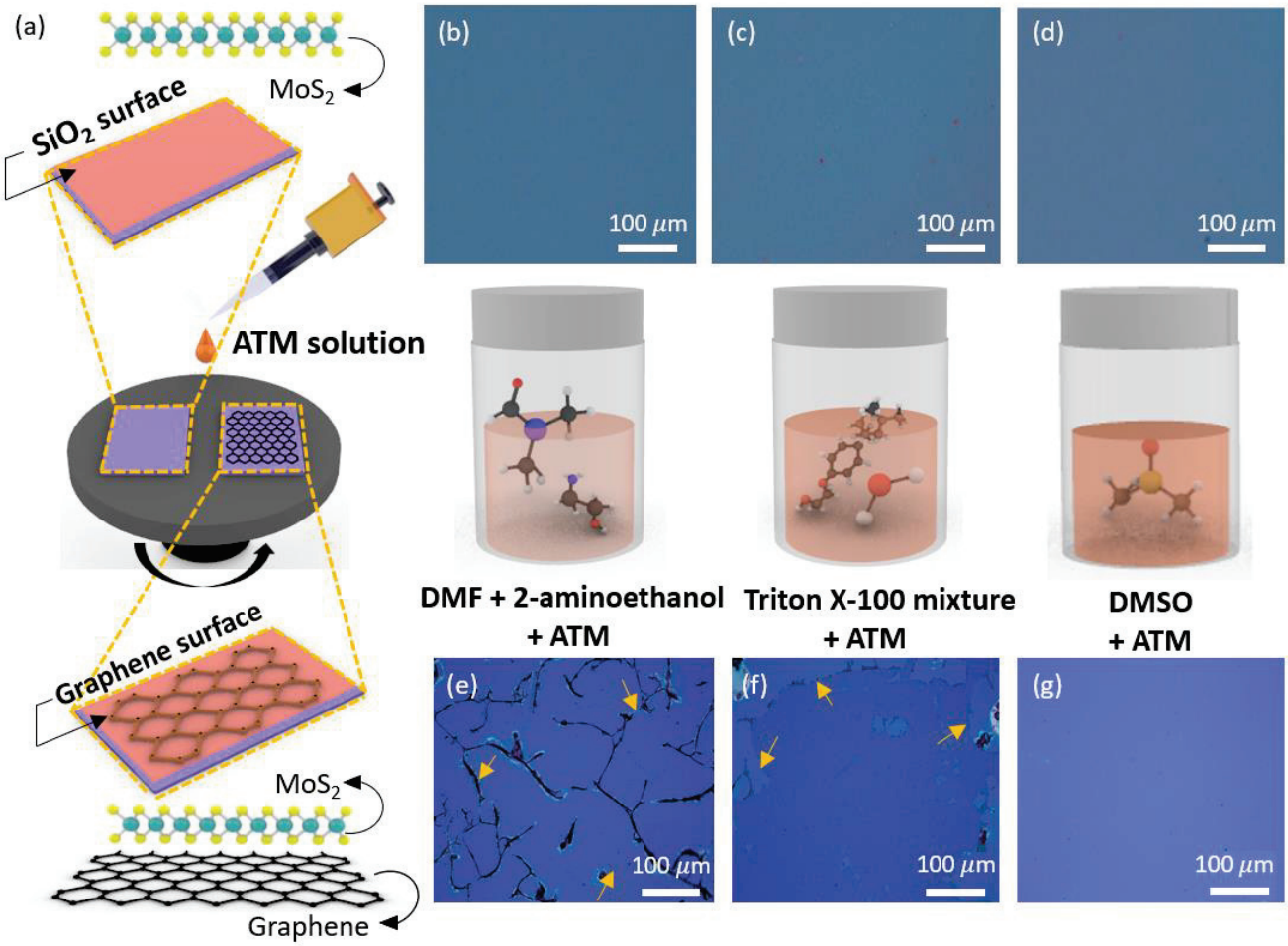

Figure 2. (**a**) Schematic illustration of the coating process for the $(NH_4)_2MoS_4$ precursor on SiO_2 and graphene/SiO_2 surfaces. Optical-microscopy images showing the $(NH_4)_2MoS_4$ precursor spin-coated onto a SiO_2 surface with different solvents: (**b**) DMF + 2-aminoethanol, (**c**) Triton X-100 mixture, and (**d**) DMSO. Optical-microscopy images of the $(NH_4)_2MoS_4$ precursor spin-coated onto a graphene/SiO_2 substrate using the following solvents: (**e**) DMF + 2-aminoethanol, (**f**) Triton X-100 mixture, and (**g**) DMSO.

The developed graphene/MoS_2-based Schottky junction was characterized in terms of its optical responsiveness to external light by periodically turning the light on and off. To this end, the optoelectronic device employs the configuration mentioned in Figure 1b, wherein the intersection of the graphene and MoS_2 patterns spans an area of 100 μm × 100 μm. Detailed specifications of the device dimensions are described in the Supplementary Materials, accompanied by illustrative schematics. We used a commercial visible-light halogen lamp (FOK-100 W, Fiber Optic Korea Co., Ltd., Cheonan, Republic of Korea) with a peak wave-

length of 650 nm as the light source. As shown in Figure 4a–d, a difference in photocurrent was observed depending on the bias strength even under a consistent light intensity of 1.92 mW/cm^2. To clarify, the optoelectronic device we have constructed incorporates two Schottky junctions encompassing both the graphene/MoS_2 junction and MoS_2/metal electrode junction. We assessed the photocurrent induced in each region utilizing a focused monochromatic laser beam (refer to Supplementary Material, Figure S4). The result of Figure S4 confirmed that the photocurrent generated at the MoS_2/metal electrode junction was markedly lower than that at the graphene/MoS_2 junction. The dominant mechanisms that influenced the photocurrent in graphene/MoS_2-based optoelectronic devices were photoconductivity and photogating [55]. The difference in photoconductivity appeared as an increase in the number of free charge carriers owing to photon absorption. Additionally, charge trapping occurred owing to disorders and defects, resulting in differences in photogating. We plotted the change in photocurrent upon light activation against the photocurrent variation in darkness (I/I_0), testing two distinct bias voltages under forward and reverse biases. A larger photocurrent is observed in the case of forward bias. This can be considered to be due to the effect of the internal barrier depending on the direction of the applied bias as mentioned in Figure 3.

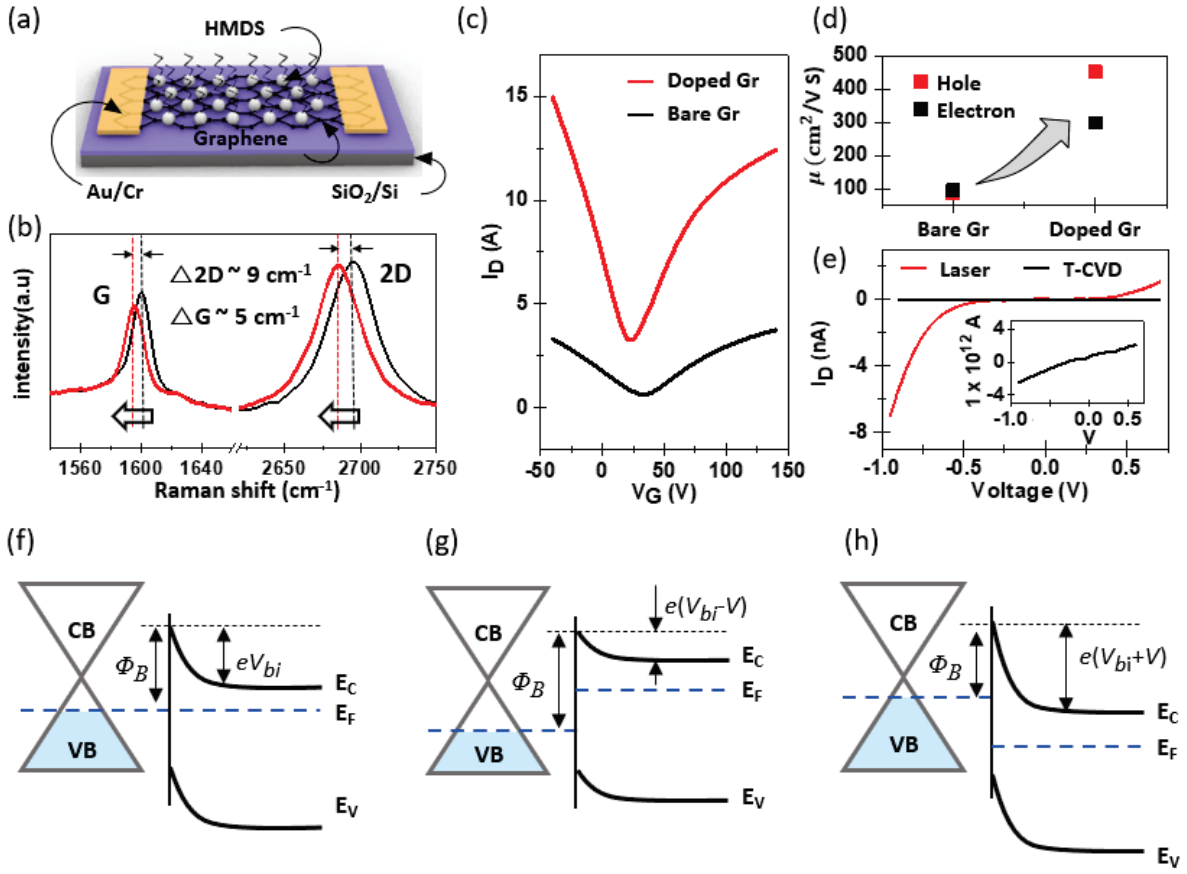

Figure 3. (**a**) Three-dimensional schematic diagram of an HMDS-doped graphene transistor; (**b**) Raman peak shift of graphene before and after HMDS doping; (**c**) transfer characteristic of graphene transistor with and without HMDS; (**d**) comparison of hole and electron carrier mobility before and after HMDS doping; (**e**) comparison of the rectification characteristics between graphene/MoS_2 produced by the laser method and graphene/MoS_2 produced by the T-CVD method. (Inset: detailed current characteristics of the device fabricated by T-CVD: (**f**) band diagram of graphene/MoS_2 heterostructure; (**g**) reverse-bias condition; (**h**) forward-bias condition.

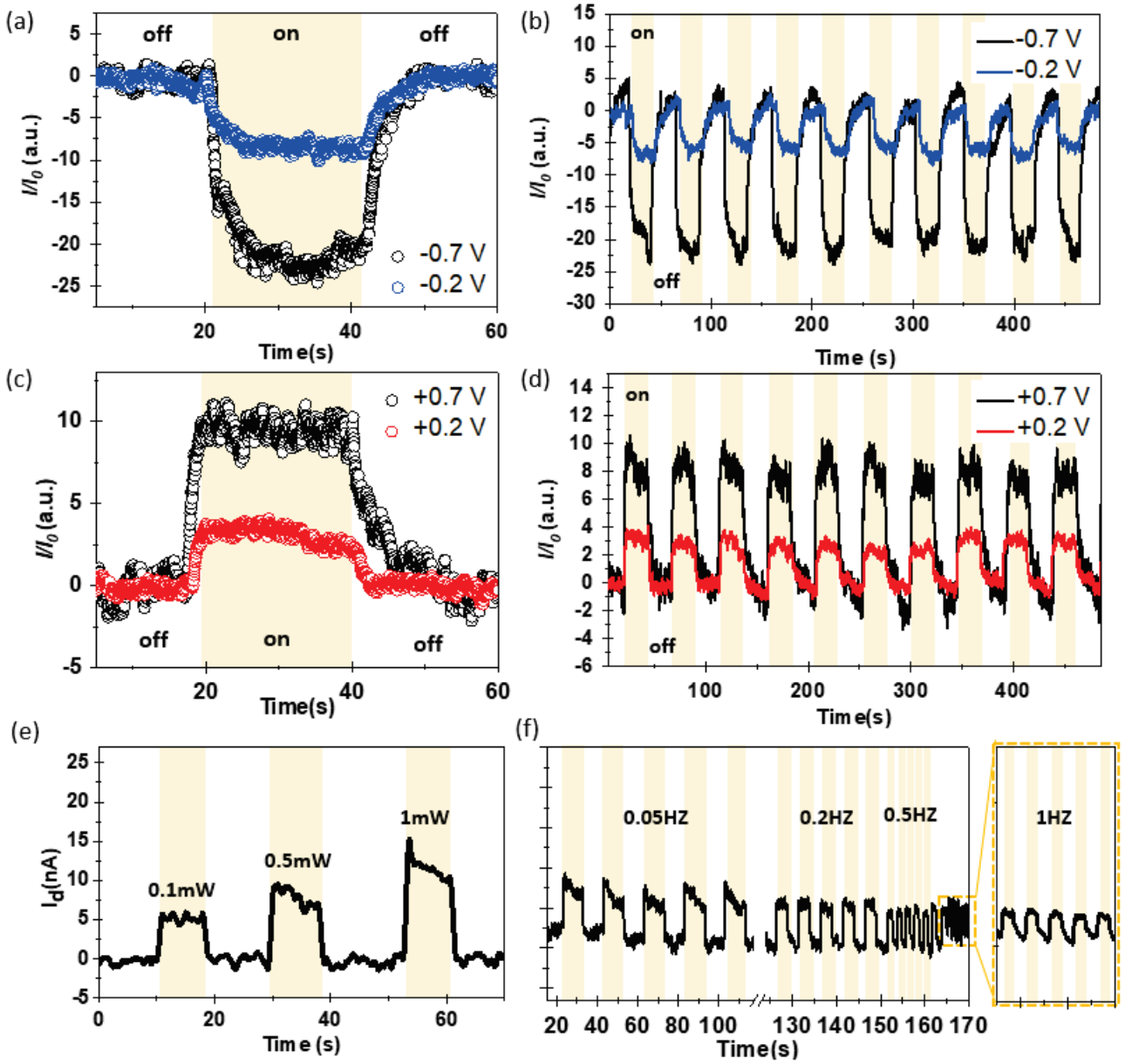

Figure 4. (**a**) Photocurrent characteristic of graphene/MoS_2 heterostructure under reverse bias; (**b**) cycle stability under reverse bias; (**c**) photocurrent characteristic of graphene/MoS_2 heterostructure under forward bias; (**d**) cycle stability under forward bias; (**e**) current–time characteristic with power of light source; (**f**) current–time characteristic with frequency.

When considering the rise time (τ_{rise}) and decay time (τ_{decay}) of the charge carrier, which represent the duration of charge transfer and production of the maximum output current (ranging between 10 and 90% intensity), respectively, we extracted the following values: τ_{rise} = 10.3 s (τ_{decay} = 8.49 s) at −0.7 V, 10.96 s (8.9 s) at −0.2 V, 4.6 s (7.26 s) at 0.2 V, and 6.41 s (7.74 s) at 0.7V [56,57]. From an on/off photoresponsivity-ratio perspective, the reverse bias exhibited enhanced light reactivity. However, the forward bias demonstrated swifter responsiveness. For a comparative analysis, we fabricated graphene/MoS_2-based junction devices using the CVD method and evaluated their characteristics. Upon analyzing the photoresponse under the same illumination conditions, it was found that the device fabricated using CVD synthesis exhibited negligible photocurrent generation. A detailed examination of the individual components revealed that the graphene had almost entirely lost its conductivity. These findings suggest that the graphene underwent signif-

icant damage during the MoS_2 synthesis process (process temperature > 700 °C), which accounts for the absence of the rectifying effect as presented in Figure 3e. The tendency of currents to respond to light was shown to increase monotonically and proportionally as the intensity of the light increased linearly with no evidence of hysterysis (Figure 4e). We also investigated the temporal photoresponse, which indicated the potential of a photodetector, by monitoring the photocurrent under pulsed illumination in the frequency range of 0.05–1 Hz (Figure 4f). The graphene/MoS_2-based Schottky diode was highly responsive to the incident pulsed light, with excellent stability and reproducibility over multiple cycles.

4. Conclusions

In this study, we introduced a facile approach for the selective synthesis of MoS_2 on graphene by employing laser-based photothermal treatment, which enabled the direct formation of graphene/MoS_2 heterostructures. Notably, this innovative technique offered a means of designing heterostructures from thermally sensitive materials by confining the heat treatment to the intended layer, effectively addressing the challenges that existing T-CVD methodologies cannot overcome. Central to our study is the understanding that the choice of the laser source is crucial. It must efficiently induce the thermal decomposition of the precursor without compromising the structural integrity of the synthesized MoS_2 and graphene. This balance was achieved by harnessing the differential light-absorption rates of the ATM precursor and MoS_2. Furthermore, we provided solutions for mitigating the surface irregularities introduced by graphene, thereby paving the way for achieving a uniform coating. The introduction of an HMDS buffer layer was a pivotal step that safeguarded the electrical characteristics of graphene throughout the fabrication sequence. Comprehensive evaluation of the electrical properties of the synthesized graphene/MoS_2 heterostructures yielded encouraging results. Although this study did not specifically address contact resistance issues, it expects that the optimization of contact resistance between the two-dimensional semiconductor and the metal electrode could significantly enhance the operational efficiency of the photoelectric device [58–63]. As we venture deeper into the expansive field of this pioneering synthesis technique, we anticipate its widespread adoption and its pivotal role in driving next-generation devices and technologies.

Supplementary Materials: The following supporting information can be downloaded at: https://www.mdpi.com/article/10.3390/nano13222937/s1, Figure S1: Schematic diagram of Graphene/MoS_2 based optoelectronic device; Figure S2: AFM measurement; Figure S3 Transfer/ouput characteristics of MoS_2 FET; Figure S4: Photocurrent Comparison between Graphene/MoS_2 and MoS_2/Cr/Au Junctions; Figure S5: Schematic diagram for manufacturing a CVD type device array; Figure S6: Photo-responsiveness of CVD type device.

Author Contributions: M.J.J. and S.-K.H. conceived and performed the experiments. H.Y.J. prepared the materials. J.M. and T.-W.K. analyzed the data. S.B. and S.-K.L. wrote the manuscript. All authors have read and agreed to the published version of the manuscript.

Funding: This work was financially supported by a National Research Foundation of Korea (NRF) grant funded by the Korean government (Grant No. 2022R1F1A1072339) and Development of core technologies for advanced measuring instruments funded by Korea Research Institute of Standards and Science (KRISS–2023–GP2023-0012) and the Ministry of Trade, Industry & Energy of Korea (20019508).

Data Availability Statement: Data are contained within the article and Supplementary Materials.

Conflicts of Interest: The authors declare no conflict of interest.

References

1. Sun, Y.; Choi, W.M.; Jiang, H.; Huang, Y.Y.; Rogers, J.A. Controlled buckling of semiconductor nanoribbons for stretchable electronics. *Nat. Nanotechnol.* **2006**, *1*, 201–207. [CrossRef]
2. Baca, A.J.; Meitl, M.A.; Ko, H.C.; Mack, S.; Kim, H.S.; Dong, J.; Ferreira, P.M.; Rogers, J.A. Printable single-crystal silicon micro/nanoscale ribbons, platelets and bars generated from bulk wafers. *Adv. Funct. Mater.* **2007**, *17*, 3051–3062. [CrossRef]

3. Yoon, J.; Jo, S.; Chun, I.S.; Jung, I.; Kim, H.-S.; Meitl, M.; Menard, E.; Li, X.; Coleman, J.J.; Paik, U. GaAs photovoltaics and optoelectronics using releasable multilayer epitaxial assemblies. *Nature* **2010**, *465*, 329–333. [CrossRef]
4. Solís-Fernández, P.; Bissett, M.; Ago, H. Synthesis, structure and applications of graphene-based 2D heterostructures. *Chem. Soc. Rev.* **2017**, *46*, 4572–4613. [CrossRef]
5. Wassei, J.K.; Kaner, R.B. Graphene, a promising transparent conductor. *Mater. Today* **2010**, *13*, 52–59. [CrossRef]
6. Azadmanjiri, J.; Srivastava, V.K.; Kumar, P.; Sofer, Z.; Min, J.; Gong, J. Graphene-supported 2D transition metal dichalcogenide van der waals heterostructures. *Appl. Mater. Today* **2020**, *19*, 100600. [CrossRef]
7. Gong, C.; Hu, K.; Wang, X.; Wangyang, P.; Yan, C.; Chu, J.; Liao, M.; Dai, L.; Zhai, T.; Wang, C. 2D nanomaterial arrays for electronics and optoelectronics. *Adv. Funct. Mater.* **2018**, *28*, 1706559. [CrossRef]
8. Guan, S.-X.; Yang, T.H.; Yang, C.-H.; Hong, C.-J.; Liang, B.-W.; Simbulan, K.B.; Chen, J.-H.; Su, C.-J.; Li, K.-S.; Zhong, Y.-L. Monolithic 3D integration of back-end compatible 2D material FET on Si FinFET. *npj 2d Mater. Appl.* **2023**, *7*, 9. [CrossRef]
9. Chung, Y.-Y.; Chou, B.-J.; Hsu, C.-F.; Yun, W.-S.; Li, M.-Y.; Su, S.-K.; Liao, Y.-T.; Lee, M.-C.; Huang, G.-W.; Liew, S.-L. First Demonstration of GAA Monolayer-MoS_2 Nanosheet nFET with 410 μA μm I_D 1V V_D at 40 nm gate length. In Proceedings of the 2022 International Electron Devices Meeting (IEDM), San Francisco, CA, USA, 3–7 December 2022; pp. 34.35.31–34.35.34.
10. Kang, K.; Xie, S.; Huang, L.; Han, Y.; Huang, P.Y.; Mak, K.F.; Kim, C.-J.; Muller, D.; Park, J. High-mobility three-atom-thick semiconducting films with wafer-scale homogeneity. *Nature* **2015**, *520*, 656–660. [CrossRef]
11. Tan, L.K.; Liu, B.; Teng, J.H.; Guo, S.; Low, H.Y.; Loh, K.P. Atomic layer deposition of a MoS_2 film. *Nanoscale* **2014**, *6*, 10584–10588. [CrossRef]
12. Poh, S.M.; Tan, S.J.; Zhao, X.; Chen, Z.; Abdelwahab, I.; Fu, D.; Xu, H.; Bao, Y.; Zhou, W.; Loh, K.P. Large area synthesis of 1D-$MoSe_2$ using molecular beam epitaxy. *Adv. Mater.* **2017**, *29*, 1605641. [CrossRef] [PubMed]
13. Kim, K.S.; Lee, D.; Chang, C.S.; Seo, S.; Hu, Y.; Cha, S.; Kim, H.; Shin, J.; Lee, J.-H.; Lee, S. Non-epitaxial single-crystal 2D material growth by geometric confinement. *Nature* **2023**, *614*, 88–94. [CrossRef] [PubMed]
14. Sawka, A. MOCVD growth of gadolinium oxide layers on tubes. *Ceram. Int.* **2023**, *49*, 23835–23843. [CrossRef]
15. Wofford, J.M.; Nakhaie, S.; Krause, T.; Liu, X.; Ramsteiner, M.; Hanke, M.; Riechert, H.; Lopes, J.M.J. A hybrid MBE-based growth method for large-area synthesis of stacked hexagonal boron nitride/graphene heterostructures. *Sci. Rep.* **2017**, *7*, 43644. [CrossRef] [PubMed]
16. Song, Y.; Zou, W.; Lu, Q.; Lin, L.; Liu, Z. Graphene transfer: Paving the road for applications of chemical vapor deposition graphene. *Small* **2021**, *17*, 2007600. [CrossRef]
17. Zhang, G.; Güell, A.G.; Kirkman, P.M.; Lazenby, R.A.; Miller, T.S.; Unwin, P.R. Versatile polymer-free graphene transfer method and applications. *ACS Appl. Mater. Interfaces* **2016**, *8*, 8008–8016. [CrossRef]
18. Nagareddy, V.K.; Octon, T.J.; Townsend, N.J.; Russo, S.; Craciun, M.F.; Wright, C.D. Humidity-Controlled Ultralow Power Layer-by-Layer Thinning, Nanopatterning and Bandgap Engineering of MoTe. *Adv. Funct. Mater.* **2018**, *28*, 1804434. [CrossRef]
19. Zhai, X.; Zhang, R.; Sheng, H.; Wang, J.; Zhu, Y.; Lu, Z.; Li, Z.; Huang, X.; Li, H.; Lu, G. Direct observation of the light-induced exfoliation of molybdenum disulfide sheets in water medium. *ACS Nano* **2021**, *15*, 5661–5670. [CrossRef]
20. Park, S.; Song, J.; Kim, T.K.; Choi, K.H.; Hyeong, S.K.; Ahn, M.; Kim, H.R.; Bae, S.; Lee, S.K.; Hong, B.H. Photothermally Crumpled MoS_2 Film as an Omnidirectionally Stretchable Platform. *Small Methods* **2022**, *6*, 2200116. [CrossRef]
21. Park, S.; Park, J.; Kim, Y.-g.; Bae, S.; Kim, T.-W.; Park, K.-I.; Hong, B.H.; Jeong, C.K.; Lee, S.-K. Laser-directed synthesis of strain-induced crumpled MoS_2 structure for enhanced triboelectrification toward haptic sensors. *Nano Energy* **2020**, *78*, 105266. [CrossRef]
22. Cho, S.; Kim, S.; Kim, J.H.; Zhao, J.; Seok, J.; Keum, D.H.; Baik, J.; Choe, D.-H.; Chang, K.J.; Suenaga, K. Phase patterning for ohmic homojunction contact in MoTe. *Science* **2015**, *349*, 625–628. [CrossRef]
23. Park, S.; Lee, A.; Choi, K.-H.; Hyeong, S.-K.; Bae, S.; Hong, J.-M.; Kim, T.-W.; Hong, B.H.; Lee, S.-K. Layer-selective synthesis of MoS_2 and WS_2 structures under ambient conditions for customized electronics. *ACS Nano* **2020**, *14*, 8485–8494. [CrossRef]
24. Goto, T.; Saito, K.; Imaizumi, F.; Hatanaka, M.; Takimoto, M.; Mizumura, M.; Gotoh, J.; Ikenoue, H.; Sugawa, S. LTPS thin-film transistors fabricated using new selective laser annealing system. *IEEE Trans. Electron Devices* **2018**, *65*, 3250–3256. [CrossRef]
25. Song, M.S.; Park, K.; Lee, K.; Cho, J.W.; Lee, T.Y.; Park, J.; Chae, S.C. Selective Crystallization of Ferroelectric Hf x Zr1–x O2 via Excimer Laser Annealing. *ACS Appl. Electron. Mater.* **2023**, *5*, 117–122. [CrossRef]
26. Xu, M.; Peng, C.; Yuan, Y.; Li, X.; Zhang, J. Enhancing the performance of solution-processed thin-film transistors via laser scanning annealing. *ACS Appl. Electron. Mater.* **2020**, *2*, 2970–2975. [CrossRef]
27. Lee, J.B.; Lim, Y.R.; Katiyar, A.K.; Song, W.; Lim, J.; Bae, S.; Kim, T.W.; Lee, S.K.; Ahn, J.H. Direct synthesis of a self-assembled WSe_2/MoS_2 heterostructure array and its optoelectrical properties. *Adv. Mater.* **2019**, *31*, 1904194. [CrossRef]
28. Lee, S.K.; Lee, J.B.; Singh, J.; Rana, K.; Ahn, J.H. Drying-Mediated Self-Assembled Growth of Transition Metal Dichalcogenide Wires and their Heterostructures. *Adv. Mater.* **2015**, *27*, 4142–4149. [CrossRef]
29. Gong, Y.; Lin, J.; Wang, X.; Shi, G.; Lei, S.; Lin, Z.; Zou, X.; Ye, G.; Vajtai, R.; Yakobson, B.I. Vertical and in-plane heterostructures from WS_2/MoS_2 monolayers. *Nat. Mater.* **2014**, *13*, 1135–1142. [CrossRef]
30. Seok, H.; Megra, Y.T.; Kanade, C.K.; Cho, J.; Kanade, V.K.; Kim, M.; Lee, I.; Yoo, P.J.; Kim, H.-U.; Suk, J.W. Low-temperature synthesis of wafer-scale MoS_2–WS_2 vertical heterostructures by single-step penetrative plasma sulfurization. *ACS Nano* **2021**, *15*, 707–718. [CrossRef]

31. Pak, S.; Lee, J.; Lee, Y.-W.; Jang, A.-R.; Ahn, S.; Ma, K.Y.; Cho, Y.; Hong, J.; Lee, S.; Jeong, H.Y. Strain-mediated interlayer coupling effects on the excitonic behaviors in an epitaxially grown MoS_2/WS_2 van der Waals heterobilayer. *Nano Lett.* **2017**, *17*, 5634–5640. [CrossRef]
32. Losurdo, M.; Giangregorio, M.M.; Capezzuto, P.; Bruno, G. Graphene CVD growth on copper and nickel: Role of hydrogen in kinetics and structure. *Phys. Chem. Chem. Phys.* **2011**, *13*, 20836–20843. [CrossRef]
33. Im, M.J.; Hyeong, S.-K.; Lee, J.-H.; Kim, T.-W.; Lee, S.-K.; Jung, G.Y.; Bae, S. High uniformity and stability of graphene transparent conducting electrodes by dual-side doping. *Appl. Surf. Sci.* **2022**, *605*, 154569. [CrossRef]
34. Lee, J.-S.; Choi, Y.-K.; Ha, D.; Balasubramanian, S.; King, T.-J.; Bokor, J. Hydrogen annealing effect on DC and low-frequency noise characteristics in CMOS FinFETs. *IEEE Electron Device Lett.* **2003**, *24*, 186–188.
35. Sun, Y.; Yan, X.; Zheng, X.; Liu, Y.; Zhao, Y.; Shen, Y.; Liao, Q.; Zhang, Y. High on–off ratio improvement of ZnO-based forming-free memristor by surface hydrogen annealing. *ACS Appl. Mater. Interfaces* **2015**, *7*, 7382–7388. [CrossRef]
36. Ferrah, D.; Renault, O.; Petit-Etienne, C.; Okuno, H.; Hourani, W.; Dipankar, K.; Berne, C.; Bouchiat, V. Photoemission investigation of the graphene surface cleaning by hydrogen/nitrogen plasma. In Proceedings of the 16th European Conference on Applications of Surface and Interface Analysis (ECASIA'15), Granada, Spain, 28 September–1 October 2015.
37. Bae, S.; Kim, H.; Lee, Y.; Xu, X.; Park, J.-S.; Zheng, Y.; Balakrishnan, J.; Lei, T.; Ri Kim, H.; Song, Y.I. Roll-to-roll production of 30-inch graphene films for transparent electrodes. *Nat. Nanotechnol.* **2010**, *5*, 574–578. [CrossRef]
38. Shin, D.H.; Kim, Y.-j.; Lee, S.-K.; Bae, S.; Ahn, S. Atomically thin alkane passivation layer for flexible and transparent graphene electronics. *Appl. Surf. Sci.* **2023**, *612*, 155695. [CrossRef]
39. Liu, K.-K.; Zhang, W.; Lee, Y.-H.; Lin, Y.-C.; Chang, M.-T.; Su, C.-Y.; Chang, C.-S.; Li, H.; Shi, Y.; Zhang, H. Growth of large-area and highly crystalline MoS_2 thin layers on insulating substrates. *Nano Lett.* **2012**, *12*, 1538–1544. [CrossRef]
40. Liang, L.; Meunier, V. First-principles Raman spectra of MoS_2, WS_2 and their heterostructures. *Nanoscale* **2014**, *6*, 5394–5401. [CrossRef]
41. Li, H.; Zhang, Q.; Yap, C.C.R.; Tay, B.K.; Edwin, T.H.T.; Olivier, A.; Baillargeat, D. From bulk to monolayer MoS_2: Evolution of Raman scattering. *Adv. Funct. Mater.* **2012**, *22*, 1385–1390. [CrossRef]
42. Prydatko, A.V.; Belyaeva, L.A.; Jiang, L.; Lima, L.M.; Schneider, G.F. Contact angle measurement of free-standing square-millimeter single-layer graphene. *Nat. Commun.* **2018**, *9*, 4185. [CrossRef]
43. Yang, J.; Gu, Y.; Lee, E.; Lee, H.; Park, S.H.; Cho, M.-H.; Kim, Y.H.; Kim, Y.-H.; Kim, H. Wafer-scale synthesis of thickness-controllable MoS_2 films via solution-processing using a dimethylformamide/n-butylamine/2-aminoethanol solvent system. *Nanoscale* **2015**, *7*, 9311–9319. [CrossRef]
44. Lee, J.-B.; Rana, K.; Seo, B.H.; Oh, J.Y.; Jeong, U.; Ahn, J.-H. Influence of nonionic surfactant-modified PEDOT: PSS on graphene. *Carbon* **2015**, *85*, 261–268. [CrossRef]
45. Maleski, K.; Mochalin, V.N.; Gogotsi, Y. Dispersions of two-dimensional titanium carbide MXene in organic solvents. *Chem. Mater.* **2017**, *29*, 1632–1640. [CrossRef]
46. Gao, W.; Xiao, P.; Henkelman, G.; Liechti, K.M.; Huang, R. Interfacial adhesion between graphene and silicon dioxide by density functional theory with van der Waals corrections. *J. Phys. D Appl. Phys.* **2014**, *47*, 255301. [CrossRef]
47. Lee, B.; Chen, Y.; Duerr, F.; Mastrogiovanni, D.; Garfunkel, E.; Andrei, E.; Podzorov, V. Modification of electronic properties of graphene with self-assembled monolayers. *Nano Lett.* **2010**, *10*, 2427–2432. [CrossRef]
48. Lee, W.H.; Park, J.; Kim, Y.; Kim, K.S.; Hong, B.H.; Cho, K. Control of graphene field-effect transistors by interfacial hydrophobic self-assembled monolayers. *Adv. Mater.* **2011**, *23*, 3460–3464. [CrossRef]
49. Ramadan, S.; Zhang, Y.; Tsang, D.K.H.; Shaforost, O.; Xu, L.; Bower, R.; Dunlop, I.E.; Petrov, P.K.; Klein, N. Enhancing structural properties and performance of graphene-based devices using self-assembled HMDS monolayers. *ACS Omega* **2021**, *6*, 4767–4775. [CrossRef]
50. Ferrari, A.C.; Basko, D.M. Raman spectroscopy as a versatile tool for studying the properties of graphene. *Nat. Nanotechnol.* **2013**, *8*, 235–246. [CrossRef]
51. Liu, X.; Qu, D.; Ryu, J.; Ahmed, F.; Yang, Z.; Lee, D.; Yoo, W.J. P-type polar transition of chemically doped multilayer MoS_2 transistor. *Adv. Mater.* **2016**, *28*, 2345–2351. [CrossRef]
52. Guo, B.; Liu, Q.; Chen, E.; Zhu, H.; Fang, L.; Gong, J.R. Controllable N-doping of graphene. *Nano Lett.* **2010**, *10*, 4975–4980. [CrossRef]
53. Chowdhury, S.F.; Sonde, S.; Rahimi, S.; Tao, L.; Banerjee, S.; Akinwande, D. Improvement of graphene field-effect transistors by hexamethyldisilazane surface treatment. *Appl. Phys. Lett.* **2014**, *105*, 33117. [CrossRef]
54. Cernetic, N.; Wu, S.; Davies, J.A.; Krueger, B.W.; Hutchins, D.O.; Xu, X.; Ma, H.; Jen, A.K.Y. Systematic Doping Control of CVD Graphene Transistors with Functionalized Aromatic Self-Assembled Monolayers. *Adv. Funct. Mater.* **2014**, *24*, 3464–3470. [CrossRef]
55. Han, P.; Marie, L.S.; Wang, Q.X.; Quirk, N.; El Fatimy, A.; Ishigami, M.; Barbara, P. Highly sensitive MoS2 photodetectors with graphene contacts. *Nanotechnology* **2018**, *29*, 20LT01. [CrossRef] [PubMed]
56. Deng, W.; Chen, Y.; You, C.; Liu, B.; Yang, Y.; Shen, G.; Li, S.; Sun, L.; Zhang, Y.; Yan, H. High detectivity from a lateral graphene–MoS_2 schottky photodetector grown by chemical vapor deposition. *Adv. Electron. Mater.* **2018**, *4*, 1800069. [CrossRef]
57. Lopez-Sanchez, O.; Lembke, D.; Kayci, M.; Radenovic, A.; Kis, A. Ultrasensitive photodetectors based on monolayer MoS. *Nat. Nanotechnol.* **2013**, *8*, 497–501. [CrossRef] [PubMed]

58. Schauble, K.; Zakhidov, D.; Yalon, E.; Deshmukh, S.; Grady, R.W.; Cooley, K.A.; McClellan, C.J.; Vaziri, S.; Passarello, D.; Mohney, S.E. Uncovering the effects of metal contacts on monolayer MoS. *ACS Nano* **2020**, *14*, 14798–14808. [CrossRef] [PubMed]
59. Shen, P.-C.; Su, C.; Lin, Y.; Chou, A.-S.; Cheng, C.-C.; Park, J.-H.; Chiu, M.-H.; Lu, A.-Y.; Tang, H.-L.; Tavakoli, M.M. Ultralow contact resistance between semimetal and monolayer semiconductors. *Nature* **2021**, *593*, 211–217. [CrossRef]
60. Leong, W.S.; Luo, X.; Li, Y.; Khoo, K.H.; Quek, S.Y.; Thong, J.T. Low resistance metal contacts to MoS_2 devices with nickel-etched-graphene electrodes. *ACS Nano* **2015**, *9*, 869–877. [CrossRef]
61. McDonnell, S.; Addou, R.; Buie, C.; Wallace, R.M.; Hinkle, C.L. Defect-dominated doping and contact resistance in MoS. *ACS Nano* **2014**, *8*, 2880–2888. [CrossRef]
62. English, C.D.; Shine, G.; Dorgan, V.E.; Saraswat, K.C.; Pop, E. Improved contacts to MoS_2 transistors by ultra-high vacuum metal deposition. *Nano Lett.* **2016**, *16*, 3824–3830. [CrossRef]
63. Sano, K.; Takahashi, T.; Uchida, K. Large variability of contact resistance in $Au/Cr/MoS_2$ system and its suppression by Cr thinning. *Jpn. J. Appl. Phys.* **2016**, *55*, 36501. [CrossRef]

nanomaterials

MDPI

Article

Mechanical Exfoliation of Expanded Graphite to Graphene-Based Materials and Modification with Palladium Nanoparticles for Hydrogen Storage

Darren Chow [1], Nicholas Burns [2], Emmanuel Boateng [1], Joshua van der Zalm [1], Stefan Kycia [2,*] and Aicheng Chen [1,*]

[1] Electrochemical Technology Center, Department of Chemistry, University of Guelph, 50 Stone Road East, Guelph, ON N1G 2W1, Canada; dchow07@uoguelph.ca (D.C.); eboate01@uoguelph.ca (E.B.); vanderzj@uoguelph.ca (J.v.d.Z.)

[2] Department of Physics, University of Guelph, 50 Stone Road East, Guelph, ON N1G 2W1, Canada; burnsn@uoguelph.ca

* Correspondence: skycia@uoguelph.ca (S.K.); aicheng@uoguelph.ca (A.C.)

Abstract: Hydrogen is a promising green fuel carrier that can replace fossil fuels; however, its storage is still a challenge. Carbon-based materials with metal catalysts have recently been the focus of research for solid-state hydrogen storage due to their efficacy and low cost. Here, we report on the exfoliation of expanded graphite (EG) through high shear mixing and probe tip sonication methods to form graphene-based nanomaterial ShEG and sEG, respectively. The exfoliation processes were optimized based on electrochemical capacitance measurements. The exfoliated EG was further functionalized with palladium nanoparticles (Pd-NP) for solid-state hydrogen storage. The prepared graphene-based nanomaterials (ShEG and sEG) and the nanocomposites (Pd-ShEG and Pd-sEG) were characterized with various traditional techniques (e.g., SEM, TEM, EDX, XPS, Raman, XRD) and the advanced high-resolution pair distribution function (HRPDF) analysis. Electrochemical hydrogen uptake and release (Q_H) were measured, showing that the sEG decorated with Pd-NP (Pd-sEG, 31.05 mC cm^{-2}) and ShEG with Pd-NP (Pd-ShEG, 24.54 mC cm^{-2}) had a notable improvement over Pd-NP (9.87 mC cm^{-2}) and the composite of Pd-EG (14.7 mC cm^{-2}). Q_H showed a strong linear relationship with an effective surface area to volume ratio, indicating nanoparticle size as a determining factor for hydrogen uptake and release. This work is a promising step toward the design of the high-performance solid-state hydrogen storage devices through mechanical exfoliation of the substrate EG to control nanoparticle size and dispersion.

Keywords: hydrogen storage device; graphene-based nanocomposites; liquid phase exfoliation; high shear mixing; probe tip sonication; palladium nanoparticle

1. Introduction

The reliance of fossil fuels as a fuel source has had clear effects on environmental pollution and threatens human health due to the emission of greenhouse gases. An attractive alternative fuel carrier is hydrogen, which only produces water as a product of its combustion [1]. In addition, hydrogen has a remarkable gravimetric energy density of 142 MJ/kg, which is larger than other fuels such as gasoline, which has a gravimetric energy density of 47 MJ/kg [2]. One challenge with the use of hydrogen as a fuel carrier is its storage. This is due to hydrogen being gaseous at room temperature and having a low volumetric energy density. The current traditional methods of storage for hydrogen include pressurized gas and cryogenic compression which both have intrinsic issues such as safety concerns, low volumetric density, and boil off [3]. However, materials-based storage processes involving physical adsorption onto a material constitute a more attractive storage method that has been under the recent focus of research [4–6].

In recent years, the use of nanomaterials has been efficacious in various energy applications as well as hydrogen storage applications [7,8]. Carbon-based materials and nanomaterials such as graphene [9,10], graphitic carbon [11], carbon nanotubes [12,13], and activated carbon [14] are all of particular interest to hydrogen storage applications. Graphene specifically has unique properties including low cost, lightweight, fast reaction kinetics, and high specific surface area [10,15]. To further improve the hydrogen sorption abilities of graphene, various metal nanoparticles such as Pd, Ni, and Ti have been used due to the hydrogen spillover mechanism [9,10,16]. The spillover mechanism involves the sorption of dissociated hydrogen onto the metal nanoparticles followed by migration and diffusion onto the supporting material [17]. Of particular interest is the use of Pd due to its high affinity for hydrogen sorption as well as its low cost compared to other metallic catalysts [18]. A common approach therefore would include the use of Pd-decorated graphene nanomaterials and nanocomposites [19]. The Pd acts to absorb high amounts of hydrogen, which diffuses as atomic hydrogen onto the supporting graphene-based nanomaterials via the spillover process.

The use of high shear force mixing and sonication for the liquid phase exfoliation (LPE) of graphite has recently been the focus of research to prepare graphene and improve the properties of the prepared graphene [20–24]. LPE has attracted considerable research interest due to several advantages. Firstly, in traditional chemical exfoliation techniques, such as Hummer's method, a large amount of harsh acids is utilized, which causes environmental issues [25]. In contrast, the LPE techniques are commonly conducted in aqueous solutions without the need for use of acids [24,26–28]. Furthermore, chemical methods introduce oxygen functional groups and defects in the graphene sheet, which may reduce the electrochemical activity of the formed graphene-based materials [29,30]. To overcome this issue, a reduction step is often required to reduce the oxygen functional groups, which is not needed in LPE methods as they do not create oxygen functional groups. Another reason that LPE has been the focus of research is the scalability and simplicity [20].

In the case of sonication, two separate mechanisms for the exfoliation of graphite are involved. The primary mechanism involves cavitation caused by the ultrasonic vibration, acting upon the graphite layers and generating tensile stress followed by exfoliation. The secondary mechanisms include the wedge effect, where a microjet is produced acting as a wedge driven between graphite layers causing exfoliation, and a shear effect caused by opposing forces acting on adjacent sheets [31]. Meanwhile, the high level of shear forces generated in high-shear mixing is from the low clearance between the rotor and stator of roughly 100 μm. For the exfoliation of graphite, the opposing shear forces acting on individual graphite sheets cause exfoliation, separating the sheets laterally. The use of LPE may facilitate a more uniform distribution and the formation of smaller nanoparticles [32].

Commonly, one method for solid-state hydrogen storage is the use of physisorption onto materials with the aid of high pressures. As extreme high pressures are required for hydrogen storage which also commonly include extreme low temperatures, notable energy requirements give poor efficiency generally reporting less than 1 wt.% hydrogen storage under ambient conditions [5]. In contrast, an alternative method of solid-state hydrogen storage utilizes electrochemistry as the method for hydrogen sorption. The use of electrochemistry has been an attractive method due to the ability for in situ hydrogen uptake, where up to 2.2 wt.% has been reported under ambient conditions [33].

This work reports on the effects of the high shear force mixing and the probe sonication on the exfoliation of expanded graphite (EG) as a pretreatment for the deposition of Pd nanoparticles (Pd-NP). The synthesized nanomaterials and nanocomposites were characterized through several techniques including scanning electron microscopy (SEM), transmission electron microscopy (TEM), energy-dispersive X-ray spectroscopy (EDX), X-ray photoelectron spectroscopy (XPS), X-ray diffraction crystallography (XRD), high-resolution pair distribution function (HRPDF) analysis, Raman spectroscopy, and various electrochemical techniques. To the best of our knowledge, the use of high shear mixing and

probe sonication prior to the deposition of Pd for the use in hydrogen storage has not been previously reported.

2. Materials and Methods

2.1. Materials

Graphite was obtained from Zentek Ltd. (Guelph, ON, Canada). Phosphoric and sulfuric acid were purchased from Fisher Scientific. Iron (III) chloride hexahydrate, potassium permanganate, palladium (II) nitrate, sodium borohydride, and Nafion perfluorinated resin solution (5 wt% in lower aliphatic alcohols and water) were all used as received from Sigma-Aldrich (St. Louis, MO, USA). Ultrapure argon gas was also used as received from Linde Canada. Purified water (18.2 MΩ) was obtained by a ThermoFisher Scientific (San Diego, CA, USA) Barnstead NANOpure Diamond UV ultrapure water system. Powdered diamond nanoparticles were obtained from Sigma-Aldrich for the calibration in the HRPDF analysis.

2.2. Synthesis of EG

EG was prepared as previously described [19]. Briefly, using an ice–water bath for cooling, 40 mL of a 4:1 v/v acidic solution of phosphoric and sulfuric acid was added to 1 g of graphite powder and was stirred using a magnetic stir bar for 5 min. Then, 4 g of potassium permanganate was added while mixing. After 30 min, 0.5 g of iron (III) chloride was added, and the solution was left to stir for an additional 1 h. The solution was then centrifuged and rinsed with purified water. The obtained sedimented graphite intercalated compound (GIC) was left to dry completely in an oven at 60 °C. The GIC was crushed with a mortar and pestle, loaded into a ceramic crucible, covered with a steel lid, and thermally expanded at 600 °C for 5 min to produce EG.

2.3. Synthesis of Mechanically Exfoliated Nanomaterials

To prepare the mechanically exfoliated materials, a 4 mg/mL suspension of EG was prepared in a solvent ratio of 30% v/v EtOH in pure water. The experiments were conducted using a 50 mL centrifuge tube cut to 75 mm tall and 29 mm diameter.

2.4. Synthesis of ShEG Nanomaterials

For the high-shear exfoliation of EG, a Silverson L5M-A rotor stator mixer was used. The mixer head was lowered into the suspension, roughly 10 mm from the bottom of the vessel, and shear mixed for 30, 45, 60, and 75 min at 10,000 RPM to determine the optimum mixing time (ShEG-XX where XX denotes the time shear mixed). To prevent excessive heating and to improve exfoliation as reported by previous studies [26], the experiment was conducted with the vessel partially submerged in an ice water bath.

2.5. Synthesis of sEG Nanomaterials

For the probe sonication exfoliation of EG, a Fisher Scientific Model 705 sonic dismembrator was used with a 127 mm replaceable tip probe. The probe was lowered into the EG suspension in the same manner as the shear mixing procedure, roughly 10 mm from the bottom, and was sonicated at 50% amplitude for various times using a 3 s on and 3 s off pulse for total sonication times of 10, 15, 20, 25, and 30 min to determine the optimum sonication time (sEG-XX where XX denotes the period of time sonicated). The pulse was used to avoid excessive heating or evaporation of solvent along with submerging the vessel in an ice–water bath. The solution was also monitored by a temperature probe to keep the solution below 65 °C. The ShEG and sEG samples were freeze dried (Buchi Lyovapor L-200, Buchi Corporation, New Castle, DE, USA). The purpose of the freeze drying was to attempt to retain the separation of the graphene sheets [34,35].

2.6. Synthesis of Pd-Decorated Nanocomposites

Palladium (II) nitrate was added to 4 mg/mL of ShEG and sEG solutions with a target of a 20 wt.% Pd loading and stirred for 15 min. Sodium borohydride was then added in excess and stirred for an additional 30 min. The solution was centrifuged, rinsed 3 times and then left to dry in a 50 °C oven. As a control sample, EG that was not treated with the mechanical exfoliation was first bath sonicated to be dispersed in the same solvent ratio of 30% v/v ethanol/water for 25 min; then, it was subjected to the same procedure as previously described to prepare Pd-EG. Furthermore, Pd-NP was prepared in the same approach but without the addition of EG.

2.7. Structural Characterization

Scanning Electron Microscopy (SEM) (FEI Quanta FEG 250, FEI Company, Hillsboro, OR, United States) and Transmission Electron Microscopy (TEM) (FEI Titan 80-300 LB, FEI Company, Hillsboro, OR, USA) were used to investigate the morphology of the synthesized materials. Energy-dispersive X-ray spectroscopy (EDX) (Oxford XMax20, Oxford Instruments Group, Concord, MA, USA) was employed to investigate the elemental composition and distribution. X-ray photoelectron spectroscopy (XPS) (Scienta Omicron Inc., Colorado, MA, USA) was used to investigate the elemental composition as well as the valence states of the materials. C 1s, O 1s, Pd 3d, and Pd 3p high-resolution XPS spectra and survey spectra were obtained for all samples. The XPS data were analyzed using CasaXPS V2.3.23 software. All XPS spectra were corrected by the C 1s sp^3 peak which was set to 285.0 eV. X-ray diffraction (XRD) crystallography was conducted on a PANanalytical Empyrean powder diffractometer with a Cu Kα (λ = 1.5405 Å) radiation source. Diffraction patterns were obtained using a spinner stage with a 2θ range of 10 to 90°. XRD patterns were analyzed using X'Pert HighScore Plus V2.2.4 software. Raman spectroscopy (Renishaw InVia, Renishaw, Mississauga, ON, Canada) was conducted using a 532 nm laser from a range of 1200 to 2800 cm^{-1}.

Further X-ray diffraction experiments were performed at the Canadian Light Source using the Brockhouse sector high-energy wiggler beamline [36]. All samples were measured at a temperature of 80 K using 55 keV X-rays. The total scattering patterns were collected using the Varex XRD 4343CT (Varex Imaging, Salt Lake City, UT, USA) flat-panel area detector. The detector was positioned at an inclined geometry bisected by the vertical scattering plane with a pitch angle of 30°. The detector was then translated such that the incident X-ray beam strikes the pixels along the bottom edge and 125° scattered X-rays impinge on the center-most pixel along the top edge. The scattering area used in the analysis was a wedge covering 90° in the azimuthal scattering angle χ and 40 $Å^{-1}$ in Q. The collected total scattering patterns are simultaneously integrated to one-dimensional patterns in Q and corrected for measurement distortions using custom python code. The measurement distortions were quantified for the inclined geometry using a procedure outlined previously [37]. $G(r)$ data analysis was performed using the PDFGUI [38].

2.8. Electrochemical Measurements

All electrochemical experiments were conducted using a CHI Potentiostat (CHI660E, CH Instruments, Inc., Bee Cave, TX, USA) with a three-electrode system. Cyclic voltammetry (CV) was conducted in a single chamber cell at 0.010 V/s, while linear sweep voltammetry (LSV) and chronoamperometry (CA) were conducted in a two-chamber U-cell with a cation exchange membrane separating the counter electrode from the working and reference electrode. A standard calomel electrode (SCE) (Hg/Hg_2Cl_2) filled with a 3 M KCl solution was used as a reference electrode, and a cleaned platinum wire was used as the counter electrode. To prepare the working electrode, 4 mg of the prepared materials was mixed with 100 µL Nafion binding agent (5 wt.%), 300 µL ethanol, and 600 µL pure water and sonicated for 20 min in a bath sonicator to disperse the mixture. Graphite foil was cut and pretreated by bath sonication for 10 min each in the sequence of pure water, 0.1 M HCl, pure water, and ethanol. Then, 70 µL of the nanomaterial ink was then drop

cast on the pretreated carbon paper to have a geometric surface area of 1 cm^2 and then left to dry overnight. Prior to each measurement, the electrolyte (0.5 M H_2SO_4) was purged with ultrapure argon for 20 min. The double-layer capacitance of the ShEG and sEG was calculated by CV using a potential window of 0.00 to 0.10 V at different scan rates varied from 0.010 to 0.100 V/s. The change in current at 0.05 V vs SCE was plotted against the scan rate, and the generated linear slope was used to calculate the double-layer capacitance.

3. Results and Discussion

3.1. Capacitance Studies of Mechanically Exfoliated EG

To determine the optimum period of processing time for the LPE procedure, the electrochemical double-layer capacitance in materials processed for different periods of time were compared. The samples which underwent high-shear for different times were compared first using CVs, as shown in Figure 1A. In Figure 1B, ShEG-45 is used as a representative sample in CV and shows sweeps at varying scan rates from 0.010 to 0.100 V/s where the difference in current density between the oxidative and reductive sweeps at 0 V was taken and is used to determine the capacitance of each material. It can be observed that 45 min has a higher capacitance than the other shear exfoliation times, as seen in Figure 1C, and thus was used for further experiments. The same experiments were conducted for the probe sonication exfoliation method. The CV curves shown in Figure 1D demonstrate that sEG-25 has the highest double-layer capacitance. Representative CV curves are shown in Figure 1E for the determination of the capacitance in the same manner as previously described. To confirm the highest capacitance, the same calculation as the ShEG materials was conducted and is shown in Figure 1F. Capacitance is commonly used to compare the performance of graphene. Additionally, the shape of the curve can also be used to describe the electrochemical behavior of the material, where a more rectangular CV curve implies higher capacitive performance [39]. The comparison in Figure 1B,E shows that sonication has a more rectangular CV shape. The electrochemically active surface area (ECSA) is associated with the capacitance. As shown in Table S1, sEG-25 exhibits the highest ECSA.

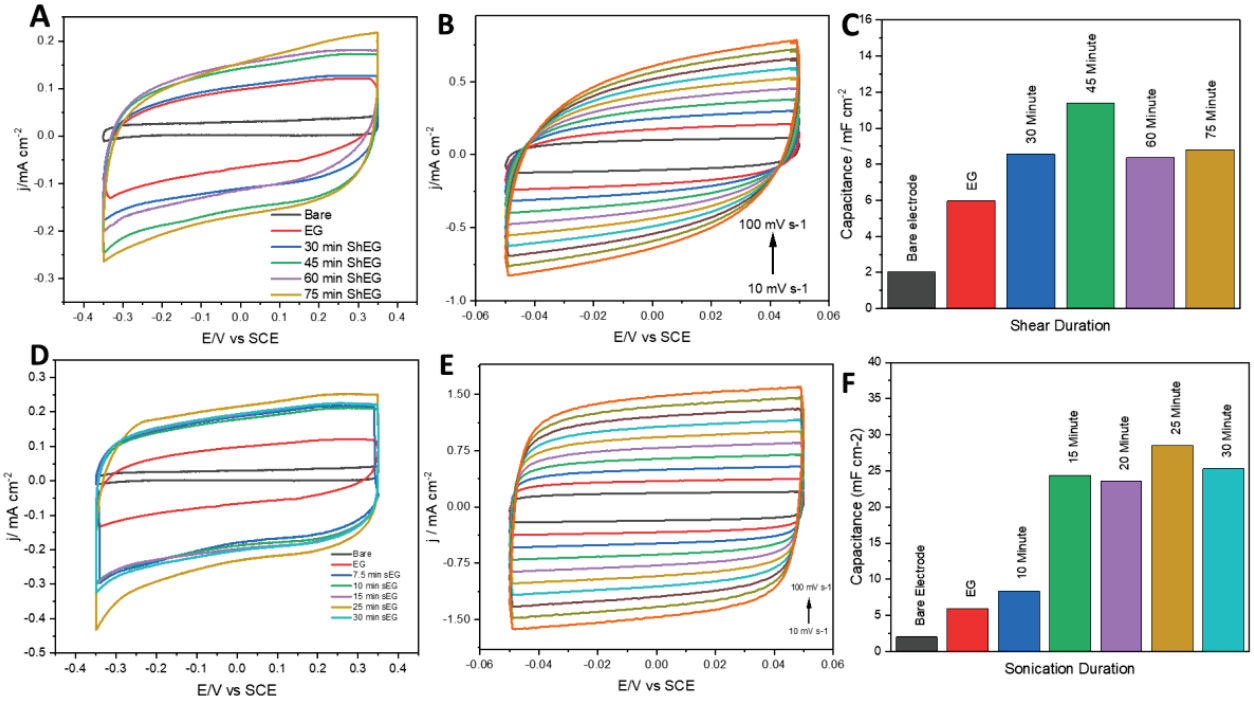

Figure 1. (**A**) Shear duration time study comparing the double-layer capacitance of bare graphite foil, EG, and EG after shearing for 30, 45, 60, and 75 min. (**B**) Cyclic voltammetry sweeping scan rate used

to determine capacitance of ShEG after shear mixing for 45 min. (**C**) Summary of capacitances of the shear mixed materials. (**D**) Sonication duration time study comparing the double-layer capacitance of bare graphite foil, EG, and EG after high-powered tip sonication for 10, 15, 20, 25, and 30 min. (**E**) Cyclic voltammetry sweeping scan rate used to determine capacitance of ShEG after shear mixing for 45 min. (**F**) Summary of capacitances of the sonicated materials.

3.2. Morphological Characterization of Graphene-Based Nanomaterials

SEM and TEM were used to investigate the morphology of the synthesized nanomaterials and nanocomposites. Representative images of EG, ShEG, sEG are shown in Figure 2. The starting material EG in Figure 2A had a porous sponge-like structure which is comparable to untreated graphite flakes but with higher interlayer distances. The increase in interlayer distance between the carbon sheets was a result of the oxidative chemical procedure and the intercalation of ions followed by thermal treatment, which caused an expansion and mild exfoliation of graphite. The mechanical LPE process was successful in producing characteristic crumpled graphene sheets, as seen in Figure 2B,C. Figure 2D displays the EDX spectra of the samples, where the presence of C and O was confirmed for the EG, sEG and ShEG samples. The atomic percentages of C and O for each sample were calculated and are listed in Table S2. It is confirmed that the mechanical exfoliation procedures do not introduce oxygen content to the nanomaterials. Further TEM images of ShEG and sEG are shown in Figure 2E,F, respectively, where characteristic graphene wrinkled sheets were observed. The ShEG showed a lower degree of exfoliation with darker areas representing a thicker stack of interconnected graphene sheets while sEG exhibited a lighter and more exfoliated material.

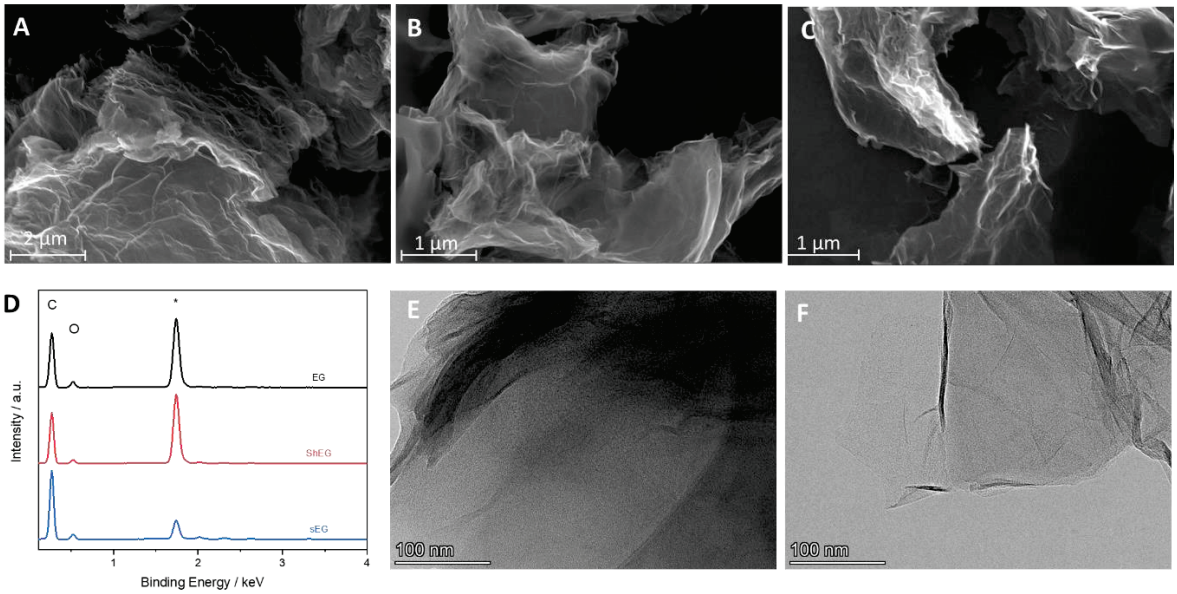

Figure 2. SEM images of (**A**) EG, optimized (**B**) ShEG, (**C**) sEG samples. (**D**) EDX of the prepared graphene-based nanomaterials where the carbon and oxygen peaks are labeled and the substrate silicon peak labelled with *. TEM images of optimized (**E**) ShEG and (**F**) sEG samples.

Further elemental analysis in XPS also confirmed the presence of C and O in the nanomaterials. Figure 3A survey scans reveal that each sample has a C 1s peak at roughly 284 eV and an O 1s peak at roughly 532 eV. In Figure 3B,C, high-resolution scans of the C 1s peak are shown for the optimized sEG and ShEG nanomaterials. Peaks at roughly 284, 286, 287, 289, and 290 eV are attributed to C=C/C-C, C-O-C/C-OH, C=O, O-C=O, and π-π*, respectively. Similar results were seen in Figure S3B. The primary peak observed is the C=C peak, which is characteristic of graphitic materials.

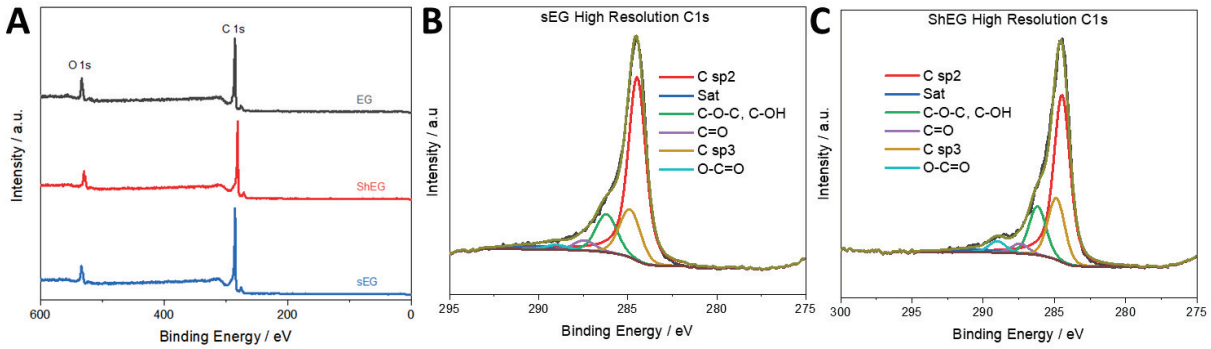

Figure 3. (**A**) XPS survey scan of the synthesized nanomaterials. (**B**) XPS high-resolution C1s scan of the prepared sEG nanomaterial and (**C**) ShEG.

Radial distribution function $R(r)$ analysis of the substrates can provide unique information about the degree of defects and quantity of functional groups which conduct the dispersion and size of the nanoparticles grown in situ within the substratum. In Figure 4A, the $R(r)$ for all substrates is shown. Each $R(r)$ shows a similar pattern with slight variations in intensity. Taking the differential radial distribution functions $\Delta R(r)$ between substrates, more information is gleaned about the changes that each of the LPE techniques introduce into the substrate. In Figure 4B, the $\Delta R(r)$ was calculated between the LPE substrates (ShEG, sEG) and the untreated EG. The LPE substrates show increased and sharper correlations in the characteristic graphene C-C basal-plane nearest-neighbor (NN) distances of 1.43, 2.45 and 2.84 Å. These changes are in conjunction with a decrease in intensity around the respective peaks. The correlations around the characteristic graphene NN distances are a result of functional groups such as O-H, C-H, C-O and C-C defects from pristine graphene locations. In concert, these changes indicate a reduction in the basal–plane defects and functional groups for both LPE substrates, as compared to EG. Furthermore, comparing the LPE substrates to one another, ShEG shows an increase in only the 1st and 2nd nearest-neighbor distances at 1.43 and 2.45 Å, respectively. This indicates that defects are reduced in degree but are not completely removed due to the missing 3rd nearest-neighbor distance at 2.84 Å. Defects which could explain the missing intensity of the 3rd NN include intrinsic graphene defects such as Stone–Wales, single and multiple vacancy. Conversely, sEG produces a similar trend; however, additional intensity is observed at the 3rd NN distance, indicating a mix of partial and complete reduction in defects occurred as compared to ShEG. The changes between ShEG and sEG substrates are further highlighted in Figure 4C.

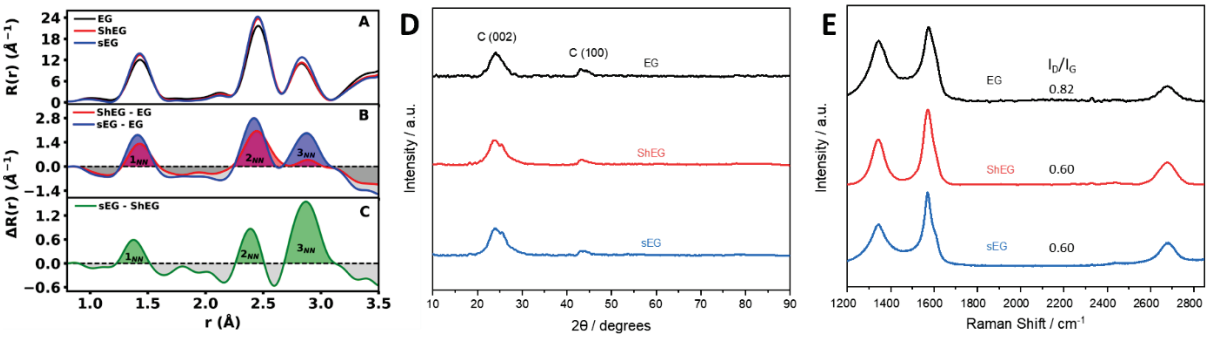

Figure 4. (**A**) Experimental $R(r)$ of the substrates EG, optimized ShEG and sEG samples. (**B**) Experimental $\Delta R(r)$ of ShEG and sEG by subtraction of EG substrate. (**C**) Experimental $\Delta R(r)$ of sEG by subtraction of ShEG substrate. The increased intensity for the characteristic graphene C-C basal-plane nearest-neighbor (NN) distances are shaded in red, blue and green while the reduced functional group intensities are shaded in gray. (**D**) XRD patterns of nanomaterials prepared through mechanical exfoliation using shear and sonication. (**E**) Raman spectroscopy of the various prepared nanomaterials with the defect density, I_D/I_G, listed for each nanomaterial.

Further investigation of the nanomaterials was conducted with XRD measurements to probe the structural and crystallite characteristics. Each pattern shows a characteristic C (002) plane peak at roughly $2\theta = 25°$ in Figure 4D. The samples presented show evidence of successful exfoliation of the graphite sheets into graphene sheets from the broadening of the C (002) peak.

Through Raman spectroscopy, the relative number of defects in the samples can also be investigated. By taking the intensity of the D-band (I_D) at roughly 1350 cm^{-1} and dividing the intensity of the G-band (I_G) at roughly 1600 cm^{-1} as seen in Figure 4E, the I_D/I_G ratio is obtained, where higher ratios imply an increased number of defects in the graphene sheet. A third peak is also present at roughly 2700 cm^{-1} known as the 2D-band, which is an overtone of the D-band. The G-band relates to the in-plane stretching of the graphene sheet, while the D-band relates to the in-phase vibrations of the hexagonal ring of carbon atoms in a radial direction [40]. The change in I_D/I_G from the starting material, EG, to the mechanically exfoliated samples demonstrates that the process did not introduce any additional defects but produces graphene with reduced defects. This trend agrees well with the reduction in graphene defects observed in the $R(r)$ analysis of the substrates.

3.3. Characterization of Palladium Nanoparticle Functionalized Nanocomposites

Similar to the non-functionalized nanocomposites, the Pd-NP functionalized nanocomposites were investigated through SEM, EDX, and TEM. The decoration of Pd on EG did not change the morphology but had a notably larger sized Pd-NP on the edges of the EG structures as seen in Figure 5A. In contrast, small Pd particles were seen for both Pd-ShEG (Figure 5B) and Pd-sEG (Figure 5C), showing that the higher degree of exfoliation produced by the sonication was favorable for the uniform distribution of the Pd-NP. EDX was also used to investigate the elemental composition of the prepared nanocomposites in Figure 5D. The presence of C, O, and Pd was confirmed for all materials with similar compositions as listed in Table S1 and had a consistent Pd-NP atomic percent of roughly 2%. In the case of EDX mapping (Figure S1), the uniform distribution of Pd on the sEG surface was observed. Further imaging using TEM was conducted, showing finely exfoliated graphene with Pd-NP functionalized on the sheet. Further analysis allowed for the determination of particle sizes, where smaller Pd-NP sizes in Pd-sEG (~3.8 nm) were found compared to Pd-ShEG (~7.0 nm).

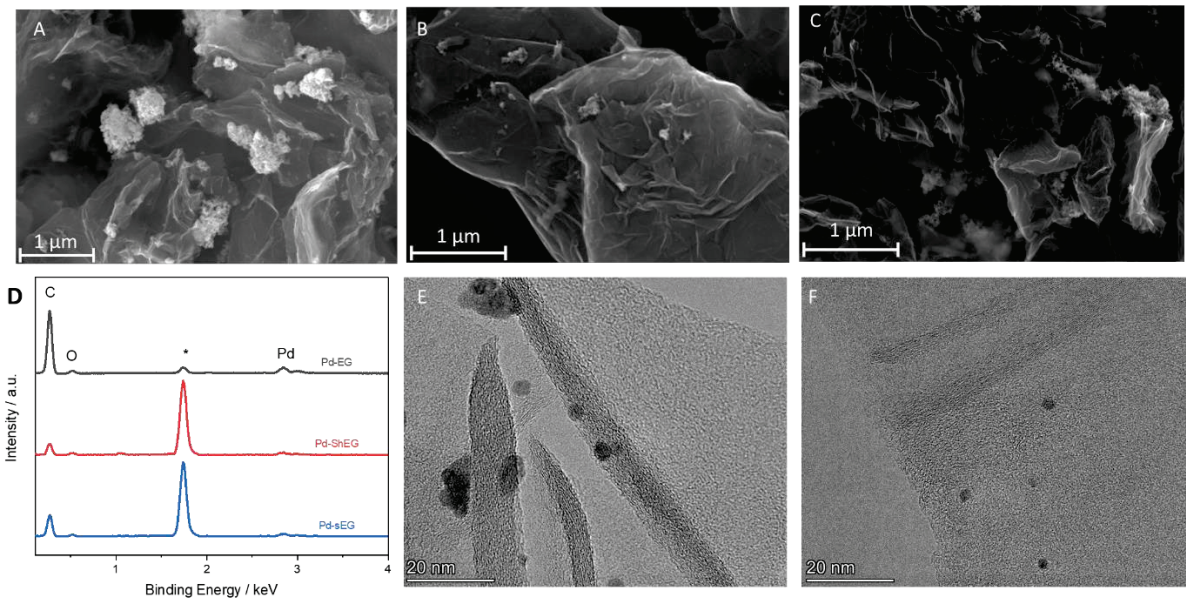

Figure 5. SEM images of (**A**) Pd-EG (**B**) Pd-ShEG (**C**) Pd-sEG nanocomposites. (**D**) EDX spectra of Pd-functionalized nanocomposites with the carbon, oxygen, and palladium peaks are labelled and the substrate silicon peak labelled with *.TEM images of (**E**) Pd-ShEG and (**F**) Pd-sEG nanocomposites.

XRD analysis was also conducted on the nanocomposites. In Figure 6A, Pd-NP is shown and compared to the Pd-NP functionalized nanocomposites. In each pattern, the peaks present are at roughly 40, 45, 67, and 80°, which are attributed to the Pd (111), Pd (200), Pd (220), and Pd (311) planes, respectively, with Pd (111) being the dominant plane observed. The characteristic C (002) peak is still observed at θ = 25 °. As the FWHM of the C (002) peak was consistent with non-functionalized samples, the functionalization process did not affect the degree of exfoliation. To confirm EDX results, XPS was also conducted on the nanocomposites. Using the material with the highest activity, Pd-sEG, as an example, the high-resolution scan of C 1s (Figure 6B) shows that the carbon structure is similar to non-functionalized materials, as seen in Figure S3B. Furthermore, a high-resolution XPS scan of Pd 3p (Figure 6C) confirms the presence of Pd metal. In the survey scan (Figure S2), the Pd-NP-decorated samples also contain Pd 3d peaks at roughly 340 and 344 eV, which imply the presence of metallic Pd, as seen in Figure S3A in high-resolution scans of the Pd 3d peaks. Furthermore, for these samples, the Pd $3p_{3/2}$ peak is deconvoluted from the O 1s intensity using the Pd $3p_{1/2}$ peak, which results due to spin orbit coupling. The Pd $3p_{1/2}$ peak intensity is known to have a 1:2 ratio to the Pd $3p_{3/2}$ such that the remaining area of the convoluted peak can be attributed to oxygen intensity [41], as seen in Figure 6C.

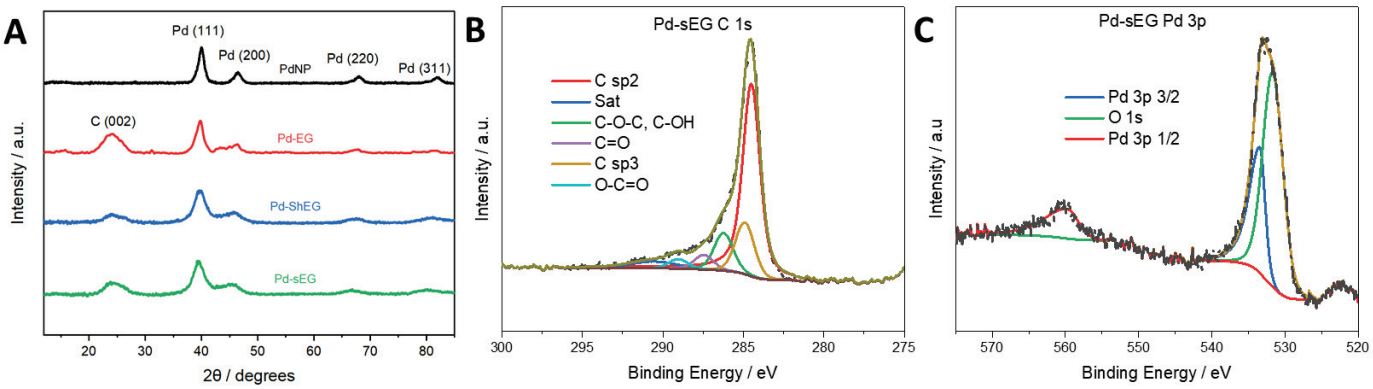

Figure 6. (**A**) XRD patterns of Pd-functionalized nanomaterials with peaks attributed to the Pd (111), Pd (200), Pd (220), and Pd (311) planes. (**B**) XPS high-resolution scan of Pd-sEG C 1s. (**C**). XPS high-resolution scan of the Pd 3p and O 1s peaks of Pd-sEG nanocomposite.

Nanoparticle size determination is conducted through Bragg diffraction, TEM images, and $G(r)$ analysis. Specifically, through modeling of the $G(r)$, accurate mean spherical nanoparticle diameters can be determined for each sample. Methods such as TEM images and Bragg diffraction can often under-represent smaller-sized particles [42]. For accurate size determination, the instrument broadening factors are first determined through $G(r)$ modeling of a Sigma-Aldrich powdered diamond sample. The palladium mean diameter was refined to values of 8.4 $\pm$ 0.13, 5.6 $\pm$ 0.12, 4.2 $\pm$ 0.11 and 3.5 $\pm$ 0.09 nm for nanoparticles deposited in ex-substratum, EG, ShEG and sEG substrates, respectively. This trend in nanoparticle size is observed between all methodologies and is listed in Table S2. Additionally, the trend follows that of the defect and functional group concentration observed within the substrates from Raman and $R(r)$ analysis. As the defect density decreases and functional groups are reduced, there are fewer binding sites available, resulting in smaller, more well-dispersed nanoparticles [32].

Pd-NP has a high affinity for hydrogen sorption, making them an ideal additive to EG for solid-state hydrogen storage. Total scattering studies of Pd-NP using pair $G(r)$ and radial $R(r)$ distribution function analysis can provide unique information about the structural characterization, deformation, and composition of these nanoparticles. Total scattering studies were performed for all palladium nanoparticles grown in situ for all investigated LPE methodologies. Additionally, total scattering studies were performed for all substrates prepared using all LPE methodologies. Through subtraction of the substrate signal from the respective Pd deposited substrates, the total scattering from only the Pd

nanoparticles is isolated. We observed the formation of core–shell PdH_x nanoparticles in all cases. The core component is found to be nanocrystalline, while conversely, the shell component is disordered. PdH_x has previously been shown to form core–shell structures [43–45]. Commonly, the nanocrystalline component is reported as face-centered cubic (FCC) PdH_x. Here, both core and shell components are fit to a strained FCC PdH_x phase. The strain occurs along the $<110>_c$ slip direction for the cubic $\{111\}_c$ slip plane. Similarly strained pseudo-cubic systems have been observed through X-ray and neutron powder diffraction [46–49]. To simplify the unit cell distortion caused by the strain, a hexagonal convention of FCC can be chosen. The strain along the $<110>_H$ direction is then accounted for by producing a pseudo-hexagonal unit cell with an α, β angle of 89.25° for the core and 81.65° for the shell, which produces a tilt angle Φ of 1.5° and 16.7°, respectively. The tilt angle is found to be constant for all nanoparticle sizes. The conversion from cubic to hexagonal convention used is shown in Figure 7A. Expansion of the a_H and b_H axes and the compression of the c_H axis are found to be proportional to the surface area to volume ratio. Conversely, the lattice constants of the shell phase were found to be constant for all nanoparticle sizes. The comparison of the core component lattice constants to the surface area to volume ratio is shown in Figure 7B.

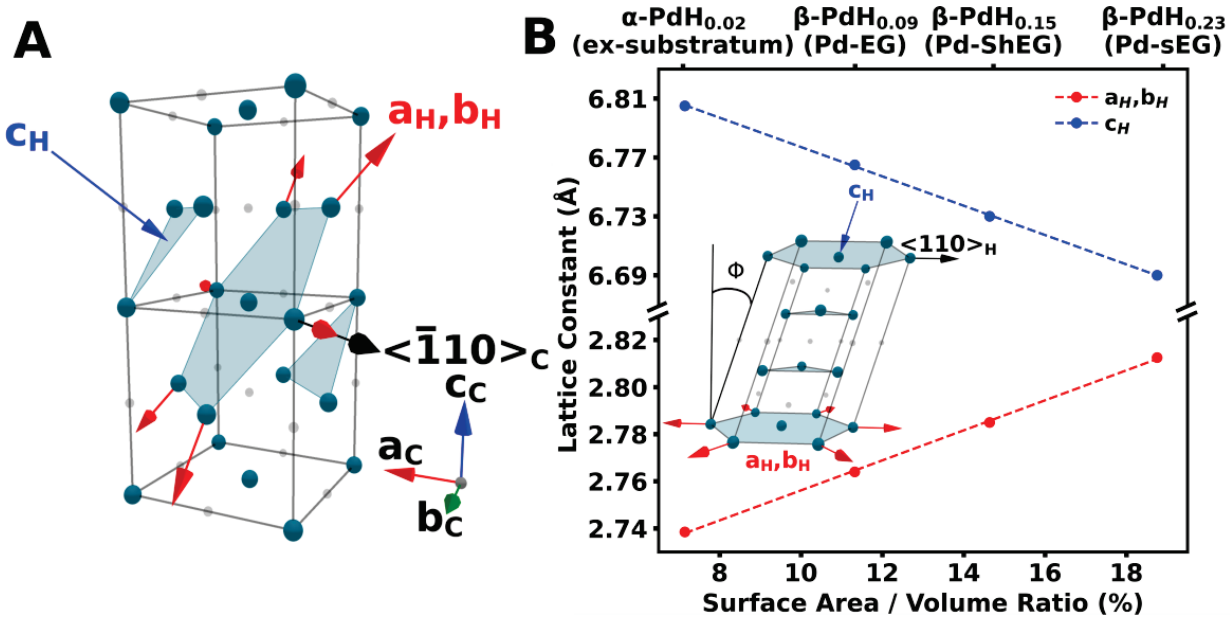

Figure 7. (**A**) Diagram highlighting the choice between cubic and hexagonal conventions for the face-centered cubic PdH_x unit cell. (**B**) Comparison of the pseudo-hexagonal lattice constants and the surface area to volume ratio. Inset shows the pseudo-hexagonal unit cell convention. Blue arrows represent the compression along the c_H axis, red arrows represent expansion along a_H, b_H axes and black is the strain of the cubic $\{111\}_c$ plane in the $<110>_c$ or equivalently $<110>_H$ direction. Additionally, the tilt angle Φ is shown.

Using the pseudo-hexagonal unit cell, the experimentally measured $G(r)$ for palladium nanostructures grown in situ in each substrate were modeled. The calculated $G(r)$ core–shell model for β-$PdH_{0.23}$/sEG is shown in Figure 8A. The phase fractions of the core and shell components were found to be proportional to thesurface area to volume ratio as expected for a core–shell system. The phase fractions are shown in Figure S4 in the supplemental materials. The core and shell components are separated, and the total model error is split between each component by a phase fraction.

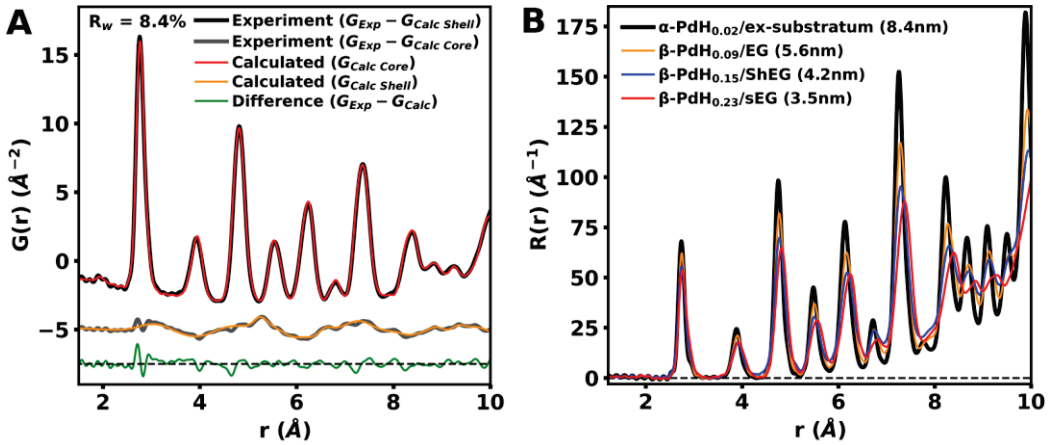

Figure 8. (**A**) Experimental $G(r)$ of the remaining Pd structures after subtraction of the sEG substrate. Experimental $G(r)$ is fit to the theoretical core–shell model using a β-$PdH_{0.23}$ pseudo-hexagonal core and a disordered PdH_x pseudo-hexagonal outer shell. (**B**) Experimental $R(r)$ of PdH_x core components grown in situ on ex-substratum, EG, ShEG and sEG substrates. The $R(r)$ highlights the distortion which is occurring from the ideal PdH_x FCC unit cell with decreasing nanoparticle size and increased hydrogen content.

The appearance of a small peak in the $G(r)$ as observed in Figure S5C,D for Pd-ShEG and Pd-sEG at 2 Å confirms the presence of hydrogen within the system, and that hydrogen content is increasing as the nanoparticle size decreases. The hydrogen content of the PdH_x is often calculated as a function of the cubic lattice constant b [50–52]. Here, the system is pseudo-cubic; to account for this, the relationship provided [51] is recalculated as a function of pseudo-hexagonal unit cell volume, as shown in Figure S6A. Using this relationship, the hydrogen content for each group of palladium nanoparticles is calculated. The calculated hydrogen content is found to be proportional to the surface area to volume ratio, as observed in Figure S6B. The remaining experimental $G(r)$ values are presented in the supplementary materials in Figure S7. The aforementioned HRPDF results were consistent with the hydrogen uptake measured by the electrochemical technique.

3.4. Hydrogen Uptake and Release Performance of Pd-EG Nanomaterials

To test the material's hydrogen uptake and release ability, CV curves of the palladium-decorated nanomaterials were conducted in the same conditions as previously stated. Figure 9A compares Pd-NP vs. the prepared nanomaterials from a potential range of −0.3 to 0.6 V vs. SCE with two clear peaks. The peaks are interpreted as the adsorption of hydrogen from roughly 0 to −0.3 V and desorption of hydrogen from roughly −0.3 to 0.05 V. The material with the highest adsorption and desorption is Pd-sEG, which demonstrates that sonification exfoliation has the ability to improve hydrogen storage. Similarly, Pd-ShEG, high shear mixing exfoliation is also shown to improve the adsorption and desorption of hydrogen over the base Pd-EG material. Moreover, Pd-NP with their electrochemical activity normalized by Pd wt.% demonstrates that a synergistic effect occurred when they were combined with EG in Figure 9A. The mechanism for the hydrogen uptake and release can be derived based on the Volmer process [53]. The process can therefore be explained through the scheme $M + e^- + H^+ \rightleftharpoons H_{ad} - M$, where M represents the material or sample. Further analysis was conducted by taking the integration of the anodic desorption peak to calculate the hydrogen desorption charge, Q_H, which gives a measure of how much hydrogen is released after uptake. Figure 9B confirms that Pd-sEG has the highest hydrogen desorption charge (31.05 mC cm^{-2}) as compared to Pd-ShEG (24.54 mC cm^{-2}), Pd-EG (14.70 mC cm^{-2}) and Pd-NP (9.87 mC cm^{-2}). This demonstrates again that sonication is effective in improving the hydrogen storage ability. The improvement might be explained by the effective exfoliation caused by the sonication and high

shear mixing process and increase in surface area allowing for a higher availability of Pd-NP for hydrogen uptake and release.

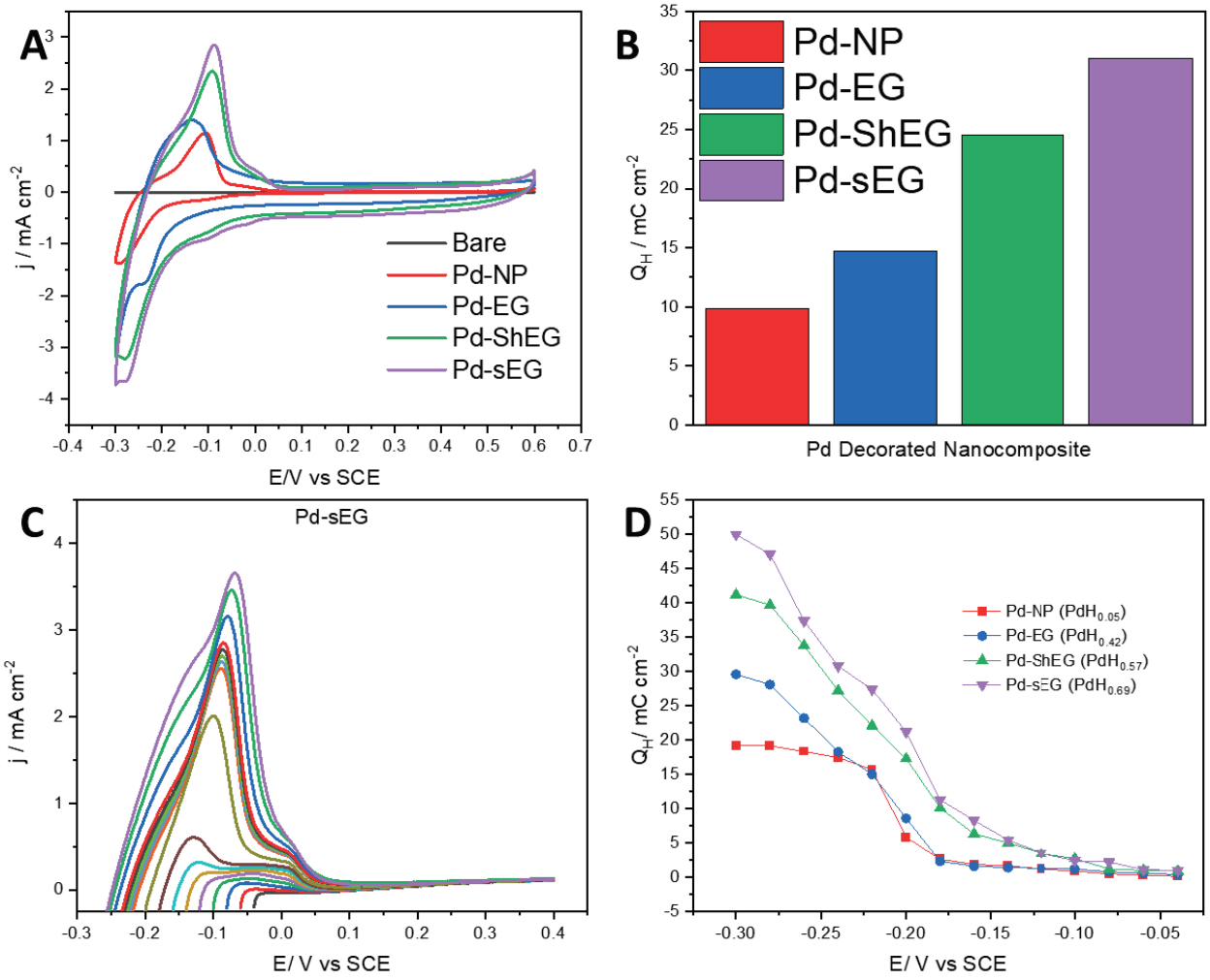

Figure 9. (**A**) Cyclic voltammetry of the various nanomaterials prepared without mechanical exfoliation, with sonication and shear, as well as Pd-NP, EG, and bare carbon paper. (**B**) The associated integration of the curve for the desorption charge for nanomaterials with Pd deposition. (**C**) LSV after holding the potential at −0.300 V for 5 min and varying the starting potential from −0.300 to −0.040 V. (**D**) Overall hydrogen desorption charge, Q_H, obtained from integration of LSVs of the various nanomaterials including Pd-NP, Pd-EG, Pd-ShEG, and Pd-sEG.

Further electrochemical testing was conducted using a U-cell with the working electrode separated from the Pt wire counter electrode with a cation exchange membrane. The use of a U-cell to separate the working electrode from the counter electrode is to address concerns relating to the deposition of Pt on the working electrode. Pt deposition is more likely to occur in experiments with held potentials and repeated cycling [54]. As a result, this effect was only considered for the following analysis. First, the time required to achieve maximum hydrogen storage capacity was determined using LSV and CA. CA was conducted by holding the potential at −0.3 V for 1, 3, 5, 7 and 10 min. After each hold time, an LSV was conducted sweeping from −0.3 to 0.6 V at a 0.010 V/s scan rate. It was seen that the current density was increased to a maximum. To determine the optimum holding time, the integration of the anodic sweep was calculated for each curve for each nanocomposite and compared against the hold time. It is seen that across all materials, there is a plateau of Q_H after 3 min, indicating a complete saturation of hydrogen. To ensure a maximized hydrogen sorption, CA was conducted for 5 min for all further experiments. In a different

set of experiments, after a 5-min CA hold was conducted at different potentials, LSVs were immediately run at the held potentials from −0.3 to −0.04 V to a consistent 0.4 V upper potential. The set of LSV scans for Pd-sEG is shown as a representative graph in Figure 9C. For each material, the Q_H was determined for each different held potential shown in Figure 9D.

For the scans shown, a major desorption peak is seen with a shoulder peak present. The two desorption peaks can be attributed to different phases of Pd-hydride, which are dependent on the applied potential. The α-phase hydride is associated with hydrogen sorption at lower concentrations as a solid solution, while the β-phase hydride relates to higher concentrations of hydrogen in the material as a hydride. Furthermore, an intermediate α-β or α' phase exists between the α and β phases [19,55,56]. It is shown that over the range of the different potential sweeps, Pd-sEG had the highest Q_H (50.40 mC cm^{-2}), while Pd-ShEG showed slightly lower activity (41.20 mC cm^{-2}), and both LPE samples had notably improved activity over the base materials (29.60 mC cm^{-2} for Pd-EG and 19.15 mC cm^{-2} for Pd-NP). From Figure 9D, insight into the phases of Pd-hydride can also be obtained. The slight increase in Q_H in the potential range from −0.040 to −0.190 V is attributed to increased capacity for α-phase hydride, while the range from roughly −0.200 to −0.260 V would be the α-β phase hydride transition phase. Finally, the higher potential range of roughly −0.280 to −0.300 V can be attributed to β-hydride formation. For Pd-NP and Pd-EG, it is also seen that a plateau of Q_H is seen from −0.220 to −0.300 V, which implies a maximized hydrogen sorption, while there is continued increase for the LPE samples. This increase in hydrogen sorption could be attributed to the increased hydrogen spillover caused by the higher exfoliation as evidenced in SEM and XRD as well as higher capacitance. In previous studies, it has been reported that the transition between the α-β phase hydride affects the hydrogen sorption as the rate-determining step [57]. It can therefore be inferred that a higher α-β phase also implies a higher hydrogen uptake. The PdH_x was also calculated and listed in Figure 9D based on Q_H.

It was previously confirmed in Table S1 that the exfoliation methods increased the surface area of materials. The increase in surface area can therefore be correlated to the hydrogen uptake and release ability of materials. It has been seen that samples that have increased surface area allow for a more uniform distribution of Pd-NP and higher Q_H. This could be due to a higher number of active sites allowing for more effective hydrogen spillover effect through a more effective diffusion of H [33].

Stability testing was also conducted on the Pd-functionalized nanocomposites through repeated cycling of cyclic voltammetry. The experiments were conducted at a 0.020 V/s scan rate with a potential window of −0.3 to 0.6 V. As previously stated, due to concerns regarding the deposition of Pt from the counter electrode, the experiments were conducted using a U-cell with a cation exchange membrane separating the working and reference electrode from a Pt wire counter electrode. The electrolyte utilized was the same as previous experiments: 0.5 M H_2SO_4 initially purged with Ar gas. The cycling stability tests demonstrated there is a only slight decrease in activity, as shown in Figure S8.

4. Conclusions

To conclude, the use of mechanical liquid phase exfoliation of expanded graphite increases the surface area to allow for a more dispersed decoration of Pd-NP compared to the base material. The increased surface area and higher dispersed Pd-NP allows for more accessibility for H-sorption due to a higher number of active sites. This is confirmed based on morphological and electrochemical characterization demonstrating the efficacy of the utilized high-shear mixing exfoliation and probe-tip sonication as pretreatments. The optimized processing time for both high-shear mixing and probe-tip sonication was determined through the use of capacitance studies. After the mechanical exfoliation of graphite to graphene, the use of freeze drying was used to prevent the agglomeration of the carbon sheets prior to the decoration with Pd-NP. The hydrogen storage uptake and release of Pd-sEG was the highest when compared to the base materials of Pd-EG and Pd-NP,

while Pd-ShEG also improved the capacity. The advanced HRPDF analysis confirmed the formation of PdH_x and provided insights in the enhancement of hydrogen storage of Pd-sEG and Pd-ShEG. The strong linear relationship with effective surface area to volume ratio revealed nanoparticle size as a determining factor for the hydrogen uptake and release. Ultimately, the investigation in this work of using LPE over traditional chemical methods to improve solid-state hydrogen storage took a notable step away from fossil fuels toward a hydrogen economy using safer synthesis methods. Future work could include the use of heteroatom doping, which could further improve the hydrogen uptake/release of mechanically exfoliated graphene nanomaterials.

Supplementary Materials: The following supporting information can be downloaded at: https://www.mdpi.com/article/10.3390/nano13182588/s1, Figure S1: EDX element maps of Pd-sEG showing the distribution of carbon, oxygen, and palladium on the nanocomposite. Figure S2: XPS survey scans of the Pd-functionalized nanomaterials. Figure S3: (A) High-resolution XPS scans of Pd 3d of each palladium-decorated nanomaterial and (B) high-resolution XPS scans of each nanomaterial and functionalized nanocomposite. Figure S4: Comparison of the PdHx nanoparticle core–shell phase fractions and the particle surface area to volume ratio. Both core and shell phase fractions are found to be proportional to the nanoparticle surface area volume ratios. Figure S5: Experimental $G(r)$'s of the remaining Pd structures after subtraction of the substrates (a) ex-substratum (b) EG, (c) ShEG and (d) sEG. The experimental $G(r)$ values are fit to a theoretical core–shell model using a nanocrystalline PdHx pseudo-hexagonal core and a disordered PdHx pseudo-hexagonal outer shell. The core and shell components are separated, and the total model error is split between each component by phase concentration. Figure S6: (A) Comparison of PdHx H/Pd ratio and the hexagonal unit cell volume. The H/Pd ratios are given as a function of cubic lattice constant. Under the hexagonal convention, the H/Pd ratios can be replotted against unit cell volume. Using this new relationship, the H/Pd ratio of the palladium nanoparticles in this experiment can be calculated. (B) Comparison of the calculated PdHx H/Pd ratio and the surface area to volume ratio. The calculated H/Pd ratio is found to be proportional to the surface area to volume ratio. Figure S7: Experimental G(r) values of the remaining Pd structures after subtraction of the substrates: (a) ex-substratum, (b) EG, (c) ShEG and (d) sEG. The experimental G(r) values are fit to the theoretical core–shell model using a nanocrystalline PdHx pseudo-hexagonal core and a disordered PdHx pseudo-hexagonal outer shell. The mean spherical diameter is refined to 8.4 ± 0.13, 5.6 ± 0.12, 4.2 ± 0.11, 3.5 ± 0.09 nm for ex-substratum, EG, ShEG and sEG, respectively. Figure S8: Stability testing of Pd-functionalized nanocomposites (A) Pd-ShEG and (B) Pd-sEG conducted through repeated CV cycling. Table S1: Capacitances of the graphene-based nanomaterials. Table S2: EDX results showing the atomic percent of carbon, oxygen, and palladium of each material and nanocomposite. Table S3: PdHx nanoparticle pseudo-hexagonal core–shell model parameters.

Author Contributions: D.C.: conceptualization, methodology, investigation, writing—original draft; N.B.: methodology, investigation, formal analysis, writing—original draft; E.B.: methodology, writing—original draft; J.v.d.Z.: investigation; S.K.: supervision, resources, funding acquisition; A.C.: conceptualization; supervision, resources, funding acquisition, writing—review and editing. All authors have read and agreed to the published version of the manuscript.

Funding: This work was financially supported by discovery grants from the Natural Sciences and Engineering Research Council of Canada (S.K.: RGPIN-2017-06453; A.C.: RGPIN-2022-04238).

Data Availability Statement: The data presented in this study are available on request from the corresponding author.

Acknowledgments: A.C. acknowledges the NSERC and the Canada Foundation for Innovation (CFI) for the Tier 1 Canada Research Chair Award in Electrochemistry and Nanoscience. The X-ray Diffraction Facility of the Chemistry Department and the Molecular and Cellular Imaging Facility at the University of Guelph were acknowledged for XRD and SEM characterization, respectively. The X-ray total scattering experiments in this work were conducted at the Canadian Light Source. Special thanks to Al Rahemtulla and Beatriz Moreno of the CLS for help with total scattering measurements.

Conflicts of Interest: The authors declare no conflict of interest.

References

1. Crabtree, G.W.; Dresselhaus, M.S. The Hydrogen Fuel Alternative. *MRS Bull.* **2008**, *33*, 421–428. [CrossRef]
2. Schlapbach, L.; Züttel, A. Hydrogen-Storage Materials for Mobile Applications. *Nature* **2001**, *414*, 353–358. [CrossRef] [PubMed]
3. Heinemann, N.; Alcalde, J.; Miocic, J.M.; Hangx, S.J.T.; Kallmeyer, J.; Ostertag-Henning, C.; Hassanpouryouzband, A.; Thaysen, E.M.; Strobel, G.J.; Schmidt-Hattenberger, C.; et al. Enabling Large-Scale Hydrogen Storage in Porous Media-the Scientific Challenges. *Energy Environ. Sci.* **2021**, *14*, 853–864. [CrossRef]
4. Tzimas, E.; Filiou, C.; Peteves, S.D.; Veyret, J. *Hydrogen Storage: State-of-the-Art and Future Perspective*; European Commission: Petten, The Netherlands, 2003; ISBN 92-894-6950-1.
5. Boateng, E.; Chen, A. Recent Advances in Nanomaterial-Based Solid-State Hydrogen Storage. *Mater. Today Adv.* **2020**, *6*, 100022. [CrossRef]
6. Boateng, E.; Thiruppathi, A.R.; Hung, C.K.; Chow, D.; Sridhar, D.; Chen, A. Functionalization of Graphene-Based Nanomaterials for Energy and Hydrogen Storage. *Electrochim. Acta* **2023**, *452*, 142340. [CrossRef]
7. Lu, Q.; Zhang, B.; Zhang, L.; Zhu, Y.; Gong, W. Monolayer AsC5 as the Promising Hydrogen Storage Material for Clean Energy Applications. *Nanomaterials* **2023**, *13*, 1553. [CrossRef] [PubMed]
8. Pal, N.; Chakraborty, D.; Cho, E.-B.; Seo, J.G. Recent Developments on the Catalytic and Biosensing Applications of Porous Nanomaterials. *Nanomaterials* **2023**, *13*, 2184. [CrossRef]
9. Wei, L.; Mao, Y. Enhanced Hydrogen Storage Performance of Reduced Graphene Oxide Hybrids with Nickel or Its Metallic Mixtures Based on Spillover Mechanism. *Int. J. Hydrogen Energy* **2016**, *41*, 11692–11699. [CrossRef]
10. Huo, Y.; Zhang, Y.; Wang, C.; Fang, Y.; Li, K.; Chen, Y. Boron-Doping Effect on the Enhanced Hydrogen Storage of Titanium-Decorated Porous Graphene: A First-Principles Study. *Int. J. Hydrogen Energy* **2021**, *46*, 40301–40311. [CrossRef]
11. Wang, P.; Xia, K.; Chen, Y.; Tian, Q.; Xiong, R.; Han, B.; Gao, Q.; Zhou, C.; Yu, D. Acid-Assisted Synthesis of Nitrogen-Deficient Mesoporous Graphitic Carbon Nitride for Hydrogen Storage. *Mater. Lett.* **2021**, *301*, 130347. [CrossRef]
12. Mosquera-Vargas, E.; Tamayo, R.; Morel, M.; Roble, M.; Díaz-Droguett, D.E. Hydrogen Storage in Purified Multi-Walled Carbon Nanotubes: Gas Hydrogenation Cycles Effect on the Adsorption Kinetics and Their Performance. *Heliyon* **2021**, *7*, e08494. [CrossRef] [PubMed]
13. Lobo, R.; Ribeiro, J.; Inok, F. Hydrogen Uptake and Release in Carbon Nanotube Electrocatalysts. *Nanomaterials* **2021**, *11*, 975. [CrossRef] [PubMed]
14. Andrews, J.; Ojha, R.; Rezaei Niya, S.M.; Seibt, S. Electrochemical Storage Reactions of Hydrogen in Activated Carbon from Phenolic Resin. *Catal. Today* **2021**, *397–399*, 155–164. [CrossRef]
15. Thiruppathi, A.R.; Sidhureddy, B.; Boateng, E.; Soldatov, D.V.; Chen, A. Synthesis and Electrochemical Study of Three-Dimensional Graphene-Based Nanomaterials for Energy Applications. *Nanomaterials* **2020**, *10*, 1295. [CrossRef]
16. Adams, B.D.; Ostrom, C.K.; Chen, S.; Chen, A. High-Performance Pd-Based Hydrogen Spillover Catalysts for Hydrogen Storage. *J. Phys. Chem. C* **2010**, *114*, 19875–19882. [CrossRef]
17. Parambhath, V.B.; Nagar, R.; Sethupathi, K.; Ramaprabhu, S. Investigation of Spillover Mechanism in Palladium Decorated Hydrogen Exfoliated Functionalized Graphene. *J. Phys. Chem. C* **2011**, *115*, 15679–15685. [CrossRef]
18. Tian, W.; Zhang, Y.; Wang, Y.; Liu, T.; Cui, H. A Study on the Hydrogen Storage Performance of Graphene–Pd(T)–Graphene Structure. *Int. J. Hydrogen Energy* **2020**, *45*, 12376–12383. [CrossRef]
19. Boateng, E.; Van Der Zalm, J.; Chen, A. Design and Electrochemical Study of Three-Dimensional Expanded Graphite and Reduced Graphene Oxide Nanocomposites Decorated with Pd Nanoparticles for Hydrogen Storage. *J. Phys. Chem. C* **2021**, *125*, 22970–22981. [CrossRef]
20. Paton, K.R.; Varrla, E.; Backes, C.; Smith, R.J.; Khan, U.; O'Neill, A.; Boland, C.; Lotya, M.; Istrate, O.M.; King, P.; et al. Scalable Production of Large Quantities of Defect-Free Few-Layer Graphene by Shear Exfoliation in Liquids. *Nat. Mater.* **2014**, *13*, 624–630. [CrossRef]
21. Lynch-Branzoi, J.K.; Ashraf, A.; Tewatia, A.; Taghon, M.; Wooding, J.; Hendrix, J.; Kear, B.H.; Nosker, T.J. Shear Exfoliation of Graphite into Graphene Nanoflakes Directly within Polyetheretherketone and a Spectroscopic Study of This High Modulus, Lightweight Nanocomposite. *Compos. B Eng.* **2020**, *188*, 107842. [CrossRef]
22. Liang, S.; Shen, Z.; Yi, M.; Liu, L.; Zhang, X.; Ma, S. In-Situ Exfoliated Graphene for High-Performance Water-Based Lubricants. *Carbon N. Y.* **2016**, *96*, 1181–1190. [CrossRef]
23. Liang, B.; Liu, K.; Liu, P.; Qian, L.; Zhao, G.; Pan, W.; Chen, C. Organic Salt-Assisted Liquid-Phase Shear Exfoliation of Expanded Graphite into Graphene Nanosheets. *J. Mater.* **2021**, *7*, 1181–1189. [CrossRef]
24. Costinas, C.; Salagean, C.A.; Cotet, L.C.; Baia, M.; Todea, M.; Magyari, K.; Baia, L. Insights into the Stability of Graphene Oxide Aqueous Dispersions. *Nanomaterials* **2022**, *12*, 4489. [CrossRef] [PubMed]
25. Hummers, W.S.; Offeman, R.E. Preparation of Graphitic Oxide. *J. Am. Chem. Soc.* **1958**, *80*, 1339. [CrossRef]
26. Lund, S.; Kauppila, J.; Sirkiä, S.; Palosaari, J.; Eklund, O.; Latonen, R.M.; Smått, J.H.; Peltonen, J.; Lindfors, T. Fast High-Shear Exfoliation of Natural Flake Graphite with Temperature Control and High Yield. *Carbon N. Y.* **2021**, *174*, 123–131. [CrossRef]
27. Gao, M.; Zong, H.; Li, Y.; Zhou, Y.; Yu, L.; Qin, L.; Zhao, S. Novel Cyclic Ultrasound-Assisted Liquid Phase Exfoliation of Graphene in Deionized Water: A Parameter Study. *Mater. Lett.* **2023**, *337*, 134011. [CrossRef]

28. Tyurnina, A.V.; Morton, J.A.; Kaur, A.; Mi, J.; Grobert, N.; Porfyrakis, K.; Tzanakis, I.; Eskin, D.G. Effects of Green Solvents and Surfactants on the Characteristics of Few-Layer Graphene Produced by Dual-Frequency Ultrasonic Liquid Phase Exfoliation Technique. *Carbon N. Y.* **2023**, *206*, 7–15. [CrossRef]
29. Sidhureddy, B.; Thiruppathi, A.R.; Chen, A. From Graphite to Interconnected Reduced Graphene Oxide: One-Pot Synthesis and Supercapacitor Application. *Chem. Commun.* **2017**, *53*, 7828–7831. [CrossRef]
30. Liu, L.; Qing, M.; Wang, Y.; Chen, S. Defects in Graphene: Generation, Healing, and Their Effects on the Properties of Graphene: A Review. *J. Mater. Sci. Technol.* **2015**, *31*, 599–606. [CrossRef]
31. Alshamkhani, M.T.; Keat, L.; Kurnianditia, L.; Rahman, A.; Lahijani, P.; Mohammadi, M. Journal of Environmental Chemical Engineering Effect of Graphite Exfoliation Routes on the Properties of Exfoliated Graphene and Its Photocatalytic Applications. *J. Environ. Chem. Eng.* **2021**, *9*, 106506. [CrossRef]
32. Huang, H.; Wang, X. Pd Nanoparticles Supported on Low-Defect Graphene Sheets: For Use as High-Performance Electrocatalysts for Formic Acid and Methanol Oxidation. *J. Mater. Chem.* **2012**, *22*, 22533–22541. [CrossRef]
33. Baird, A.; Andrews, J. Storage of Atomic Hydrogen in Multilayer Graphene. *Int. J. Hydrogen Energy* **2023**, *48*, 27944–27959. [CrossRef]
34. Li, Z.; Gadipelli, S.; Yang, Y.; Guo, Z. Design of 3D Graphene-Oxide Spheres and Their Derived Hierarchical Porous Structures for High Performance Supercapacitors. *Small* **2017**, *13*, 1702474. [CrossRef] [PubMed]
35. Hsieh, Y.T.; Ho, H.N.; Hsu, K.T.; Liu, W.R. Improvement of Electromagnetic Interference Properties of 3D Few-Layer Graphene Composite by Means of Freeze-Drying. *Ceram Int.* **2022**, *48*, 26107–26115. [CrossRef]
36. Gomez, A.; Dina, G.; Kycia, S. The High-Energy X-ray Diffraction and Scattering Beamline at the Canadian Light Source. *Rev. Sci. Instrum.* **2018**, *89*, 063301. [CrossRef]
37. Burns, N.; Rahemtulla, A.; Annett, S.; Moreno, B.; Kycia, S. An Inclined Detector Geometry for Improved X-ray Total Scattering Measurements. *J. Appl. Crystallogr.* **2023**, *56*, 510–518. [CrossRef]
38. Farrow, C.L.; Juhas, P.; Liu, J.W.; Bryndin, D.; Boin, E.S.; Bloch, J.; Proffen, T.; Billinge, S.J.L. PDFfit2 and PDFgui: Computer Programs for Studying Nanostructure in Crystals. *J. Phys. Condens. Matter.* **2007**, *19*, 335219. [CrossRef]
39. Li, Z.; He, W.; Wang, X.; Wang, X.; Song, M.; Zhao, J. N/S Dual-Doped Graphene with High Defect Density for Enhanced Supercapacitor Properties. *Int. J. Hydrogen Energy* **2020**, *45*, 112–122. [CrossRef]
40. Hulman, M. Raman Spectroscopy of Graphene. In *Graphene: Properties, Preparation, Characterization and Applications*, 2nd ed.; Elsevier: Amsterdam, The Netherlands, 2021; pp. 381–411. ISBN 9780081028483.
41. Stevie, F.A.; Donley, C.L. Introduction to X-ray Photoelectron Spectroscopy. *J. Vac. Sci. Technol. A* **2020**, *38*, 063204. [CrossRef]
42. Morelhão, S.L.; Kycia, S.W. A simple formula for determining nanoparticle size distribution by combining small-angle X-ray scattering and diffraction results. *Acta Crystallogr. Sect. A Found. Adv.* **2022**, *78*, 1. [CrossRef]
43. Pinos-Vélez, V.; Osegueda, O.; Crivoi, D.G.; Llorca, J.; García-García, F.J.; Álvarez, M.G.; Medina, F.; Dafinov, A. Insights into Palladium Deactivation during Advanced Oxidation Processes. *Chem. Mater.* **2022**, *34*, 8760–8768. [CrossRef] [PubMed]
44. Bugaev, A.L.; Guda, A.A.; Lomachenko, K.A.; Shapovalov, V.V.; Lazzarini, A.; Vitillo, J.G.; Bugaev, L.A.; Groppo, E.; Pellegrini, R.; Soldatov, A.V.; et al. Core-Shell Structure of Palladium Hydride Nanoparticles Revealed by Combined X-ray Absorption Spectroscopy and X-ray Diffraction. *J. Phys. Chem. C* **2017**, *121*, 18202–18213. [CrossRef]
45. Akiba, H.; Kofu, M.; Kobayashi, H.; Kitagawa, H.; Ikeda, K.; Otomo, T.; Yamamuro, O. Nanometer-Size Effect on Hydrogen Sites in Palladium Lattice. *J. Am. Chem. Soc.* **2016**, *138*, 10238–10243. [CrossRef] [PubMed]
46. Hou, D.; Zhao, C.; Paterson, A.R.; Li, S.; Jones, J.L. Local Structures of Perovskite Dielectrics and Ferroelectrics via Pair Distribution Function Analyses. *J. Eur. Ceram Soc.* **2018**, *38*, 971–987. [CrossRef]
47. Kennedy, B.J.; Vogt, T. Powder X-ray Diffraction Study of the Rhombohedral to Cubic Phase Transition in TiF 3. *Res. Bull.* **2002**, *37*, 77–83. [CrossRef]
48. Ma, Z.; Tan, L.; Huang, H.; He, L.; Chen, J.; Lu, H.; Deng, S.; Yin, W.; Zhang, J.; Tian, H.; et al. Neutron Powder-Diffraction Study of Phase Transitions in Strontium-Doped Bismuth Ferrite: 1. Variation with Chemical Composition. *Phys. Condens. Matter.* **2022**, *34*, 255401. [CrossRef]
49. Zheng, Z.; Su, X.; Deng, R.; Stoumpos, C.; Xie, H.; Liu, W.; Yan, Y.; Hao, S.; Uher, C.; Wolverton, C.; et al. Rhombohedral to Cubic Conversion of GeTe via MnTe Alloying Leads to Ultralow Thermal Conductivity, Electronic Band Convergence, and High Thermoelectric Performance. *J. Am. Chem. Soc.* **2018**, *140*, 2673–2686. [CrossRef]
50. Schirber, J.E.; Morosin, B. Lattice Constants of β-PdHx and P-PdDx with x near 1.0. *Phys. Rev. B* **1975**, *12*, 117. [CrossRef]
51. Hijazi, I.; Zhang, Y.; Fuller, R. A Simple Palladium Hydride Embedded Atom Method Potential for Hydrogen Energy Applications. *J. Energy Resour. Technol. Trans. ASME* **2019**, *141*, 061202. [CrossRef]
52. Zhou, X.W.; Zimmerman, J.A.; Wong, B.M.; Hoyt, J.J. An Embedded-Atom Method Interatomic Potential for Pd-H Alloys. *J. Mater. Res.* **2008**, *23*, 704–718. [CrossRef]
53. Askari, M.B.; Salarizadeh, P. Ultra-Small ReS2 Nanoparticles Hybridized with RGO as Cathode and Anode Catalysts towards Hydrogen Evolution Reaction and Methanol Electro-Oxidation for DMFC in Acidic and Alkaline Media. *Synth. Met.* **2019**, *256*, 116131. [CrossRef]
54. Jerkiewicz, G. Applicability of Platinum as a Counter-Electrode Material in Electrocatalysis Research. *ACS Catal.* **2022**, *12*, 2661–2670. [CrossRef]
55. Wheeler, J.M.; Clyne, T.W. Nanoindentation of Palladium-Hydrogen. *Int. J. Hydrogen Energy* **2012**, *37*, 14315–14322. [CrossRef]

56. Manchester, F.D.; San-Martin, A.; Pitre, J.M. The H-Pd (Hydrogen-Palladium) System. *J. Phase Equilibria* **1994**, *15*, 62–83. [CrossRef]
57. Chen, S.; Adams, B.D.; Chen, A. Synthesis and Electrochemical Study of Nanoporous Pd-Ag Alloys for Hydrogen Sorption. *Electrochim. Acta* **2010**, *56*, 61–67. [CrossRef]

nanomaterials

MDPI

Article

Temperature-Dependent Optical Properties of Oxidized Graphenes

Talia Tene [1,*], Paola G. Vinueza-Naranjo [2], Yesenia Cevallos [2,3], Fabian Arias Arias [4], Matteo La Pietra [5,6], Andrea Scarcello [7,8], Yolenny Cruz Salazar [7,8], Melvin Arias Polanco [9], Salvatore Straface [10], Cristian Vacacela Gomez [5,*], Lorenzo S. Caputi [7,8] and Stefano Bellucci [5,*]

1 Department of Chemistry, Universidad Técnica Particular de Loja, Loja 110160, Ecuador
2 College of Engineering, Universidad Nacional de Chimborazo, Riobamba 060108, Ecuador
3 Diego de Robles y Vía Interoceánica, Universidad San Francisco de Quito, Quito 170901, Ecuador
4 Facultad de Ciencias, Escuela Superior Politécnica de Chimborazo (ESPOCH), Riobamba 060155, Ecuador
5 INFN—Laboratori Nazionali di Frascati, 00044 Frascati, Italy
6 Department of Information Engineering, Polytechnic University of Marche, 60131 Ancona, Italy
7 UNICARIBE Research Center, University of Calabria, 87036 Rende, Italy
8 Surface Nanoscience Group, Department of Physics, University of Calabria, Via P. Bucci, Cubo 33C, 87036 Rende, Italy
9 Instituto Tecnológico de Santo Domingo, Área de Ciencias Básicas y Ambientales, Av. Los Próceres, Santo Domingo 10602, Dominican Republic
10 Department of Environmental Engineering (DIAm), University of Calabria, Via P. Bucci, Cubo 42B, 87036 Rende, Italy
* Correspondence: tbtene@utpl.edu.ec (T.T.); cristianisaac.vacacelagomez@fis.unical.it (C.V.G.); bellucci@lnf.infn.it (S.B.)

Abstract: In this study, we investigate how changing important synthesis-related parameters can affect and control the optical characteristics of graphene oxide (GO) and reduced graphene oxide (rGO). These parameters include drying time and reduction time at two different temperatures. We obtain an understanding of their impact on optical transitions, optical bandgap, absorption coefficient, and absorbance spectrum width by analyzing these factors. Accordingly, GO has an optical bandgap of about 4 eV, which is decreased by the reduction process to 1.9 eV. Both GO and rGO display greater absorption in the visible spectrum, which improves photon capture and boosts efficiency in energy conversion applications. Additionally, our results show that GO and rGO have higher absorption coefficients than those previously reported for dispersions of exfoliated graphene. Defects in GO and rGO, as well as the presence of functional oxygen groups, are the main contributors to this increased absorption. Several measurements are carried out, including spectroscopic and morphological studies, to further support our findings.

Keywords: graphene oxide; reduced graphene oxide; citric acid; optical bandgap; absorption coefficient

1. Introduction

The basic building block of carbon-based materials such as graphite is called graphene, which is made up of a single layer of carbon atoms organized in a hexagonal lattice [1]. The remarkable physical and chemical characteristics of this two-dimensional (2D) material include exceptional electrical and thermal conductivity, mechanical strength, and a large surface area [2]. However, there are some difficulties related to graphene. For instance, it cannot be further processed because it is insoluble in water and the majority of organic solvents [3]. Graphene also has a zero bandgap, which makes it act more as a semimetal than a semiconductor. The functional groups that might be advantageous for bioapplications are also absent [4].

In this context, it has suggested derivatives such as graphene oxide (GO) and reduced graphene oxide (rGO) to get around the drawbacks of pure graphene [5]. Graphene is given

oxygen-containing functional groups, such as hydroxyl (-OH), epoxy (-O-), and carboxyl (-COOH) groups, to produce GO [6]. With this change, GO becomes hydrophilic and is easier to manipulate. Additionally, GO develops a finite bandgap due to the presence of oxygen functional groups, which turns it into a semiconductor or insulating material [7]. However, reducing GO results in the production of rGO, which partially restores the electrical and mechanical properties of graphene due to the removal of oxygen functional groups [8]. Both GO and rGO have unique features and have potential in a range of applications, such as energy storage, water treatment, biosensors, composites, and catalysis [9,10].

On the other hand, the physical and chemical characteristics of GO and rGO are significantly influenced by the oxidation method [11–13] as well as the reducing agent (e.g., hydrazine, ascorbic acid, and citric acid [14–16]). Indeed, there are different levels of oxidation or reduction as a result of these processes. A thorough investigation of crucial factors such as temperature and contact time with the reducing agent is still lacking, although much research has been devoted to the synthesis processes and reducing agents for synthesizing GO and rGO. There has recently been a focus on comprehending the crucial parameters, such as drying time and reduction time, that enable control over oxygen functionalization [17]. This is crucial because it may speed up the preparation of GO and rGO with bandgaps that are comparable to those of silicon, making them ideal for next-generation devices. [18]

In a previous study conducted by Kumar et al. [19], a straightforward thermal annealing technique was developed, eliminating the need for any chemical treatments to modify as-made GO. This method successfully converts the mixed sp^2–sp^3 hybridized GO phases into distinct oxidized and graphitic phases during annealing, resulting in significant improvements and a noticeable enhancement in visible absorption characteristics. However, the study does not specifically address the optical bandgap, electronic transitions, or absorption coefficient of the material. Also, the study does not cover the manipulation of rGO. Therefore, further exploration is necessary to fully understand the potential of this strategy in manipulating the properties of both GO and rGO.

In the present work, we focus on examining the influence of drying time and low-temperature reduction treatment on the optical properties of various GO and rGO samples. The optical characteristics are investigated using UV-visible spectroscopy by the absorbance spectra and Tauc analysis [20]. In addition, energy-dispersive X-ray spectroscopy (EDS), X-ray powder diffraction (XRD), and scanning electron microscopy (SEM) techniques are employed to analyze the elemental composition, crystallinity, and morphology of the materials. The results indicate that increasing the drying time up to 120 h at 80 °C leads to a modification of the optical bandgap of GO from approximately 4 to 2.8 eV. Similarly, the reduction of GO-using citric acid (CA) at 80 °C for 120 h adjusts the optical bandgap of rGO from approximately 2.5 to 1.9 eV. Additionally, this study discusses in detail the estimated values of the optical absorption coefficient, shifts in electronic transitions, and relevant photosensitive characteristics.

2. Material and Methods

Figure 1a summarizes the synthesis of GO and rGO. The reader is advised to study our earlier work [21] for a more thorough description of the entire procedure. The uses of GO and rGO in the elimination of pollutants are also extensively covered in our earlier research [22,23].

2.1. Materials

Without further purification, we used all chemical compounds exactly as they were given to us. Graphite powder (<150 μm, 99.9%) (Sigma Aldrich, St. Louis, MO, USA), sulfuric acid (H_2SO_4, ACS reagent, 95.0–98.0%) (Sigma Aldrich), potassium permanganate ($KMnO_4$, ACS reagent, 99.0%) (Sigma Aldrich), hydrochloric acid (HCl, ACS reagent, 37%) (Sigma Aldrich), citric acid (CA, $C_6H_8O_7$, ≥99.5%) (Sigma Aldrich), and hydrogen peroxide (H_2O_2, 30%) (Merk, Rahway, NJ, USA).

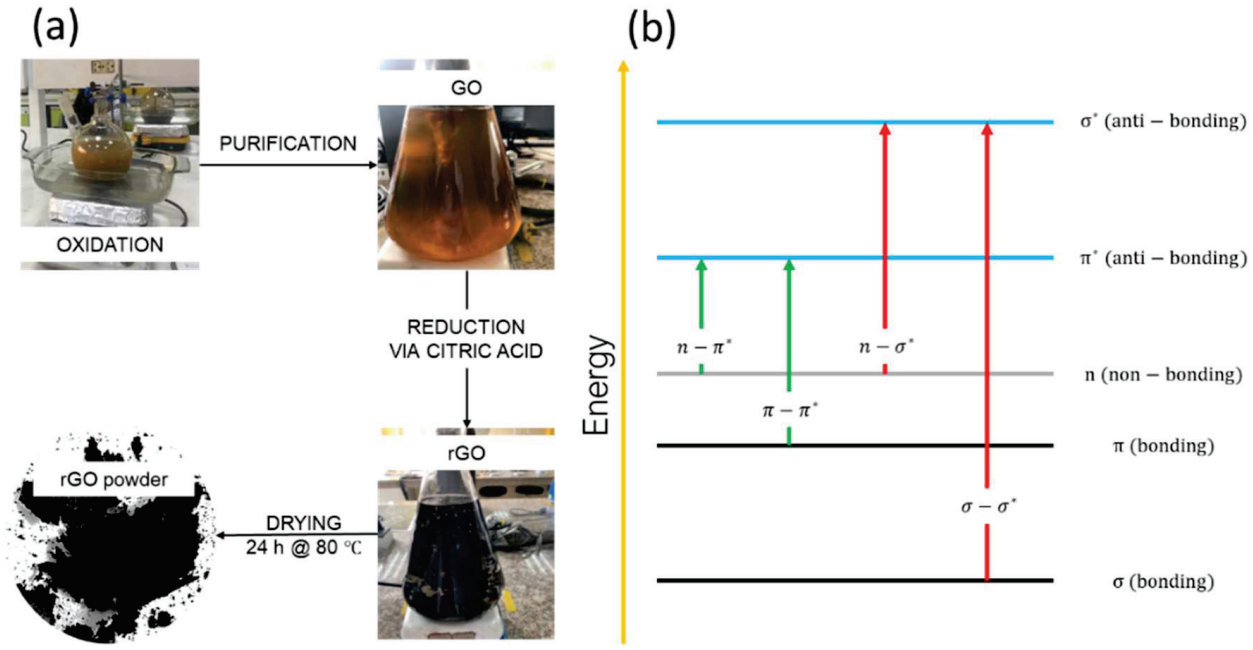

Figure 1. (**a**) Schematic illustration of the method used to prepare GO and rGO. (**b**) UV-visible theory.

2.2. Synthesis of GO and rGO

To prepare the mixture (Figure 1a), 3.0 g of graphite powder was combined with 70 mL of H_2SO_4 in an ice bath. Then, 9 g of $KMnO_4$ was added while keeping the temperature below 20 °C. After 0.5 h, the mixture was transferred to a water bath and stirred at 50 °C for 0.5 h. Gradually, 150 mL of distilled water was added to the solution, ensuring the temperature stayed below 90 °C. An additional 500 mL of distilled water and 15 mL of H_2O_2 were added. After 1 h, the resulting mixture was divided into centrifuge tubes and washed with a 1:10 solution of HCl and distilled water using several centrifugations at 10,000 rpm for 10 min. The obtained precipitate was dried at 45 °C for 48 h in a Teflon container to obtain graphite oxide powder.

In a typical experiment, 100 mg of graphite oxide powder was sonicated for 0.5 h in 500 mL of distilled water. The suspension was then centrifuged at 500 rpm for 10 min to obtain a homogeneous GO suspension. This suspension was dried at 80 °C for varying drying times ranging from 0 h to 120 h.

Following the drying process, under vigorous stirring, 500 mg of CA was gradually added to a 250 mL GO aqueous solution (1:1). Different reduction times from 1 h to 120 h were tested at 50 °C and 80 °C. To remove excess CA, the resulting black precipitates were washed with distilled water through centrifugation at 3000 rpm for 0.5 h. Finally, the precipitated material was dried at 80 °C for 24 h to obtain rGO powder.

We encountered a technical limitation when operating at temperatures exceeding 80 °C. Given that water serves as the primary medium for the synthesis process involving oxidation and reduction, evaporation becomes a significant concern, leading to a reduction in the initial water volume. Consequently, for example, at 100 °C, we must replenish the water to maintain a constant supply throughout the entire 120 h duration. However, this adjustment directly affects the initial concentration of GO, thereby impacting the resulting absorbance spectra. To mitigate this challenge and promote a more uniform procedure, we deliberately selected these two temperatures, i.e., 50 °C and 80 °C.

2.3. Characterization

The absorption spectra of GO and rGO were recorded using a Jenway 6850 spectrophotometer with a resolution of 0.1 nm in a wavelength window from 190 to 1000 nm. After the specified drying time or reduction time, the obtained samples were sonicated briefly to

redisperse GO or rGO before measuring their absorbance spectra. The optical absorption coefficient was obtained by setting $\lambda = 660$ nm. Quartz cuvettes (3.5 mL) with a 10 mm optical path were used. Spectra were normalized to the maximum of the prominent peak and conventional Lorentz functions were used to fit the curve. Additionally, absorbance spectra were smoothed using a 7-point moving average.

Using a scanning electron microscope (SEM, JSM-IT100 InTouchScope, JEOL, Tokyo, Japan) with an accelerating voltage of 20 kV and tailored with an energy-dispersive X-ray spectrometer (EDS), the surface morphology of the acquired samples was examined. Using a Panalytical Pro X-ray diffractometer with Cu K irradiation with an acceleration voltage of 60 kV and a current of 55 mA, measurements of X-ray diffraction (XRD) were made.

3. Results and Discussion

To emphasize even more, our team [23] and others [24,25] have successfully shown how to convert GO into rGO utilizing CA as a less dangerous and more environmentally friendly reducing agent. Due to the potential health dangers connected with hydrazine, CA is a preferable choice even though its reduction efficiency is not as high as that of hydrazine. As a result, the findings of this study can be utilized to compare and extrapolate the effectiveness of different green or non-green reducing agents.

3.1. Optical Properties of GO

To facilitate an effective comparison, our study initially focused on analyzing the properties of GO under varying drying times. Figure 2a (Figure S2) displays the absorption spectra of GO with drying times of up to 120 h. The spectrum reveals two distinct absorption peaks: one at approximately 230 nm and the other at 300 nm. Based on the UV-visible theory (Figure 1b), these peaks correspond to the $\pi - \pi^*$ transition of C=C in amorphous carbon systems, and a broad $n - \pi^*$ transition of C=O bonds, respectively. All spectra are featureless in the visible region.

Notably, a redshift in the primary absorption peak is observed (Figure S1) from 229.6 nm at 0 h to 243.8 nm at 120 h (Table S1), which was not previously reported by Kumar [19]. This finding is intriguing since the evaporation of surface water molecules and water molecules within the structure of GO is expected to occur during the drying process. Such evaporation would result in a decrease in the number of functional groups and a partial reduction of the material, which could explain the observed redshift.

Our study confirms that increasing the drying time leads to a significant improvement in absorption in the visible region (Figure 1a, the color bar from 400 to 700 nm), which is a crucial factor for many applications, such as solar cells. Specifically, an improvement in photon collection is observed of almost 40% at 400 nm and 15% at 700 nm when the drying time of GO is increased. This result implies that the optical properties of GO can be tuned by adjusting the drying time, which could have significant implications for the design and optimization of various optoelectronic devices.

The Tauc approach is a common method used to estimate the optical bandgap of GO [26,27]. The Tauc approach involves plotting the absorption coefficient ($\propto$) against photon energy and extrapolating the linear portion of the curve to the point where it intersects the x-axis. This enables the estimation of the optical bandgap, which is associated with the energy of photons that can be absorbed by the material.

With this in mind, the optical bandgap of the GO samples was estimated by fitting the linear portion between 4 eV and 5 eV for each drying time (Figure S3). It is worth noting that the optical bandgap of GO at 0 h is located outside the visible region, but as the drying time increases, the bandgap energy decreases and enters the visible region.

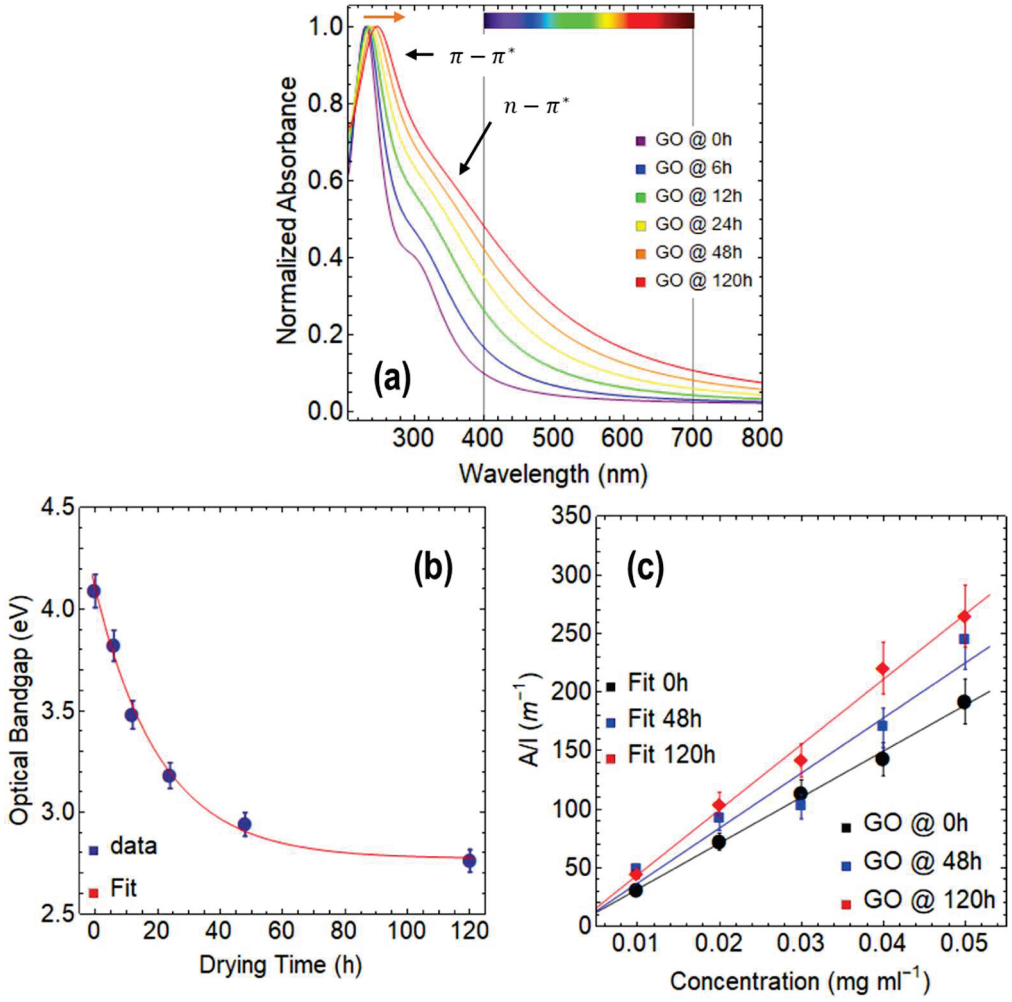

Figure 2. (**a**) Absorbance spectra of GO for different drying times at 80 °C from 200 to 800 nm. (**b**) Optical bandgap of GO as a function of drying time. (**c**) Optical absorbance at 660 nm as a function of concentration, considering three drying times. The color bar in (**a**) represents the visible region of the spectrum, spanning from 400 to 700 nm.

The numerical values for the optical bandgap can be observed in Figure 2b and Table S2. As the drying time increases, a decreasing exponential behavior is observed, with the bandgap reducing from 4.1 eV at 0 h to 2.8 eV at 120 h. After fitting the data, we obtained the equation: $y = 1.33\ \mathrm{Exp}\left[-4.77 \times 10^{-2}\ t\right] + 2.77$ ($R^2 = 0.999$), which implies that the effect of drying time on the optical bandgap diminishes after 120 h, as the maximum predicted reduction in optical bandgap is 2.77 eV. This result is further supported by the small rate of decrease observed, which is $-4.77 \times 10^{-2}\ \mathrm{s}^{-1}$. The largest impact of drying time is observed between 0 and 24 h, resulting in a decrease of 0.91 eV.

To calculate the absorption coefficient, we followed the Lambert–Beer law ($A = \alpha_{660} \cdot c \cdot l$) and prepared multiple GO dispersions with varying concentrations ranging from 0.01 to 0.05 mg mL^{-1}. This method is commonly used for exfoliated graphene dispersions in water or alcohols [28,29] and has now been applied to GO samples at different drying times. The linear relationship between concentration (c) and absorbance (A), which is independent of drying time, is confirmed by Figure 2c. Additionally, it can be observed that the ratio of A/l increases as the drying time increases, indicating a rise in the absorption coefficient. The absorption coefficient of GO at different drying times was found to be 3932.22 mL mg^{-1} m^{-1} at 0 h, 4586.71 mL mg^{-1} m^{-1} at 48 h, and 5507.15 mL mg^{-1} m^{-1} at 120 h (Table S3). These values are significantly higher than those reported for exfoliated graphene dispersions, which typically have an absorption coefficient of around 2460 mL mg^{-1} m^{-1} [28].

The higher absorption coefficient of GO compared to exfoliated graphene is likely due to the presence of oxygen functional groups in its structure [30]. These functional groups create defects in the carbon lattice, which can interact with photons at a wider range of energies than exfoliated graphene. Additionally, the oxygen functional groups on the surface of GO can induce dipole moments and charge transfer, further enhancing the absorption of electromagnetic radiation. It is crucial to note that as the drying time increases (from 0 h to 120 h) (Figure 2d), the absorption coefficient also increases. This observation suggests that while the number of oxygen functional groups may decrease, a disordered and defective structure might prevail due to the increase in the number of vacancies [30].

With these results in mind, GO seems useful in applications such as photovoltaics, photocatalysis, and optoelectronics where high absorption coefficients are required.

On the other hand, we have noticed a quasi-linearity in the position of the main absorption peak ($\pi - \pi^*$ transition) as a function of drying time (Figure S4a) as well as the optical bandgap as a function of the position of the $\pi - \pi^*$ transition (Figure S4b). Perfect linearity is also observed between the optical bandgap and the full width at half maximum (FWHM) (Figure S4c). Beyond these interesting results, we can note something important: as the drying time increases, the FWHM significantly increases (Table S1).

3.2. Optical Properties of rGO Reduced at 80 °C

We now proceed to analyze the properties of rGO (Figures 3 and 4). For the reduction and seeing the potential scalability of the process, we focused on the GO samples dried at 80 °C for 24 h, which showed the most efficient result of the drying process. These GO samples resulted in a bandgap of 3.2 eV (Table S2) and a $\pi - \pi^*$ transition at 233.3 nm (Table S1). However, it is worth considering the possibility of utilizing the samples dried for 120 h, which would result in a partially reduced material due to the thermal reduction treatment. This would undoubtedly impact the reduction time required or even the choice of reducing agent. This concept serves as a motivation for future extensive studies aimed at optimizing the process and evaluating the cost-benefit of employing a material subjected to prolonged drying time.

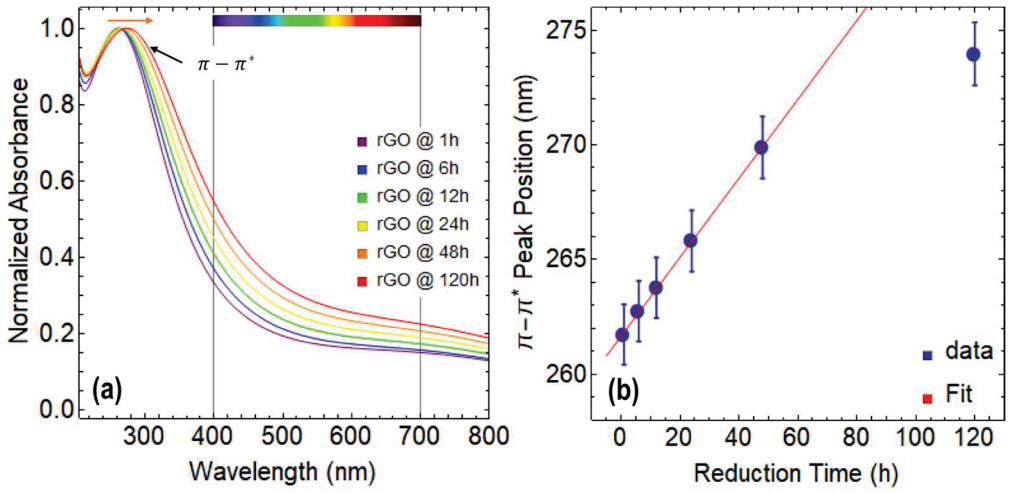

Figure 3. (**a**) Absorbance spectra of rGO reduced at 80 °C from 200–800 nm. (**b**) Position of $\pi - \pi^*$ transition as a function of reduction time. The color bar in (**a**) represents the visible region of the spectrum, spanning from 400 to 700 nm.

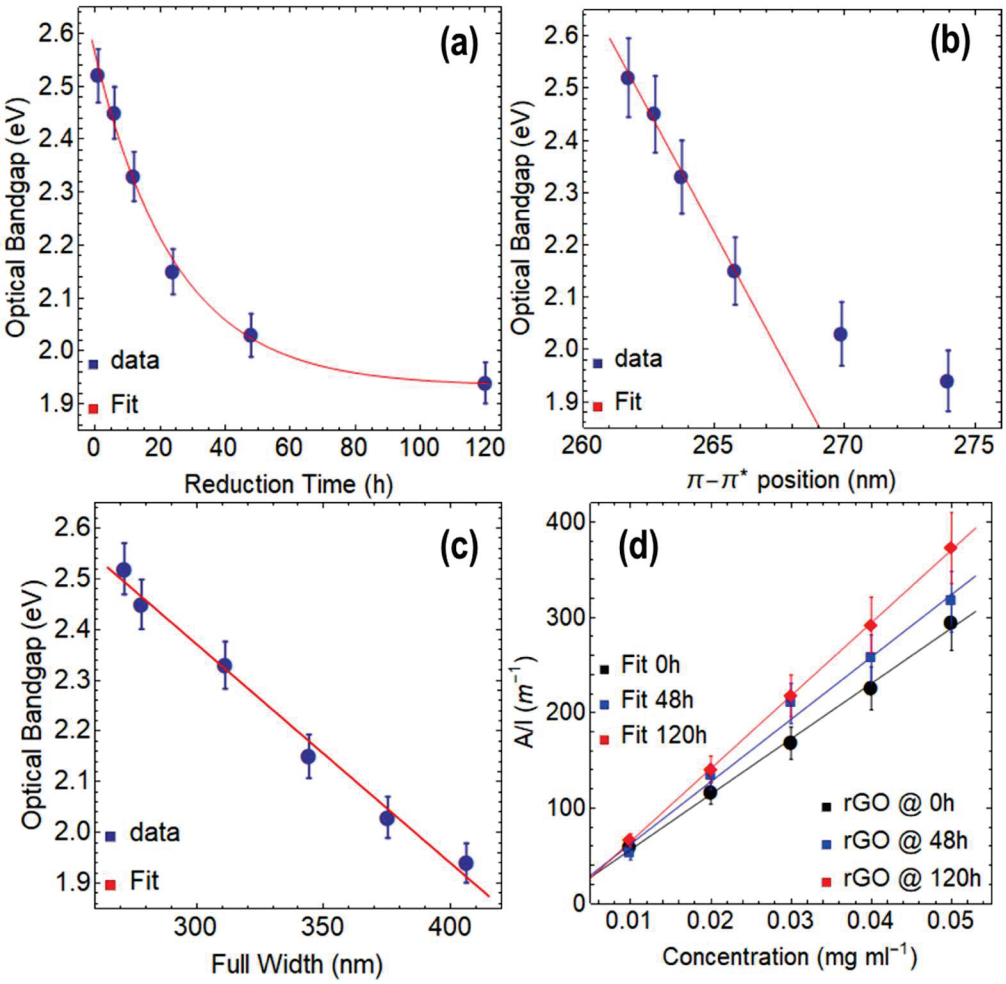

Figure 4. Optical bandgap of rGO reduced at 80 °C as a function of: (**a**) reduction time, (**b**) position of $\pi - \pi^*$ transition, and (**c**) full-width at half maximum (FWHM). (**d**) Optical absorbance at 660 nm as a function of concentration, considering three reduction times.

Figure 3a displays the absorption spectra of rGO reduced at 80 °C using CA under various reduction times ranging from 1 h to 120 h. Notably, all the spectra appear featureless in the visible region, indicating that the reduction process did not introduce any extra species (Figure S6). Additionally, it is noteworthy that only the $\pi - \pi^*$ transition is observed, while the $n - \pi^*$ transition is absent in all the spectra.

In Figure S5, a redshift of the $\pi - \pi^*$ transition is observed, which shifts from 261.7 nm at 1 h of reduction with CA to 273.9 nm at 120 h of reduction (Table S4). This shift is much more significant compared to the one observed in GO, indicating that the reduction process has occurred, and the structure and properties of graphene are progressively recovering.

Upon careful analysis of Figure 3a, an important rise in absorption in the visible region can be observed, with up to a 22% increase at 400 nm and a 9% increase at 700 nm as the reduction time increases. Although these results are lower than those observed for GO, the improved absorption in the visible region makes rGO a promising material with several potential applications.

On the other hand, the position of the $\pi - \pi^*$ transition follows a clear linear trend until 48 h of reduction time, after which it starts to plateau because the point at 120 h strongly deviates from this linearity and the position of this peak cannot increase indefinitely (Figure 3b). It is worth noting that the maximum position of the $\pi - \pi^*$ transition for exfoliated graphene dispersions is around 280 nm [31]. Similar to GO, the FWHM of the $\pi - \pi^*$ transition observed in rGO also increases as the reduction time progresses, indicating a broadening of the main absorption peak (Table S4).

We now focus on discussing the optical bandgap (Table 1 and Figure S7) and absorption coefficient (Table 2) of rGO. Figure 4a shows a decrease in the optical bandgap from 2.52 eV at 1 h of reduction to 1.94 eV at 120 h of reduction, which can be described by a decreasing exponential function ($y = 0.63\ \mathrm{Exp}\left[-4.04 \times 10^{-2}\ t\right] + 1.93$, $R^2 = 0.999$). The total drop in the optical bandgap through the reduction process at 80 °C via CA is 0.58 eV. Compared to GO at 0 h of drying time and GO at 24 h of drying time, the optical bandgap decreases down to 2.15 eV and 1.24 eV, respectively. The most significant decrease in the optical bandgap occurs during the first 24 h of reduction, with a difference of 0.37 eV. Beyond this point, the effect of the reducing agent on the optical bandgap continues to slightly decrease with a small decreasing rate of $-4.04 \times 10^{-2}\ \mathrm{s}^{-1}$, leading to a minimum optical bandgap of 1.93 eV by using CA.

Table 1. Estimated optical bandgaps of rGO reduced at 80 °C under different reduction times ranging from 0 to 120 h.

Reduction Time (h)	Optical Bandgap (eV)	R^2
1	2.52	0.999
6	2.45	0.999
12	2.33	0.999
24	2.15	0.999
48	2.03	0.999
120	1.94	0.999

Table 2. The estimated optical absorption coefficient of rGO reduced at 80 °C, considering three reduction times.

Material	Absorption Coefficient (mL $\mathrm{mg}^{-1}\ \mathrm{m}^{-1}$)	R^2
rGO @ 1 h/80 °C	5803.89	0.997
rGO @ 48 h/80 °C	6534.43	0.989
rGO @ 120 h/80 °C	7638.10	0.989

Figure 4b shows a linear relationship between the optical bandgap and the position of the $\pi - \pi^*$ transition up to 24 h of reduction time, which can be expressed by data fitting (Table 1) as $y = -9.27 \times 10^{-2}\ t + 26.80$ ($R^2 = 0.995$). The plot demonstrates that the data points at 48 h and 120 h of reduction do not align with the linear fit, indicating that both the optical bandgap and the position of the $\pi - \pi^*$ transition have reached a saturation point, and the reduction with CA has almost entirely taken place. The slope is -9.27×10^{-2} eV nm^{-1}, indicating that the reduction of the optical bandgap for each nm of the redshift of the $\pi - \pi^*$ transition is slow but steady.

Figure 4c shows a linear relationship between the optical bandgap and the FWHM, which can be described by the following equation: $y = -4.32 \times 10^{-3}\ t + 3.66$ ($R^2 = 0.989$). Although the slope is very small (-4.32×10^{-3} eV nm^{-1}), the impact of reduction time on the FWHM is significant. For instance, rGO reduced for 1 h has an optical bandgap of 2.52 eV and an FWHM of 271.57 nm, while rGO at 120 h of reduction shows an optical bandgap of 1.94 eV and an FWHM of 406.23 nm. These results further highlight the importance of controlling the reduction time to obtain rGO with desirable features.

Figure 4d shows the ratio of A/l, which exhibits a linear increase with increasing the concentration of rGO, regardless of the reduction time. By fitting the data, absorption coefficient values of 5803.89 mL $\mathrm{mg}^{-1}\ \mathrm{m}^{-1}$ at 1 h, 6534.43 mL $\mathrm{mg}^{-1}\ \mathrm{m}^{-1}$ at 48 h, and 7638.10 mL $\mathrm{mg}^{-1}\ \mathrm{m}^{-1}$ at 120 h were attained (Table 2). These values are almost three times larger than those reported for exfoliated graphene dispersions (~2460 mL $\mathrm{mg}^{-1} \cdot \mathrm{m}^{-1}$ [28]), indicating the superior light absorption capability of rGO. Compared to GO, the absorption coefficients of rGO show an increase of nearly 28%.

To gain a deeper understanding of these results, we propose the following idea: the superior absorption coefficient of rGO can be attributed to the reduction process, which

removes oxygen functional groups and restores the sp^2 hybridization of carbon atoms in certain regions of the graphene lattice. This restoration leads to a significant increase in the number of confined $\pi-$ electrons perpendicular to the plane, thereby enhancing light absorption. This effect is well-documented in the field of graphene plasmonics [32]. Additionally, it is worth noting that the reduction process may induce defects and vacancies in certain regions of the graphene lattice, which also contribute substantially to increased light absorption [30].

3.3. Optical Properties of rGO Reduced at 50 °C

Similar to the previous section, we now analyze rGO reduced at 50 °C (Figures 5 and 6). Figure 5a shows the absorbance spectra of rGO for different reduction times. Although the spectra do not present significant features in the visible region (Figure S9), the broad structure of the $\pi - \pi^*$ peak remains remarkable. On the other hand, Figure S8 shows a slight redshift from 260.33 nm at 1 h of reduction to 269.36 nm at 120 h of reduction (Table S5). This smaller displacement of the $\pi - \pi^*$ peak can be attributed to the fact that reduction temperature critically affects the kinetics of the reduction process.

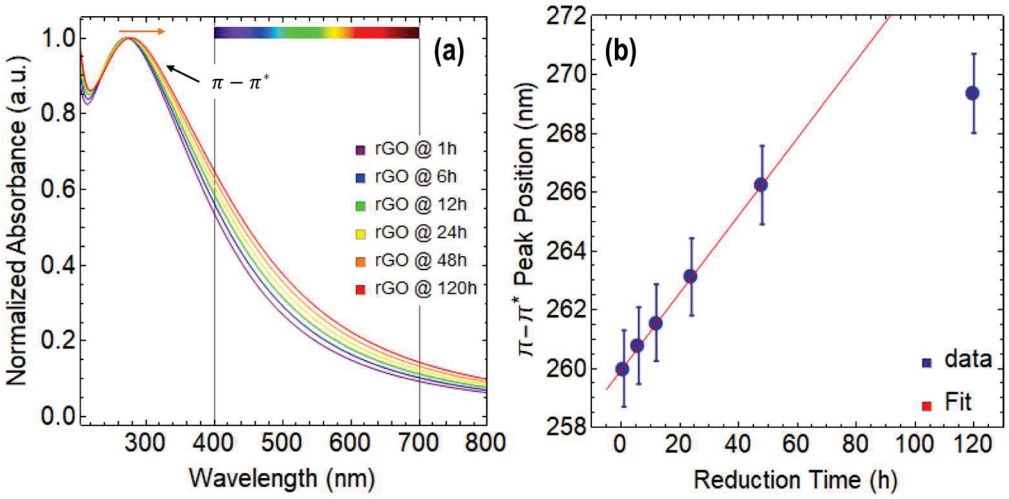

Figure 5. (**a**) Absorbance spectra of rGO reduced at 50 °C from 200 to 800 nm. (**b**) Position of $\pi - \pi^*$ transition as a function of reduction time. The color bar in (**a**) represents the visible region of the spectrum, spanning from 400 to 700 nm.

Additionally, Figure 5a demonstrates an increase in light absorption in the visible region for rGO reduced at 50 °C, but the enhancement is significantly less when compared to GO. At 400 nm, the improvement is only around 10%, and at 700 nm, it is about 5%. Nonetheless, these findings showcase the adaptability of GO and rGO in adjusting their interaction with light by manipulating various parameters, including the oxidation-reduction processes and the reducing agents employed.

A plateau in the position of the $\pi - \pi^*$ peak is observed in Figure 5b at 120 h of reduction time, even at 50 °C, indicating that the peak position reaches saturation after 48 h of reduction where a clear linearity is observed from 1 h to 48 h of reduction. This behavior is similar to that observed for rGO reduced at 80 °C. Additionally, the FWHM of the absorbance spectrum also increases as the reduction time increases (Table S5) in rGO reduced at 50 °C. However, the increase is much lower compared to rGO reduced at 80 °C. As an example, at 1 h, the FWHM is 208.94 nm, and at 120 h, it is 271.41 nm.

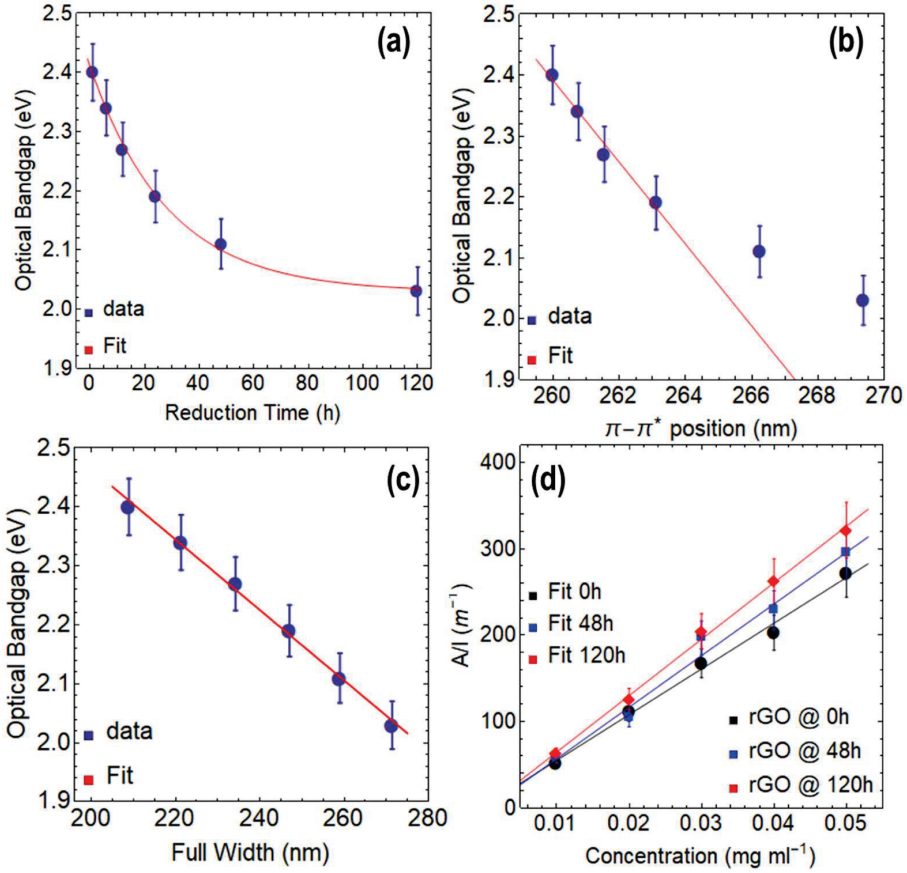

Figure 6. Optical bandgap of rGO reduced at 50 °C as a function of: (**a**) reduction time, (**b**) position of $\pi - \pi^*$ transition, and (**c**) full-width at half maximum (FWHM). (**d**) Optical absorbance at 660 nm as a function of concentration, considering three reduction times.

Interestingly, when rGO is reduced at 50 °C for 1 h (Figures 6a and S10a), the resulting optical bandgap is 2.40 eV (Table 3), which is a more efficient outcome than the one obtained at 80 °C for the same duration (2.52 eV). The reason for this observation is not yet clear, but it is possible that at higher temperatures, secondary reactions such as oxidation or degradation of GO occur, leading to structural defects. At lower temperatures, more stable reduction products with fewer defects may be formed. In the case of reducing GO at 50 °C, it is possible that at the lower temperature, the reducing agent used has a stronger affinity for the oxygen functional groups of GO, leading to a more efficient reduction in a shorter time. However, further research is needed to determine the specific factors that influence the efficiency of the process. Notably, after 120 h, the optical bandgap is 2.03 eV (Table 3, Figure S10f), which is higher than the value observed in the reduction of GO at 80 °C at the same duration (1.94 eV).

Table 3. Estimated optical bandgaps of rGO reduced at 50 °C under different reduction times ranging from 0 to 120 h.

Reduction Time (h)	Optical Bandgap (eV)	R^2
1	2.40	0.999
6	2.34	0.999
12	2.27	0.999
24	2.19	0.999
48	2.11	0.999
120	2.03	0.999

A good linear relationship can be observed between the optical bandgap and the position of the $\pi - \pi^*$ peak (Figure 6b) for up to 24 h. However, the data points at 48 h and 120 h deviate from this linear trend, indicating that a saturation point is approaching. A strong linear relationship can be observed between the optical bandgap and the FWHM (Figure 6c).

The absorbance coefficients of rGO reduced at 50 °C for various reduction times are shown in Figure 6d and Table 4. The acquired values are lower than those seen for rGO reduced at 80 °C (Table 2) but greater than those reported for dispersions of exfoliated graphene and GO (Table S3), demonstrating the major influence of the reduction temperature on the final optical characteristics of the resulting oxidized graphene derivative.

Table 4. The estimated optical absorption coefficient of rGO reduced at 50 °C, considering three reduction times.

Material	Absorption Coefficient (mL mg^{-1} m^{-1})	R^2
rGO @ 1 h/50 °C	5294.11	0.993
rGO @ 48 h/50 °C	5975.30	0.983
rGO @ 120 h/50 °C	6540.53	0.999

3.4. Spectroscopic and Morphological Measurements

To clarify and support our findings, we have conducted additional measurements using EDS (Figure 7), XRD (Figure 8), and SEM (Figure 9). Notably, we placed particular emphasis on samples subjected to 24 h of drying time for GO and 24 h of reduction time for rGO at both 50 °C and 80 °C. These specific conditions were chosen to strike a balance between production time and achieving the desired optical bandgap, thereby exploring the potential for scalability as discussed in earlier sections. We would like to highlight that our EDS study encompasses a comprehensive range of drying times, spanning from 0 to 120 h, as well as different reduction times at 80 °C or 50 °C, ranging from 1 to 120 h. The corresponding results for these variations can be found in Figures S11–S13 of the Supplementary Material. Additionally, we have included the numerical data associated with these measurements in Tables S6–S8.

Figure 7a displays the EDS measurement of graphite, which presents a single peak and a mass percentage of 99.6% (Table S6). This peak confirms the presence of only carbon atoms in the sample, which is consistent with the expected composition of graphite. The mass percentage of 99.9% indicates that the sample is highly pure. Figure S11a shows the EDS measurement on GO at 0 h of drying time, where two peaks are observed for carbon and oxygen with percentage masses of 41.47% and 58.53%, respectively (Table S6). These results indicate that the sample is primarily composed of carbon and oxygen, which is expected for GO regardless of the method used for oxidation.

Figure 7b displays the EDS measurement of GO at 24 h of drying time, which reveals two peaks for carbon and oxygen, indicating the presence of both elements. The carbon peak with a percentage mass of 51.42% suggests that carbon is the major constituent of the sample, while the oxygen peak with a percentage mass of 48.58% indicates a significant amount of oxygen is present. The decrease in the percentage of oxygen from 58.53% (0 h) to 48.58% (24 h) confirms that the drying process has removed some of the oxygen functional groups from GO.

The EDS measurements on rGO at 80 °C (Figure 7c) and 50 °C (Figure 7d) for 24 h of reduction time show two peaks for carbon and oxygen, indicating the presence of both elements in the samples. The peak for carbon in both cases has a higher percentage mass, with 68.53% at 80 °C (Table S7) and 68.17% at 50 °C (Table S8), suggesting that carbon is the major constituent of the sample. Meanwhile, the peak for oxygen in both cases has a lower percentage mass, with 31.47% at 80 °C and 31.83% at 50 °C, indicating a significant amount of oxygen is still present in rGO.

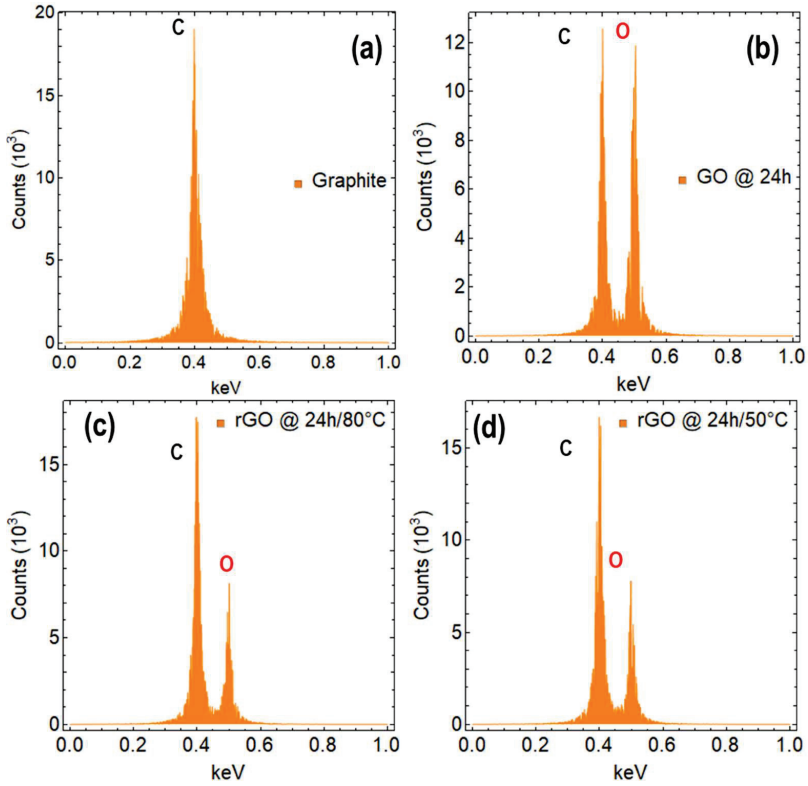

Figure 7. EDS measurement of (**a**) graphite, (**b**) GO dried at 80 °C for 24 h, (**c**) rGO reduced at 80 °C for 24 h, and (**d**) rGO reduced at 50 °C for 24 h. C and O denotes the chemical elements of carbon and oxygen, respectively.

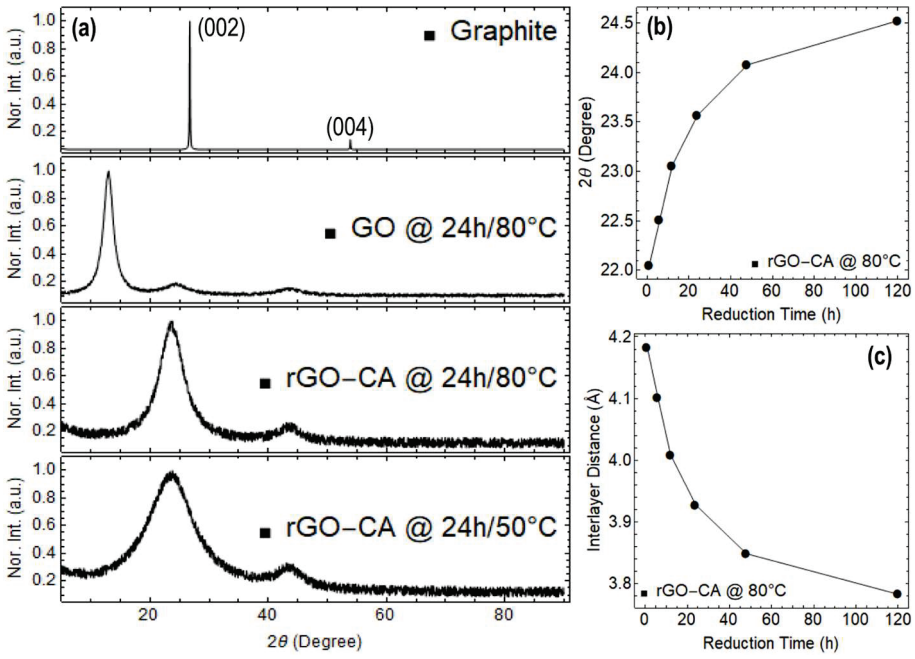

Figure 8. (**a**) XRD measurements on power graphite, GO, and rGO. (**b**) Variation of the 2θ peak position as a function of reduction time. (**c**) Variation of interlayer distance as a function of the reduction time. The spectra were normalized to the maximum of the prominent peak.

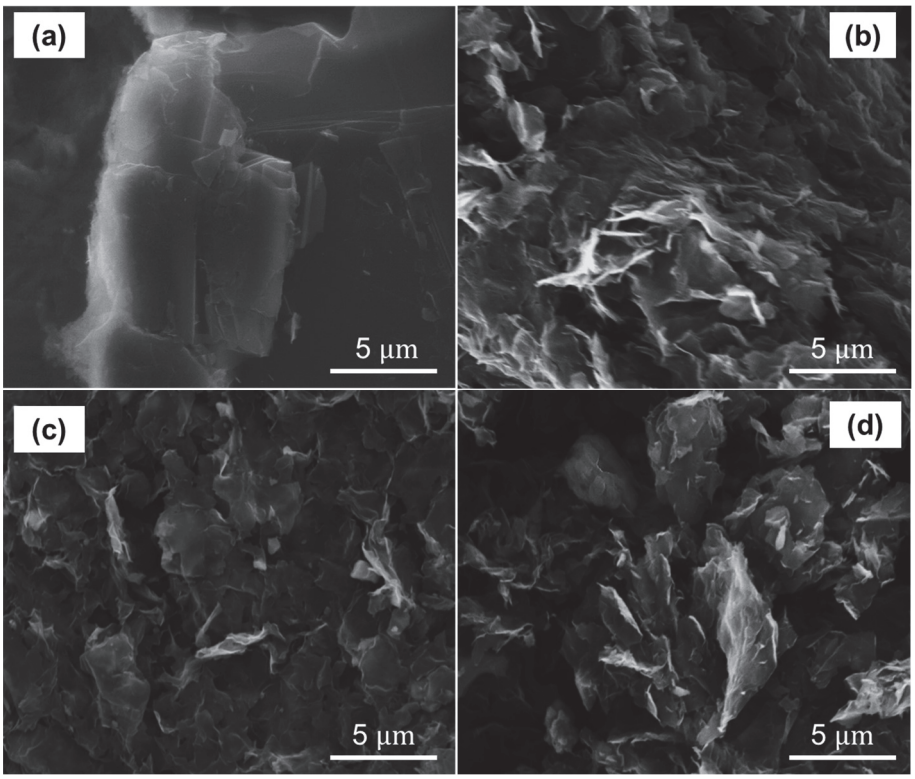

Figure 9. SEM measurements of (**a**) power graphite, (**b**) GO dried at 80 °C for 24 h, (**c**) rGO reduced at 80 °C for 24 h, and (**d**) rGO reduced at 50 °C for 24 h.

These results suggest that the reduction process has not completely removed all of the oxygen functional groups from GO. However, the decrease in the percentage of oxygen confirms that the reduction process has successfully converted GO into rGO. The higher percentage of carbon in both cases of rGO compared to GO indicates that the reduction process has resulted in the restoration of some of the sp^2 hybridized carbon bonds, which is a characteristic of graphene. Additionally, Figures S12 and S13 depict the evolution over time of the mass percentage of carbon and oxygen in rGO samples subjected to different reduction times and different temperatures. Similarly, the evolution over time of the mass percentage of carbon and oxygen in GO samples subjected to different drying times can be observed in Figure S11.

To support EDS results, Figure 8 shows the XRD measurements on the same samples. For comparison purposes, Figure 8 shows XRD measurements of graphite, which displays the (002) peak at 26.73° and the (004) peak at 55.17°, indicating the high crystalline structure of graphite. In particular, the (002) peak corresponds to the d-spacing between adjacent carbon planes in the graphite structure, which is approximately 3.35 Å.

The XRD measurement of GO dried at 80 °C for 24 h exhibits a single peak at 12.95°, indicating the presence of an interlayer spacing distance between adjacent GO layers of 6.12 Å. This value is significantly larger than the interlayer spacing distance of graphite (3.35 Å) and can be attributed to the presence of intercalated oxygen functional groups. Furthermore, this single peak in the XRD pattern suggests that GO has a disordered structure.

For rGO, a relatively narrow peak is observed at 23.57° in rGO reduced at 80 °C, indicating a recovered highly ordered structure with a narrow distribution of interlayer spacing distances between adjacent graphene sheets. On the other hand, the broad peak observed at 23.38° in rGO reduced at 50 °C suggests a less ordered structure with a wider distribution of interlayer spacing distances.

The variation of the 2θ peak position and interlayer distance in rGO as a function of reduction are shown in Figure 8b,c, respectively. In particular, the values of interlayer

distance ranging from 4.18 to 3.78 Å are significantly smaller than the interlayer spacing distance in GO and can be attributed in fact to the reduction of oxygen functional groups and the restoration of the sp^2 hybridization.

The XRD results are complemented by SEM measurements, as shown in Figure 9. The SEM image of graphite (Figure 9a) displays a regular and layered structure. Conversely, GO dried for 24 h at 80 °C exhibits a distinct structure, characterized by numerous folds in the plane and on the edges (Figure 9b). The surface is also corrugated and lacks a homogeneous structure.

Instead, rGO reduced at 80 °C for 24 h (Figure 9c) exhibits a relatively regular structure with folded edges and a moderate degree of surface roughness. In contrast, rGO reduced at 50 °C (Figure 9d) displays a stacked and disordered structure with numerous folds on the edges, but also with a relatively smooth surface. Notably, rGO reduced at 50 °C exhibits a micro- and mesoporous structure, which may be attributed to the presence of residual oxygen functional groups and defects resulting from the reduction process.

4. Conclusions

In conclusion, we have carefully studied the optical characteristics of GO and rGO by considering various oxidation–reduction process parameters, such as drying time, reduction time, temperature, and reduction by employing CA as a green reducing agent. The key findings of our study are summarized below:

- According to our research, GO has an optical bandgap of around 4 eV at 0 h of drying time, which gradually drops to 2.77 eV after 120 h. On the other side, rGO shows a bandgap reduction with longer reduction times. After 120 h of reduction time, the optical bandgaps of rGO at 80 °C and 50 °C were 1.94 eV and 2.03 eV, respectively.
- The $\pi - \pi^*$ transition predominately defines the absorbance spectra of both GO and rGO. Significantly, the aforementioned oxidation–reduction process parameters have a strong influence on this transition. For instance, the $\pi - \pi^*$ transition in GO occurs at about 230 nm at 0 h of drying time. On the other hand, regardless of the temperature at which the reduction is carried out, these transitions occur for rGO with only 1 h of reduction at wavelengths larger than 260 nm.
- Our study further validates that extending the drying time yields a notable enhancement in absorption within the visible region. Specifically, we observed a substantial improvement in photon collection of approximately 40% at 400 nm and 15% at 700 nm when increasing the drying time of GO. Similarly, in the case of rGO reduced at 80 °C, we observed a significant increase in absorption within the visible region, with up to a 22% rise at 400 nm and a 9% increase at 700 nm as the reduction time is extended.
- We measured high absorption coefficients in both GO and rGO, surpassing those reported for exfoliated graphene dispersions by two to three times. These findings confirm the superior optical properties of oxidized graphenes, highlighting their improved capacity for absorbing light.

Supplementary Materials: The supporting information can be downloaded at: https://www.mdpi.com/article/10.3390/nano13152263/s1.

Author Contributions: T.T. conducted conceptualization, data curation, formal analysis, investigation, supervision, writing—original draft, and funding acquisition. P.G.V.-N. conducted formal analysis, software, and investigation. Y.C. conducted validation, investigation. F.A.A. conducted investigation, methodology, and data curation. M.L.P., A.S. and Y.C.S. conducted investigation. M.A.P. conducted validation, investigation, and funding acquisition. S.S. conducted conceptualization, and investigation. C.V.G. conducted conceptualization, investigation, formal analysis, and writing—original draft. L.S.C. conducted conceptualization, investigation, and resources. S.B. conducted conceptualization, supervision, investigation, and writing—original draft. All authors have read and agreed to the published version of the manuscript.

Funding: This work was funded by Universidad Técnica Particular de Loja (UTPL-Ecuador) under the project: "Análisis de las propiedades térmicas del grafeno y zeolita" Grand No.: PROY_INV_QU_2022_362. This work was also supported by the FONDOCyT from the Ministry of Higher Education Science and Technology of the Dominican Republic (grant no. CBA-230600-2021-P-1).

Data Availability Statement: Not applicable.

Acknowledgments: C.V.G. and T.T. wish to thank Escuela Superior Politécnica de Chimborazo for their hospitality during the completion of this work. This work was partially supported by LNF-INFN: Progetto HPSWFOOD Regione Lazio—CUP I35F20000400005.

Conflicts of Interest: The authors declare no conflict of interest.

References

1. Yee, K.; Ghayesh, M.H. A review on the mechanics of graphene nanoplatelets reinforced structures. *Int. J. Eng. Sci.* **2023**, *186*, 103831. [CrossRef]
2. Liu, Y.; Tian, Y.; Xu, J.; Wang, C.; Wang, Y.; Yuan, D.; Chew, J.W. Electrosorption performance on graphene-based materials: A review. *RSC Adv.* **2023**, *13*, 6518–6529. [CrossRef]
3. Wu, W.; Du, M.; Shi, H.; Zheng, Q.; Bai, Z. Application of graphene aerogels in oil spill recovery: A review. *Sci. Total Environ.* **2023**, *856*, 159107. [CrossRef]
4. Demirel, E.; Durmaz, Y.Y. PEGylated Reduced Graphene Oxide as nanoplatform for Targeted Gene and Drug Delivery. *Eur. Polym. J.* **2023**, *186*, 111841. [CrossRef]
5. Wu, J.; Lin, H.; Moss, D.J.; Loh, K.P.; Jia, B. Graphene oxide for photonics, electronics and optoelectronics. *Nat. Rev. Chem.* **2023**, *7*, 162–183. [CrossRef] [PubMed]
6. Ferrari, I.; Motta, A.; Zanoni, R.; Scaramuzzo, F.A.; Amato, F.; Dalchiele, E.A.; Marrani, A.G. Understanding the nature of graphene oxide functional groups by modulation of the electrochemical reduction: A combined experimental and theoretical approach. *Carbon* **2023**, *203*, 29–38. [CrossRef]
7. Gomez, C.V.; Robalino, E.; Haro, D.; Tene, T.; Escudero, P.; Haro, A.; Orbe, J. Structural and electronic properties of graphene oxide for different degree of oxidation. *Mater. Today Proc.* **2016**, *3*, 796–802. [CrossRef]
8. Chen, T.; Huang, Y.; Wei, L.; Xu, T.; Xie, Y. Thermal and electrical transport in partly-reduced graphene oxide films: The effect of low temperature and structure domain size. *Carbon* **2023**, *203*, 130–140. [CrossRef]
9. Manikandan, V.; Lee, N.Y. Reduced graphene oxide: Biofabrication and environmental applications. *Chemosphere* **2023**, *311*, 136934. [CrossRef] [PubMed]
10. Joshi, S.; Bobade, H.; Sharma, R.; Sharma, S. Graphene derivatives: Properties and potential food applications. *J. Ind. Eng. Chem.* **2023**, *123*, 1–18. [CrossRef]
11. Shahriary, L.; Athawale, A.A. Graphene oxide synthesized by using modified hummers approach. *Int. J. Renew. Energy Environ. Eng.* **2014**, *2*, 58–63.
12. Marcano, D.C.; Kosynkin, D.V.; Berlin, J.M.; Sinitskii, A.; Sun, Z.; Slesarev, A.; Alemany, L.B.; Lu, W.; Tour, J.M. Improved Synthesis of Graphene Oxide. *ACS Nano* **2010**, *4*, 4806–4814. [CrossRef] [PubMed]
13. Chen, J.; Yao, B.; Li, C.; Shi, G. An improved Hummers method for eco-friendly synthesis of graphene oxide. *Carbon* **2013**, *64*, 225–229. [CrossRef]
14. Park, S.; An, J.; Potts, J.R.; Velamakanni, A.; Murali, S.; Ruoff, R.S. Hydrazine-reduction of graphite-and graphene oxide. *Carbon* **2011**, *49*, 3019–3023. [CrossRef]
15. De Silva, K.K.H.; Huang, H.H.; Yoshimura, M. Progress of reduction of graphene oxide by ascorbic acid. *Appl. Surf. Sci.* **2018**, *447*, 338–346. [CrossRef]
16. Tene, T.; Bellucci, S.; Guevara, M.; Arias Arias, F.; Sáez Paguay, M.Á.; Quispillo Moyota, J.M.; Torres, F.J. Adsorption of Mercury on Oxidized Graphenes. *Nanomaterials* **2022**, *12*, 3025. [CrossRef] [PubMed]
17. Gupta, B.; Kumar, N.; Panda, K.; Kanan, V.; Joshi, S.; Visoly-Fisher, I. Role of oxygen functional groups in reduced graphene oxide for lubrication. *Sci. Rep.* **2017**, *7*, 45030. [CrossRef] [PubMed]
18. Gong, L.; Cai, C.; Liang, H.; Huang, Y.; Zhang, Y.; Jia, T.; Liu, T. Nonlinear variable band gap of reduced graphene oxide examined by in-situ absorption spectrum and light response. *Diam. Relat. Mater.* **2022**, *122*, 108822. [CrossRef]
19. Kumar, P.V.; Bardhan, N.M.; Tongay, S.; Wu, J.; Belcher, A.M.; Grossman, J.C. Scalable enhancement of graphene oxide properties by thermally driven phase transformation. *Nat. Chem.* **2014**, *6*, 151–158. [CrossRef]
20. Makuła, P.; Pacia, M.; Macyk, W. How to correctly determine the band gap energy of modified semiconductor photocatalysts based on UV–Vis spectra. *J. Phys. Chem. Lett.* **2018**, *9*, 6814–6817. [CrossRef]
21. Tene, T.; Usca, G.T.; Guevara, M.; Molina, R.; Veltri, F.; Arias, M.; Caputi, L.S.; Gomez, C.V. Toward Large-Scale Production of Oxidized Graphene. *Nanomaterials* **2020**, *10*, 279. [CrossRef]
22. Tene, T.; Bellucci, S.; Guevara, M.; Viteri, E.; Polanco, M.A.; Salguero, O.; Vera-Guzmán, E.; Valladares, S.; Scarcello, A.; Alessandro, F.; et al. Cationic Pollutant Removal from Aqueous Solution Using Reduced Graphene Oxide. *Nanomaterials* **2022**, *12*, 309. [CrossRef]

23. Tene, T.; Arias, F.A.; Guevara, M.; Nuñez, A.; Villamagua, L.; Tapia, C.; Pisarra, M.; Torres, F.J.; Caputi, L.S.; Gomez, C.V. Removal of mercury(II) from aqueous solution by partially reduced graphene oxide. *Sci. Rep.* **2022**, *12*, 6326. [CrossRef] [PubMed]
24. Wijaya, R.; Andersan, G.; Permatasari Santoso, S.; Irawaty, W. Green reduction of graphene oxide using kaffir lime peel extract (Citrus hystrix) and its application as adsorbent for methylene blue. *Sci. Rep.* **2020**, *10*, 667. [CrossRef]
25. Begum, H.; Ahmed, M.S.; Cho, S.; Jeon, S. Simultaneous reduction and nitrogen functionalization of graphene oxide using lemon for metal-free oxygen reduction reaction. *J. Power Sources* **2017**, *372*, 116–124. [CrossRef]
26. Gul, M.M.; Ahmad, K.S.; Thomas, A.G.; Ibrahim, S.M. Remarkable energy storage and photocatalytic remediation potential of novel graphene oxide loaded bi-metal sulphide Ba4Fe2S6-GO nanocomposite thin film. *Opt. Mater.* **2023**, *138*, 113682. [CrossRef]
27. Khan, A.; Kamal, T.; Saad, M.; Ameen, F.; Bhat, S.A.; Khan, M.A.; Rahman, F. Synthesis and antibacterial activity of nanoenhanced conjugate of Ag-doped ZnO nanorods with graphene oxide. *Spectrochim. Acta Part A Mol. Biomol. Spectrosc.* **2023**, *290*, 122296. [CrossRef] [PubMed]
28. Hernandez, Y.; Nicolosi, V.; Lotya, M.; Blighe, F.M.; Sun, Z.; De, S.; McGovern, I.T.; Holland, B.; Byrne, M.; Gun'Ko, Y.K.; et al. High-yield production of graphene by liquid-phase exfoliation of graphite. *Nat. Nanotechnol.* **2008**, *3*, 563–568. [CrossRef]
29. Nicolosi, V.; Chhowalla, M.; Kanatzidis, M.G.; Strano, M.S.; Coleman, J.N. Liquid exfoliation of layered materials. *Science* **2013**, *340*, 1226419.
30. Su, R.; Lin, S.F.; Chen, D.Q.; Chen, G.H. Study on the absorption coefficient of reduced graphene oxide dispersion. *J. Phys. Chem. C* **2014**, *118*, 12520–12525. [CrossRef]
31. Gomez, C.V.; Guevara, M.; Tene, T.; Villamagua, L.; Usca, G.T.; Maldonado, F.; Caputi, L.S. The liquid exfoliation of graphene in polar solvents. *Appl. Surf. Sci.* **2021**, *546*, 149046. [CrossRef]
32. Fei, Z.; Goldflam, M.D.; Wu, J.-S.; Dai, S.; Wagner, M.; McLeod, A.S.; Liu, M.K.; Post, K.W.; Zhu, S.; Janssen, G.C.A.M.; et al. Edge and Surface Plasmons in Graphene Nanoribbons. *Nano Lett.* **2015**, *15*, 8271–8276. [CrossRef] [PubMed]

nanomaterials

MDPI

Article

High-Performance Graphene Nanowalls/Si Self-Powered Photodetectors with HfO_2 as an Interfacial Layer

Yuheng Shen [1,2], Yulin Li [1,2], Wencheng Chen [1,2], Sijie Jiang [1], Cheng Li [1] and Qijin Cheng [1,2,*]

[1] School of Electronic Science and Engineering, Xiamen University, Xiamen 361102, China
[2] Shenzhen Research Institute of Xiamen University, Xiamen University, Shenzhen 518000, China
* Correspondence: qijin.cheng@xmu.edu.cn

Abstract: Graphene/silicon (Si) heterojunction photodetectors are widely studied in detecting of optical signals from near-infrared to visible light. However, the performance of graphene/Si photodetectors is limited by defects created in the growth process and surface recombination at the interface. Herein, a remote plasma-enhanced chemical vapor deposition is introduced to directly grow graphene nanowalls (GNWs) at a low power of 300 W, which can effectively improve the growth rate and reduce defects. Moreover, hafnium oxide (HfO_2) with thicknesses ranging from 1 to 5 nm grown by atomic layer deposition has been employed as an interfacial layer for the GNWs/Si heterojunction photodetector. It is shown that the high-k dielectric layer of HfO_2 acts as an electron-blocking and hole transport layer, which minimizes the recombination and reduces the dark current. At an optimized thickness of 3 nm HfO_2, a low dark current of 3.85×10^{-10}, with a responsivity of 0.19 AW^{-1}, a specific detectivity of 1.38×10^{12} as well as an external quantum efficiency of 47.1% at zero bias, can be obtained for the fabricated GNWs/HfO_2/Si photodetector. This work demonstrates a universal strategy to fabricate high-performance graphene/Si photodetectors.

Keywords: hafnium oxide; graphene nanowalls; plasma-enhanced chemical vapor deposition; photodetectors

1. Introduction

Graphene is a two-dimensional material with excellent optical and electrical properties, such as extremely high carrier mobility and ultra-broadband optical absorption. The high carrier mobility enables graphene to travel for micrometers without scattering at room temperature [1]. These properties make graphene have a wide range of potential applications, including energy storage [2], polymer composites [3], biomedical science [4,5], photoelectric devices [6–11], etc. Junctions formed by graphene and silicon (Si) can function as Schottky diodes, which are widely used in solar cells and photodetectors [6–9]. The graphene/Si solar cell was first reported in 2010 with a photovoltaic conversion efficiency (PCE) of 1.5% [6], and the PCE of the graphene/Si solar cell has reached 16.2% [7] within a few years of development. Graphene has also been reported to gain significant achievements in the field of photoelectric detection, including ultrahigh photoresponsivity, ultrafast photoresponse, and ultrawideband response [8–11].

The methods of preparing graphene include mechanical exfoliation [12], chemical vapor deposition (CVD) [13], heat-induced epitaxial growth on silicon carbide (SiC) [14], etc. In 2004, Geim et al. [12] successfully exfoliated and observed a monolayer of graphene from high-directional thermal cracking graphite for the first time by mechanical exfoliation method, but mechanical exfoliation with low controllability is difficult to obtain large areas of high-quality graphene. The CVD-grown graphene, which is synthesized at a high growth temperature, high vacuum, and selective substrate, requires a catalyst that is difficult to remove, and the transfer process for the following device fabrication is fussy and complex [15]. Multilayers of graphene sheets have been prepared by catalyst-free

radio-frequency (RF) plasma-enhanced chemical vapor deposition (PECVD) technique [16]. These multilayers of graphene sheets are approximately perpendicular to the surface of the substrate, forming a wall network with a corrugated surface. Therefore, this graphene network with vertical stacking can also be called vertically oriented graphene nanowalls (GNWs). GNWs with unique characteristics of ultra-sharp edges, high aspect ratio, high specific surface area, and high stability feature an excellent electrode network, which could collect photo-generated carriers quickly [17–19]. PECVD is a catalyst-free direct growth method, which can avoid the complex transfer process for the following device fabrication. So far, GNWs have been reported to successfully grow by PECVD on Cu [20], SiO_2 [21], Al_2O_3 [22], etc. In comparison with the traditional growth methods of graphene, PECVD growth of GNWs has several advantages, such as a relatively low growth temperature, a fast growth rate, and no selectivity toward substrates, which can facilitate the application of GNWs in photodetectors and photovoltaic devices.

However, a zero bandgap and a uniform 2.3% optical absorption of the intrinsic graphene [23] result in fast recombination and a low photoresponsivity, which limits its deeper and wider application in the optoelectronics [24]. To improve the performance of graphene photodetectors, the construction of heterojunction devices through the combination of other semiconductors, such as Si, is a simple and feasible method (it is noteworthy that a lot of work has been reported on the combination of Si with other low-dimensional materials (such as WS_2, Ag nanowalls, etc.) to form a heterojunction for the optoelectronic devices [25–28]). However, the existence of numerous defects, such as dangling bonds on the Si surface, leads to carrier recombination, which seriously affects the photoelectric performance. Modification of the contact between graphene and Si with an interfacial layer is the most popular technique for reducing the charge recombination [29]. It has been reported that the deposition of an oxide layer on the Si surface as an interfacial layer can effectively reduce the effect of surface defects [30]. Among various oxides, including SiO_2, Al_2O_3, etc., hafnium oxide (HfO_2), with a band gap of ~5.5 eV and a high dielectric constant (~25), has a relatively lower effective tunneling mass and lower valence band offset, which leads to a higher tunneling probability than SiO_2 and Al_2O_3 [31].

In this work, we report a direct way to fabricate GNWs/HfO_2/Si photodetectors. The GNWs are obtained using remote PECVD at a low-power (300 W) and catalyst-free moderate temperature (900 °C). In a typical PECVD process for the growth of graphene, both the dissociation process of the precursor gases and the growth process of graphene occur on the substrate surface at the same time. The particles with high energy often cause damage to the surface of the substrate in the process of GNWs deposition, and an unwanted ion bombardment often introduces defects and degrades the performance of the fabricated photodetectors. The low-power remote PECVD proposed in our work can be used to avoid unwanted ion bombardment. In addition to the direct deposition of GNWs without using any catalyst, both lower growth power and faster growth offer more possibilities for the large-scale production of graphene. Furthermore, to improve the photoelectric performance of the pristine GNWs/Si photodetector, we introduce a HfO_2 interfacial layer grown by atomic layer deposition (ALD) to increase the Schottky barrier height, suppress the recombination in the interface, and passivate the dangling bonds on the Si. HfO_2 also acts as an electron-blocking and hole transport layer in the GNWs/HfO_2/Si photodetector, which plays an important role in reducing the dark current. To further investigate the influence of HfO_2 on the performance of GNWs/HfO_2/Si photodetectors, we optimize its thickness. The optimized thickness of HfO_2 is 3 nm, and at this thickness, a low dark current of 3.85×10^{-10} A with a high responsivity of 0.19 AW^{-1}, a specific detectivity of 1.38×10^{12} *Jones*, as well as an external quantum efficiency of 47.1% under the bias of 0 V for the fabricated GNWs/HfO_2/Si photodetector, can be obtained. Moreover, we systematically analyze the band diagram of the device and the physical mechanism of device performance improvement.

2. Materials and Methods

2.1. Growth of HfO_2 by Atomic Layer Deposition

Since GNWs are generally p-doped in the atmosphere environment, we choose n-type Si as a starting material for the fabrication of photodetectors [15]. The n-type (100) single crystalline Si with a resistivity of 1–10 Ω·cm and a thickness of 600 μm was cleaned by RCA (Radio Corporation of America, New York, NY, USA) cleaning to remove organic contaminants and natural oxide layer and then was purged with nitrogen gas and stored under vacuum to avoid reoxidation. Before the deposition of HfO_2, one-third area of the Si substrate was covered with heat tape to prevent the growth of HfO_2 in this area. A series of HfO_2 with different thicknesses were directly deposited on the Si substrate at a temperature of 150 °C using Tetrakis dimethylamido hafnium (TDMAHf) as the precursor of hafnium and H_2O as the precursor of oxygen. In this process, N_2 with a flow rate of 50 sccm was used as the carrier gas, and the temperature of TDMAHf was held at 75 °C while the temperature of H_2O was at room temperature.

2.2. Growth of GNWs

GNWs were directly grown on the Si substrate that had already been deposited with a layer of HfO_2 by remote PECVD. Specifically, a remote radio-frequency plasma-enhanced horizontal tube furnace deposition system has been used to grow GNWs (shown in Figure 1a). The plasma is generated at the coil position, and the frequency of the plasma generator is 13.6 MHz. It is worthwhile to mention that the plasma generator is away from the center of the tube furnace where the Si substrate was placed (the distance between the plasma generator and the center of the tube furnace is 40 cm). Before the synthesis process of GNWs, the entire tubular furnace was pumped to a pressure of approximately 10^{-3} mbar by a vacuum pump, and thereafter, the tube was heated to 900 °C. Then we introduced a mixture of methane (CH_4) with a flow rate of 10 sccm and argon with a flow rate of 40 sccm. The plasma was turned on to grow GNWs under an RF power of 300 W (the power density was 0.093 W/cm^3) with a growth time of 60, 90, 120, and 150 s, respectively. After the growth of GNWs, the sample was naturally cooled to room temperature.

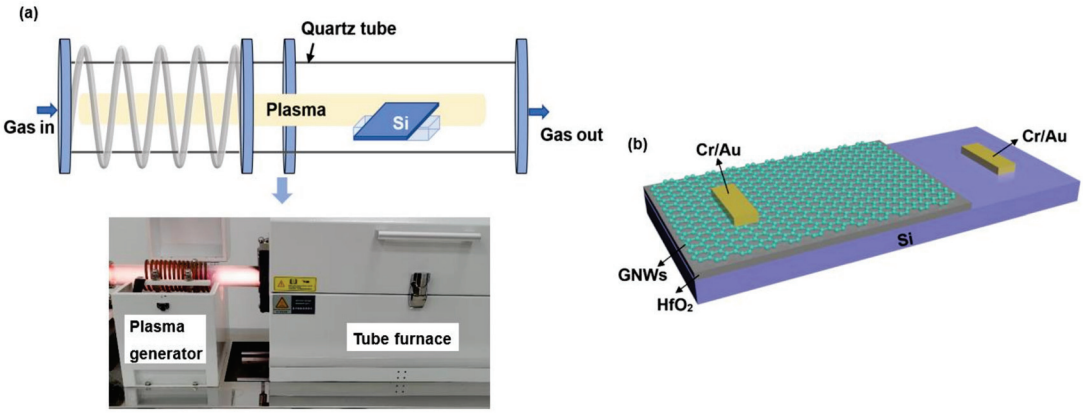

Figure 1. (**a**) A schematic and photo of a remote radio-frequency plasma-enhanced horizontal tube furnace deposition system, respectively. (**b**) Schematic structure of the GNWs/HfO_2/Si photodetector.

2.3. Fabrication of Photodetectors

The GNWs grown for 120 s were used to fabricate GNWs/HfO_2/Si photodetectors. GNWs were spin-coated with UV-positive photoresist (AZ 5214) and then dried at 96 °C for 4 min. Then we used a metal mask to shield the 2/3 area of the sample grown with HfO_2. Afterward, the sample was exposed to UV light with a power of 1 W for 15 s and immersed in the developer. In this process, a photoresist, which had not been removed by the developer, was used to protect the graphene on the HfO_2 in our experiment. After removing the excess photoresist, we purged it with oxygen plasma (60 sccm O_2 and 80 W

RF power) for 5 min to remove extra GNWs without the protection of the photoresist on Si. At this time, GNWs were only retained on the side of HfO_2. Then, acetone was used to remove the remaining photoresist. After that, we used physical vapor deposition (PVD) to sputter metal electrodes (Cr/Au). The electrodes both kept quasi-ohmic contacts with Si and GNWs (the corresponding contact characteristic curves can be found in Figure S1). The schematic structure of the GNWs/HfO_2/Si photodetector is shown in Figure 1b. The overall fabrication process of the GNWs/HfO_2/Si photodetector is shown in Figure 2. In addition, the real apparatus and intermediate fabrication products are shown in Figure S2.

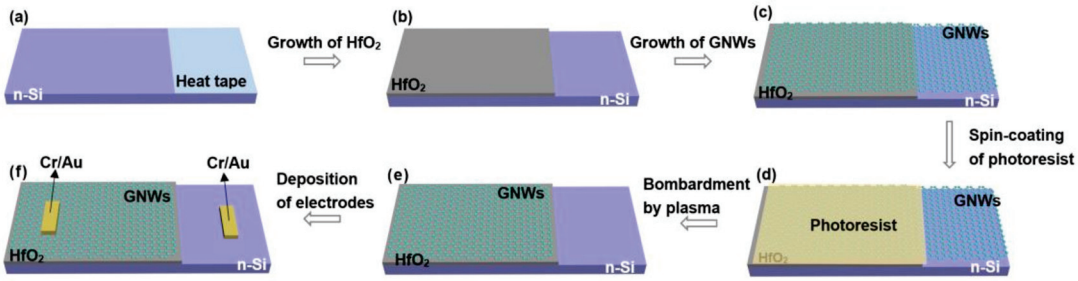

Figure 2. Fabrication process of the GNWs/HfO_2/Si photodetector: (**a**) one-third of the Si substrate was shielded with heat tape; (**b**) HfO_2 was grown by ALD on two-thirds of the Si substrate that has not been covered by heat tape; (**c**) GNWs were grown by PECVD; (**d**) photoresist was coated to protect GNWs on HfO_2; (**e**) GNWs were removed by plasma bombardment, and photoresist was removed by acetone; (**f**) electrodes were deposited by PVD.

2.4. Characterization Technique

Xplora Raman Spectroscope was used to measure the Raman spectra of the GNWs with a 532 nm line of the semiconductor laser. A Zeiss Supra 55 field emission scanning electron microscope (SEM) was used to observe the surface morphology of the synthesized GNWs. The optical transmittance of GNWs was measured by UV-Vis-NIR spectrometer (UV-2600) in the wavelength range from 300 to 1400 nm. The electrical properties of the GNWs were measured by the Hall effect measurement system (HMS 5000). High-resolution transmission electron microscopy (HRTEM) images were taken on a JEOL 2100 TEM microscope operated at 300 kV. The thickness of HfO_2 was measured using a profilometer (Bruker, DektakXT-A). The surface roughness of GNWs was characterized by S600LS atomic force microscope (AFM). The capacitance–voltage (C–V) of the fabricated Al/HfO_2/p-Si metal–oxide–semiconductor (MOS) capacitor was measured using a Keithley 4200 semiconductor parameter analyzer. The current–voltage (I–V) characteristics of the fabricated photodetectors were measured by Keithley 4200 source meter. Illumination was generated using a light-emitting diode (LED) with a beam diameter of 4 mm and a spectral wavelength of 532 nm in air.

3. Results and Discussion

The surface morphology of GNWs plays an important role in the performance of the GNWs/HfO_2/Si photodetector. Figure 3a–d shows the SEM images of GNWs grown on the Si substrate with different growth times of 60 s (a), 90 s (b), 120 s (c), and 150 s (d), respectively. As shown in Figure 3a, for the GNWs prepared at a deposition time of 60 s, the density of the GNWs on the substrate is very low, and the size of the GNWs is very small. Moreover, one can notice that the GNWs do not form a continuous film at a growth time of 60 s. Both the size and the density of GNWs have been found to increase significantly with the increase in the growth time from Figure 3a–d. Particularly, when the growth time is 150 s, we can find that all the substrate has been covered with the GNWs and that all the GNWs are interconnected. It is generally considered that with the increase in the growth time, more C_2 radicals, which were produced from CH_4 precursor, could have enough time to deposit on the Si substrate for the synthesis of GNWs, which made GNWs have a larger size and density [32].

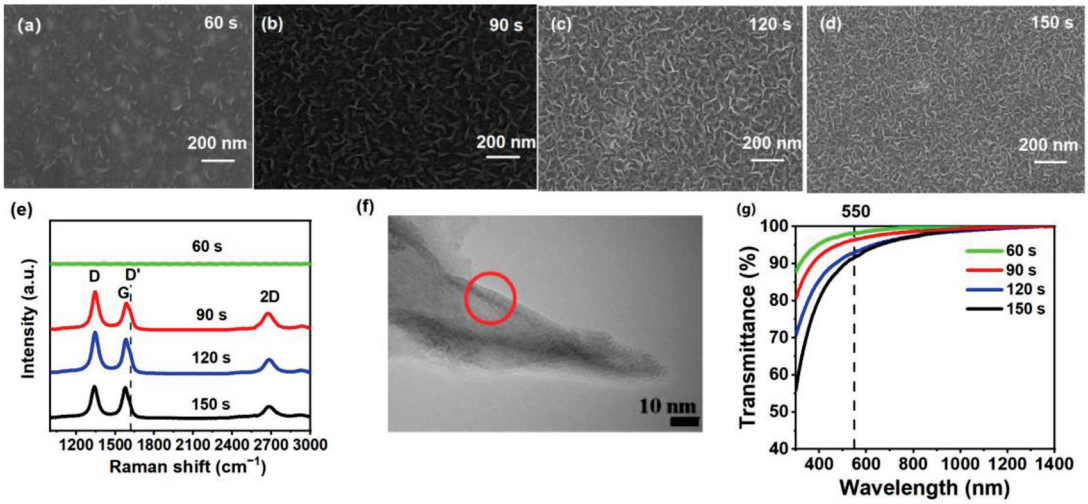

Figure 3. SEM images of GNWs grown on the Si substrate with different growth times: (**a**) 60 s; (**b**) 90 s; (**c**) 120 s; (**d**) 150 s; (**e**) Raman spectra of GNWs on HfO_2/Si with different growth times (the spectra have been displaced vertically for clarity); (**f**) a typical HRTEM image for the GNWs grown for 120 s; (**g**) transmittance spectra of GNWs grown on the clean quartz substrate with different growth times.

Figure 3e shows the Raman spectra of GNWs grown on HfO_2/Si with different growth times of 60, 90, 120, and 150 s, respectively. From Figure 3e, we can't detect any Raman peak in the GNWs when their growth time was 60 s, while all other samples show the three most prominent Raman peaks, i.e., D (~1350 cm^{-1}), G (~1580 cm^{-1}), and 2D (~2700 cm^{-1}). Additionally, the Raman peak of D′ (~1620 cm^{-1}), which presents as a shoulder of the G peak in Raman spectra for GNWs prepared with 90, 120, and 150 s, can be associated with the defects and edges of graphene [33]. All samples do not have an obvious peak of D′, indicating a small amount of inter-crystalline defects [34]. The strong D peak originated from sp^3 carbon clusters of the GNWs, indicating the main sources of defects in our samples [35–37]. The graphitized structure and the sp^2 hybridization of carbon atoms in the synthesized GNWs are mainly shown in the sharp G peak of all samples [36]. Furthermore, the 2D peak represents the band structure of graphene and originates from a two-phonon double resonance process [35].

To identify the number of layers of the GNWs, we carried out HRTEM measurements. Figure 3f shows a typical HRTEM image for the GNWs grown for 120 s. One can notice that GNWs consist of multi-layered graphene. It is noteworthy that we don't use 2D/G to determine the number of layers of the GNWs in our work. This is because 2D/G is used to calculate the number of layers in graphene materials grown in very well-controlled conditions where well-defined and homogeneous materials with very few layers (and a very narrow distribution of a number of layers) are synthesized [38]. In our case, using such a growing time in the fast-growing process used, very dense graphene material is produced, and thus, it is quite difficult to extract information from 2D/G.

Figure 3g displays the transmittance spectra of GNWs grown on clean quartz substrates with varying growth times from 60 to 150 s. As observed in Figure 3g, the transmittance of GNWs gradually decreases with an increase in the growth time. For example, the transmittance of GNWs at an incident wavelength of 550 nm, denoted as T_{550}, is 96.4% for a growth time of 90 s and 91.5% for a growth time of 150 s. Table 1 presents the electrical and optical properties of GNWs grown for 90, 120, and 150 s. One can notice that the carrier concentration, mobility, and conductivity increase, while the sheet resistance decreases with an increase in the growth time. Specifically, as the growth time increases from 90 to 150 s, the sheet resistance of GNWs decreases from 254.3 to 123.5 Ω/sq., while the mobility, conductivity, and carrier concentration increase from 1.08 cm^{2}V^{-1}s^{-1}, 0.131 Ω^{-1}cm^{-1}, 1.18×10^{16} cm^{-3} to 2.62 cm^{2}V^{-1}s^{-1}, 0.270 Ω^{-1}cm^{-1}, and 6.42×10^{17} cm^{-3}, respectively.

The electrical properties of GNWs grown for 150 s are superior to those of the other two samples due to a large amount of interconnected graphene. However, the T_{550} for GNWs grown for 150 s is lower than the other two samples. The properties of GNWs grown for 120 s achieve a compromise between sheet resistance and transmittance.

Table 1. Electrical and optical properties of GNWs prepared with different growth times of 90, 120, and 150 s.

Time (s)	Sheet Resistance (Ω/sq.)	Mobility ($cm^2V^{-1}s^{-1}$)	Conductivity ($\Omega^{-1}cm^{-1}$)	Carrier Concentration (cm^{-3})	Transmittance at 550 nm
90	254.3	1.08	0.131	1.18×10^{16}	96.4%
120	211.7	1.77	0.157	5.55×10^{17}	93.1%
150	123.5	2.62	0.270	6.42×10^{17}	91.5%

Figure 4 shows the AFM images of GNWs grown on the Si substrate with different growth times of 90 s (a) and 120 s (b), respectively. From Figure 4, one can notice that the growth time can affect the surface roughness of GNWs. The root mean square (RMS) roughness of the GNWs with a growth time of 90 s is about 4.231 nm, while the RMS roughness of the GNWs with a growth time of 120 s is about 16.890 nm. The edges of GNWs are significantly larger with a longer growth time, which makes the surface rougher.

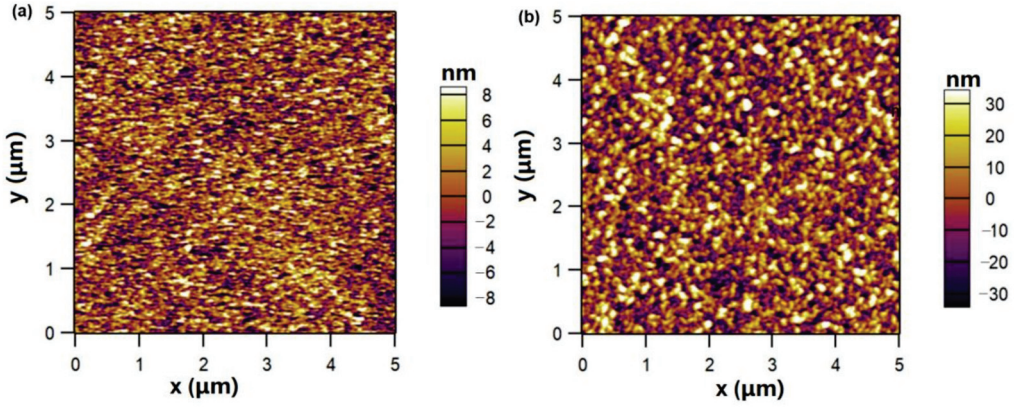

Figure 4. AFM images of GNWs grown on the Si substrate with different growth times: (**a**) 90 s; (**b**) 120 s.

Let's now briefly discuss the benefits of remote PECVD on the growth of GNWs. Generally, in the typical PECVD growth of GNWs, there exist two main processes, i.e., the process of gas phase reaction and the process of surface reaction. During the process of gas phase reaction, the dissociation process of the precursor gases is always accompanied by the unwanted ionization process of the precursor gases under the glow discharge. This complex reaction process would generate various free radicals (such as CH, CH_2), ions (such as CH^+, H^+), and electrons [39]. Afterward, the deposition of the reactive carbon dimer C_2 in the process of surface reaction contributes to the formation of the graphene. At the same time, active hydrogen ions (H^+, etc.) have an etching effect on grown graphene. Remote PECVD decouples these two processes (the process of gas phase reaction and the process of surface reaction) and effectively reduces the ion bombardment, which leads to a lower defect density in GNWs [32] (optical emission spectroscopy (OES) measurement shown in Figure S3 demonstrates that the ion bombardment by Ar-related radicals and the etching effect by H-related radicals are lower at the position of the surface reaction in comparison with those at the position of the plasma generation). Compared with the traditional CVD growth of graphene, there exist a large number of free radicals in the remote PECVD process, which makes it possible to grow GNWs within a few minutes.

The properties of HfO_2 also play an important role in the GNWs/HfO_2/Si photodetector in this work. Figure 5a,b shows height profiles of HfO_2 grown on the Si substrate

measured by profilometer for 200 and 400 cycles of ALD growth, respectively. The thickness of HfO_2 in Figure 5a is about 21 ± 1 nm, and the thickness of HfO_2 in Figure 5b is about 43 ± 2 nm. It is concluded that the thickness of the obtained HfO_2 is approximately linear with the number of growth cycles. The growth rate deduced from Figure 5a,b is approximately 1.07 Å/cycle (the cross-sectional SEM image of HfO_2 grown on the Si substrate for 500 cycles presented in Figure S4 further confirms that the growth rate is approximately 1.07 Å/cycle). Figure 5c shows the AFM image of HfO_2 grown on the Si substrate for 400 cycles. The RMS roughness of HfO_2 films is about 0.718 nm, indicating that the HfO_2 film is rather smooth. Figure 5d shows the UV-visible absorption spectrum of HfO_2 grown on the clean quartz substrate for 400 cycles. For HfO_2 with an indirect band gap, the band gap of HfO_2 can be estimated using the following formula [40]:

$$(\alpha h\upsilon)^{\frac{1}{2}} = B(h\upsilon - Eg) \quad (1)$$

where α is the absorption coefficient, which is derived from the absorption spectrum; hυ is the photon energy; Eg is the band gap, and B is a constant. The inset of Figure 5d shows the plot of $(\alpha h\upsilon)^{1/2}$ versus $h\upsilon$ to extract the band gap of HfO_2, which is roughly estimated to be 4.88 ± 0.12 eV. The C–V characteristic curve of the Al/HfO_2/p-Si MOS capacitor is shown in Figure 5e. The dielectric constant of HfO_2 can be obtained using the following formula [41]:

$$C_{ox} = A\left|\frac{dQ_G}{dV_{ox}}\right| = A\,\frac{\varepsilon_0\varepsilon_{r0}}{d_{ox}} \quad (2)$$

where A is the area of electrode (A is 10^{-8} m^2 in this work); Q_G is the total gate charge; V_{ox} is the oxide voltage; ε_0 is the vacuum permittivity (ε_0 is 8.854 × 10^{-12} F/m^2); C_{ox} is the capacitance of gate oxide (C_{ox} is 2.78 × 10^{-10} F obtained from Figure 5e); d_{ox} is the thickness of HfO_2 (d_{ox} is 10 nm in this work), and ε_{r0} is the dielectric constant of HfO_2. Based on Equation (2), ε_{r0} of HfO_2 can be calculated as 31.398 in this work.

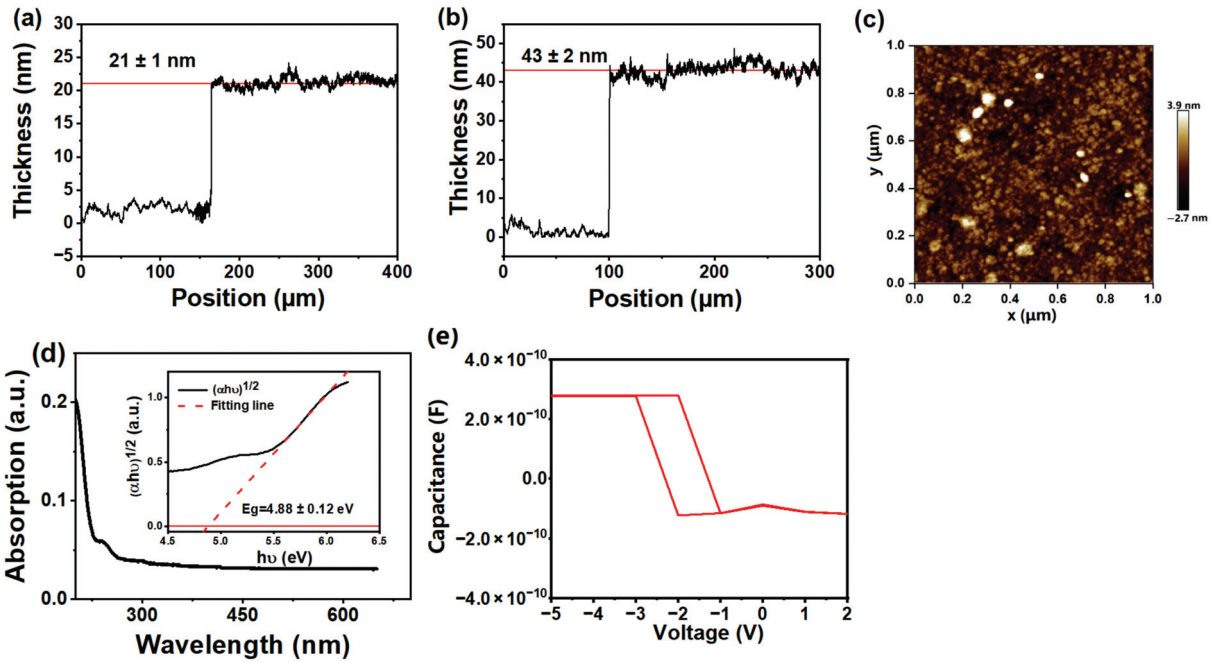

Figure 5. Height profiles of HfO_2 grown on the Si substrate for (**a**) 200 cycles and (**b**) 400 cycles of ALD growth. (**c**) AFM images of HfO_2 grown on the Si substrate for 400 cycles. (**d**) UV-visible absorption spectrum of HfO_2 grown on the clean quartz substrate for 400 cycles, and the inset shows the plot of $(\alpha h\upsilon)^{1/2}$ versus hυ (α is the absorption coefficient of HfO_2). (**e**) C–V characteristic curve of the Al/HfO_2/p-Si metal–oxide–semiconductor capacitor.

In this work, GNWs grown for a deposition time of 120 s were selected to fabricate the GNWs/Si photodetector due to the highest photo-to-dark current ratio (I–V curves of the fabricated GNWs/Si photodetectors for GNWs grown for 90, 120, and 150 s are shown in Figure S5). For photoelectric characterization, Figure 6a shows the I–V characteristics of the GNWs/Si Schottky junction photodetectors with or without HfO_2 under the condition of darkness and illumination. From Figure 6a, we can find that with the introduction of HfO_2, the dark current shows a pronounced drop from 10^{-9} to 10^{-10} A, while the photo-generated current shows an increase from 10^{-8} to 10^{-7} A under the bias of 0 V. The photo-to-dark current ratio (PDCR) of our devices with or without HfO_2 under the bias of 0 V are 617 and 69, respectively. Clearly, our device exhibits a distinct self-powered characteristic, and this characteristic has been enhanced with the introduction of HfO_2.

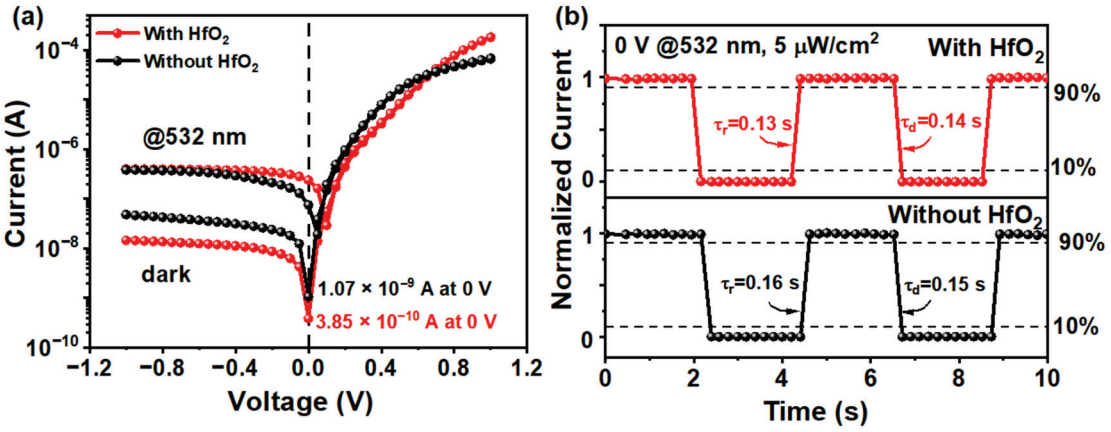

Figure 6. (**a**) I–V characteristics of the GNWs/Si Schottky junction photodetectors with or without HfO_2 under the condition of darkness and illumination. (**b**) Time-dependent photoresponse of the GNWs/Si photodetectors with or without HfO_2 under the bias of 0 V.

Figure 6b shows the time-dependent photoresponse of these two devices under a bias of 0 V and an incident power of 5 $\mu W/cm^2$. From Figure 6b, we can find the rise time (τ_r, which is defined as the time of the current ranging from 10–90%) and the decay time (τ_d, which is defined as the time of the current ranging from 90–10%) both decrease slightly with the introduction of HfO_2. Specifically, the rise time and the decay time of the GNWs/HfO_2/Si photodetector are 0.13 and 0.14 s, respectively, while the rise time and the decay time of the GNWs/Si photodetector are 0.16 and 0.15 s, respectively. The introduction of this interface layer makes it more difficult for electrons to transport through the barrier [42]. Therefore, the recombination of holes and electrons at the interface is reduced, and the strong built-in electric field in the GNWs/HfO_2/Si heterojunction can greatly improve the separation of the photo-generated carriers [43]. The introduction of the HfO_2 layer here passivates the surface states of the Si, and the defects of GNWs could be reduced, resulting in the shortening of the rise time [42]. It should be noted that the time response characterization shown in Figure 6b was limited by the acquisition time resolution and that the actual response time is expected to be faster than what is shown in Figure 6b. Additionally, the carrier lifetime in GNWs is expected to be longer than in graphene, which could lead to a longer time for carriers to be collected by the electrodes [44]. Despite the promising results, the response time of the device still needs to be improved.

On the basis of previously obtained data, we can calculate the responsivity (R_λ) of the fabricated photodetectors using the following formula [45]:

$$R_\lambda = \frac{I_{ph}}{A * P} \tag{3}$$

where I_{ph} is the photocurrent generated under light illumination, which is calculated by subtracting the current measured in the dark from the current measured under light

illumination (I_{light}–I_{dark}); A is the active area of the device (A is 6.25×10^{-2} cm^2 in our work), and P is the power density of the incident light (P is 5 $\mu W/cm^2$ in our work). The calculated responsivity of the device without HfO_2 is about 0.058 A/W, and the calculated responsivity of the device with HfO_2 is about 0.19 A/W.

Specific detectivity (D^*) is also an important indicator to evaluate the performance of the photodetector, and we can get it from the following formula [25]:

$$D^* \approx \frac{\sqrt{A}R_\lambda}{\sqrt{2eI_{dark}}} \tag{4}$$

where e is the electronic charge, and I_{dark} refers to the dark current. The calculated values of D^* of the fabricated photodetectors without HfO_2 and with HfO_2 are about 4.2×10^{11} and 1.38×10^{12} Jones at zero bias, respectively. One can notice that, after the introduction of HfO_2 as an interfacial layer, D^* has a significant increase.

External quantum efficiency (EQE) is also an important parameter to evaluate the performance of the photodetector. It can be interpreted as the ratio of the number of the photo-generated electron–hole pairs, which contributes to the photocurrent, to the total number of the incident photons. The EQE can be obtained by the following formula [45]:

$$EQE = \frac{Rhc}{e\lambda} \tag{5}$$

where h is the Planck's constant (6.626×10^{-34} $m^2 \cdot kg/s$); λ is the wavelength of the incident light (λ is 532 nm in our work); and c is the speed of light. The EQEs of the GNWs/Si and GNWs/HfO_2/Si photodetectors are about 13.5% and 47.1%, respectively.

From the above analysis, one can notice that in comparison with the photodetector without HfO_2, the GNWs/HfO_2/Si photodetector has a lower dark current, a higher PDCR, and a faster response time. To explain the underlying physical mechanism behind this phenomenon, the energy band diagrams for the GNWs/Si and GNWs/HfO_2/Si photodetectors are shown in Figure 7. Without a HfO_2 interfacial layer, photo-generated electrons of Si can easily move toward GNWs through thermal emission because of the low built-in potential between GNWs and Si, as shown in Figure 7a. Then, the unwanted recombination occurs immediately as the short lifetime of the carriers in the GNWs [46], giving rise to the poor performance of the GNWs/Si photodetector. The existence of a HfO_2 interfacial layer modifies the band alignment, resulting in a band bending in the valence band of Si and an increased Schottky barrier height in the interface, as shown in Figure 7b. When a thin HfO_2 interfacial layer is introduced, the movement of the photo-generated electrons from Si toward GNWs would be significantly blocked by the increased φ_{SBH} (the Schottky barrier height), while photo-generated holes can tunnel through HfO_2 due to its higher probability of tunneling (after the introduction of a HfO_2 interfacial layer, the barrier height for photogenerated electrons is significantly higher than that of photogenerated holes, leading to a higher probability of photogenerated holes than photogenerated electrons). Therefore, the recombination of the carriers in GNWs can be suppressed effectively [15,42,47,48], leading to the excellent performance of the GNWs/HfO_2/Si photodetector. However, if the thickness of HfO_2 is too thick, the tunneling probability of holes through HfO_2 decreases, and therefore, holes accumulate at the interface. This will result in a higher recombination rate of photo-generated carriers and deteriorate the performance of the GNWs/HfO_2/Si photodetector. At this time, the quasi-Fermi level for holes in the silicon shows obvious bending due to the accumulation of the holes, as shown in Figure 7c. Our experimental result demonstrates that the optimal thickness of HfO_2 is 3 nm in our work, which will be presented later.

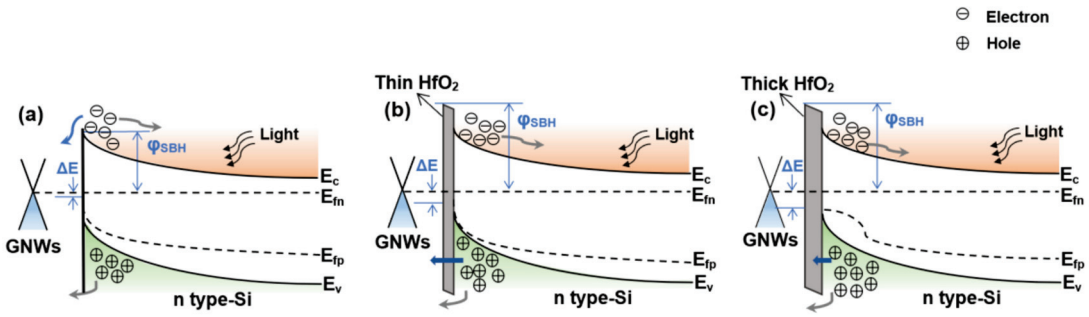

Figure 7. Energy band diagrams of the GNWs/Si photodetectors (**a**) without a HfO_2 interfacial layer, (**b**) with a thin HfO_2 interfacial layer, and (**c**) with a thick HfO_2 interfacial layer under illumination conditions. Here φ_{SBH} represents the Schottky barrier height; ΔE is the difference between GNWs Fermi level and quasi-Fermi energy level for holes in Si; E_c and E_v are the energy levels of conduction band and valence band for Si, respectively; E_{fn} and E_{fp} are quasi-Fermi energy levels of electrons and holes for Si, respectively.

The increase in φ_{SBH} can be confirmed by thermionic emission theory according to the following equation [49]:

$$J_{dark}\mathrm{V} = J_s\left[\exp\left(\frac{eV}{nkT}\right) - 1\right] \tag{6}$$

where J_s is the reverse saturation current density; e is the elementary charge; V is the applied voltage; n is an ideality factor; k is a Boltzmann constant, and T is the temperature. Furthermore, J_s also satisfies the following equation [47]:

$$J_s(T) = A^*T^2\exp\left(-\frac{e(\varphi_{SBH})}{kT}\right) \tag{7}$$

where A^* is Richardson constant (252 $\mathrm{A{\cdot}cm^{-2}K^{-2}}$ for n-type Si). Taking the logarithm of both sides of the Equation (6), with the assumption that $\exp\left(\frac{eV}{nkT}\right) \gg 1$, we can obtain n and φ_{SBH} by fitting the linear part of the curve based on the Equations (6) and (7). Figure 8a shows the I–V characteristics of the GNWs/Si photodetectors with and without a HfO_2 layer. Figure 8b shows the lnJ–V curves of photodetectors with and without a HfO_2 layer. The results of the barrier height for photodetectors with and without HfO_2 are 0.87 ± 0.02 and 0.82 ± 0.02 eV, respectively. According to a previous study [47], there is a strong positive correlation between build-in potential (V_{bi}) and φ_{SBH}. For Schottky heterojunction photodetectors, the photo-generated carriers can be separated by the built-in electric field in the depletion region [50]. A larger V_{bi} and φ_{SBH} could facilitate the separation and migration of photo-generated carriers, which enhances the transfer of the photo-generated holes at the interface. Moreover, the increase in φ_{SBH} blocks the thermal emission of the photo-generated electrons from the side of Si toward the side of GNWs. As a result, both the leakage current and the recombination at GNWs can be greatly reduced. The ideality factor n is also a critical factor that needs to be taken into consideration. The ideality factor decreases from 1.32 ± 0.02 to 1.17 ± 0.02, as shown in Figure 8b, indicating that the fabricated photodetector with HfO_2 has a better junction quality and the recombination of the carriers has significantly reduced. Through calculation and comparison, it is found that the barrier of our devices is slightly higher than other graphene/Si-based devices [15,42] and that the value of n is slightly higher than an ideal Schottky junction (n = 1). The increase in φ_{SBH} and the decrease in n further confirm the improvement of our devices due to the introduction of HfO_2.

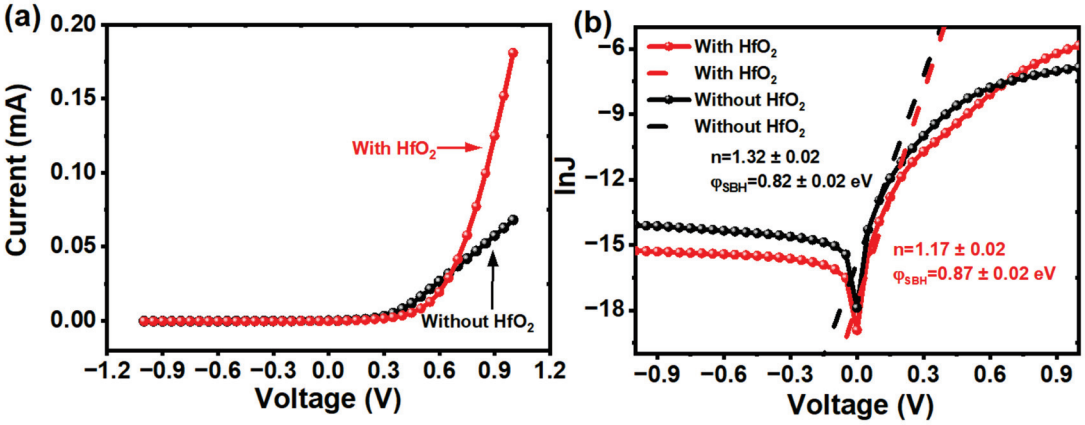

Figure 8. (**a**) I–V characteristics of the GNWs/Si photodetectors with and without a HfO_2 layer. (**b**) lnJ–V curves of the GNWs/Si photodetectors with and without a HfO_2 layer under dark conditions.

Last but not least, the optimization of the thickness of HfO_2 must be taken into account for the achievement of high-performance photodetectors. Figure 9 shows the I–V curves of the GNWs/HfO_2/Si photodetectors with different thicknesses of the HfO_2 interface layer. Table 2 lists the calculated parameters of the GNWs/HfO_2/Si photodetectors with different thicknesses of HfO_2. The result of the experiment is consistent with previous theoretical analysis. The introduction of HfO_2 increases the height of the Schottky barrier and blocks the transport of electrons toward graphene when the interface layer is thin. As shown in Figure 9a, the dark current of our devices under 0 V bias has only a slight difference with different thicknesses. Meanwhile, a thicker HfO_2 results in a lower dark current. The current under illumination condition keeps rising under zero bias until the thickness of HfO_2 reaches 3 nm due to the enhancement of φ_{SBH}, as shown in Figure 9b. However, there is a slight decrease when the thickness continuously increases up to 5 nm. From Table 2, the ideal factor has been reduced from 1.35 ± 0.02 to 1.17 ± 0.02, and the φ_{SBH} increases from 0.82 ± 0.02 to 0.87 ± 0.02 eV when the thickness of HfO_2 increases from 0 to 3 nm. However, with a further increase in the HfO_2 interface layer to 5 nm, n increases to 1.33 ± 0.02, at which point the recombination of the carriers is no longer suppressed, and the φ_{SBH} doesn't show a continuous increase (the detailed n and φ_{SBH} of the GNWs/Si photodetectors with the thickness of 1 and 5 nm HfO_2 layer can be found in Figure S6). As a result, the PDCR of the photodetector with 5 nm thick HfO_2 is worse than the photodetector with an ideal thickness (3 nm) of HfO_2. Although an interface layer with thin thickness enhances the built-in potential and reduces the interface trap state density, an excessively thick oxide layer also limits the transport of the photo-generated holes. A large number of holes accumulate at the interface, resulting in the recombination at the interface and the increase in n. The variation tendencies of PDCR and responsivity are the same as n, according to Table 2. The above discussion further confirms that when the thickness of HfO_2 is 3 nm, we can get better photodetector performance.

Performance parameters of typical graphene/Si-based photodetectors with different structures are compared in Table 3. One can notice that the specific detectivity and responsivity of our photodetector are comparable to those reported works. The reasons for the performance improvement of the GNWs/HfO_2/Si photodetector in this work are as follows. Firstly, the remote plasma decouples the whole process of GNWs growth and independent control of precursor gas dissociation and other growth parameters. Secondly, the introduction of the HfO_2 interface layer passivates the surface of Si and reduces the density of interface states, enhancing the junction characteristic of the GNWs/HfO_2/Si photodetector. Finally, the precise control of the thickness of the interface layer effectively maintains a balance between electron blocking and hole transporting.

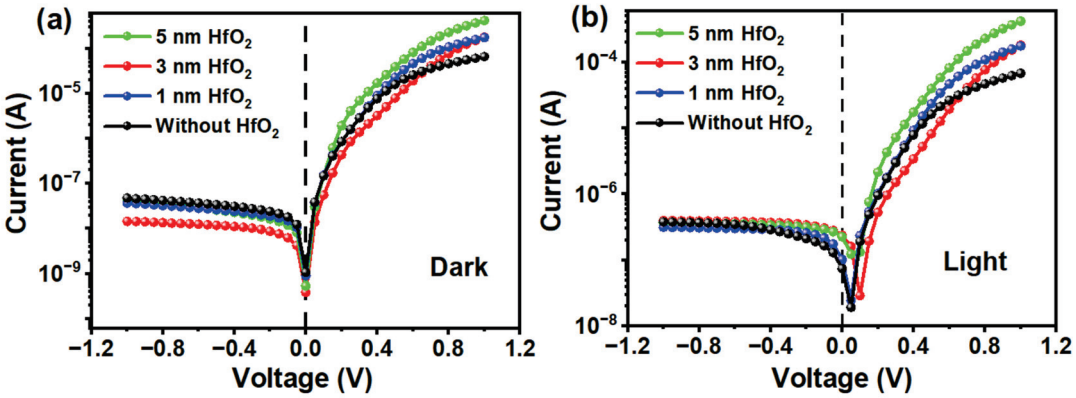

Figure 9. (**a**) I–V characteristic of the GNWs/HfO_2/Si photodetectors under dark conditions and (**b**) under illumination of the devices with varying thicknesses of HfO_2.

Table 2. The calculated parameters of the GNWs/HfO_2/Si photodetectors with different thicknesses of HfO_2.

Thickness (nm)	PDCR @ 0 V	Responsivity (A/W)	Ideal Factor	Schottky Barrier Height (eV)
0	69	0.058	1.35 ± 0.02	0.82 ± 0.02
1	113	0.18	1.24 ± 0.02	0.85 ± 0.02
3	617	0.19	1.17 ± 0.02	0.87 ± 0.02
5	425	0.08	1.33 ± 0.02	0.86 ± 0.02

Table 3. Performance comparison of different graphene/Si-based photodetectors.

Ref.	Device Structure	Responsivity (A/W)	Response Time (τ_{rise}/τ_{decay})	Specific Detectivity (cm·$Hz^{1/2}$/W)
[44]	GNWs/Si	0.012 @0 V	-	7.85×10^6
[51]	GNWs/Si	0.015	43/69 μs	1.5×10^{11}
[52]	GNWs/Si	0.52 @0 V	40 μs	5.88×10^{13}
[53]	Graphene/Si	0.225 @−2 V	-	7.69×10^9
[54]	GQDs/WSe_2/Si	0.707 @−3 V	0.2/0.14 ms	4.51×10^9
[55]	Graphene/Si	1.38×10^{-4} @0 V	0.37 ms	1.6×10^9
[56]	GNWs/DLC/Si	2400	13/36 μs	1.07×10^{11}
This work	GNWs/HfO_2/n-Si	0.19 @0 V	0.13/0.14 s	1.38×10^{12}

4. Conclusions

In this work, we successfully grew GNWs using a remote PECVD and fabricated self-powered GNWs/Si photodetectors with different structures to systematically explore the possible influencing factors of the GNWs/HfO_2/Si photodetector. Remote plasma enhances the deposition rate and reduces structural defects of GNWs. After the introduction of the HfO_2 interface layer with a thickness of 3 nm, the dark current decreases from 10^{-9} to 10^{-10} A, the PDCR increases from 69 to 617, and the specific detectivity increases from 4.2×10^{11} to 1.38×10^{12} Jones at the bias of 0 V. Based on the experimental result, we have also proposed a physical mechanism to shed light on the improvement of the photoelectric performance of the GNWs/Si photodetector after introducing HfO_2 as an interface layer with an appropriate thickness. The approach of using HfO_2 as an interfacial layer for the improvement of GNWs/Si photodetectors can be applied in other heterojunction-based photoelectric devices. Our work offers effective guidance for fabricating GNWs-based photodetectors and pushes forward the application of graphene in photodetectors.

Supplementary Materials: The following supporting information can be downloaded at: https://www.mdpi.com/article/10.3390/nano13101681/s1. Figure S1: Ohmic contact of (a) GNWs and (b) Si. Figure S2: (a) Photograph of the Si substrate with a 3 nm HfO_2 layer (the two-thirds area of the Si substrate was covered with a 3 nm HfO_2 layer). (b) Photograph of the GNWs/HfO_2/Si photodetector. (c) Photograph of lithography equipment. (d) Photograph of ALD equipment. Figure S3: OES spectra at different positions of the remote PECVD system: (a) at the position of the plasma generation and (b) at the position of the surface reaction. Figure S4: A cross-sectional SEM image of HfO_2 grown on the Si substrate for 500 cycles. Figure S5: I–V characteristic curves of the GNWs/HfO_2/Si photodetectors with different growth times of GNWs (a) 90 s, (b) 120 s, and (c) 150 s, respectively. Table S1: Photoelectric parameters of the GNWs/HfO_2/Si photodetectors with different growth times of GNWs. Figure S6: lnJ–V curves of the GNWs/Si photodetectors with the thickness of (a) 1 nm and (b) 5 nm HfO_2 layer.

Author Contributions: Methodology, Y.L.; formal analysis, Y.S.; resources, C.L.; data curation, S.J.; writing—original draft, Y.S. and Y.L.; writing—review and editing, W.C. and Q.C.; visualization, Y.S.; supervision, Q.C.; project administration, Q.C.; funding acquisition, Q.C. All authors have read and agreed to the published version of the manuscript.

Funding: This research was funded by the Natural Science Foundation of Fujian Province (Grant No. 2021J01054) and the Shenzhen Science and Technology Innovation Committee (Grant No. JCYJ20190809160401653), China.

Data Availability Statement: The datasets used and analyzed during the current study are available from the corresponding author on reasonable request.

Conflicts of Interest: The authors declare no conflict of interest.

References

1. Geim, A.K. Graphene: Status and Prospects. *Science* **2009**, *324*, 1530–1534. [CrossRef] [PubMed]
2. Jia, Y.; Zhang, J.; Kong, D.; Zhang, C.; Han, D.; Han, J.; Tao, Y.; Lv, W.; Yang, Q.H. Practical Graphene Technologies for Electrochemical Energy Storage. *Adv. Funct. Mater.* **2022**, *32*, 2204272. [CrossRef]
3. Irshad, H.M.; Hakeem, A.S.; Raza, K.; Baroud, T.N.; Ehsan, M.A.; Ali, S.; Tahir, M.S. Design, Development and Evaluation of Thermal Properties of Polysulphone-CNT/GNP Nanocomposites. *Nanomaterials* **2021**, *11*, 2080. [CrossRef] [PubMed]
4. Plachá, D.; Jampilek, J. Graphenic Materials for Biomedical Applications. *Nanomaterials* **2019**, *9*, 1758. [CrossRef]
5. Kaczmarek-Szczepańska, B.; Michalska-Sionkowska, M.; Binkowski, P.; Lukaszewicz, J.P.; Kamedulski, P. 3D-Structured and Blood-Contact-Safe Graphene Materials. *Int. J. Mol. Sci.* **2023**, *24*, 3576. [CrossRef]
6. Li, X.; Zhu, H.; Wang, K.; Cao, A.; Wei, J.; Li, C.; Jia, Y.; Li, Z.; Li, X.; Wu, D. Graphene-On-Silicon Schottky Junction Solar Cells. *Adv. Mater.* **2010**, *22*, 2743–2748. [CrossRef]
7. Kim, J.M.; Kim, S.; Shin, D.H.; Seo, S.W.; Lee, H.S.; Kim, J.H.; Jang, C.W.; Kang, S.S.; Choi, S.-H.; Kwak, G.Y.; et al. Si-Quantum-Dot Heterojunction Solar Cells with 16.2% Efficiency Achieved by Employing Doped-Graphene Transparent Conductive Electrodes. *Nano Energy* **2018**, *43*, 124–129. [CrossRef]
8. Wang, Z.; Yu, X.; Qiu, X.; Fu, J.; Yang, D. High-Responsivity Graphene/Hyperdoped-Silicon Heterostructure Infrared Photodetectors. *Opt. Laser Technol.* **2022**, *153*, 108291. [CrossRef]
9. Xia, F.; Mueller, T.; Lin, Y.-M.; Valdes-Garcia, A.; Avouris, P. Ultrafast Graphene Photodetector. *Nat. Nanotechnol.* **2009**, *4*, 839–843. [CrossRef]
10. Lin, H.; Sturmberg, B.C.P.; Lin, K.-T.; Yang, Y.; Zheng, X.; Chong, T.K.; De Sterke, C.M.; Jia, B. A 90-nm-thick Graphene Metamaterial for Strong and Extremely Broadband Absorption of Unpolarized Light. *Nat. Photonics* **2019**, *13*, 270–276. [CrossRef]
11. Casalino, M.; Sassi, U.; Goykhman, I.; Eiden, A.; Lidorikis, E.; Milana, S.; De Fazio, D.; Tomarchio, F.; Iodice, M.; Coppola, G.; et al. Vertically Illuminated, Resonant Cavity Enhanced, Graphene–Silicon Schottky Photodetectors. *ACS Nano* **2017**, *11*, 10955–10963. [CrossRef] [PubMed]
12. Novoselov, K.S.; Geim, A.K.; Morozov, S.V.; Jiang, D.; Zhang, Y.; Dubonos, S.V.; Grigorieva, I.V.; Firsov, A.A. Electric Field Effect in Atomically Thin Carbon Films. *Science* **2004**, *306*, 666–669. [CrossRef] [PubMed]
13. Bi, H.; Sun, S.; Huang, F.; Xie, X.; Jiang, M. Direct Growth of Few-Layer Graphene Films on SiO_2 Substrates and Their Photovoltaic Applications. *J. Mater. Chem.* **2012**, *22*, 411–416. [CrossRef]
14. Riedl, C.; Coletti, C.; Iwasaki, T.; Zakharov, A.A.; Starke, U. Quasi-Free-Standing Epitaxial Graphene on SiC Obtained by Hydrogen Intercalation. *Phys. Rev. Lett.* **2009**, *103*, 246804. [CrossRef] [PubMed]
15. Rehman, M.A.; Akhtar, I.; Choi, W.; Akbar, K.; Farooq, A.; Hussain, S.; Shehzad, M.A.; Chun, S.-H.; Jung, J.; Seo, Y. Influence of an Al_2O_3 Interlayer in a Directly Grown Graphene-Silicon Schottky Junction Solar Cell. *Carbon* **2018**, *132*, 157–164. [CrossRef]
16. Song, X.; Liu, J.; Yu, L.; Yang, J.; Fang, L.; Shi, H.; Du, C.; Wei, D. Direct Versatile PECVD Growth of Graphene Nanowalls on Multiple Substrates. *Mater. Lett.* **2014**, *137*, 25–28. [CrossRef]

17. Yang, H.; Yang, J.; Bo, Z.; Zhang, S.; Yan, J.; Cen, K. Edge Effects in Vertically-Oriented Graphene Based Electric Double-Layer Capacitors. *J. Power Sources* **2016**, *324*, 309–316. [CrossRef]
18. Santhosh, N.; Filipič, G.; Tatarova, E.; Baranov, O.; Kondo, H.; Sekine, M.; Hori, M.; Ostrikov, K.; Cvelbar, U. Oriented Carbon Nanostructures by Plasma Processing: Recent Advances and Future Challenges. *Micromachines* **2018**, *9*, 565. [CrossRef]
19. Huang, F.; Zhang, L.; Li, S.; Fu, J.; Zhang, K.H.L.; Cheng, Q. Direct Growth of Graphene Nanowalls on Inverted Pyramid Silicon for Schottky Junction Solar Cells. *ACS Appl. Energy Mater.* **2021**, *4*, 6574–6584. [CrossRef]
20. Mao, S.; Yu, K.; Chang, J.; Steeber, D.A.; Ocola, L.E.; Chen, J. Direct Growth of Vertically-oriented Graphene for Field-Effect Transistor Biosensor. *Science* **2013**, *3*, 1696. [CrossRef]
21. Yu, K.; Bo, Z.; Lu, G.; Mao, S.; Cui, S.; Zhu, Y.; Chen, X.; Ruoff, R.S.; Chen, J. Growth of Carbon Nanowalls at Atmospheric Pressure for One-Step Gas Sensor Fabrication. *Nanoscale Res. Lett.* **2011**, *6*, 202. [CrossRef] [PubMed]
22. Wang, J.J.; Zhu, M.Y.; Outlaw, R.A.; Zhao, X.; Manos, D.M.; Holloway, B.C.; Mammana, V.P. Free-Standing Subnanometer Graphite Sheets. *Appl. Phys. Lett.* **2004**, *85*, 1265–1267. [CrossRef]
23. Nair, R.R.; Blake, P.; Grigorenko, A.N.; Novoselov, K.S.; Booth, T.J.; Stauber, T.; Peres, N.M.R.; Geim, A.K. Fine Structure Constant Defines Visual Transparency of Graphene. *Science* **2008**, *320*, 1308. [CrossRef] [PubMed]
24. Nan, H.; Zhou, R.; Gu, X.; Xiao, S.; Ostrikov, K. Recent Advances in Plasma Modification of 2D Transition Metal Dichalcogenides. *Nanoscale* **2019**, *11*, 19202–19213. [CrossRef]
25. Kim, H.S.; Patel, M.; Kim, J.; Jeong, M.S. Growth of Wafer-Scale Standing Layers of WS_2 for Self-Biased High-Speed UV-Visible-NIR Optoelectronic Devices. *ACS Appl. Mater. Interfaces* **2018**, *10*, 3964–3974. [CrossRef]
26. Patel, M.; Kim, H.S.; Kim, J. Wafer-scale Production of Vertical SnS Multilayers for High-performing Photoelectric Devices. *Nanoscale* **2017**, *9*, 15804–15812. [CrossRef]
27. Mahala, P.; Patel, M.; Gupta, N.; Kim, J.; Lee, B.H. Schottky Junction Interfacial Properties at High Temperature: A Case of AgNWs Embedded Metal Oxide/p-Si. *Phys. B Condens. Matter* **2018**, *537*, 228–235. [CrossRef]
28. Patel, M.; Kim, H.-S.; Park, H.-H.; Kim, J. Silver Nanowires-templated Metal Oxide for Broadband Schottky Photodetector. *Appl. Phys. Lett.* **2016**, *108*, 141904. [CrossRef]
29. Lillington, D.R.; Townsend, W.G. Effects of Interfacial Oxide Layers on the Performance of Silicon Schottky-Barrier Solar Cells. *Appl. Phys. Lett.* **1976**, *28*, 97–98. [CrossRef]
30. Hájková, Z.; Ledinský, M.; Vetushka, A.; Stuchlík, J.; Müller, M.; Fejfar, A.; Bouša, M.; Kalbáč, M.; Frank, O. Photovoltaic Characterization of Graphene/Silicon Schottky Junctions from Local and Macroscopic Perspectives. *Chem. Phys. Lett.* **2017**, *676*, 82–88. [CrossRef]
31. Kim, J.; Kim, S.; Jeon, H.; Cho, M.H.; Chung, K.B.; Bae, C. Characteristics of HfO_2 Thin Films Grown by Plasma Atomic Layer Deposition. *Appl. Phys. Lett.* **2005**, *87*, 053108. [CrossRef]
32. Cuxart, M.G.; Šics, I.; Goñi, A.R.; Pach, E.; Sauthier, G.; Paradinas, M.; Foerster, M.; Aballe, L.; Fernandez, H.M.; Carlino, V.; et al. Inductively Coupled Remote Plasma-Enhanced Chemical Vapor Deposition (rPE-CVD) as a Versatile Route for the Deposition of Graphene Micro- and Nanostructures. *Carbon* **2017**, *117*, 331–342. [CrossRef]
33. Wang, C.; Zhou, Y.; He, L.; Ng, T.-W.; Hong, G.; Wu, Q.-H.; Gao, F.; Lee, C.-S.; Zhang, W. In Situnitrogen-Doped Graphene Grown from Polydimethylsiloxane by Plasma Enhanced Chemical Vapor Deposition. *Nanoscale* **2013**, *5*, 600–605. [CrossRef] [PubMed]
34. Zhang, N.; Li, J.; Liu, Z.; Yang, S.; Xu, A.; Chen, D.; Guo, Q.; Wang, G. Direct Synthesis of Vertical Graphene Nanowalls on Glass Substrate for Thermal Management. *Mater. Res. Express.* **2018**, *5*, 065606. [CrossRef]
35. Wu, J.; Shao, Y.; Wang, B.; Ostrikov, K.K.; Feng, J.; Cheng, Q. Plasma-Produced Vertical Carbonous Nanoflakes for Li-Ion Batteries. *Plasma Process. Polym.* **2016**, *13*, 1008–1014. [CrossRef]
36. Lin, G.; Wang, H.; Zhang, L.; Cheng, Q.; Gong, Z.; Ostrikov, K.K. Graphene Nanowalls Conformally Coated with Amorphous/Nanocrystalline Si as High-Performance Binder-Free Nanocomposite Anode for Lithium-Ion Batteries. *J. Power Sources* **2019**, *437*, 226909. [CrossRef]
37. Ni, Z.; Wang, Y.; Yu, T.; Shen, Z. Raman Spectroscopy and Imaging of Graphene. *Nano Res.* **2008**, *1*, 273–291. [CrossRef]
38. Zólyomi, V.; Koltai, J.; Kürti, J. Resonance Raman Spectroscopy of Graphite and Graphene. *Phys. Status Solidi B* **2011**, *248*, 2435–2444. [CrossRef]
39. Yamada, Y.; Tasaka, S.; Inagaki, N. Surface Modification of Poly(tetrafluoroethylene) by Remote Hydrogen Plasma. *Macromolecules* **1996**, *29*, 4331–4339. [CrossRef]
40. Dhanunjaya, M.; Manikanthababu, N.; Ojha, S.; Pojprapai, S.; Pathak, A.P.; Nageswara Rao, S.V.S. Effects of Growth Parameters on HfO_2 Thin-films Deposited by RF Magnetron Sputtering. *Radiat. Eff. Defects Solids* **2022**, *177*, 15–26. [CrossRef]
41. Hoffmann, M.; Slesazeck, S.; Mikolajick, T. Progress and Future Prospects of Negative Capacitance Electronics: A Materials Perspective. *APL Mater.* **2021**, *9*, 020902. [CrossRef]
42. Alnuaimi, A.; Almansouri, I.; Saadat, I.; Nayfeh, A. High Performance Graphene-Silicon Schottky Junction Solar Cells with HfO_2 Interfacial Layer Grown by Atomic Layer Deposition. *Sol. Energy* **2018**, *164*, 174–179. [CrossRef]
43. Mao, J.; Yu, Y.; Wang, L.; Zhang, X.; Wang, Y.; Shao, Z.; Jie, J. Ultrafast, Broadband Photodetector Based on $MoSe_2$/Silicon Heterojunction with Vertically Standing Layered Structure Using Graphene as Transparent Electrode. *Adv. Sci.* **2016**, *3*, 1600018. [CrossRef] [PubMed]
44. Li, L.; Dong, Y.; Guo, W.; Qian, F.; Xiong, F.; Fu, Y.; Du, Z.; Xu, C.; Sun, J. High-Responsivity Photodetectors Made of Graphene Nanowalls Grown on Si. *Appl. Phys. Lett.* **2019**, *115*, 081101. [CrossRef]

45. Ezhilmaran, B.; Patra, A.; Benny, S.; Bhat, S.V.; Rout, C.S. Recent Developments in the Photodetector Applications of Schottky Diodes Based on 2D Materials. *J. Mater. Chem. C* **2021**, *9*, 6122–6150. [CrossRef]
46. Limmer, T.; Feldmann, J.; Da Como, E. Carrier Lifetime in Exfoliated Few-Layer Graphene Determined from Intersubband Optical Transitions. *Phys. Rev. Lett.* **2013**, *110*, 217406. [CrossRef]
47. Song, Y.; Li, X.; Mackin, C.; Zhang, X.; Fang, W.; Palacios, T.; Zhu, H.; Kong, J. Role of Interfacial Oxide in High-Efficiency Graphene-Silicon Schottky Barrier Solar Cells. *Nano Lett.* **2015**, *15*, 2104–2110. [CrossRef]
48. Li, X.; Zhu, M.; Du, M.; Lv, Z.; Zhang, L.; Li, Y.; Yang, Y.; Yang, T.; Li, X.; Wang, K.; et al. High Detectivity Graphene-Silicon Heterojunction Photodetector. *Small* **2016**, *12*, 595–601. [CrossRef]
49. Zhang, L.; Huang, F.; Li, S.; He, S.; Yu, M.; Fu, J.; Yang, Q.; Huang, R.; Cheng, Q. Interface Engineering for Graphene Nanowalls/Silicon Schottky Solar Cells Prepared by Polymer-free Transfer Method. *J. Appl. Phys.* **2020**, *128*, 025301. [CrossRef]
50. Alnuaimi, A.; Almansouri, I.; Saadat, I.; Nayfeh, A. Interface Engineering of Graphene-Silicon Schottky Junction Solar Cells with an Al_2O_3 Interfacial Layer Grown by Atomic Layer Deposition. *RSC Adv.* **2018**, *8*, 10593–10597. [CrossRef]
51. Cong, J.; Khan, A.; Li, J.; Wang, Y.; Xu, M.; Yang, D.; Yu, X. Direct Growth of Graphene Nanowalls on Silicon Using Plasma-Enhanced Atomic Layer Deposition for High-Performance Si-Based Infrared Photodetectors. *ACS Appl. Electron. Mater.* **2021**, *3*, 5048–5058. [CrossRef]
52. Shen, J.; Liu, X.; Song, X.; Li, X.; Wang, J.; Zhou, Q.; Luo, S.; Feng, W.; Wei, X.; Lu, S.; et al. High-performance Schottky Heterojunction Photodetector with Directly Grown Graphene Nanowalls as Electrodes. *Nanoscale* **2017**, *9*, 6020–6025. [CrossRef] [PubMed]
53. An, X.; Liu, F.; Jung, Y.J.; Kar, S. Tunable Graphene–Silicon Heterojunctions for Ultrasensitive Photodetection. *Nano Lett.* **2013**, *13*, 909–916. [CrossRef] [PubMed]
54. Sun, M.; Fang, Q.; Xie, D.; Sun, Y.; Qian, L.; Xu, J.; Xiao, P.; Teng, C.; Li, W.; Ren, T.; et al. Heterostructured Graphene Quantum Dot/WSe_2/Si Photodetector with Suppressed Dark Current and Improved Detectivity. *Nano Res.* **2018**, *11*, 3233–3243. [CrossRef]
55. Liu, X.; Zhou, Q.; Luo, S.; Du, H.; Cao, Z.; Peng, X.; Feng, W.; Shen, J.; Wei, D. Infrared Photodetector Based on the Photothermionic Effect of Graphene-Nanowall/Silicon Heterojunction. *ACS Appl. Mater. Interfaces* **2019**, *11*, 17663–17669. [CrossRef]
56. Yang, J.; Tang, L.; Luo, W.; Feng, S.; Leng, C.; Shi, H.; Wei, X. Interface Engineering of a Silicon/Graphene Heterojunction Photodetector via a Diamond-Like Carbon Interlayer. *ACS Appl. Mater. Interfaces* **2021**, *13*, 4692–4702. [CrossRef]

nanomaterials

MDPI

Article

Single-Electron Transport and Detection of Graphene Quantum Dots

Xinxing Li [1,2,†], Jinggao Sui [3,†] and Jingyue Fang [1,*]

[1] School of Physics and Electronics, Central South University, Changsha 410083, China
[2] Key Laboratory of Nanodevices, Suzhou Institute of Nano-Tech and Nano-Bionics, CAS, Suzhou 215213, China
[3] National Innovation Institute of Defense Technology, Academy of Military Sciences PLA China, Beijing 100071, China
* Correspondence: jyfang@csu.edu.cn
† These authors contributed equally to this work.

Abstract: The integrated structure of graphene single-electron transistor and nanostrip electrometer was prepared using the semiconductor fabrication process. Through the electrical performance test of the large sample number, qualified devices were selected from low-yield samples, which exhibited an obvious Coulomb blockade effect. The results show that the device can deplete the electrons in the quantum dot structure at low temperatures, thus, accurately controlling the number of electrons captured by the quantum dot. At the same time, the nanostrip electrometer coupled with the quantum dot can be used to detect the quantum dot signal, that is, the change in the number of electrons in the quantum dot, because of its quantized conductivity characteristics.

Keywords: graphene; nanodevices; single-electron transistor; electrometer

1. Introduction

Due to its exceptional electronic properties, graphene displays various electron transport phenomena, such as the single-electron tunneling effect [1], the anomalous quantum Hall effect [2,3], and the electron coherence effect [4]. Among them, graphene single-electron transistors (GSETs) based on single-electron tunneling and the Coulomb blockade effect can realize quantum computing functions at the nanoscale or in single-charge ultra-high sensitivity electrical quantity detection. It has wide application prospects in ultra-sensitive electrometers [5,6], single-photon detectors [7–9], high-density information storage [10,11], and quantum information devices [12,13].

Plenty of jobs have been performed toward GSET fabrication and electronic measurement studies. Ponomarenko et al. prepared GSET by electron beam lithography, oxygen plasma etching, and other processes [14]. The narrow graphene region between the graphene quantum dots and the source or drain electrode forms a quantum tunnel barrier. At low temperatures, the conductance of GSET shows a periodic function of the gate voltage, which is caused by the Coulomb blockade effect. When the diameter of graphene quantum dots in the device is reduced to ~15 nm, the width of the quantum barrier is only ~1 nm. By tuning the source, drain, and gate voltages, a clear Coulomb diamond image can be obtained. Even at room temperature, the device still has good switching-off performance.

Ihn et al. carried out extensive and in-depth research on GSET [15]. They fabricated GSET with a multi-gate structure and studied the energy gap in graphene nanoribbons [16], the electron–hole inversion effect of graphene quantum dots in the case of a vertical magnetic field [17], and the spin state of graphene quantum dots. Under the action of a planar magnetic field, Zeeman splitting of the spin state occurred, with a g factor of 2 [18].

The conductance of quantum point contact (QPC) is quantized. In the transport between quantum conductance platforms, it is very sensitive to the electrostatic environment, including the number of electrons n on the nearby quantum dot. This characteristic makes it possible to determine the absolute number of electrons on the quantum dot even if the electron tunneling is so weak that the current passing through the quantum dot cannot be detected. Moreover, Kouwenhoven et al. took the lead in realizing charge-sensing measurements in quantum dots by using quantum point contact (QPC) in two-dimensional electronic gas (2DEG) quantum dot devices [19]. J. Güttinger et al. performed charge detection experiments on graphene quantum dots at a low temperature of 1.7 K [5], with a 45 nm wide graphene strip as a charge detector, which is 60 nm apart from the Coulomb island with a diameter of ~200 nm. L. Lv et al. [20] and G. P. Guo et al. [21–24] have also carried out a lot of research on GSET devices. They have successfully realized the coupling of graphene quantum dots quantum bits and superconducting microwave cavity quantum data bus, which takes an important step toward the realization of integrated quantum chips.

Inspired by previous work, we fabricate an integrated structure of GSET and nanostrip electrometer based on the chemical vapor deposition (CVD) growth of graphene using semiconductor fabrication techniques, such as electron beam exposure, ultraviolet lithography, oxygen plasma etching, and electron beam evaporation. Combined with low-temperature and low-noise phase-locked amplification measurement technology, the electrometer is able to detect the change in the number of charges in the coupled quantum dot, thus, achieving sensitivity detection of a few electrons or even a single charge. Using graphene grown by CVD to design and prepare devices, the sample survival rate is not high, so we prepare a large number of devices for testing in the laboratory, but we explore the future of the mass production of devices. Perhaps, this sensing and detection technology will play a role in the research of two-dimensional material quantum information.

2. Method

2.1. Device Preparation

Figure 1A shows a scanning electron microscope (SEM) image of a graphene quantum dot device chip. The pattern of device electrodes is shown in Figure 1B, which corresponds to the electrodes in the SEM image of the quantum dot and nanostrip electrometer structure shown in Figure 1C. The device was based on ~500 μm thick doped silicon with an oxide insulating layer of ~300 nm (Figure 1D). Graphene was grown on copper foil using the chemical vapor deposition (CVD) method before being transferred and patterned by electron beam lithography (EBL) and oxygen plasma etching. Metal graphene contact resistance is one of the main limiting factors of graphene technology development in electronic devices and sensors [25]. Ohmic contact electrodes such as source electrodes, drain electrodes, gate electrodes, and nanostrip electrometers were prepared using ultraviolet lithography and evaporation processes. We used Ti/Au with a thickness of 10/300 nm to form ohmic contact with graphene. The metal evaporation rate was 0.5/3 Å/s, the sample fixture rotation speed was 8 rpm, and the metal evaporation time was 20 min. During the evaporation process, the substrate temperature rose from 27 °C to 45 °C. The back gate was used to adjust the Fermi energy level of graphene to control the electron injection ability of the device.

Graphene nanostrip showed quantized conductance due to the quantum confinement effect. We used a graphene nanostrip near quantum dots as an electrometer (Figure 1C). Similar to QPC, it can realize the function of charge sensing. The tunnel barrier of the nanostrip is determined by its size, the gate voltages, and other auxiliary mechanisms.

For the preparation of CVD graphene quantum dot devices, the process flow can be divided into the following steps: making nested marks, etching graphene mesas, depositing ohmic contact electrodes, etching quantum dot structures, preliminary screening of devices, fragmentation, bonding, and packaging. Before adhering the chip to the socket for bonding, we used a diamond knife to cut the oxide layer of the silicon substrate, applied silver glue,

and cured it at 180 °C for 30 min to complete the fabrication of the back gate. Finally, in order to reduce the influence of the residual impurities on the surface of graphene, control the introduction of scattering sources, and improve the electrical performance of the device, we annealed graphene at 300 °C in a mixed atmosphere of hydrogen and argon (at flow rates of 400 and 200 sccm, respectively).

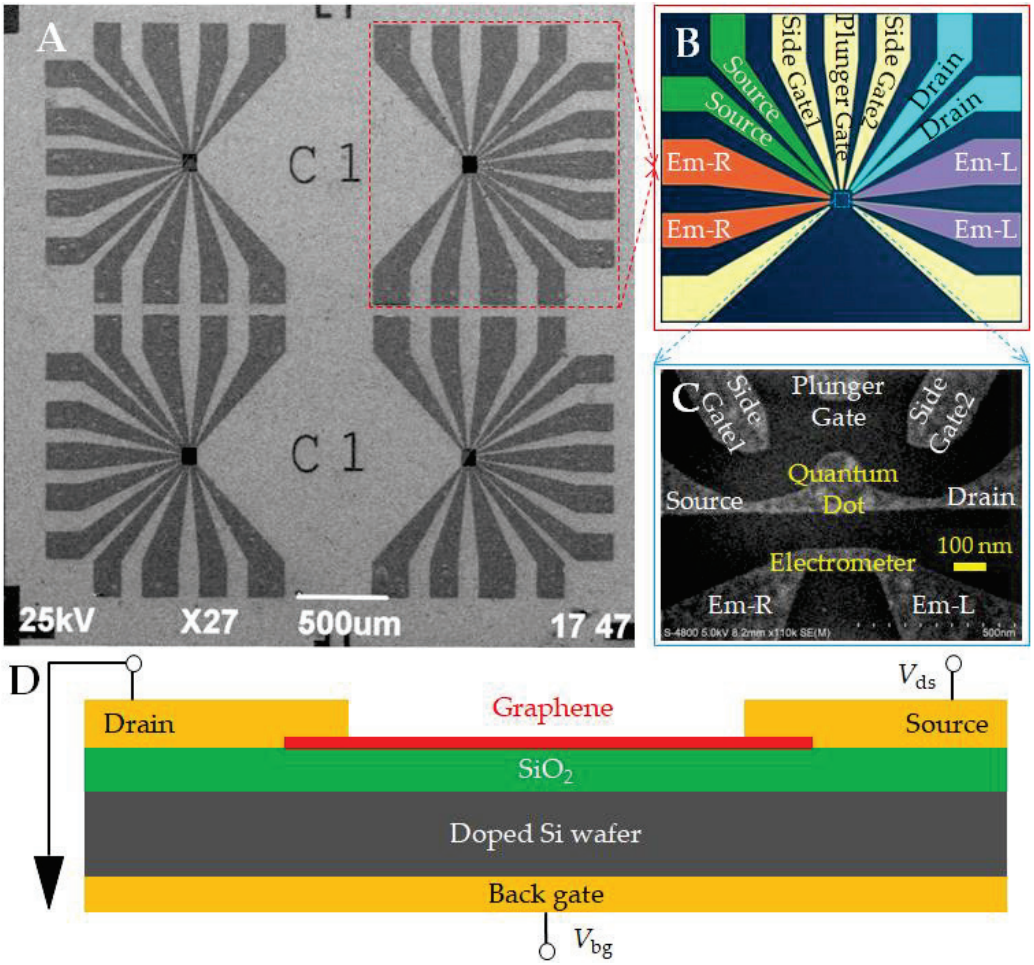

Figure 1. (**A**) SEM image of graphene quantum dot device chip; (**B**) electrode arrangement; (**C**) SEM image of quantum dot and nanostrip electrometer structure; and (**D**) device cross-section diagram. The source and drain are connected with the quantum dot via graphene nanoribbon.

2.2. Device Test

Before device chip packaging, a preliminary screening at room temperature should be carried out. Under the protection of photoresist, we used a probe table to measure the resistance of the source and drain channels and measure the continuity of the test system circuit and its corresponding relationship with the device pins. For devices with source–drain channel resistance greater than 26 kΩ and in the order of 100 kΩ, the devices marked as possibly qualified can enter the next step of bonding packaging and testing. Secondly, we conducted a leakage test of the device gate. With the source and drain grounded, the leakage current of the device's back gate and plunger gate electrodes was measured. Next, we tested the control ability of the device back gate. On the one hand, we set different back gate voltages to measure the source and drain current of the device by scanning the source and drain bias voltage. On the other hand, we set a certain source–drain bias voltage and measured the source–drain current of the device by scanning the back gate voltage to find the range of the Dirac point. Then, the control performance of the device plunger gate was tested. We set the back gate voltage in the Dirac point range, the source and drain

bias voltage to certain values, and scanned the plunger gate voltage to measure the source and drain current of the device. After this, we tested the source–drain I–V characteristics of the device. We ground the device gate, adjusted the source meter, and determined the source and drain voltage range within ±10 nA of the source and drain current; then, data acquisition software was used to repeatedly scan the source leakage voltage range and collect the source leakage current data. Using the same method, we measured the I–V characteristics of the nanostrip electrometer. Finally, the charge stability diagram of the device was tested. The differential conductance of source–drain was measured by scanning the back gate and source–drain bias voltage at the same time by setting the plunger gate voltage to a certain value; alternatively, the source–drain differential conductance was measured by scanning the plunger gate and source–drain bias voltage by setting the back gate voltage in the Dirac point range.

3. Results

As graphene grown by CVD is transferred from copper foil to a Si substrate, its adhesion is not strong, and graphene is very vulnerable to damage or fall off during the process, thus, affecting the survival rate of samples. After etching the worktops of the three samples, we made statistics on the intactness and damage of the graphene worktops. The survival rates of the worktops were 29%, 40%, and 53%. The yield of graphene used to prepare quantum dot single-electron devices is not high, and the damage to graphene by the process is one of the important reasons. Using paraffin instead of polymer for transfer can effectively reduce wrinkles and polymer residues and reduce defects and damage [26]. In addition, in the process, acetone immersion and ultrasonic cleaning may also cause pollution or damage to the surface of graphene, which needs to be improved.

The integrated device of graphene quantum dots and nanostrip prepared based on the semiconductor process was placed in the He^3 closed-cycle cryostat (Cryo Industries of America, Inc., Manchester, NH 03103, USA) shown in Figure 2A for testing. The chip was fixed on the socket with silver glue (Figure 2B), and the pins correspond to the individual device electrodes. The core structure of the device is a graphene quantum dot, nanostrip, and other structures obtained by semiconductor processes, such as oxygen plasma etching (Figure 2C). Figure 2D,E show SEM pictures of one single quantum dot device and one integrated device of quantum dot and nanostrip, respectively.

3.1. Source–Drain Channel Resistance and Back Gate Leakage Test

As shown in Figure 3A, the source–drain channel resistance of the device measured by the four-probe method at room temperature is about 37.5 kΩ, which is greater than the quantum resistance (~26 kΩ) and less than 1 MΩ, indicating that the tunnel barrier resistance of the device is in a reasonable range. In the device structure design, the ~500 μm thick Si sheet is the substrate, and there is a 300 nm oxide layer on the surface. The substrate silicon is the back gate, and the oxide layer is the back gate insulation layer. The back gate leakage characteristic curve at ~7.7 K is shown in Figure 3B. The insulation layer resistance of the back gate electrode is 6.0×10^9 Ω. This indicates that the back gate insulating layer of the device has good performance and no leakage occurs.

3.2. Test of Regulation Capability of Back Gate and Plunger Gate

The ability of gate regulation is very important for quantum dot single-electron devices. Coulomb blocking can be removed by changing the gate voltage. For graphene quantum dot devices, the back gate voltage can effectively adjust the Fermi level shift in the entire graphene nanostructure, while the plunger gate electrode can be used to locally adjust the chemical potential level in the quantum dot [27]. The performance of the device can be checked by testing the regulation ability of the gates.

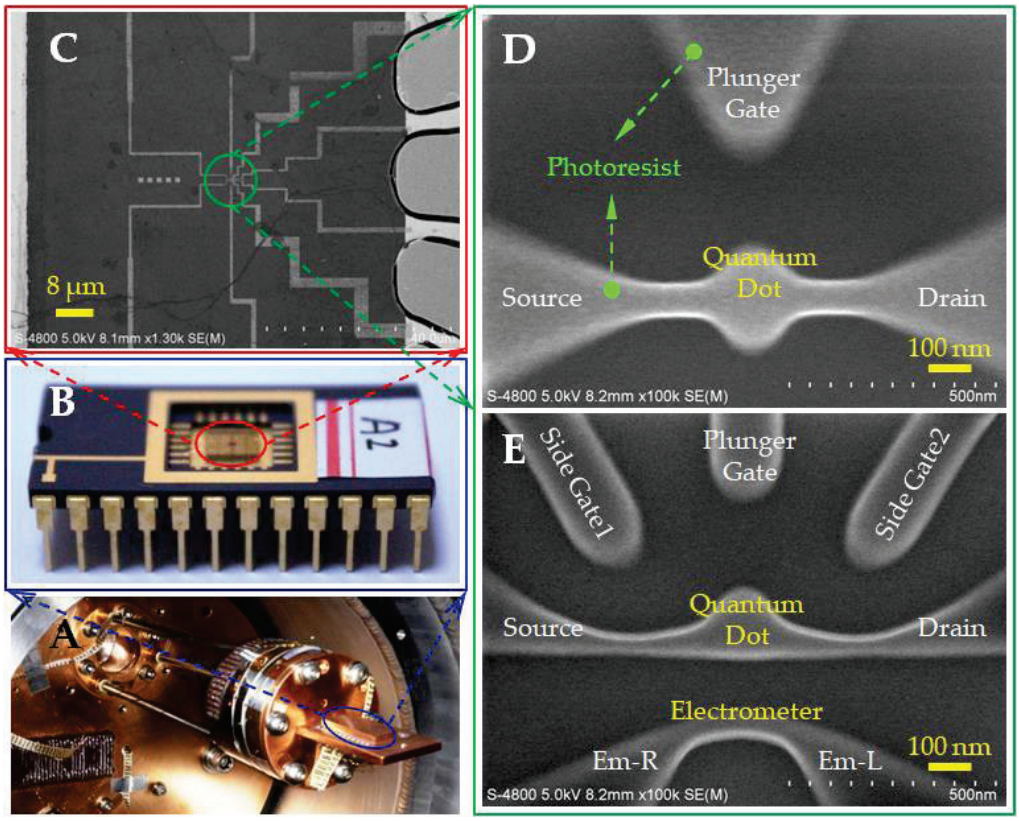

Figure 2. (**A**) He^3 closed-cycle cryostat cold head for device test; (**B**) the chip carrier matched with the cold head. After the chip is fixed on the tube base, each electrode of the device is led to the corresponding pin by means of gold wire ball welding; (**C**) SEM images of graphene functional areas in the device; (**D**,**E**) SEM image of photoresist mask on graphene mesa before etching quantum dot structure.

As shown in Figure 4A, the back gate is set with different voltages V_{bg}, the source–drain electrode is connected to the source meter, the source–drain bias voltage V_{ds} is scanned, and the source–drain current I_{ds} is measured at 250 K, as shown in Figure 4B. The results show that the slope of the source–drain I–V characteristic curve of the device changes significantly with the change in the back gate voltage V_{bg}, indicating that the back gate voltage effectively regulates the graphene energy level and changes the carrier concentration of the graphene channel. When V_{bg} is in the range of 0 V to 40 V, the equivalent resistance of the source–drain channel increases with the increase in voltage; however, as V_{bg} changes from 40 V to 60 V, the source–drain channel equivalent resistance decreases. This is the result of the back gate regulating the potential barrier of graphene nanoribbons and the discrete energy levels of graphene quantum dots. It shows that the back gate voltage changes the carrier concentration of the graphene channel, and the Dirac point is near 40 V.

Then, we set the source–drain bias voltage as the fixed value V_{ds} = 75 mV, the current preamplification factor as 10^{-9} A/V, and the rise time as 300 ms. Under a temperature of ~8K, the regulating curve of the device back gate to the source–drain current can be obtained, as shown in Figure 4C.

The results show that the back gate can fully adjust the Fermi surface of graphene in the device and change the carrier concentration involved in transport. We adjusted the transmission from the hole (left side) to the electronic state. The back gate voltage can inhibit transmission in the range of 19 mV < V_{bg} < 46 mV ($\Delta V_{bg} \approx$ 27 mV). In the region of the restraining current, there are a lot of sharp resonances because there is an effective energy gap in the bias direction within the transmission gap of the back gate

voltage. Outside the suppression area, the current peaks a~e, as shown in Figure 4C, are the Coulomb oscillation peaks obtained by back gate regulation.

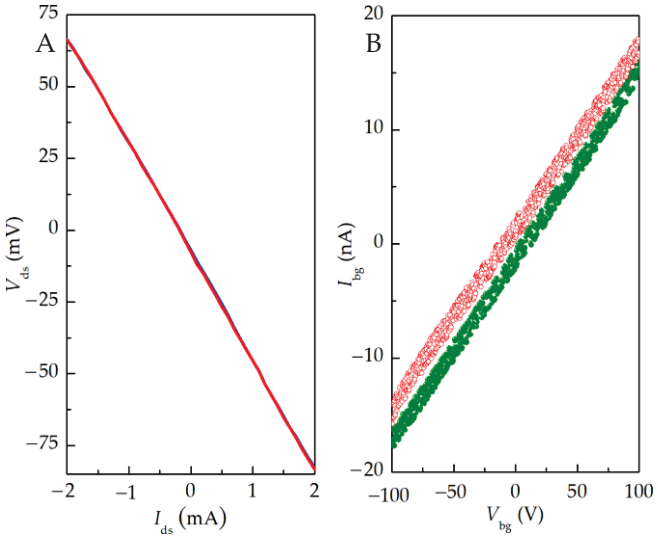

Figure 3. (**A**) I–V curve of device source–drain channel measured by four-probe method. The device source is connected to the source meter YOKOGAWA GS200 and a digital multimeter Agilent 34461A, and the back gate and drain are grounded. At room temperature, two points A–B on the outside of the source–drain channel are connected to a constant current source, and the voltage of two points a–b on the inside is measured. (**B**) Leakage characteristics of device back gate. The source–drain was grounded, the leakage current of the back gate electrode was measured with a Keithley 2410 at ~7.7 K. The red and green curves represent the leakage current obtained when the back gate voltage was scanned from −100 V to +100 V and +100 V to −100 V. The curves with different colors represent the data obtained by different scans, with good repeatability.

The edge configuration of graphene quantum dots and nanoribbons has a great influence on their properties. Uncontrolled factors, such as the size of graphene quantum structures and the location and concentration of surface defects (vacancies and impurities), will also affect the energy gap. Because graphene quantum dots and nanoribbon structures have different quantum confinement effects at different positions, as well as the local states caused by rough edges [16], the back gate electric field will have different effects on the discrete energy levels of quantum dots and the potential barriers of nanoribbon structures at the same time (Figure 4E). This edge-induced disordered potential energy will affect the transport of graphene nanoribbons. With the increase in the scanning range of the back gate voltage, the discrete energy levels of the quantum dots will be located in the source–drain bias window. At this time, the equivalent resistance of the source–drain channel decreases, the current increases, and Coulomb oscillation occurs.

In the range of −70 mV to 100 mV, we set the source–drain bias voltage V_{ds} to a series of determined values at equal intervals (10 mV), scanned the back gate voltage V_{bg}, and measured the current I_{ds} passing through the quantum dot, and we obtained the results shown in Figure 4D under a temperature of ~8 K. The I–V characteristic curve shows the rudiment of the Coulomb diamond.

As shown in Figure 5A, the source–drain bias voltage is set to $V_{ds} = -7.4$ mV, the back gate electrode is grounded, and the source–drain current I_{ds} is measured by scanning the plunger gate voltage V_{pg} at ~6.9 K to obtain the curve shown in Figure 5B. The repeated test results show that the device has obvious Coulomb oscillation characteristics under plunger gate control. The current peak indicates that there is an electrochemical potential level corresponding to the continuous ground state transport, which is located between the source and drain and generates a single-electron tunneling current. The wave trough indicates that the Coulomb blocking effect has occurred, and the number of electrons on

the quantum dot is stable. By adjusting the plunger gate voltage, the current can move from one trough to the next so that the number of electrons on the quantum dot can be accurately controlled.

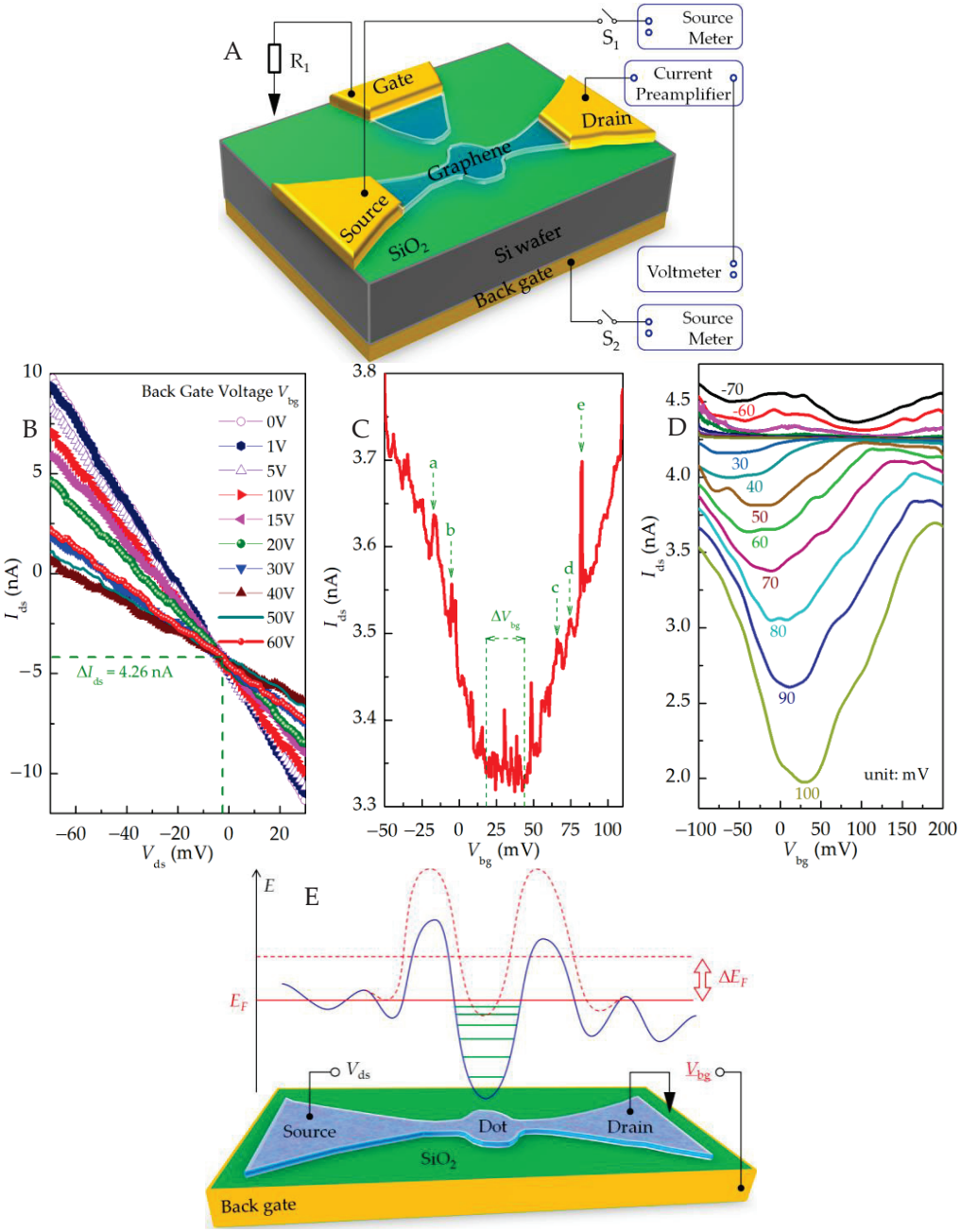

Figure 4. (**A**) Circuit diagram of back gate regulation test. The source–drain current I_{ds} is measured with a current preamplifier (DL Instrument 1211; amplification factor, 10^{-5} A/V; rise time, 300 ms) and a digital multimeter. (**B**) Source–drain I–V characteristic curves under different back gate voltages intersect at $V_{ds} \approx -2$ mV, and the source–drain current has a bias current of ~4.26 nA, which is introduced by the preamplifier test circuit. Back gate regulation characteristics under (**C**) a certain source–drain bias and (**D**) different source–drain bias voltages. (**E**) Diagram of potential energy along the graphene source–drain channel. The blue solid line represents the potential energy curve of graphene source and drain channel. The movement and change of different positions under the control of the back grid are different, and may finally have the shape of red dotted line.

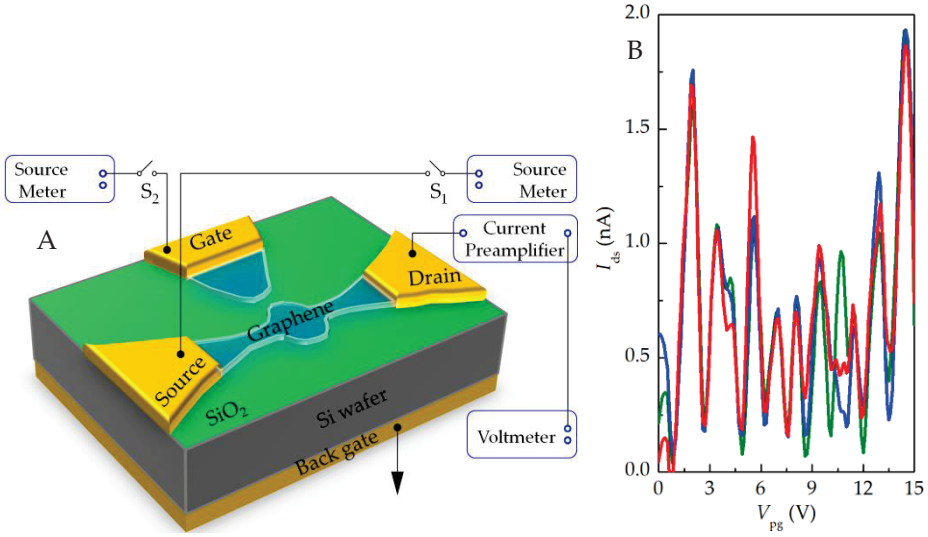

Figure 5. (**A**) Circuit diagram of plunger gate regulation test; (**B**) plunger gate regulation curve under certain source–drain bias voltage. The different color curves of red, green and blue represent the test curves obtained by different scanning, and the data repeatability is good.

3.3. Source–Drain I–V Characteristic Test

Coulomb repulsion between electrons on a quantum dot causes an external electron to consume energy when entering the quantum dot. This phenomenon is called the Coulomb blockade effect. When the external magnetic field is zero, for a quantum dot system containing a certain number of electrons in an equilibrium state, the electron transmission can only occur when the electron level in the quantum dot corresponding to the transport is in the source–drain bias window. If this condition is not satisfied, the number of electrons on the quantum dot will be fixed. Coulomb blockade can be removed by changing the source–drain voltage.

The electrical circuit of the device measurement is shown in Figure 6A. The resistance $R_1 = R_2 = 1$ MΩ on the source–drain channel plays the role of current-limiting protection and voltage division. The resistance $R_3 = 1$ kΩ, R_2, and R_3 form a voltage divider to improve the voltage resolution and achieve the effect of improving the test signal-to-noise ratio. Assuming that the source–drain channel resistance R_0~10^5 Ω ($R_0 >> R_3$), then $V_a = R_3 V_{ds}/(R_2 + R_3)$. Since $R_2 >> R_3$, the voltage of the input device can be obtained as $V_a \approx V_{ds}/R_2 = V_{ds}/1000$, thus, realizing the 1000-time subdivision of the DC bias voltage.

The back gate and plunger gate are grounded. By scanning the source–drain voltage V_{ds} and simultaneously measuring the current passing through the quantum dot I_{ds}, the curve shown in Figure 6B can be obtained. The results show that the device shows an obvious Coulomb blocking effect at a low temperature of ~8.4 K. It can be obtained that the voltage width of the blocking area near $V_{ds} = 0$ V is about 103 mV. It is believed that the charging energy E_C of the device Coulomb island is 103 meV, which is far greater than the thermal energy at 8.4 K (≈0.72 meV). The total capacitance of the Coulomb island is $e^2/E_C \approx 1.55$ aF.

The constant current part of the current step shows that the Coulomb blockade effect occurs and the number of electrons on the quantum dot is stable. However, the quantum dot has an electrochemical potential level corresponding to the continuous ground state transport, which is located between the source and drain and can continuously generate a single-electron tunneling current. The rising section of the current step shows that by adjusting the source–drain voltage, the number of electrochemical potential energy levels of the quantum dot at the source–drain bias window changes, the number of electrons on the quantum dot changes, and the current moves from one step to the next. Based on this, the number of electrons on the quantum dot can be precisely controlled.

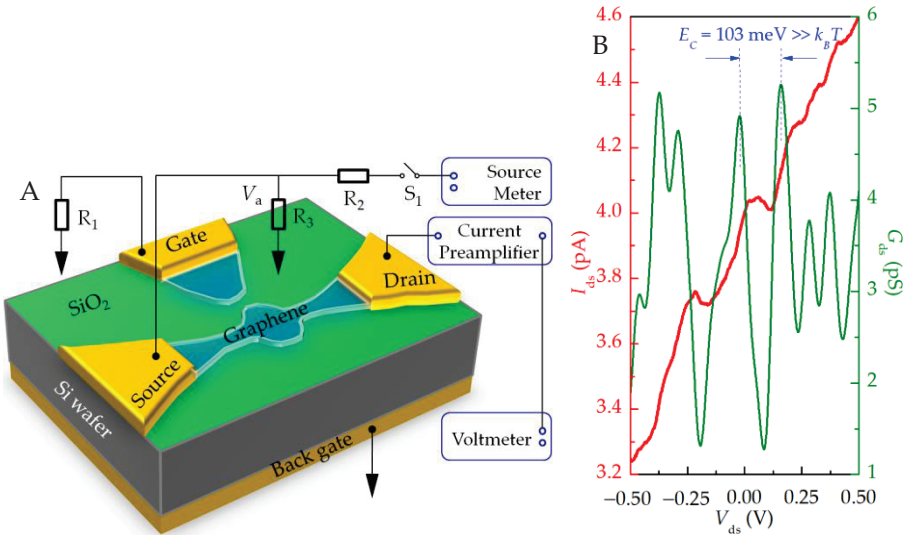

Figure 6. (**A**) Electrical connection of device test. In the measurement, the current preamplification factor is 10^{-9} A/V, and the rise time is 300 ms; (**B**) I–V characteristic test curve of source–drain. The red curve corresponds to the left ordinate, indicating the source leakage current; The green curve corresponds to the ordinate on the right, indicating the differential conductance.

3.4. Charge Stability Diagram Test

The finite size of quantum dots in three dimensions will affect the electronic dynamics, resulting in quantum effects, thus, forming the discrete energy spectrum of quantum dots. Therefore, Coulomb blocking, Coulomb oscillation, and Coulomb prisms can be measured and single-electron states can be prepared in quantum dot single-electron devices. When the gate voltage and the source–drain voltage are changed at the same time, the Coulomb step effect and the Coulomb oscillation effect work together; thus, we can observe the Coulomb diamond of the conductance of the quantum dot device. The diamond area indicates that the conductance is zero, and the charge cannot tunnel through the dot. Each diamond corresponds to a stable charge configuration of several occupied electrons on the quantum dot. The difference in the number of charges on the quantum dots represented by adjacent diamonds is one.

Using the standard electrical transport measurement method of quantum dot single-electron device shown in Figure 7A, the results shown in Figure 7B can be obtained. The device was placed in a vacuum cryogenic dewar, and the electrical test was carried out only after the system temperature dropped to 2.7 K. The device gate was connected to the DC voltage source meter through a 1 MΩ protection resistor, and the scanning range was 10 V to 20 V; the AC voltage reference signal (0.265 V rms at 177 Hz) given by the lock-in amplifier (Stanford Research Systems, Inc., SR830, Sunnyvale, California 94089, USA) and DC voltage (−28 mV ↔ +28 mV) given by the source meter was added to the source end of the device, and the current flows out of the drain and enters the current preamplifier (amplification factor, 10^{-8} A/V; rise time, 0.01 ms), which is converted into a voltage signal and enters the phase-locked amplifier for correlation operation (time constant, 500 ms) and, finally, is read by a digital multimeter.

In the circuit shown in Figure 7A, the capacitance C = 1 μF acts as a DC isolation. According to the Kirchhoff current conservation law, the node voltage V_b meets

$$V_b = \frac{R_5 \left|\right| \left(\frac{1}{jwC} + R_3 \left|\right| R_{dev}\right)}{R_4 + R_5 \left|\right| \left(\frac{1}{jwC} + R_3 \left|\right| R_{dev}\right)} V_{out} \quad (1)$$

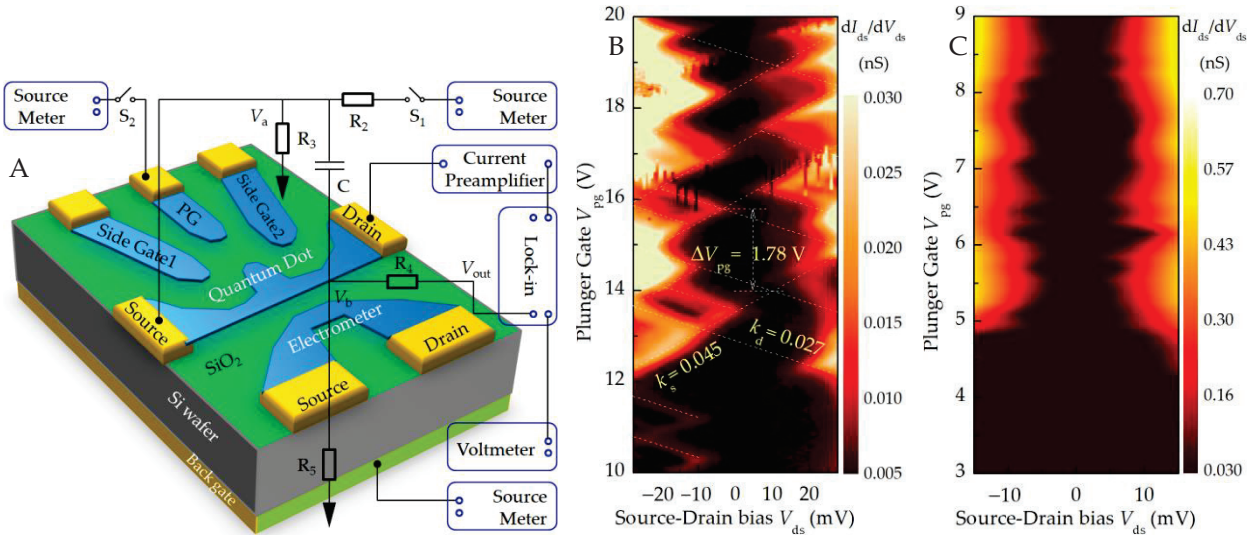

Figure 7. (**A**) AC phase-locked differential conductance current amplification test circuit. Differential conductance diagram of (**B**) the single-electron transistor and (**C**) nanostrip integrated with quantum dots measured at 2.7 K liquid helium temperature.

The resistance R_5 = 1 Ω, the AC signal amplitude of the phase-locked amplifier is 1 V, and the frequency is 137 Hz. Since R_2, R_4, 1/(jwC) >> R_3, R_5, Equation (1) can be simplified as:

$$V_b \approx \frac{R_5||(1/jwC + R_3)}{R_4 + R_5||(1/jwC + R_3)} V_{out} \approx \frac{R_5}{R_4 + R_5} V_{out} \approx \frac{R_5}{R_4} V_{out} \quad (2)$$

Thus, the voltage divider composed of R_4 and R_5 realizes the purpose of obtaining a small signal from the reference signal of the lock-in amplifier and inputting it to the device.

Further analysis shows that the current at node V_a meets the following formula:

$$\frac{V_{ds} - V_a}{R_2} + jwC(V_b - V_a) = \frac{V_a}{R_3} + \frac{V_a}{R_{dev}} \approx \frac{V_a}{R_3} \quad (3)$$

Calculated as $V_a \approx (V_{ds}$ + j1.37 × 10^{-4} $V_{out})/(1001$ + j0.137), which realizes the addition and subdivision of the DC bias voltage and the AC signal.

It can be seen from Figure 7B that the plunger gate voltage variation in the adjacent rhombus is $\Delta V_{pg} \approx 1.78$ V; thus, the gate capacitance is $C_{pg} \approx 0.09$ aF. The slope of the two edges of the Coulomb diamond is $k_d = -C_{pg}/C_d = -0.027$ and $k_s = C_{pg}/(C_{pg} + C_s) = 0.045$, so C_d = 3.33 aF and C_s = 1.91 aF. As $C_s \neq C_d$ is asymmetric, it shows that the source and drain tunneling resistances are different, and their junction capacitances are different, so the Coulomb diamond is inclined.

When the source–drain voltage is large enough, more energy levels in the quantum dot will participate in electron tunneling, and more excited state energy levels will be located in the bias window, which will lead to the transition from single-electron tunneling to multi-electron tunneling. In Figure 7B, we can observe the excited state energy spectrum of the single-electron transistor. The absence of charge transfer on the left side of Figure 7B shows that the electrons in the quantum dot structure are completely depleted, that is, the number of free transfer charges on the quantum dot is zero. With this area as a reference, the absolute number of electrons in the area of interest can be known. If the gate voltage and source–drain bias voltage are changed, the number of electrons on the quantum dot will change, and the conductance can go from one diamond to the next. The gate voltage changes by $\Delta V_{pg} = |e|/C_{pg}$, so the number of electrons on the quantum dot can be precisely controlled.

Figure 7C shows that the nanostrip exhibits Coulomb-blocking transmission characteristics because the fluctuation in the strip edge causes the change in tunneling ability, making the nanostrip behave like quantum dots in series.

The integrated structures of the quantum dot and nanostrip are jointly tested at 310 mK. The results shown in Figure 8 indicate that the device has a sensitive charge detection capability. The single-electron transport in the quantum dot will certainly cause a change in the number of charges in the quantum dot. The electrometer is very sensitive to the electrostatic potential in its neighborhood and can measure the change in the electrostatic potential caused by the change in the number of single charges in the quantum dot. This is because the nanostrip electrometer has quantized conductivity due to the quantum confinement effect, and its function is similar to that of quantum point contact. The transport between adjacent conductive steps is extremely sensitive to the electrostatic environment of its neighborhood, thus, realizing the single-charge ultra-high sensitivity electricity detection.

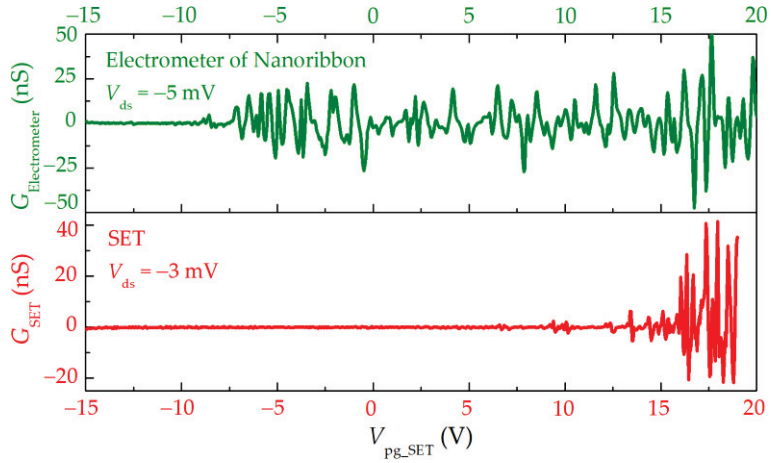

Figure 8. Comparison diagram of conductance curve of quantum-dot–nanostrip-integrated device.

In these measurements, the back gate voltage is set to 5.0 V, where the quantum dot is nearly electrically neutral and within the transmission gap of the electrometer. We manipulate the electrometer under the condition that strong resonant interaction can be obtained between electrons and energy levels in the nanostrip so as to use the steep slope of conductance regulated by the gate to detect a single-charge event of the quantum dot. At this time, the detection sensitivity is the highest.

Because the low-energy particles in graphene are Dirac fermions, which have the Klein tunneling effect, graphene is usually patterned to nanoribbon to form a potential barrier that constrains electrons in order to obtain quantum dot structures. The nanoribbon should not be too wide; otherwise, the resistance is small and cannot act as a potential barrier; the nanoribbon should not be too narrow; otherwise, the resistance is small and the barrier has no tunneling function. At the same time, the strip length should not be too long; otherwise, an effect similar to that of multiple quantum dots in a series may be formed due to irregular edges.

The integration of the graphene quantum dot structure and the nanostrip electrometer can be realized by using EBL and oxygen plasma etching technology. By reasonably designing the length and width of graphene nanoribbons connecting graphene quantum dots with source and drain electronic libraries, the tunnel barrier between the quantum dots and source and drain electrodes can be controlled to ensure that the conduction impedance between source and drain is in the range of 50~500 kΩ at room temperature. The single-electron transport properties of the quantum-dot- and nanostrip-integrated structure and the gate-controlled conductivity of the electrometer were measured, and the sensitivity of the nanostrip electrometer to the electrostatic environment was verified.

4. Conclusions

In summary, we used electron beam exposure and reactive ion etching (oxygen flow, 50 SCCM; RF power, 500 W; pre-stage power, 200 W; air pressure, 100 mTorr; and etching time, 20 s) and other techniques to pattern CVD graphene, obtained graphene quantum dots with a diameter of ~100 nm, and connected to the source and drain electrodes through a narrow nanoribbon with a width of ~40 nm to prepare back gate graphene quantum dot devices. We used plasma cleaning, high-temperature annealing, and other measures to effectively reduce the interaction between graphene and the substrate, remove the residue on the surface of graphene, and control the introduction of impurity scattering sources to ensure the performance of the device.

The electrical properties of graphene quantum dot devices were tested, and the precise control of the number of electrons captured by the quantum dots was realized. In the charge stability diagram, the absence of charge transfer indicates that the electrons in the quantum dot structure are completely depleted. It can be seen that by adjusting the gate voltage and the source–drain bias voltage, the number of electrons on the quantum dot can be accurately controlled, and the preparation of single-electron states in the quantum dot can be realized. The electron transport can change the number of charges in the quantum dot and affect the electrostatic potential of the electrometer. The conductivity-quantized nano-strip electrometer is very sensitive to the electrostatic environment in the neighborhood and realizes sensitive charge detection.

The limit of traditional current measurement is ~10 fA, and the lower limit of the corresponding tunneling probability is ~100 kHz. To measure the quantum dot signal with the tunneling probability of the electronic library of less than 100 kHz, using the electrometer- and quantum-dot-integrated structure is an optional method. The electrometer is integrated near the quantum dot as a charge detection mechanism, which can detect the number of electrons in the quantum dot without affecting the electron transport in the quantum dot and has high measurement sensitivity. It is expected that this technology will play an important role in the research of quantum information.

Author Contributions: Conceptualization and methodology, J.F.; device preparation and data test, X.L. and J.F.; theoretical analysis, J.S. All authors have read and agreed to the published version of the manuscript.

Funding: This work was supported by the Natural Science Foundation of Hunan Province (Grant 2022JJ30717).

Data Availability Statement: All data, models, and code generated or used during the study appear in the submitted article. They are available from the author by request (J.Y. Fang).

Conflicts of Interest: The authors declare no conflict of interest.

References

1. Efimkin, D.K.; Burg, G.W.; Tutuc, E.; MacDonald, A.H. Tunneling and fluctuating electron-hole Cooper pairs in double bilayer graphene. *Phys. Rev. B* **2015**, *101*, 035413. [CrossRef]
2. Wang, L.; Guo, L.; Zhang, Q. A light-controllable topological transistor based on quantum tunneling of anomalous topological edge states. *Appl. Phys. Express* **2022**, *15*, 115003. [CrossRef]
3. McIver, J.; Schulte, B.; Stein, F.-U.; Matsuyama, T.; Jotzu, G.; Meier, G.; Cavalleri, A. Light-induced anomalous Hall effect in graphene. *Nat. Phys.* **2020**, *16*, 38–41. [CrossRef]
4. De Laissardière, G.T.; Mayou, D. Conductivity of Graphene with Resonant and Nonresonant Adsorbates. *Phys. Rev. Lett.* **2013**, *111*, 146601. [CrossRef]
5. Güttinger, J.; Stampfer, C.; Hellmüller, S.; Molitor, F.; Ihn, T.; Ensslin, K. Charge detection in graphene quantum dots. *Appl. Phys. Lett.* **2008**, *93*, 212102. [CrossRef]
6. Kurzmann, A.; Overweg, H.; Eich, M.; Pally, A.; Rickhaus, P.; Pisoni, R.; Lee, Y.; Watanabe, K.; Taniguchi, T.; Ihn, T.; et al. Charge Detection in Gate-Defined Bilayer Graphene Quantum Dots. *Nano Lett.* **2019**, *19*, 5216–5221. [CrossRef]
7. Yeh, P.-C.; Ohkatsu, G.; Toyama, R.; Tue, P.T.; Ostrikov, K.; Majima, Y.; Chiang, W.-H. Towards single electron transistor-based photon detection with microplasma-enabled graphene quantum dots. *Nanotechnology* **2021**, *32*, 1. [CrossRef]
8. Seifert, P.; Lu, X.; Stepanov, P.; Retamal, J.R.D.; Moore, J.N.; Fong, K.-C.; Principi, A.; Efetov, D.K. Magic-Angle Bilayer Graphene Nanocalorimeters: Toward Broadband, Energy-Resolving Single Photon Detection. *Nano Lett.* **2020**, *20*, 3459–3464. [CrossRef]

9. Walsh, E.D.; Efetov, D.K.; Lee, G.-H.; Heuck, M.; Crossno, J.; Ohki, T.A.; Kim, P.; Englund, D.; Fong, K.C. Graphene-Based Josephson-Junction Single-Photon Detector. *Phys. Rev. Appl.* **2017**, *8*, 024022. [CrossRef]
10. Chen, Y.; Zhang, L.; Liu, J.; Lin, X.; Xu, W.; Yue, Y.; Shen, Q.-D. Ferroelectric domain dynamics and stability in graphene oxide-P(VDF-TrFE) multilayer films for ultra-high-density memory application. *Carbon* **2019**, *144*, 15–23. [CrossRef]
11. Chen, S.; Mahmoodi, M.R.; Shi, Y.; Mahata, C.; Yuan, B.; Liang, X.; Wen, C.; Hui, F.; Akinwande, D.; Strukov, D.B.; et al. Wafer-scale integration of two-dimensional materials in high-density memristive crossbar arrays for artificial neural networks. *Nat. Electron.* **2020**, *3*, 638–645. [CrossRef]
12. Bockrath, M. Unprecedented Charge State Control in Graphene Quantum Dots. *Nano Lett.* **2020**, *20*, 2937–2938. [CrossRef]
13. Foulger, I.; Gnutzmann, S.; Tanner, G. Quantum walks and quantum search on graphene lattices. *Phys. Rev. A* **2015**, *91*, 062323. [CrossRef]
14. Ponomarenko, L.A.; Schedin, F.; Katsnelson, M.I.; Yang, R.; Hill, E.W.; Novoselov, K.S.; Geim, A.K. Chaotic Dirac billiard in graphene quantum dots. *Science* **2008**, *320*, 356. [CrossRef]
15. Ihn, T.; Güttinger, J.; Molitor, F.; Schnez, S.; Schurtenberger, E.; Jacobsen, A.; Hellmüller, S.; Frey, T.; Dröscher, S.; Stampfer, C.; et al. Graphene single—Electron transistors. *Mater. Today* **2010**, *13*, 44. [CrossRef]
16. Stampfer, C.; Güttinger, J.; Hellmüller, S.; Molitor, F.; Ensslin, K.; Ihn, T. Energy gaps in etched graphene nanoribbons. *Phys. Rev. Lett.* **2009**, *102*, 056403. [CrossRef]
17. Güettinger, J.; Stampfer, C.; Libisch, F.; Frey, T.; Burgdoerfer, J.; Ihn, T.; Ensslin, K. Electron-hole crossover in graphene quantum dots. *Phys. Rev. Lett.* **2009**, *103*, 046810. [CrossRef]
18. Güettinger, J.; Frey, T.; Stampfer, C.; Ihn, T.; Ensslin, K. Spin states in graphene quantum dots. *Phys. Rev. Lett.* **2010**, *105*, 116801. [CrossRef]
19. Elzerman, J.M.; Hanson, R.; Greidanus, J.S.; Van Beveren, L.H.W.; De Franceschi, S.; Vandersypen, L.M.K.; Tarucha, S.; Kouwenhoven, L.P. Few-electron quantum dot circuit with integrated charge read out. *Phys. Rev. B* **2003**, *67*, 161308–161311. [CrossRef]
20. Tan, Z.B.; Liu, G.T.; Lu, L.; Yang, C.L. Observation of Coulomb blockade and ballistic tunneling in graphene single electron transistor. *Sci. China Phys. Mech. Astron.* **2012**, *55*, 7. [CrossRef]
21. Guo, G.P.; Lin, Z.R.; Tu, T.; Cao, G.; Li, X.P.; Guo, G.C. Quantum computation with graphene nanoribbon. *New J. Phys.* **2009**, *11*, 123005–123012. [CrossRef]
22. Deng, G.W.; Wei, D.; Li, S.X.; Johansson, J.R.; Kong, W.C.; Li, H.O.; Cao, G.; Xiao, M.; Guo, G.C.; Nori, F.; et al. Coupling Two Distant Double Quantum Dots with a Microwave Resonator. *Nano Lett.* **2015**, *15*, 6620–6625. [CrossRef] [PubMed]
23. Deng, G.-W.; Wei, D.; Johansson, J.R.; Zhang, M.-L.; Li, S.-X.; Li, H.-O.; Cao, G.; Xiao, M.; Tu, T.; Guo, G.-C.; et al. Charge Number Dependence of the Dephasing Rates of a Graphene Double Quantum Dot in a Circuit QED Architecture. *Phys. Rev. Lett.* **2015**, *115*, 126804. [CrossRef] [PubMed]
24. Jing, F.M.; Zhang, Z.Z.; Qin, G.Q.; Luo, G.; Cao, G.; Li, H.O.; Song, X.X.; Guo, G.P. Gate-Controlled Quantum Dots Based on 2D Materials. *Adv. Quantum Technol.* **2022**, *5*, 2100162. [CrossRef]
25. Urban, F.; Lupina, G.; Grillo, A.; Martucciello, N.; Di Bartolomeo, A. Contact resistance and mobility in back-gate graphene transistors. *Nano Express* **2020**, *1*, 010001. [CrossRef]
26. Leong, W.S.; Wang, H.; Yeo, J.; Martin-Martinez, F.J.; Zubair, A.; Shen, P.-C.; Mao, Y.; Palacios, T.; Buehler, M.J.; Hong, J.-Y.; et al. Paraffin-enabled graphene transfer. *Nat. Commun.* **2019**, *10*, 867. [CrossRef]
27. Di Bartolomeo, A.; Giubileo, F.; Iemmo, L.; Romeo, F.; Russo, S.; Unal, S.; Passacantando, M.; Grossi, V.; Cucolo, A.M. Leakage and field emission in side-gate graphene field effect transistors. *Appl. Phys. Lett.* **2016**, *109*, 023510. [CrossRef]

nanomaterials

MDPI

Article

Highly Stretchable Graphene Scrolls Transistors for Self-Powered Tribotronic Non-Mechanosensation Application

Yanfang Meng [1,2,3]

[1] State Key Laboratory of Advanced Optical Communications System and Networks, School of Electronics Engineering and Computer Science, Peking University, Beijing 100871, China; yanaimengmeng@126.com
[2] Beijing Institute of Nanoenergy and Nanosystems, Chinese Academy of Sciences, Beijing 100083, China
[3] University of Chinese Academy of Sciences, Beijing 100049, China

Abstract: Owing to highly desired requirements in advanced disease diagnosis, therapy, and health monitoring, noncontact mechanosensation active matrix has drawn considerable attention. To satisfy the practical demands of high energy efficiency, in this report, combining the advantage of multiparameter monitoring, high sensitivity, and high resolution of active matrix field-effect transistor (FET) with triboelectric nanogenerators (TENG), we successfully developed the tribotronic mechanosensation active matrix based on tribotronic ion gel graphene scrolls field-effect transistors (GSFET). The tribopotential produced by TENG served as a gate voltage to modulate carrier transport along the semiconductor channel and realized self-powered ability with considerable decreased energy consumption. To achieve high spatial utilization and more pronounced responsivity of the dielectric of this transistor, ion gel was used to act as a triboelectric layer to conduct friction and contact electrification with external materials directly to produce triboelectric charges to power GFET. This tribopotential-driving device has excellent tactile sensing properties with high sensitivity (1.125 mm^{-1}), rapid response time (~16 ms), and a durability operation of thousands of cycles. Furthermore, the device was transparent and flexible with the capability of spatially mapping touch stimuli and monitoring real-time temperature. Due to all these unique characteristics, this novel noncontact mechanosensation GSFET active matrix provided a new method for self-powered E-skin with promising potential for self-powered wearable devices and intelligent robots.

Keywords: tribotronic; mechanosensation; ion gel; graphene scrolls

1. Introduction

The great progress of flexible electronic skins (E-skins), epidermal electronics, and mechanosensation active matrix, with the aim of miming perceptive functions of human skin, has inspired great research interests for potential applications in robotics, prostheses, and wearable healthcare monitoring devices [1]. The above devices function through converting the external stimuli into quantified physical signals and further provide feedback instructions [2–7]. Mechanosensation matrix array are employed for imitating the human somatosensory system to perceive diversifying mechanical stimuli [8–11]. Scientists and researchers dedicated their great efforts in materials design and structures optimization [12–14] toward a mechanosensation active matrix array to realize high sensitivity, fast response time, mechanical flexibility, and durability multimodal sensing for practical noninvasive applications requiring long-term durability, multimodal sensing, and highly integrated, simplified fabrication processes and minimized the power consumption [15–18].

As a powerful means to monitor the physiological status of the human body, electronic skins (E-skins) based on the field-effect transistor (FET) active matrix array are capable of mimicking the functions of human skin, monitoring activity and sensing and adjusting, and demonstrating their large development horizon and research value by transducing external stimuli to electronic signals. To realize demands of wearing conformally on human skin,

transparent stretchable electronic devices have inspired extensive research interests. Three main available strategies to achieve stretchability for electronic device are (1) fabricating the device matrix with stretchable interconnectors [19–23]; (2) designing buckled- [24], spring- [25], or mesh- [26,27] shaped device configurations; and (3) developing intrinsically stretchable devices [28]. The third strategy prevails over the other two for stability and compatibility. For developing intrinsically stretchable devices, conventional intrinsically stretchable semiconductors, in general, are organic semiconductors, which may bring about detriments of a toxic, thorny procedure. As a promising alternative, a transparent stretchable electronic star material, graphene, exhibits highly desirable properties of atomic thickness, high transparency, and high conductivity [29–31]. However, its application in highly stretchable applications has been limited by its susceptibility to cracking at small strains [32]. For example, Seoung-Ki Lee et al. reported a stretchable, printable, and transparent transistor based on monolithically patterned graphene films but showed only 7% stretchability. Therefore, overcoming the above limitations of graphene is of great significance for new functional stretchable transparent devices. Fortunately, Bao et al. have designed highly stretchable graphene devices by intercalating graphene scrolls (the CVD graphene sheets with PMMA/front-graphene/Cu/back-graphene structure directly immersed into the Cu film etching liquid to dissolve Cu without traditional corrosion of back graphene prior to dissolving Cu). Then, the back graphene is transformed into a scroll-shaped configuration (~1 to 20 mm long, ~0.1 to 1 mm wide, and ~10 to 100 nm high) [33], with stretchability up to 120% strain (parallel to the direction of charge transport) and the ability to retain 60% of its original current output. However, in Bao et al.'s previous work, the referred graphene scrolls were limited to being employed as electrodes, as a semiconductor channel has not been reported yet. It can be anticipated that adopting graphene scrolls as the channel material of FET for E-skin not only to take advantage of their considerable evaluated stretchability but also their other special characteristic for monitoring humans' physical parameters. We, for the first time, demonstrated that graphene scrolls possessed higher responsiveness toward temperature variations, which unprecedentedly broadened the sensing application of the graphene-based electronic devices and removed the need for external active material for temperature monitoring with a stretchable, transparent, and nontoxic center on the device.

Given graphene scrolls as the channel of FET and active element for E-skin, self-powering has also been emphasized to address issues of mobility restriction and undesired high energy consumption. That is, harvesting mechanical energy from the human's body to drive personalized electronics for tactile sensing functions. Fortunately, the triboelectric nanogenerator (TENG), coupling triboelectrifriction and electrostatic induction, has been demonstrated to be a powerful means to convert mechanical energy into electricity. The high voltage output of triboelectric nanogenerators (TENG) facilitates its converting mechanical energy into electrical energy with high productivity [34–38], as well as its combining with sensors to monitor velocity, temperature, humidity, and the other physical parameters by means of converting movement into electrical signals [39–41]. The TENG can also being integrated into FET Matrix as tribotronics FET to further merge the merits of FET: multiparameter monitoring, high sensitivity, and high resolution [42–45]. With respect to the tribotronics-based active matrixes, tribopotential replaces of the gate voltage source to modulate the carrier concentration along the conductive channel, allowing a direct control drain–source current by means of the external mechanical stimulus [46–48]. The tribotronics shows great prospects for applications as personal healthcare [49] and human–machine interaction [50]. In our previous work, we presented a self-powered noncontact mechanosensation active matrix based on an ion gel double-layer gate dielectric GFET powered by triboelectric potential form ion gel and external friction layers [51] for detecting spatial contact distances and visualizing a 2D map.

In this manuscript, we first report a highly stretchable graphene scrolls field-effect transistor (GSFET) for self-powered tribotronic distance–temperature dual-modes mechanosensation application. In this mechanosensation active matrix, tribopotential stemming from

the dielectric layer of ion gel and other friction material acted as the gate voltage. This transparent tribopotential-driven device has extremely stretchable properties (up to 120% strain (parallel to the direction of charge transport) and kept 35% of its original current output) compared to inherent graphene and layer-stacking style graphene sheets; excellent temperature sensitivity (precision as low as 1) and tactile sensing properties including high sensitivity (1.125 mm^{-1}); fast response time (~16 ms); and excellent durability (over 1000 cycles test). Combining all these merits, this graphene scrolls mechanosensation active matrix achieved spatial distance and temperature dual-mapping and achieved real-time monitoring. These outstanding performances of graphene scrolls mechanosensation active arrays not only hold great potential for noncontact sensation but also will open an avenue for advanced flexible electronics both the fundamental research and practical applications.

2. Experiment

Graphene Growth on a Cu Foil by CVD

According to previous procedures [52], monolayer graphene films of high quality were prepared on a Cu foil (thickness 25 μm, 99.8%) via CVD: first, a Cu foil (25 μm) was cleaned by a mixed solution containing 98 wt% H_2SO_4 and 30 wt%H_2O_2 for 15 min. Then, Cu foil was immersed into DI water and dried under a nitrogen flow. The Cu foil was inserted into a quartz tube prior to pumping air in the chamber. Upon the pressure in the quartz tube reaching 5×10^{-3} Torr, the Cu foil was annealed by flowing H_2 (10 sccm) atmosphere and heating under 1000 °C for 30 min, under a flowing H_2 (10 sccm) atmosphere continually; 5 sccm CH_4 was introduced to allow graphene growth. After 30 min, the CH_4 flow shutoff, and under the same H_2 flow conditions, the tube was cooled to room temperature. Thus, large-area (10×10 cm^2) monolayer graphene was obtained on a Cu foil.

3. Preparation of the Active Matrix GFET Array

3.1. Electrodes Fabrication

A layer of Cr/Au as the source/drain electrodes (5 nm/50 nm) was thermal evaporation, which was prior to patterning using UV-photolithography (AZ 5214 as photo-resistor, exposure time 10 s, 275 W) and etching using Au and Cr etchants, respectively.

3.2. The Graphene Patterns Fabrication

The preparation of graphene patterns involved the following: Poly(methyl methacrylate) (PMMA) supporting layer was spin-coated at 4000 rpm for 5 s onto the graphene patterns on the Cu foil. Prior to being transferred onto a PDMS substrate (thickness of 500 μm), the Cu foil was chemically etched using an aqueous 0.2 M ammonium persulfate solution. Subsequently, the supporting layer was removed by dipping into the hot acetone (~60 °C) for 5 min. To fabricate trilayer graphene scrolls, the above procedure was repeated 3 times, followed by UV-photolithography (AZ 5214 as photo-resistor, exposure time 10 s, 275 W) and oxygen plasma etching (O_2 20 sccm, 150 W, 5 s) of the graphene film.

3.3. The Ion Gel Patterns Fabrication

Ion gel gate dielectrics were patterned by a UV-photolithography. The ion gel consisting of 1-ethyl-3-methylimidazolium bis(trifluoromethyl sulfonyl)imide ((EMIM) (TFSI)) ion liquid, the poly(ethylene glycol) diacrylate (PEGDA) monomer, and the 2-hydroxy-2methylpropiophenone (HOMPP) photo-initiator (weight ratio of 90:7:3) were cast onto the patterned graphene. Under UV exposure, polymerization of PEGDA was initiated by the reaction between monomers and radicals originated from HOMPP to produce the cross-linked structure. The nonexposed areas that failed to cross-link could be washed away using DI water. The graphene area in contact with the ion gel served as the active channel (L = 300 μm and W = 50 μm), whereas the other region functioned as the source/drain electrodes.

4. Fabrication of the Triboelectric Generator

The fabricated TENG is based on the contact/separation between a PTFE film (pulling at 5000 V 5 min, connected with an Al electrode) and a cupper film, which was connected to the ground.

5. Device Characterization

UV-vis measurements were carried out on an ultraviolet spectrophotometer (HOPBA). The electrical performance and triboelectronic performance of the GFETs were measured by a Keysight B1500A Semiconductor Device analyzer. A displacement motor driven by a computer-controlled stepping motor was connected with a probe station for the triboelectronic performance test. All above measurements were conducted under ambient conditions.

6. Results and Discussion

Figure 1a,b show the schematic illustration of the graphene scrolls FET (GSFET) array (4 × 4 pixels) with a coplanar geometry on a stretchable substrate PDMS and the corresponding circuit diagram.

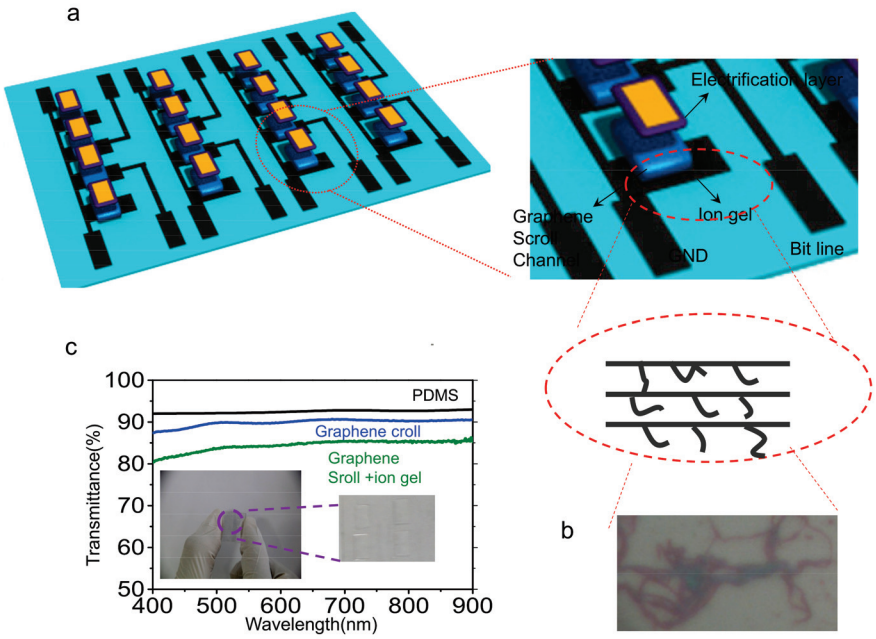

Figure 1. (**a**) Schematic illustration of the noncontact mechanosensation active matrix based on the tribotronic planar graphene transistors array. Inset is the zoomed-in schematic diagram of the single sensing unit. (**b**) Structure and microscopy image of the trilayer graphene scrolls. (**c**) UV-vis transmittance spectrum of PDMS, trilayer graphene scrolls on PDMS, and GSFET on PDMS, respectively. Inset is the photo image of transparent trilayer graphene scrolls.

We pioneeringly adopted graphene scrolls as a semiconductor stretchable channel to substitute for conventional monolayer/multilayer graphene. The fabrication process of graphene scrolls is according to Bao et al.'s previous work. It is well-established that CVD growth of graphene on both sides of the copper film forms Gr/Cu/Gr structures. In regard to transferring graphene, a thin layer of poly(methyl methacrylate) (PMMA) was spin-coated to protect the front side of the graphene; followed by that the entire film (PMMA/front graphene/Cu/back graphene) was floated on $(NH_4)_2S_2O_8$ solution to etch away the Cu foil. The backside graphene without the PMMA coating inescapably had cracks and defects that allowed an etchant to penetrate through [53,54]. It was observed that the released graphene domains rolled up into scrolls originated from surface tension and immediately attached to the remaining front-G/PMMA film. The as-prepared

front-G/G scrolls could be transferred onto pre-UV/O_3-treated PDMS, and PMMA was given away by using acetone and repeating the transfer to another layer subsequently. The obtained monolayer graphene scrolls had similar characteristics to the monolayer back-etched graphene (Figure S1 left panel), while there was evident discrepancy between the obtained monolayer graphene scrolls and the monolayer back-etched graphene (Figure S1 right panel). As shown in Figure S1 left panel, Raman spectra of the monolayer back-etched graphene (black curve) and monolayer graphene scrolls (blue curve) exhibited two characteristic peaks of G band at ~1597 cm^{-1} and ~1569 cm^{-1}, respectively, and 2D band at ~2694 cm^{-1} and ~2696 cm^{-1}, respectively. The monolayer characteristic of graphene was verified by both the full width at half-maximum (~29 cm^{-1}) of the symmetric 2D band and the 2D/G intensity ratio (~2.5). As shown in Figure S1 right panel, the Raman spectra of trilayer graphene scrolls (blue curve) have similar positions of G (1581 cm^{-1}) and 2D (2687 cm^{-1}) peaks as the monolayer characteristic of graphene (black curve) but with a distinguishing variation of the 2D/G intensity ratio (~0.22) for the 2D/G intensity ratio of the monolayer characteristic of graphene, which is about (~2.5). It is worth noting that no other surplus peak exists in the Raman spectra of trilayer graphene scrolls, suggesting no newly generated structure besides graphene. Ion gel (composed of 1-ethyl-3-methylimidazolium bis(trifluoromethyl sulfonyl)imide ((EMIM)(TFSI)) ion liquid, poly(ethylene glycol) diacrylate (PEGDA) monomers, and 2-hydroxy-2-methylpropiophenone (HOMPP) photoinitiator in a weight ratio of 90:7:3), acting as both the gate dielectrics of GSFET and a tribo-electrification layer, was patterned by photolithography above the graphene channel. (The specific fabrication procedure is the same as our previous work, as shown in Figure S2). The graphene layer was applied as the transistor channel (in contact with the ion gel), as well as serving as the source and drain electrodes due to its semimetal characteristic. The width and length of the graphene channel were 100 μm and 1000 μm, respectively. The microscopy image of trilayer graphene scrolls is presented in Figure 1b. The GSFET array also exhibited good optical transparency, being substantiated by UV-vis spectroscopy. As shown in Figure 1c, the PDMS film exhibited a transmittance of 91.5% in the visible and near-infrared region. In the cases of the monolayer graphene film on PDMS and graphene scrolls film with ion gel on PDMS, the transmittance are almost consistent with values of 88% and 83.2%, respectively. Photographs of the flexible GSFET array inserted in Figure 1c demonstrated its flexibility and transparency.

To demonstrate advantages of graphene scrolls as the active element for mechanosensation application, we comprehensively investigated the properties of graphene scrolls. Bao et al. justified that the scrolls are rolled graphene in nature by methods of studying on the monolayer front-G/G scroll structures by high-resolution transmission electron microscopy (TEM) and electron–energy loss (EEL) spectroscopy [33]. The atomic force microscopy (AFM) images provide insight into the monolayer graphene (Figure S3 left panel) and the distribution of graphene scrolls in microstructure (Figure S3 right panel). As shown in Figure S3 right panel, the scrolls are arbitrarily distributed on the surface, and their in-plane density increases proportionally to the number of stacked layers. The length and the width are about 1 to 10 mm and 0.1 to 0.8 mm, respectively. By contrast, the monolayer graphene exhibits plat configuration.

Besides structure characterization, the electrical properties of graphene scrolls were also investigated by making comparison to monolayer and layer-stacking styles of graphene (during the transferring of the graphene procedure, corrosion of back graphene prior to dissolving Cu). Different styles of graphene films, trilayer graphene scrolls, trilayer graphene, bilayer graphene scrolls, and monolayer graphene were transferred onto Ecoflex and patterned into 500 μm-wide and 2000 μm-long channels by photolithography. Two-end resistances as a function of strain deformations and bending deformations were tested under ambient conditions. As shown in Figure 2a (left panel), when strain deformations were perpendicular to the direction of current flow, trilayer graphene scrolls realized the highest relative strain before breaking: up to 120%, exceeding trilayer graphene (110%) and bilayer graphene scrolls (90%) and standing out be far superior to monolayer graphene

(7%). More importantly, the resistance tolerance toward strain deformation of trilayer graphene scrolls was almost up to 120%, outweighing other styles of graphene. Figure 2a right panel depicts strain-dependent two-end resistances when strain deformations were parallel to current flow, basically the same trend as the aforementioned perpendicular to current flow. Trilayer graphene scrolls realized the highest strain rate before breaking: up to 120%, exceeding trilayer graphene and bilayer graphene scrolls (90%) (trilayer graphene and bilayer graphene scrolls showed exactly the same values) and prevailing much more over monolayer graphene (7%). The results of Figure 2a demonstrate the outstanding resistance tolerance toward strain of trilayer graphene scrolls.

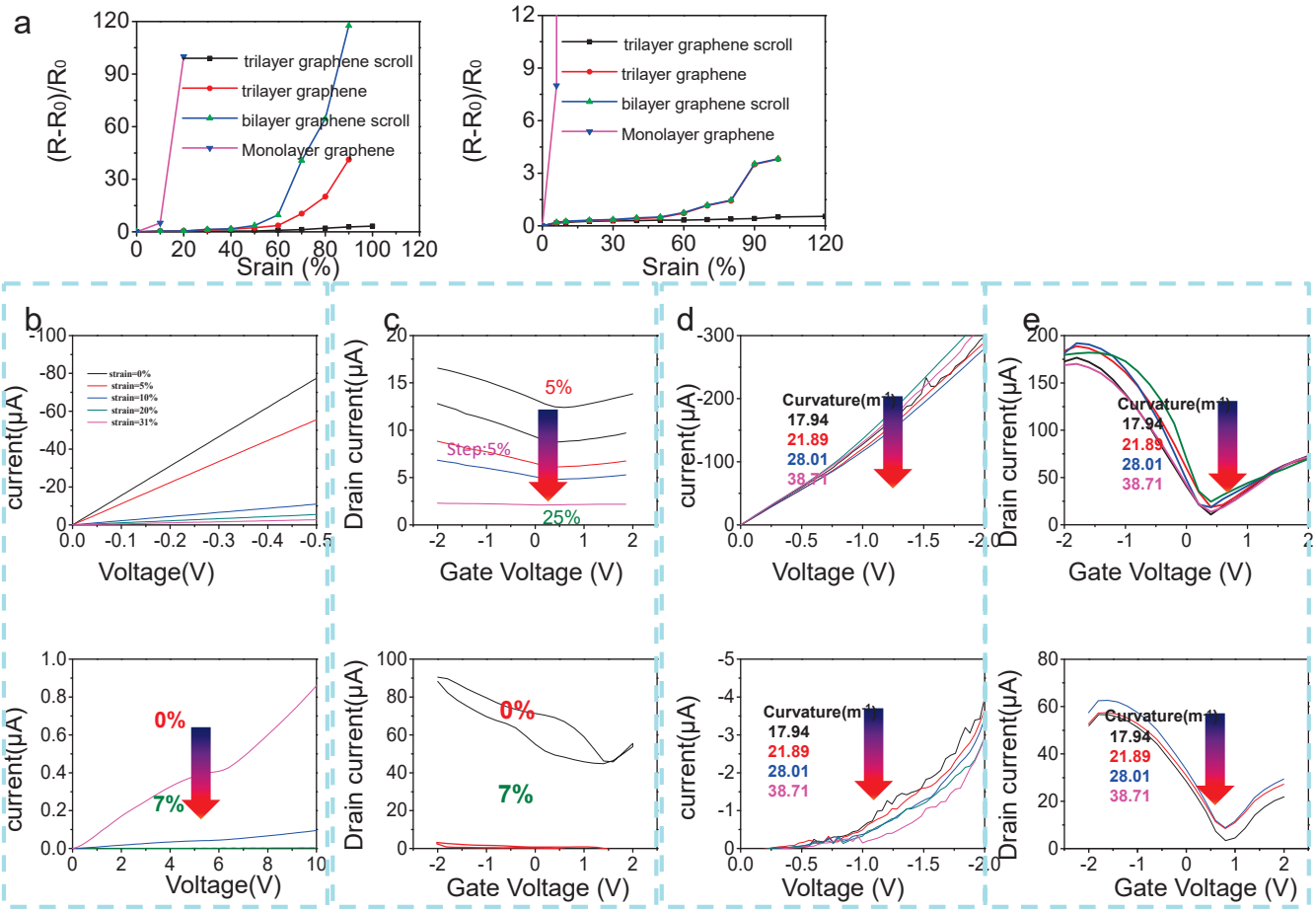

Figure 2. Electrical properties of GFET/GSFET under deformation. (**a**) Normalized relative resistance change of monolayer graphene, bilayer graphene scrolls, trilayer graphene, and trilayer graphene scrolls as a function of perpendicular (**left** panel) and parallel (**right** panel) stretch and strain to the direction of current flow. (**b**) *I-V* curve of trilayer graphene scrolls (**top** panel) and monolayer graphene (**bottom** panel) at varied strain deformations. (**c**) Transfer curve of trilayer graphene scrolls (**top** panel) and monolayer graphene (**bottom** panel) at varied strain deformations (at given V_D of 0.1 V). (**d**) *I–V* curve of trilayer graphene scrolls (**top** panel) and monolayer graphene (**bottom** panel) at varied bending deformations. (**e**) Transfer curve of trilayer graphene scrolls (**top** panel) and monolayer graphene (**bottom** panel) at varied bending deformations.

To explore the underlying reason behind excellent electrostretchability properties of trilayer graphene scrolls, Raman spectra of trilayer graphene scrolls and monolayer graphene were compared under strain (Figure S4). Figure S4 depicts the Raman spectra of monolayer graphene (left panel) and trilayer graphene scrolls (right panel) in free-standing state (blue curve) and strain state (green curve). It can be observed that the Raman spectra

of monolayer graphene experienced more pronounced variation compared with that of trilayer graphene scrolls.

Report-referred graphene scrolls proposed by Bao et al. are limited to application as the electrode; application as the semiconductor channel has not been reported yet. We, for the first time, investigated properties of GSFET based on trilayer graphene scrolls as a semiconductor channel, demonstrating their superiority. The width and length of graphene channel of the single GFET were 50 μm and 300 μm, respectively, with a 100 μm distance between gate and channel. The *I*–*V* character and transfer characteristic of trilayer graphene scrolls under variation of relative strain deformation and bending deformation were compared against those of monolayer graphene. As depicted in Figure 2b (output curve of GFET), as strain was given at the magnitude of 5%, the resistance of GSFET (FET based on trilayer graphene scrolls) increased 40% while the resistance of GFET (FET based on monolayer graphene) increased 10 folds. Trilayer graphene scrolls possess good resistance retention until experiencing strain up to 31%, while monolayer graphene undergoes breakdown when strain increased to only 7%. Figure 2c shows the transfer characteristic of GSFET (top panel) and GFET (bottom panel) under varied relative strain deformation. It can be clearly observed in Figure 2c top panel that the transfer characteristic of trilayer graphene scrolls changed a little.

Figure 2d,e display the *I*–*V* character and transfer characteristic of GSFET and GFET under varied relative bending deformation. The case is the same as the strain deformation: trilayer graphene scrolls possess good resistance retention toward deformation. It is worth noting that it was beyond our expectation that the transfer curves turned out to be same as when the monolayer graphene was the channel, with Dirac point being around 0.6.

Apart from comparing trilayer graphene scrolls with monolayer graphene, comparison of trilayer graphene scrolls and trilayer stacking graphene (during transferring graphene procedure, corrosion of back graphene prior to dissolving Cu) was also conducted.

As shown in Figure S5, as the GSFET undergoes 31% strain, both output characteristic and transfer characteristic of trilayer graphene scrolls displayed little changed (retaining 50% electrical properties) while trilayer graphene experienced electric breakdown as strain exceed 31%. The excellent electrostretchability properties of trilayer graphene scrolls demonstrate its potential application for E-skin.

In practical application of E-skin, multiple functional integrations are also highly required to simultaneously perceive the realization of biomimetic function of E-skins. Given widespread of temperature responsiveness and large in-plane thermal conductivity of graphene [55], we attempted to probe into the temperature responsiveness of trilayer graphene scrolls. The *I*–*V* character of trilayer graphene scrolls under varied temperature were compared with that of monolayer graphene (graphene films transferred on Ecoflex were patterned into 500 μm-wide and 2000 μm-long channels by photolithography). Obviously, the trilayer graphene scrolls displayed more distinct temperature-dependence than that of the counterpart monolayer graphene: every 1 °C induced a 0.7% current variation amount (Figure 3a top panel), while monolayer graphene almost was immune to temperature variation (every 1 °C induced 0.13% current variation) (Figure 3a bottom panel). Correspondingly, we calculated the relative resistance variation $(R - R_0)/R_0$ toward temperature variation of trilayer graphene scrolls (Figure 3b top panel) and monolayer graphene (Figure 3b bottom panel), verifying the more pronounced temperature-dependence of graphene scrolls. To investigate temperature responsiveness of FET based on trilayer graphene scrolls, we used two graphene field-effect transistor: the width and length of trilayer graphene scrolls and monolayer graphene channels were 50 μm and 300 μm, respectively, with a 100 μm distance between gate and channel.

Considering E-skin application, we conducted measurement near the human body's core temperature. Comparison of the transfer characteristics of GSFET and GFET under variation of temperature evidently shows that the GSFET exhibits more sensitivity to temperature variation (Figure 3c). To be specific, as the I_{DS} is fixed at 0.5 V, I_{DS} of GSFET increases from 252 μA to 277 μA when the temperature increases from 25 °C to 45 °C

with the relative variation (Figure 3c top panel) more distinct than that of the counterpart of GFET (I_{DS} of GSFET increases from 78.5 μA to 82.4 μA as the temperature increases from 25 °C to 45 °C (Figure 3b bottom panel))P. To verify feasibility of GSFET for E-skin, real-time temperature monitoring is shown in Figure 3d. Compared to the real-time temperature monitoring of GFET (right panel), GSFET (left panel) exhibited more pronounced output variation, suggesting its better feasibility for temperature monitoring. Importantly, the stability of output current upon temperature, achieving balance and reversibility, suggested GSFET as an ideal candidate for E-skin for monitoring physiological temperature. The hysteresis is one of graphene's characteristics that is relative to defect and doping, here indicated by strain and bending deformation: the defect could occur and change graphene properties. Therefore, the hysteresis probably influences GSFET and brings about temperature fluctuation to some extent.

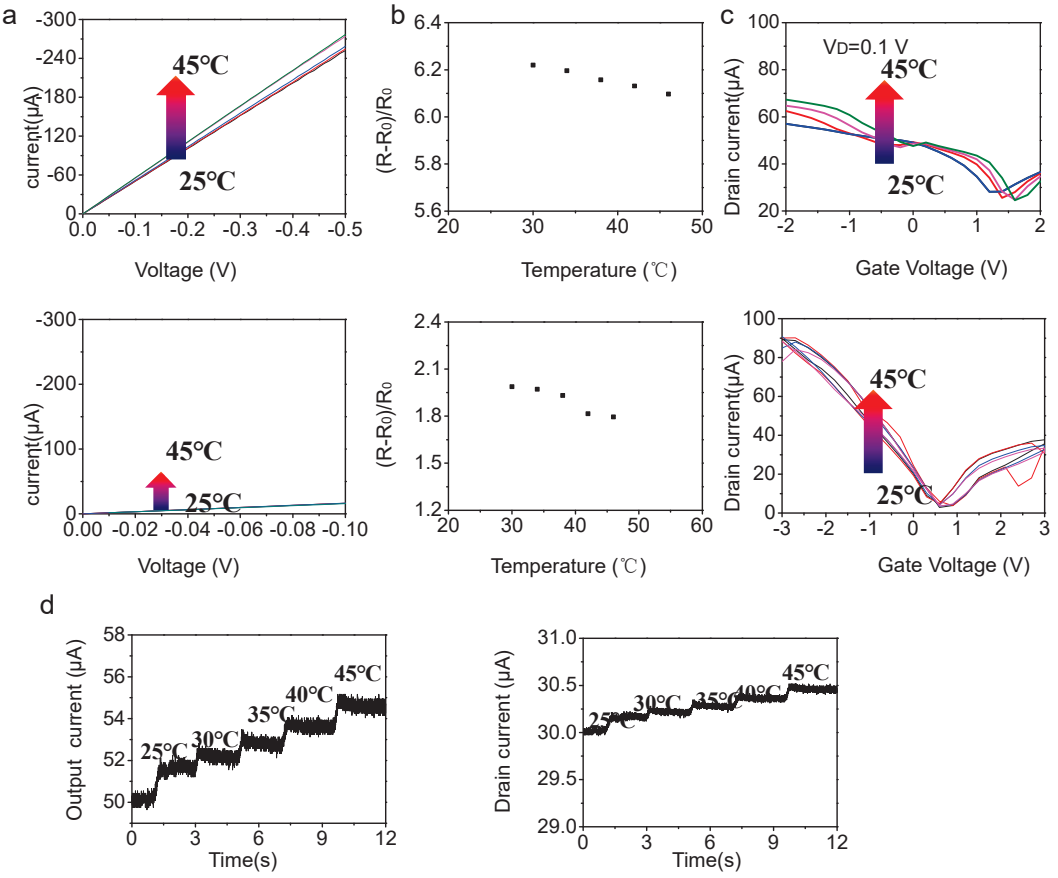

Figure 3. (**a**) The IV character of trilayer graphene scrolls (**top** panel) and monolayer graphene (**bottom** panel) (graphene films transferred on Ecoflex were patterned into 500 μm-wide and 2000 μm-long channels by photolithography). (**b**)The extracted relative resistance variation $(R - R_0)/R_0$ of trilayer graphene scrolls (**top** panel) and monolayer graphene (**bottom** panel). (**c**) Transfer characteristic of GSFET (**top** panel) and GFET (**bottom** panel) under varied temperature. (**d**) The real-time temperature monitoring of GFET (**right** panel) and GSFET (**left** panel).

To elucidate the mechanism of more pronounced temperature-dependence of GSFET than that of the counterpart GFET, Raman spectra of trilayer graphene scrolls and monolayer graphene were compared under varied temperature (Figure S6). It can be observed that Raman spectra of trilayer graphene scrolls (Figure S6 right panel) underwent greater variation toward high temperature compared to that of monolayer graphene (Figure S6 left panel).

Considering the energy consumption and based on our previous work, self-powered GFET array extends to the self-powered GSFET array. It is worth noting that ion gel dielectric is directly served as the electrifriction layer to carry out friction with external materials

to simplified fabrication procedure with high spatial compaction. Prior to studying GFET array, single tribotronic GSFET was comprehensively explored. The basic layout of the single FET is schematically illustrated in Figure 4a. The width and length of the graphene channel were 50 μm and 300 μm, respectively, with a 100 μm distance between gate and channel.

Figure 4d left panel and right panel display output characteristic and transfer characteristic of tribopotential-gated GSFET by electrification between ion gel and skin, separately. Due to skin being a positively triboelectric material relative to the ion gel, I_D experienced increase gradually as the distance between ion gel and skin increased, corresponding to the GFET performing under a negative gate voltage. This linear relationship between I_D variation and contact distance can be divided into regions I and II. I_D variation behavior was divided into two parts: when the contact distance increased from 0 to 1 mm, I_D was increased from 20.0 μA to 22.5 μA with variation gradient of 2.5 μA/mm; when the contact distance increased from 1 to 3 mm, I_D was increased from 22.5 μA to 23.8 μA with gradient of 0.65 μA/mm. The 1 mm distance variation induced I_D variation of 2.5 μA, equivalent to a gate voltage of 0.66 V. The variation ratio is about 1.125 mm^{-1} (2.5 μA/mm/20.0 μA) (as the contact distance increased from 0 to 1 mm), suggesting the excellent sensitivity of the triboelectric properties and offering sound fundamentals for the sensor application.

On basis of the triboelectric series [54], electrons transferred from the skin to ion gel, leaving net negative electrostatic charges on the surface of the ion gel layer and positive electrostatic charges on the skin. The produced triboelectric charges in opposite polarities were fully balanced and had no effect on the graphene channel. As the skin leaves the surface of the ion gel, the un-offset negative charges on the surface of the ion gel attract anions in the ion gel and produce an EDL at the interface between ion gel and the skin, leaving anions at ion gel/graphene interface, corresponding to applying a negative voltage on the GFET. Consequently, the Fermi level of graphene channel was upped downward, leading to an increase in the drain current. To investigate the dynamic triboelectric, real-time tests for the triboelectronic GSFETs were performed under repeat electrification between ion gel and skin. To demonstrate the endurability for practical application, a cyclic durability test was conducted by ion gel and skin's repeated contact–separation with triboelectric distance of 1 mm (Figure 4e left panel). One contact and separation was regarded to be one cycle. Over 3000 cycles, a consistent output current was kept during repeated triboelectrification. It is worth mentioning that the current level was kept at a constant value for a long time after stopping triboelectric termination (Figure 4e right panel). The above results support the durability and reliability of the GFET for noncontact mechanosensation E-skin practical applications.

This GSFET was compared with our previous work triboelectric GFET based on monolayer graphene (same configuration and size, friction between ion gel and PTFE as gating) (Figure S7). For GFET's triboelectricity, the 200 μm distance variation between PTFE and ion gel induced I_D variation of 3.63 μA, equivalent to a positive gate voltage of 0.31 V, while for trilayer graphene scrolls FET's triboelectricity, the 200 μm distance variation of between PTFE and ion gel induced I_D variation of 1.1 μA, equivalent to a positive gate voltage of 0.24 V. It was indicated that trilayer graphene scrolls as the channel was less susceptible to triboelectric.

EDLT analysis can provide deeper insight into the lower susceptibility of trilayer graphene scrolls toward triboelectric than monolayer graphene. According to ion gel EDLT's equivalent circuit [56,57], the total capacitance C is defined as $(1/C_G + 1/C_Q)^{-1}$. C_Q and C_G in multilayer graphene act as a function of the layer number [58]. The value of C_Q increases with increasing layer number because of increasing density of states and saturation as the layer number reaches six. The bilayer and trilayer show anomalies in their transfer curves, which can be ascribed to a second sub-band in presence at approximately 0.5 eV above the Dirac point and is generated by interlayer interactions (the features of multilayer graphene). Figure S8 shows schematic illustration of degradation of triboelectric responsiveness of trilayer graphene scroll FET.

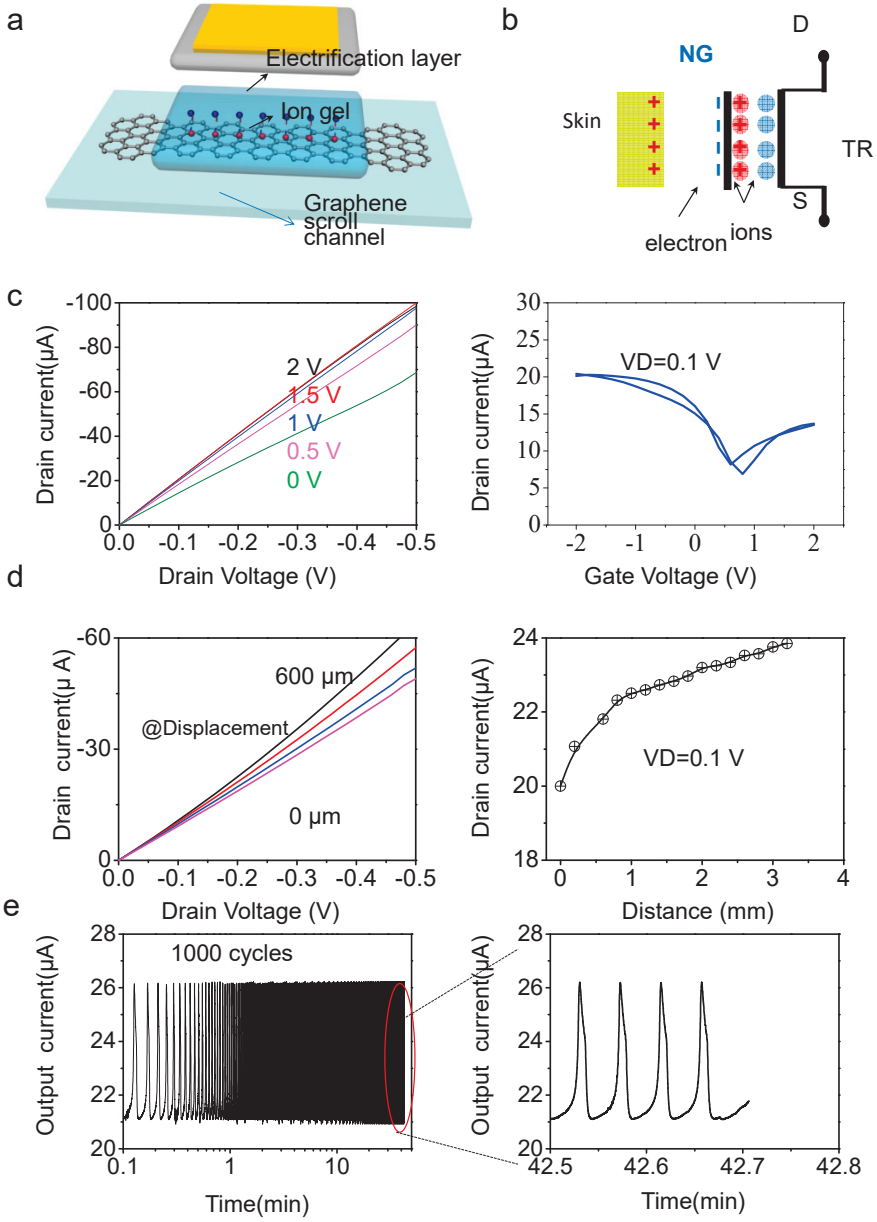

Figure 4. Triboelectric properties of the tribotronic GSFET. (**a**) Schematic illustration of the GSFET device. (**b**) Circuit diagram of tribotronic GSFET sensor contact with skin. (**c**) Output characteristic (left panel) and transfer characteristic (right panel) of GSFET by triboelectric driving. (**d**) Output characteristic (left panel) and transfer characteristic (right panel) of trilayer graphene scroll transistor by tribotronic potential (right panel). (**e**) Durability test over 3000 cycles of contact and separation (left panel) and retentivity during the last cycles (right panel). For E-skin application, ion gel dielectric was carried out friction with skin. Figure 4b shows the scheme of the working principle of ion gel-triboelectric gated GSFET. The tribo-potential, induced by friction between the ion gel and skin, causes the accumulation of negative charges on the surface of the ion gel, attracting compensating cations in the ion gel, while the anions in the ion gel migrate to the ion gel/graphene interface, acting as a negative gating potential for the graphene channel. Consequently, the electrons accumulate in graphene channel. The output characteristic of GFET under an applied gate (Figure 4c left panel) displays that the drain current (I_D) exhibits a linear relationship with drain voltage V_{DS} and increases values as gate voltage V_G increases (from 68.7 μA to 98.5 μA with V_G increased from 0 V to 2 V at a V_D of 0.5 V). The transfer curve (Figure 4c right panel) displays that the I_D values increased with increased V_G in both positive and negative directions, indicating an ambipolar charge transport property of graphene. The GFET operated at a low gate voltage (<2 V) due to the extreme high capacitance of the ion gel gate dielectric (6–7 μF/cm^2).

Compared to monolayer graphene FET, the higher-lying sub-bands are generally unreachable by conventional solid-gated FETs but were reached for the first time by utilizing ion gel (electron double layer effect EDLT), owing to the high-density charge accumulation. Taking the higher-lying sub-band into consideration, a significant capacitance increase with increasing V_G is understood.

Because the capacitance of diffuse layer is negligible, the interfacial capacitance of ion gel can be recognized as a serial combination of an electric double layer capacitance (C_{EDL}) and a quantum capacitance of the graphene (C_Q) [59]. With respect to EDLT in ion gel, the potential difference between EDL capacitance and quantum capacitance of the graphene is conformed to the following equation:

$$|V_G - V_{G,min}| = \frac{\hbar n_F \sqrt{\pi n}}{e} + \frac{ne}{C} \quad (1)$$

$$V_G = V - V(R) = -\frac{Q}{S\varepsilon_0}(d_0 + x(t)) + \frac{\sigma x(t)}{\varepsilon_0} - V(R) \quad (2)$$

where $\hbar$ represents the reduced Planck's constant, v_F is Fermi velocity (1.1106 m/s), e is the electron charge, and n is the charge density. V_{Gmin} is the gate voltage corresponding to Dirac point. According to Equation (2), the carrier concentration is closely associated with V_G and C_{EDL}. V_G is the effective voltage that triboelectric is posed on; according to Equation (2), the value of V_G is equal to that of the open voltage of the TENG substrate. The resistance consumption V(R) and open voltage of TENG followed a linear function as distance between two triboelectric materials increased.

In light of Equation (1), the increment of layer number change V_G further changes the relationship of V_G and triboelectric distance, unambiguously explaining the lower susceptibility of trilayer graphene scrolls toward triboelectric than monolayer graphene.

The working principle of tribopotential characteristic of this GSFET is the same as our previous work: noncontact mechanosensation active matrix based on tribotronic planar graphene transistors array [60]. There is no need to repeat it here.

Our highly stretchable GSFET also possesses excellent rapid dynamic response. As shown in Figure S9, the I_D response time upon application and release of the triboelectric was only 15 ms, calculated from the vertical rising and dropping of I_D. The rapid response time demonstrates the outstanding sensitivity of the device. The I_D increased upon the contact–separation cycles commenced between skin and the ion gel (under applied drain voltage of 0.1 V).

Given that the ultimate goal of triboelectric-driving GFET was applied for noncontact mechanosensation, GSFET array on substrate of PDMS was fabricated with a 4 × 4 GSFETs matrix configuration, as shown in the circuit diagram in Figure 5a. Prior to mapping the spatial temperature and distance applied to the active matrix, the electrical performances of the 16 GSFETs were characterized. The output sensing current signals from different sensors under presenting temperature were collected and plotted to obtain the corresponding 2D color maps.

The triboelectric distances applied to the active matrix were spatially mapped, as shown in Figure 5b. Two edges or two corners of the matrix were fixed, and only a 0.1 V potential was applied to the bit lines. The 2D color mapping (Figure 5c) of the temperature distribution and distances distribution on the active matrix showed the potential application of monitoring spatial interaction of human skin. Figure 5d displays the real-time temperature monitoring and distance monitoring between the ion gel and skin. The stable curves demonstrate the feasibility of the device for non-mechanosensation active matrix application. As a small application, the GSFET active matrix was conformally attached onto the knee joint of the test subject. The 2D color mapping of the distances distribution (Figure 5e) and the temperature distribution (Figure 5f) on the active matrix can reflect in real-time the situation of the human knee joint. Notably, the monitored temperature is a little lower than body temperature for body parts such as knee joints.

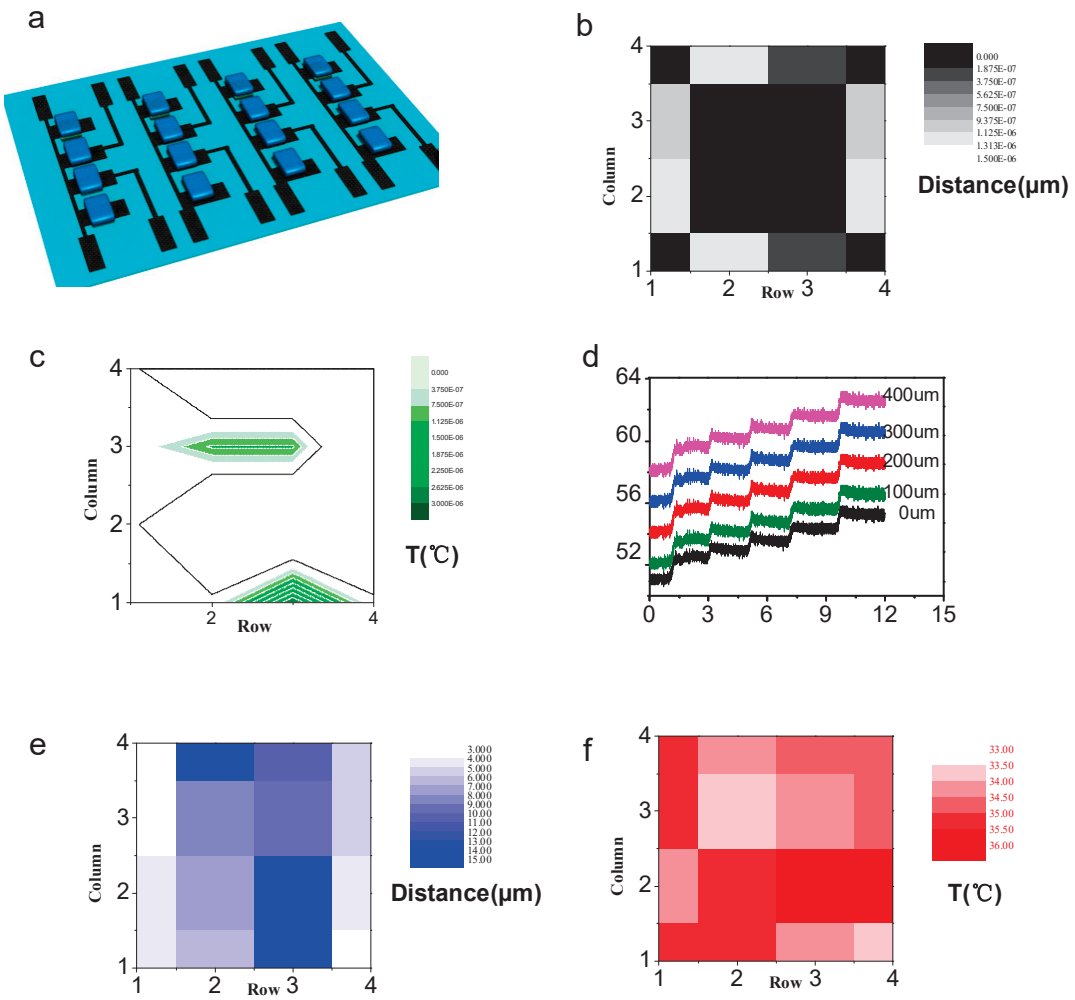

Figure 5. Characterization of GSFET noncontact mechanosensation active matrix. (**a**) Schematic illustration of the mechanosensation matrix for sensing the distance information and temperature. (**b**) 2D mapping of the distance sensing output currents for the matrix. (**c**) 2D mapping of the temperature sensing output currents for the matrix. (**d**) The real-time temperature monitoring and distance monitoring between the ion gel and skin. (**e**) 2D mapping of the distance sensing output currents for the matrix as the device is attached onto the human's knee joint and conforms to it. (**f**) 2D mapping of the temperature-sensing output currents for the matrix as the device is attached onto the human's knee joint and conforms to it.

In conclusion, we pioneeringly employed trilayer graphene scrolls as FET channel material for a self-powered tribotronics and mechanosensation matrix. This novel structure of trilayer graphene scrolls transistor endowed the triboelectronic FET with extremely stretchable properties (up to 120% strain parallel to the direction of charge transport and the ability to retain 35% of its original current output) compared to intrinsic graphene and stacking graphene sheet; excellent temperature sensitivity (precision as low as 1); and high transparency. Meanwhile, for tribotronics GSFET, both the output performances powered by distance-dependent tribopotential were in good agreement with applied gate voltage, verifying that tribotronics could serve as an effective power source to drive a mechanosensation active matrix. The mechanosensation matrix possessed tactile sensing properties of high sensitivity (1.125 mm^{-1}), rapid response time (~16 ms), and an endurability operation over thousands of cycles. Owing to all these merits, this graphene scrolls mechanosensation active matrix were spatially distance and temperature dual-mapping and achieved real-time monitoring. We can demonstrate that this device holds promising prospects for

self-powered mechanosensation matrix for application of for advanced disease diagnosis, therapy, and health monitoring.

Supplementary Materials: The following supporting information can be downloaded at: https://www.mdpi.com/article/10.3390/nano13030528/s1, Figure S1: Left panel: Comparison of Raman spectrum of the CVD single-layer graphene (blank line) and monolayer graphene scroll (blue line). Right panel: Comparison of Raman spectrum of the monolayer graphene scroll (blank line) and trilayer graphene scrolls (blue line); Figure S2: Fabrication procedure of the tribopotential-gated GSFET array.; Figure S3: AFM (atom force microscopy) of the monolayer graphene (left panel) and trilayer graphene scrolls (right panel); Figure S4: Raman characteristic of graphene under strain. Left panel: comparison of Raman spectrum of the CVD single-layer graphene under no strain (blue line) and under a 5% strain (green line). Right panel: comparison of Raman spectrum of the trilayer graphene scrolls under no strain (blue line) and under a 5% strain (green line); Figure S5: Electrical properties of GFET/GSFET under strain deformation (a) Output curve (left panel) and transfer curve (at the given V_D = 0.1 V, right panel) of GSFET under no strain deformations. (b) Output curve (left panel) and transfer curve (at the given V_D = 0.1 V, right panel) of GSFET under 5% strain deformations. (c) Output curve (left panel) and transfer curve (at the given V_D = 0.1 V, right panel) of GFET under no strain deformations. (d) Output curve (left panel) and transfer curve (at the given V_D = 0.1 V, right panel) of GFET under 5% strain deformations; Figure S6: Left panel: comparison of Raman spectrum of the CVD single-layer graphene under room temperature (blue line), 30 °C (red line) and under a 5% strain (green line). Right panel: comparison of Raman spectrum of the tri-layer graphene scrolls under room temperature (blue line), 30 °C (red line) and under a 5% strain (green line); Figure S7: Triboelectrical performances of GFET/GSFET by tribo-potential between ion gel and PTFE (a) Circuit diagram of tribotronic GFET/GSFET sensor contact with PTFE. (b) Output curve (left panel) and transfer curve (at the given V_D = 0.1 V, right panel) of GFET powered by tribopotential between ion gel and PTFE under no strain deformations. (c) Output curve (left panel) and transfer curve (at the given V_D = 0.1 V, right panel) of GSFET powered by tribopotential between ion gel and PTFE under no strain deformations; Figure S8: Schematic illustration of degradation of triboelectric responsiveness of trilayer GSFET comparing to monolayer graphene FET; Figure S9: The I_D response time of the GSFET.

Funding: This work was supported by the National Key Research and Development Program of China (2016YFA0202703, 2016YFA0202704), the National Natural Science Foundation of China (51605034, 51711540300, 51475099).

Institutional Review Board Statement: Not applicable.

Informed Consent Statement: Not applicable.

Data Availability Statement: The data is available on reasonable request from the corresponding author.

Conflicts of Interest: The authors declare no competing financial interest.

References

1. Chen, J.W.; Zhu, Y.T.; Chang, X.H.; Pan, D.; Song, G.; Guo, Z.H.; Naik, N. Recent Progress in Essential Functions of Soft Electronic Skin. *Adv. Funct. Mater.* **2021**, *31*, 2104686. [CrossRef]
2. Chortos, A.; Liu, J.; Bao, Z. Pursuing Prosthetic Electronic Skin. *Nat. Mater.* **2016**, *15*, 937–950. [CrossRef] [PubMed]
3. Cai, L.; Song, L.; Luan, P.; Zhang, Q.; Zhang, N.; Gao, Q.; Zhao, D.; Zhang, X.; Tu, M.; Yang, F.; et al. Super-Stretchable, Transparent Carbon Nanotube-Based Capacitive Strain Sensors for Human Motion Detection. *Sci. Rep.* **2013**, *3*, 3048. [CrossRef]
4. Chortos, A.; Bao, Z. Skin-Inspired Electronic Devices. *Mater. Today* **2014**, *17*, 321–331. [CrossRef]
5. Hammock, M.L.; Chortos, A.; Tee, B.C.K.; Tok, J.B.H.; Bao, Z. 25th Anniversary Article: The Evolution of Electronic Skin (ESkin): A Brief History, Design Considerations, and Recent Progress. *Adv. Mater.* **2013**, *25*, 5997–6037. [CrossRef] [PubMed]
6. Wang, X.; Dong, L.; Zhang, H.; Yu, R.; Pan, C.; Wang, Z.L. Recent Progress in Electronic Skin. *Adv. Sci.* **2015**, *2*, 1500169. [CrossRef] [PubMed]
7. Kim, D.-H.; Lu, N.; Ma, R.; Kim, Y.-S.; Kim, R.-H.; Wang, S.; Wu, J.; Won, S.M.; Tao, H.; Islam, A.; et al. Epidermal Electronics. *Science* **2011**, *333*, 838–843. [CrossRef]
8. Kim, J.; Lee, M.; Shim, H.J.; Ghaffari, R.; Cho, H.R.; Son, D.; Jung, Y.H.; Soh, M.; Choi, C.; Jung, S.; et al. Skin electronics from scalable fabrication of an intrinsically stretchable transistor array. *Nat. Commun.* **2014**, *5*, 5747. [CrossRef]
9. Ho, D.H.; Sun, Q.; Kim, S.Y.; Han, J.T.; Kim, D.H.; Cho, J.H. Stretchable and Multimodal All Graphene Electronic Skin. *Adv. Mater.* **2016**, *28*, 2601–2608. [CrossRef]

10. Lee, J.H.; Heo, J.S.; Kim, Y.J.; Eom, J.; Jung, H.J.; Kim, J.W.; Kim, I.; Park, H.H.; Mo, H.S.; Kim, Y.H.; et al. A Behavior-Learned Cross-Reactive Sensor Matrix for Intelligent Skin Perception. *Adv. Mater.* **2020**, *32*, 2000969. [CrossRef]
11. Choi, Y.J.; Sae Jo, S.B.; Cho, J.H. Monolithic Tandem Multicolor Image Sensor Based on Electrochromic Color-Radix Demultiplexing. *Adv. Mater.* **2021**, *33*, 2102725. [CrossRef] [PubMed]
12. Lipomi, D.J.; Tee, B.C.K.; Vosgueritchian, M.; Bao, Z. Stretchable Organic Solar Cells. *Adv. Mater.* **2011**, *23*, 1771. [CrossRef] [PubMed]
13. Kaltenbrunner, M.; White, M.S.; Glowacki, E.D.; Sekitani, T.; Someya, T.; Sariciftci, N.S.; Bauer, S. Ultrathin and lightweight organic solar cells with high flexibility. *Nat. Commun.* **2012**, *3*, 770. [CrossRef] [PubMed]
14. Zhang, Q.; Jiang, T.; Ho, D.; Qin, S.; Yang, X.; Cho, J.H.; Sun, Q.; Wang, Z.L. Transparent and Self-Powered Multistage Sensation Matrix for Mechanosensation Application. *ACS Nano* **2018**, *12*, 254. [CrossRef] [PubMed]
15. Chen, C.R.; Qin, H.H.; Cong, H.P.; Yu, S.H. A Highly Stretchable and Real-Time Healable Supercapacitor. *Adv. Mater.* **2019**, *31*, 1900573. [CrossRef]
16. Sun, H.; Tian, W.; Cao, F.; Xiong, J.; Li, L. Ultrahigh-Performance Self-Powered Flexible DoubleTwisted Fibrous Broadband Perovskite Photodetector. *Adv. Mater.* **2018**, *30*, 170698. [CrossRef]
17. Jang, H.; Liu, C.; Hinton, H.; Lee, M.H.; Kim, H.; Seol, M.; Shin, H.J.; Park, S.; Ham, D. An Atomically Thin Optoelectronic Machine Vision Processor. *Adv. Mater.* **2020**, *32*, 2002431. [CrossRef]
18. Choi, M.K.; Yang, J.; Kang, K.; Kim, D.C.; Choi, C.; Park, C.; Kim, S.J.; Chae, S.I.; Kim, T.H.; Kim, J.H.; et al. Wearable red–green–blue quantum dot light-emitting diode array using high-resolution intaglio transfer printing. *Nat. Commun.* **2012**, *6*, 7149. [CrossRef]
19. Choi, S.; Lee, H.; Ghaffari, R.; Hyeon, T.; Kim, D.H. Recent Advances in Flexible and Stretchable Bio-Electronic Devices Integrated with Nanomaterials. *Adv. Mater.* **2016**, *28*, 4203–4218. [CrossRef]
20. Sekitani, T.; Noguchi, Y.; Hata, K.; Fukushima, T.; Aida, T.; Someya, T. A Rubberlike Stretchable Active Matrix Using Elastic Conductors. *Science* **2008**, *321*, 1468. [CrossRef]
21. Sekitani, T.; Nakajima, H.; Maeda, H.; Fukushima, T.; Aida, T.; Hata, K.; Someya, T. Stretchable active-matrix organic light-emitting diode display using printable elastic conductors. *Nat. Mater.* **2009**, *8*, 494. [CrossRef] [PubMed]
22. Wang, L.; Wu, Y.; Li, Z.; Jiang, N.; Niu, K. Wavy graphene foam reinforced elastomeric composites for large-strain stretchable conductors. *Compos. Part B Eng.* **2021**, *224*, 109179.
23. Choi, M.K.; Park, I.; Kim, D.C.; Joh, E.; Park, O.K.; Kim, J.; Kim, M.; Choi, C.; Yang, J.; Cho, K.W.; et al. Thermally Controlled, Patterned Graphene Transfer Printing for Transparent and Wearable Electronic/Optoelectronic System. *Adv. Funct. Mater.* **2015**, *25*, 7109–7118. [CrossRef]
24. Kaltenbrunner, M.; Sekitani, T.; Reeder, J.; Yokota, T.; Kuribara, K.; Tokuhara, T.; Drack, M.; Schwoediauer, R.; Graz, I.; Bauer-Gogonea, S. An ultra-lightweight design for imperceptible plastic electronics. *Nature* **2013**, *499*, 458. [CrossRef]
25. Zhang, Y.; Bai, W.; Cheng, X.; Ren, J.; Weng, W.; Chen, P.; Fang, X.; Zhang, Z.; Peng, H. Flexible and Stretchable Lithium-Ion Batteries and Supercapacitors Based on Electrically Conducting Carbon Nanotube Fiber Springs. *Angew. Chem. Int. Ed.* **2014**, *53*, 14564–14568. [CrossRef]
26. Xu, F.; Wang, X.; Zhu, Y.T.; Zhu, Y. Wavy Ribbons of Carbon Nanotubes for Stretchable Conductors. *Adv. Funct. Mater.* **2012**, *22*, 1279–1283. [CrossRef]
27. Zhang, Z.; Yang, Z.; Deng, J.; Zhang, J.Y.; Guan, G.; Peng, H. Stretchable Polymer Solar Cell Fibers. *Small* **2015**, *11*, 675. [CrossRef]
28. Someya, T.; Kato, Y.; Sekitani, T.; Iba, S.; Noguchi, Y.; Murase, Y.; Kawaguchi, H.; Sakurai, T. Conformable, flexible, large-area networks of pressure and thermal sensors with organic transistor active matrixes. *Proc. Natl. Acad. Sci. USA* **2005**, *102*, 12321. [CrossRef]
29. Qiang, Y.; Bilgin, I.; Kar, S.; Vinegoni, C.; Weissleder, R.; Fang, H. Transparent Electrophysiology Microelectrodes and Interconnects from Metal Nanomesh. *ACS Nano* **2017**, *11*, 4365–4372.
30. Kim, C.C.; Lee, H.H.; Oh, K.H.; Sun, J.Y. Highly stretchable, transparent ionic touch panel. *Science* **2016**, *353*, 682. [CrossRef]
31. Bae, S.; Kim, H.; Lee, Y.; Xu, X.; Park, J.S.; Zheng, Y.; Balakrishnan, J.; Lei, T.; Kim, H.R.; Song, Y.I.; et al. Roll-to-roll production of 30-inch graphene films for transparent electrodes. *Nat. Nanotechnol.* **2010**, *5*, 574–578. [CrossRef] [PubMed]
32. Li, X.; Zhu, Y.; Cai, W.; Borysiak, M.; Han, B.; Chen, D.; Piner, R.D.; Colombo, L.; Ruoff, R.S. Transfer of large-area graphene films for high-performance transparent conductiveelectrodes. *Nano Lett.* **2009**, *9*, 4359–4363. [CrossRef] [PubMed]
33. Liu, N.; Chortos, A.; Lei, T.; Jin, L.H.; Kim, T.R.; Bae, W.G.; Zhu, C.X.; Wang, S.; Pfattner, R.; Chen, X.; et al. Ultra-transparent and Stretchable Graphene Electrodes. *Sci. Adv.* **2017**, *3*, e1700159. [CrossRef] [PubMed]
34. Lee, S.K.; Kim, B.J.; Jang, H.; Yoon, S.C.; Lee, C.; Hong, B.H.; Rogers, J.A.; Cho, J.H.; Ahn, J.H. Stretchable Graphene Transistors with Printed Dielectrics and Gate Electrodes. *Nano Lett.* **2011**, *11*, 4642–4646. [CrossRef]
35. Kim, K.S.; Zhao, Y.; Jang, H.; Lee, S.Y.; Kim, J.M.; Kim, K.S.; Ahn, J.H.; Kim, P.; Choi, J.Y.; Hong, B.H. Large-scale pattern growth of graphene films for stretchable transparent electrodes. *Nature* **2009**, *457*, 706–710. [CrossRef]
36. Lee, J.M.; Hong, G.S.; Lin, D.C.; Schuhmann, T.G., Jr.; Sullivan, A.T.; Viveros, R.D.; Park, H.G.; Lieber, C.M. Nanoenabled Direct Contact Interfacing of Syringe-Injectable Mesh Electronics. *Nano Lett.* **2019**, *19*, 5818–5826. [CrossRef]
37. Jia, L.Y.; Guo, Z.H.; Li, L.W.; Pan, C.X.; Zhang, P.P.; Xu, F.; Pu, X.; Wang, Z.L. Electricity Generation and Self-Powered Sensing Enabled by Dynamic Electric Double Layer at Hydrogel–Dielectric Elastomer Interfaces. *ACS Nano* **2021**, *15*, 19651–19660. [CrossRef]

38. Kim, S.; Gupta, M.K.; Lee, K.Y.; A Sohn, A.; Kim, S.W. Transparent Flexible Graphene Triboelectric Nanogenerators. *Adv. Mater.* **2014**, *26*, 3918–3925. [CrossRef]
39. Han, C.B.; Du, W.M.; Zhang, C.; Tang, W.; Wang, Z.L. Harvesting energy from automobile brake in contact and non-contact mode by conjunction of triboelectrication and electrostatic-induction processes. *Nano Energy* **2014**, *6*, 59–65. [CrossRef]
40. Tang, W.; Zhang, C.; Han, C.B.; Wang, Z.L. Enhancing Output Power of Cylindrical Triboelectric Nanogenerators by Segmentation Design and Multilayer Integration. *Adv. Funct. Mater.* **2014**, *24*, 6684–6690. [CrossRef]
41. Zhu, G.; Chen, J.; Zhang, T.J.; Jing, Q.S.; Wang, Z.L. Radial-arrayed rotary electrification for high performance triboelectric generator. *Nat. Commun.* **2014**, *5*, 3426. [CrossRef] [PubMed]
42. Yang, Y.; Zhang, H.L.; Lin, Z.H.; Wang, Z.L. Human Skin Based Triboelectric Nanogenerators for Harvesting Biomechanical Energy and as Self-Powered Active Tactile Sensor System. *ACS Nano* **2013**, *7*, 9213–9222. [CrossRef] [PubMed]
43. Li, X.H.; Han, C.B.; Jiang, T.; Wang, Z.L. A ball-bearing structured triboelectric nanogenerator for nondestructive damage and rotating speed measurement. *Nanotechnology* **2016**, *27*, 085401. [CrossRef] [PubMed]
44. Jing, Q.S.; Zhu, G.; Wu, W.Z.; Wang, Z.L. Self-powered triboelectric velocity sensor for dual-mode sensing of rectified linear and rotary motions. *Nano Energy* **2014**, *10*, 305–312. [CrossRef]
45. Yu, J.R.; Gao, G.Y.; Huang, J.R.; Yang, X.X.; Han, J.; Zhang, H.; Chen, Y.H.; Zhao, C.L.; Sun, Q.J.; Wang, Z.L. Contact-electrification-activated artificial afferents at femtojoule energy. *Nat. Commun.* **2021**, *12*, 1581. [CrossRef]
46. Yang, X.X.; Yu, J.R.; Zhao, J.; Chen, Y.H.; Gao, G.Y.; Wang, Y.; Sun, Q.J.; Wang, Z.L. Mechanoplastic Tribotronic Floating-Gate Neuromorphic Transistor. *Adv. Funct. Mater.* **2020**, *30*, 2002506. [CrossRef]
47. Zhang, H.; Yu, J.R.; Yang, X.X.; Gao, G.Y.; Qin, S.S.; Sun, J.; Ding, M.; Jia, C.; Sun, Q.J.; Wang, Z.L. Ion Gel Capacitively Coupled Tribotronic Gating for Multiparameter Distance Sensing. *ACS Nano* **2020**, *14*, 3461. [CrossRef]
48. Gao, G.Y.; Yu, J.R.; Yang, X.X.; Pang, Y.; Zhao, J.; Pan, C.F.; Sun, Q.J.; Wang, Z.L. Triboiontronic Transistor of MoS_2. *Adv. Mater.* **2019**, *31*, 1806905. [CrossRef]
49. Zhang, C.; Wang, Z.L. Tribotronics-A new field by coupling triboelectricity and Semiconductor. *Nano Today* **2016**, *4*, 521–536. [CrossRef]
50. Gu, G.Q.; Han, C.B.; Lu, C.X.; He, C.; Wang, Z.L. Triboelectric Nanogenerator Enhanced Nanofiber Air Filters for Efficient Particulate Matter Removal. *ACS Nano* **2017**, *11*, 8702–8709. [CrossRef]
51. Zhang, C.; Zhang, L.M.; Tang, W.; Wang, Z.L. Tribotronic Logic Circuits and Basic Operations. *Adv. Mater.* **2015**, *27*, 3533–3540. [CrossRef] [PubMed]
52. Sun, Q.; Kim, D.H.; Park, S.S.; Lee, N.Y.; Zhang, Y.; Lee, J.H.; Cho, K.; Cho, J.H. Transparent, Low-power Pressure Sensor Matrix based on Coplanar-gate Graphene Transistors. *Adv. Mater.* **2014**, *26*, 4735. [CrossRef] [PubMed]
53. Gao, G.Y.; Wan, B.S.; Liu, X.; Sun, Q.J.; Wang, Z.L. Tunable Tribotronic Dual-Gate Logic Devices Based on 2D MoS_2 and Black Phosphorus. *Adv. Mater.* **2018**, *30*, 1705088.
54. Jung, S.; Kim, J.H.; Kim, J.; Choi, S.; Lee, J.; Park, I.; Hyeon, T.; Kim, D.H. Reverse-Micelle-Induced Porous Pressure-Sensitive Rubber for Wearable Human–Machine Interfaces. *Adv. Mater.* **2014**, *26*, 4825–4830. [CrossRef] [PubMed]
55. Meng, Y.F.; Zhao, J.Q.; Yang, X.X.; Zhao, C.; Qin, S.S.; Cho, J.H.; Zhang, C.; Sun, Q.; Wang, Z.L. Mechanosensation-Active Matrix Based on Direct-Contact Tribotronic Planar Graphene Transistor Array. *ACS Nano* **2018**, *12*, 9381. [CrossRef] [PubMed]
56. Yazyev, O.V.; Louie, S.G. Topological defects in graphene: Dislocations and grain boundaries. *Phys. Rev. B Condens. Matter Mater. Phys.* **2020**, *81*, 195420. [CrossRef]
57. Wang, B.; Puzyrev, Y.S.; Pantelides, S.T. Enhanced chemical reactions of oxygen at grain boundaries in polycrystalline graphene. *Polyhedron* **2013**, *64*, 158–162. [CrossRef]
58. Zou, H.; Zhang, Y.; Guo, L.; Wang, P.H.; He, X.; Dai, G.Z.; Zheng, H.W.; Chen, C.Y.; Wang, A.C.; Xu, C.; et al. Quantifying the triboelectric series. *Nat. Commun.* **2019**, *10*, 1427. [CrossRef]
59. Bisri, S.Z.; Shimizu, S.; Nakano, M.; Iwasa, Y. Endeavor of Iontronics: From Fundamentals to Applications of Ion-Controlled Electronics. *Adv. Mater.* **2017**, *29*, 1607054. [CrossRef]
60. Uesugi, E.; Goto, H.; Eguchi, R.; Fujiwara, A.; Kubozono, Y. Electric double-layer capacitance between an ionic liquid and few-layer graphene. *Sci. Rep.* **2013**, *3*, 1595. [CrossRef]

nanomaterials

MDPI

Article

Highly Sensitive Electrochemical Detection of Paraquat in Environmental Water Samples Using a Vertically Ordered Mesoporous Silica Film and a Nanocarbon Composite

Weiran Zheng [1,*], Ruobing Su [2], Guoguang Yu [1], Lin Liu [1] and Fei Yan [2,*]

[1] Institute of Agro-product Safety and Nutrition, Zhejiang Academy of Agricultural Sciences, Hangzhou 310021, China
[2] Key Laboratory of Surface & Interface Science of Polymer Materials of Zhejiang Province, Department of Chemistry, Zhejiang Sci-Tech University, Hangzhou 310018, China
* Correspondence: rancki@163.com (W.Z.); yanfei@zstu.edu.cn (F.Y.)

Abstract: Herein, we demonstrate a sensitive and rapid electrochemical method for the detection of paraquat (PQ) using a glassy carbon electrode (GCE) modified with vertically ordered mesoporous silica films (VMSF) and a nanocarbon composite. The three-dimensional graphene-carbon nanotube (3DG-CNT) nanocarbon composite has a 3D network structure, a large electroactive area and oxygen-containing groups, promoting electron transfer between PQ and the underlying electrode and providing a suitable microenvironment for the stable growth of VMSF. This VMSF/3DG-CNT nanocomposite film could be prepared on the GCE's surface by a two-step electrochemical method with good controllability and convenience. Owing to the synergistic effect of the electrocatalytic ability of 3DG-CNT and the electrostatically enriched capacity of VMSF, the proposed VMSF/3DG-CNT/GCE has superior analytical sensitivity compared with the bare GCE. Furthermore, VMSF has excellent anti-fouling ability that makes the fabricated sensor exhibit satisfactory performance for direct analysis of PQ in environmental water samples.

Keywords: paraquat; electrochemically reduced graphene oxide; carbon nanotubes; vertically ordered mesoporous silica films; electrochemical detection

1. Introduction

Paraquat (1,1-dimethyl-4,4-bipyridine dichloride, PQ) is a kind of herbicide that has been widely used in a variety of applications, such as broad weed control and desiccants on crops [1,2]. Paraquat, also known as methyl viologen, is one of the active components of dipyridine compounds [3], which are easily reduced to stable free radicals and cause severe toxicity to humans and animals [4]. It has been proven that PQ may cause serious damage to the lungs, liver, kidney and heart, and also lead to neurodegenerative diseases such as Parkinson's disease [5,6]. Overuse of PQ in agriculture will produce pollution in the environment (mainly the aquatic system). The maximum residue limit (MRL) for PQ in water is 3–200 nM [7]. Therefore, it is very important to realize the sensitive detection of PQ. Currently, many analytical methods have been devoted to the detection of PQ, such as chromatography [8], spectrophotometry [9], surface-enhanced Raman spectroscopy [10] and electrochemistry [11]. By contrast, electrochemical sensors have the advantages of high sensitivity, easy operation, rapidity and low cost, and have received considerable attention. Traiwatcharanon et al. [12] prepared lead oxide nanomaterials on SPE (PBO-NPs /SPE) by using the room-temperature spark method for electrochemical detection of PQ. Wachholz et al. [11] reported that a copper-based metal–organic framework/reduced graphene oxide-modified electrode (CuMOF/rGO/Au) could be used to detect PQ. Jiang et al. [13] deposited Au and Cu_2O on the surface of an indium tin oxide (ITO) electrode for PQ detection. However, a complex electrode preparation process and sample pretreatments

are often required, limiting the application of electrochemical sensors in real samples. Therefore, it is necessary to develop a simple, sensitive and anti-fouling electrochemical sensing interface for the detection of PQ.

Porous materials have been used as important functional building blocks for the development of various high-performance sensors and nanofluidic osmotic power generators [14–16], taking advantage of the high porosity and surface area [17,18], efficient enrichment ability [19,20] and rapid mass transfer [21], as well as their ease of hybridization [22–24]. In particular, vertically ordered mesoporous silica films (VMSF) consisting of ultrasmall and uniform pores (2~3 nm), perpendicular silica nanochannels and high porosity exhibit unique characteristics in terms of their good molecular accessibility, high permselectivity (e.g., size [25], charge [26] and lipophilicity [27]) and excellent anti-fouling capacity [28]. These have emerged as attractive electrode materials for the construction of electrochemical sensors [29–31]. Generally, Stöber solution growth approaches and electrochemically assisted self-assembly (EASA) are two simple and commonly used methods for the fabrication or further surface functionalization of VMSF onto the surface of electrodes [32–34]. In comparison with the former method, EASA is faster (around several seconds) and easier to operate, and the obtained VMSF has a better long-range order. Moreover, EASA can prepare VMSF on the surface of many conductive electrodes, such as gold, platinum, copper, indium tin oxide (ITO) and glassy carbon electrodes (GCE) [35–37]. Among these, GCE is one of most commonly used commercial electrodes and displays good electrochemically activity [38]. However, VMSF have poor adhesion on the untreated carbon-based electrodes. To overcome this issue, adhesive layers (e.g., organosilanes [39] and reduced graphene oxide [40]) and pretreatment process (e.g., electroactivation [41] and O_2-plasma treatment [42]) are used. As our group reported, graphene with oxygen-containing groups, π-π structures and electrochemical activity could effectively improve the stability between VMSF and GCE, and simultaneously promote the electrode performance [40]. Furthermore, combining graphene with other nanomaterials (e.g., carbon nanotubes [43] and boron nitride [44]) could synergistically increase the specific surface area, conductivity and electroanalytical performance.

In this work, a three-dimensional nanocarbon composite composed of electrochemically reduced graphene oxide and carbon nanotubes (3DG-CNT) was used as a highly electroactive support for the stable growth of VMSF. These VMSF/3DG-CNT were prepared on the GCE's surface by a two-step electrochemical method combining the electroactive ability of the inner 3DG-CNT layer and the electrostatic amplification effect of the outer VMSF layer, showing excellent electroanalytical performance towards PQ. The fabrication process of VMSF/3G-CNT/GCE sensors is simple, time-saving and controllable. Furthermore, owing to the good anti-fouling and anti-interference capacity of VMSF, the proposed VMSF/3DG-CNT/GCE sensor showed satisfactory results in environmental water samples, with improved stability and sensitivity.

2. Materials and Methods

2.1. Chemicals and Materials

All the chemicals and reagents were of analytical grade and were used as received without further purification. An aqueous solution of graphene oxide (GO) (1 mg/mL, 3~5 μm, evenness 99%, oxygen content 30~40%) was purchased from Hangzhou Gaoxi Tech. Multiwalled carbon nanotubes (CNT, OD < 8 nm, length~30 μm, 95%) were ordered from Chengdu Institute of Organic Chemistry, Chinese Academy of Sciences. Sodium perchlorate ($NaClO_3$), sodium phosphate dibasic dodecahydrate ($Na_2HPO_4{\cdot}12H_2O$), sodium phosphate monobasic dihydrate ($NaH_2PO_4{\cdot}2H_2O$), paraquat (PQ), tetraethoxysilane (TEOS, 98%), potassium hydrogen phthalate (KHP), potassium ferricyanide ($K_3[Fe(CN)_6]$), cadmium nitrate ($CdNO_3{\cdot}4H_2O$), catechol (CC), sodium dodecyl sulfate (SDS), starch and humic acid (HA) were bought from Aladdin. Hydrochloric acid (HCl) was obtained from Hangzhou Shuanglin Chemical reagent. Cetyltrimethylammonium bromide (CTAB), hydroquinone (HQ) and *p*-aminophenol (*p*-AP) were purchased from Macklin, and *p*-nitrophenol

was obtained from Sarn Chemical Technology (Shanghai). Ethanol, sodium chloride (NaCl), calcium chloride ($CaCl_2$), potassium chloride (KCl), ferric chloride ($FeCl_2$) and magnesium chloride ($MgCl_2$, 95%) were received from Hangzhou Gaojing Fine Chemical Industry. Bovine serum albumin (BSA) and hexaammonium ruthenium chloride ($Ru(NH_3)_6Cl_3$, 98%) were ordered from Sigma Aldrich (Shanghai, China). All aqueous solutions were prepared with ultrapure water (18.2 MΩ cm). Pond water and soil were obtained from the campus of Zhejiang Sci-Tech University.

2.2. Measurements and Instrumentations

Scanning electron microscopy (SEM) measurements were performed on an SU8100 scanning electron microscope (Hitachi, Japan) with an accelerating voltage of 10 kV. X-photoelectron spectroscopy (XPS) data were obtained from a PHI5300 electron spectrometer (PE Ltd., Waltham, MA, USA) at 250 W, 14 kV and Mg Kα radiation. All electrochemical tests, including cyclic voltammetry (CV) and differential pulse voltammetry (DPV), were carried out on a PGSTAT302N Autolab electrochemical workstation (Metrohm, Herisau, Switzerland). The test adopted a conventional three-electrode system, including bare or modified GCE as the working electrode (the electrode's size was 0.5 cm × 0.5 cm), a platinum sheet as the counter-electrode and an Ag/AgCl (saturated with KCl solution) electrode as the reference electrode. DPV test parameters were as follows: the step potential was 5 mV, the pulse amplitude was 25 mV, the pulse time was 0.05 s and the time interval was 0.2 s.

2.3. Preparation of 3DG-CNT/GCE and VMSF/3DG-CNT/GCE Electrodes

According to a previous literature report [45], 3DG-CNT were prepared on the GCE's surface by using the electrochemical method (Scheme 1). GO-CNT dispersion was first achieved by mixing GO (3 mg mL^{-1}) and CNT (0.3 mg mL^{-1}) into 0.2 M $NaClO_4$ with further sonication for 30 min. After being polished with 0.3 μm and 0.05 μm alumina powders and ultrasonically washed with ethanol and distilled water for 1 min each, a clean GCE was obtained. The GCE was soaked into the above GO-CNT dispersion and underwent a constant cathodic voltage of −1.2 V for 300 s with a platinum sheet electrode as the counter-electrode and an Ag/AgCl electrode (saturated with KCl) as the reference electrode. In this process, the GO was reduced to electrochemically reduced graphene oxide (ErGO), and a 3D nanocarbon composite consisting of graphene and CNT (termed 3DG-CNT) was deposited onto the GCE's surface. Note that the CNTs, as electronic conducting wires or spacers, could not only facilitate the electrochemical reduction of GO but also greatly increased the active area of the electrode. The obtained 3DG-CNT/GCE had the advantages of both graphene and CNT.

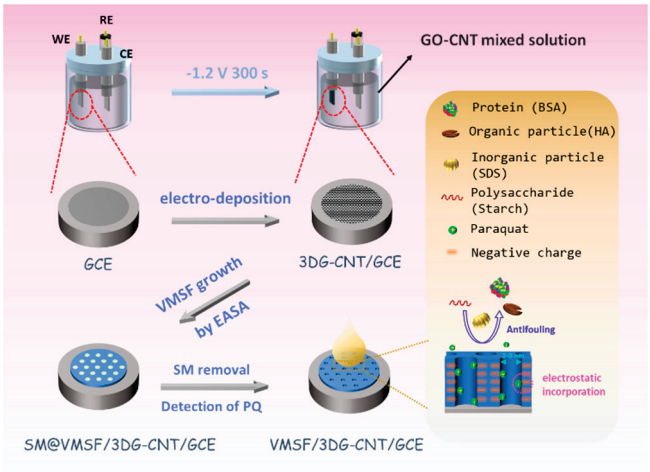

Scheme 1. Illustration of the preparation of VMSF/3DG-CNT/GCE and the direct detection of PQ in complex environmental samples.

VMSF were then grown on the 3DG-CNT/GCE using the EASA method [33]. Originating from the oxygen-containing groups of 3DG-CNT, VMSF formed a chemical bond with 3DG-CNT and displayed good stability on the GCE's surface using 3DG-CNT as the adhesive nanolayer. Briefly, TEOS (2.833 g) and CTAB (1.585 g) were added to a mixed solution of ethanol (20 mL) and $NaNO_3$ (20 mL, 0.1 M, pH = 2.6), followed by stirring for 2.5 h to prepare a silica precursor solution. Next, the platinum sheet, the Ag/AgCl electrode (saturated with KCl) and the 3DG-CNT/GCE were used as the counter-electrode, reference electrode and working electrode, respectively. These three electrodes were soaked in the precursor solution and the VMSF were prepared by applying a constant cathodic current density (–0.74 mA/cm^2) to the 3DG-CNT/GCE for 10 s. Thus, a surfactant micelle (SM)-templated VMSF formed on the surface of 3DG-CNT/GCE after being washed with distilled water and aged at 80 °C for 10 h, termed SM@VMSF/3DG-CNT/GCE. The SM@VMSF/3DG-CNT/GCE was immersed in a 0.1 M HCL–ethanol solution and stirred for 5 min to remove SM, finally achieving the VMSF/3DG-CNT/GCE with open channels.

3. Results

3.1. Characterization of 3DG-CNT/GCE and VMSF/3DG-CNT/GCE

The process of reducing GO to ErGO was studied by XPS and the results are shown in Figure 1a,b. As demonstrated, the high-resolution C1s spectra of both GO and ErGO revealed three types of carbon bonds, including C–C/C=C (sp^2 carbon, 284.4 eV), C–O (286.2 eV) and C=O (287.2 eV). When GO was electrochemically reduced to ErGO, the C-O peak could not be observed and the intensity of the C=O peak decreased, suggesting that the oxygen-containing functional groups of GO had been successfully reduced in the electrochemical process, and thus the graphene sheet had been reduced and removed. Figure 1c,d shows the SEM images of 3DG-CNT/GCE with different amplifications. As seen, there are many crumples perpendicularly aligned to the electrode's surface in the 3DG-CNT, indicating the increased effective specific surface area of the electrode and the improved accessible mass transfer. In the high-resolution SEM image shown in Figure 1b, a small amount of CNT can be observed, showing the successful preparation of 3DG-CNT.

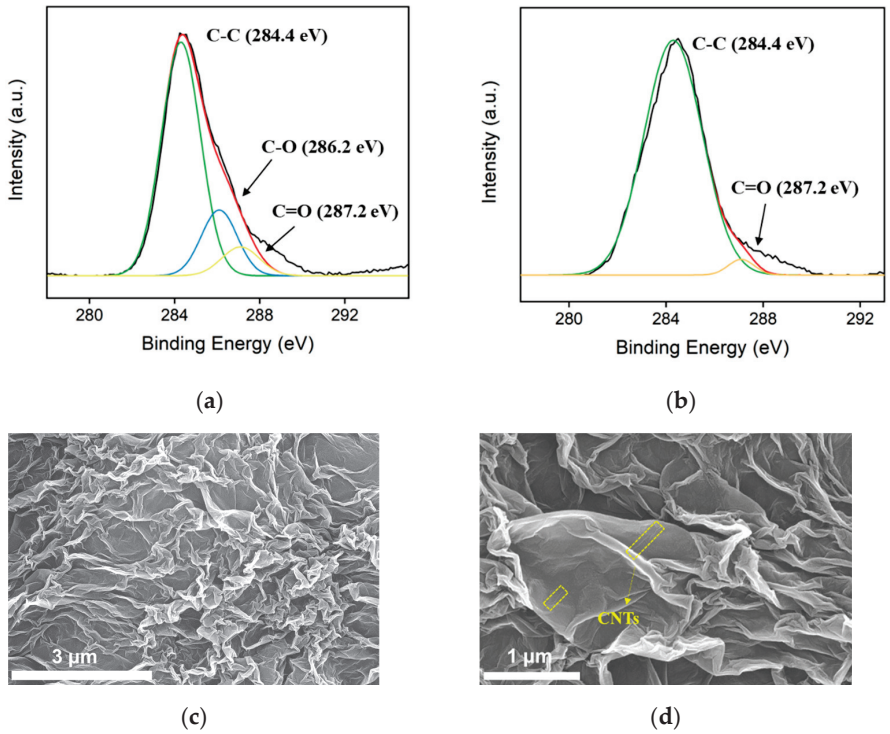

Figure 1. (**a**,**b**) The XPS C1s spectra of the GO (**a**) and ErGO (**b**). (**c**,**d**) SEM images of the 3DG-CNT network electrodeposited under a potential of −1.2 V for 300 s.

To investigate the structure and morphology of the VMSF on the 3DG-CNT/GCE, TEM measurements were performed. As shown in Figure 2a, the VMSF had uniform pores with a long-range order and the diameter was 2~3 nm. The pores were hexagonally aligned and very regular over a large domain. Cyclic voltammetry (CV) is considered to be an effective method to evaluate the intactness and permselectivity of VMSF [46]. Figure 2b displays the CV curves of bare GCE, SM@VMSF/3DG-CNT/GCE and VMSF/3DG-CNT/GCE in a 0.05 M KHP solution containing 0.5 mM $Ru(NH_3)_6^{3+}$. Due to the hinderance effect of the SM confined inside the silica nanochannels, only the charging current could be observed in the SM@VMSF/3DG-CNT/GCE. The VMSF/3DG-CNT/GCE with open channels produced a more obvious redox current peak compared with the bare GCE, showing the enrichment effect of cationic $Ru(NH_3)_6^{3+}$. This arose from the negative surface of VMSF with deprotonated silanol groups, which confirmed the potential of VMSF for the detection of cationic species.

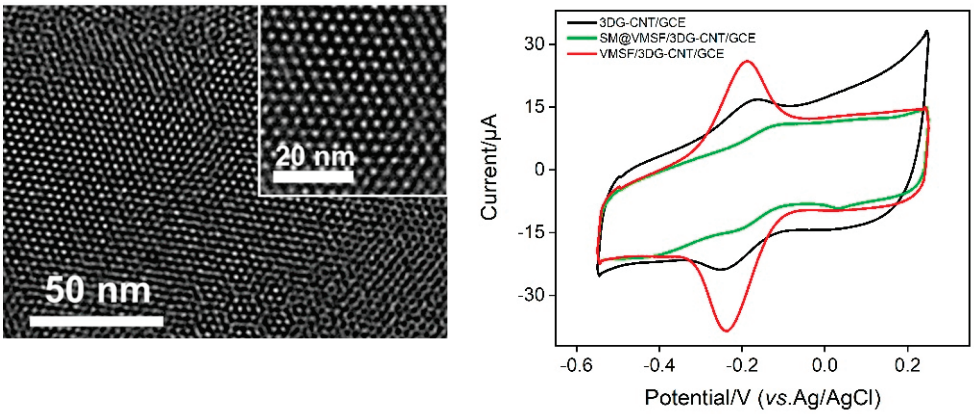

(**a**) (**b**)

Figure 2. (**a**) Top-view TEM image of the VMSF. The inset is the corresponding magnified image. (**b**) CV curves obtained for different electrodes in a 0.05 M KHP solution containing 0.5 mM $[Ru(NH_3)_6]^{3+}$.

According to previous literature reports [47], the effective electroactive areas of bare GCE and VMSF/3DG-CNT/GCE could be calculated by using the Randles–Sevcik equation

$$I_p = 0.4463nFAc(nF\nu D/RT)^{1/2} \quad (1)$$

where I_p reflects the peak current, n is the number of transferred electrons, F is the Faraday constant (96,485 c·mol^{-1}), A is the effective surface area, c is the concentration of $K_3[Fe(CN)_6]$ (mM), ν is the scan rate (ν·s^{-1}), D is the diffusion coefficient (6.67×10^{-6} cm^2·s^{-1}), R is the gas constant (8.314 J·mol^{-1}K^{-1}) and T is the Kelvin temperature (298 K).

Figure 3a shows the CV curves of the bare GCE and the VMSF/3DG-CNT/GCE in 0.1 M PBS (pH = 6). The pair of redox peaks around 0 V is due to the electrochemical reaction between the quinone and hydroxyquinone moieties in the 3DG-CNT. The cathodic current peak displayed at around –0.5 V is ascribed to the reduction of oxygen (Figure S1). As a comparison, the surface area of the VMSF/3DG-CNT/GCE is about 8.5 times larger than that of bare GCE, which is due to the formation of the 3D network structure of the 3DG-CNT nanocomposite. The effective surface area of bare GCE was calculated to be 0.0935 cm^2, according to the data shown in Figure 3b and Equation (1). Thus, the effective surface area of the VMSF/3DG-CNT/GCE was about 0.790 cm^2.

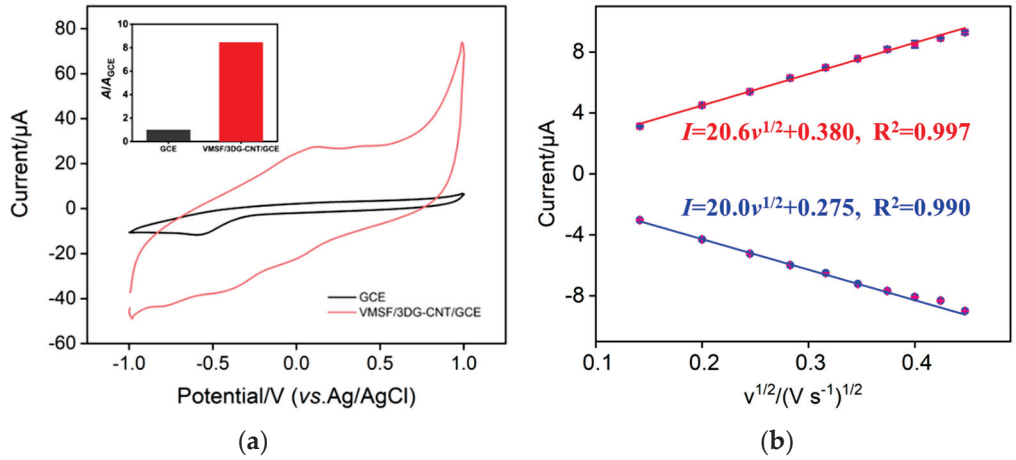

Figure 3. (**a**) CV curves of bare GCE (black) and VMSF/3DG-CNT/GCE (red) in PBS (0.1 M, pH = 6). The inset depicts the normalized electroactive surface area of each electrode. (**b**) Relationship between the peak currents and the square root of the scan rate derived from the CV curves of bare GCE in 0.05 M KHP containing 0.5 mM $K_3[Fe(CN)_6]$.

3.2. Electrochemical Behavior of PQ on the VMSF/3DG-CNT/GCE

In order to verify the feasibility and performance of the VMSF/3DG-CNT/GCE for the determination of PQ, we compared the CV and DPV responses of the bare GCE, 3DG-CNT/GCE and VMSF/3DG-CNT/GCE electrodes to PQ, and the results are shown in Figure 4. As displayed in Figure 4a, PQ showed a weak or no electrochemical response by the bare GCE and 3DG-CNT/GCE, but showed a pair of obvious reversible redox peaks with the VMSF/3DG-CNT/GCE, which involve a single-electron transfer reactions (Scheme 2) [48]. Moreover, the magnitude of the anodic peak current of PQ on the VMSF/3DG-CNT/GCE was around 15-fold greater than that of 3DG-CNT/GCE and was much higher than that of the bare GCE (Figure 4b). This excellent performance of the as-prepared VMSF/3DG-CNT/GCE is attributed to the electrocatalytic ability of the 3DG-CNT and the electrostatically enriched capacity of VMSF.

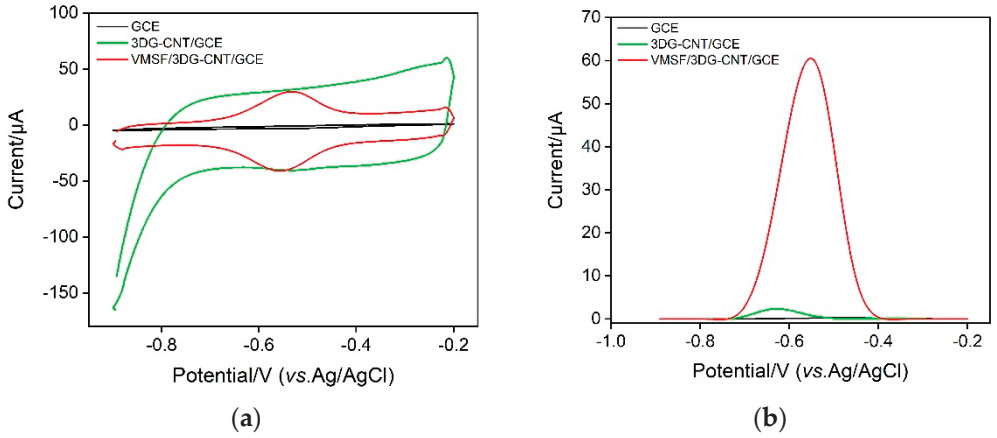

Figure 4. (**a**) CV and (**b**) DPV curves obtained with different electrodes in 0.1 M PBS (pH = 6) containing a 10 μM PQ solution.

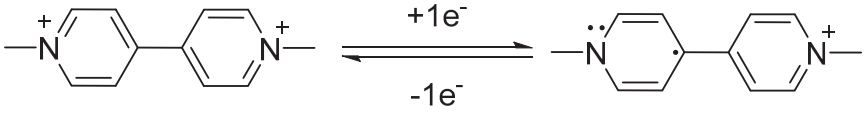

Scheme 2. Schematic diagram of PQ's reaction process.

3.3. Electrochemical Detection of PQ Using a VMSF/3DG-CNT/GCE Sensor

In order to achieve a highly sensitive performance for the detection and preparation PQ, the detection conditions, including the electrodeposition time of the 3DG-CNT, the growth time of the VMSF, the pH and the concentration of the supporting electrolyte and preconcentration time, were optimized. These results are shown in Figures S2.1–2.5 in the Supplementary Materials. As seen, a 3DG-CNT electrodeposition time of 300 s, a VMSF growth time of 10 s, 0.1 M PBS (pH = 6) and mechanical stirring for 180 s were the optimal experimental conditions. Next, the VMSF/3DG-CNT/GCE sensor was used to electrochemically detect PQ at various concentrations under optimized conditions. As revealed in Figure 5, when the PQ concentration varied from 2 nM to 10 μM, the anodic peak current (*I*) gradually increased and had a good linear relationship with the PQ's concentration (C_{PQ}), yielding two linear ranges of 2 nM–10 nM and 10 nM–10 μM. The linear regressive equations in the low and high concentration ranges are $I = 45.83\ C_{PQ} + 2.317$ ($R^2 = 0.987$) and $I = 8.129\ C_{PQ} + 2.675$ ($R^2 = 0.997$), respectively. The limit of detection (LOD) was 1.17 nM when the signal-to-noise ratio was 3 (S/N = 3). Table 1 lists the performance of different electrochemical sensors for the detection of PQ. By comparison, our sensor has a rather lower LOD and a wider linear range, showing good analytical performance.

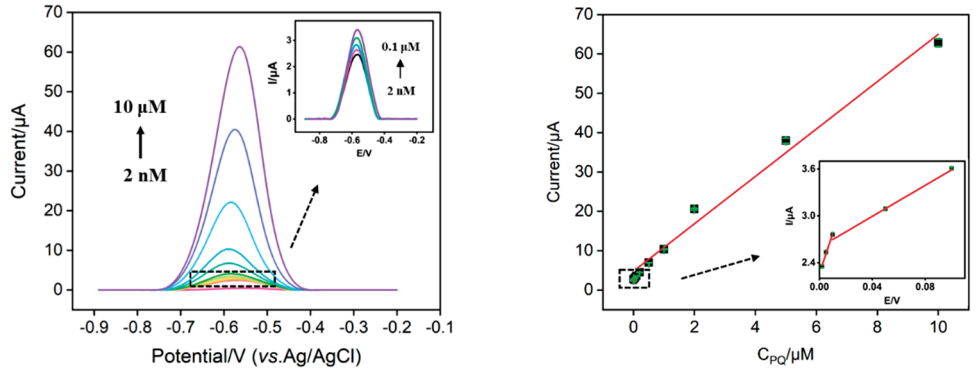

(**a**) (**b**)

Figure 5. (**a**) DPV curves of the VMSF/3DG-CNT/GCE obtained in PBS (0.1 M, pH = 6) containing different concentrations of PQ. The inset is the magnified view of the DPV curves in the low concentration region. (**b**) The calibration curve for PQ. The inset in (**b**) shows the calibration lines in the low concentration range. The error bars represent the standard deviation (SD) of three measurements.

Table 1. Comparison of the determination of PQ among different methods.

Electrode Materials	Method	Detection Range (μM)	Sensitivity (μA μM^{-1} cm^{-2})	LOD (nM)	Refs.
AuNP-MWCNT/GCE	SWV	1–2	–	32	[49]
VMSF/GCE	SWV	0.01–0.05	42	12	[48]
BW-CB/GCE	DPV	0.5–7.5	0.487	–	[50]
BN/MoS_2/Au NPs/GCE	DPV	0.1–100	4.44×10^{-5}	74	[3]
SPCE-CNT/Nafion	DPV	0.54–4.3	–	170	[1]
PPY-g-NGE/GCE	DPV	0.05–2	–	41	[51]
Micro-Cu_2O/PVP-GNs/GC-RDE	DPV	1–200	3.00×10^{-5}	260	[52]
VMSF/3DG-CNT/GCE	DPV	0.002–0.01 0.01–10	0.0578 0.0103	1.17	This work

AuNP, Au nanoparticle; MWCNT, multiwalled carbon nanotubes; SWV, square wave voltammetry; BW, beeswax; CB, carbon black; DPV, differential pulse voltammetry; BN, hexagonal boron nitride; MoS_2, molybdenum disulfide; SPCE, screen-printed carbon electrode; SI-DPV, sequential injection-differential pulse voltametric; PPY-g, polypyrrole-grafted; NGE, nitrogen-doped graphene; Micro-Cu_2O, cuprous oxide sub-microparticles; PVP, polyvinyl pyrrolidone; GNs, graphene nanosheets; GC-RED, glassy carbon-rotating disk electrode.

3.4. The Anti-Interference and Repeatability of the VMSF/3DG-CNT/GCE Sensor

The anti-interference ability of the VMSF/3DG-CNT/GCE electrode was investigated. Common interfering substances in the environment, such as metal ions (Na^+, K^+, Cd^{2+}, Mg^{2+} and Cu^{2+}), and other possible small electroactive molecules and environmental pollutants (hydroquinone (HQ), catechol (CC), *p*-aminophenol (*p*-AP) and p-nitrophenol (*p*-NP)) were added to the detection solution containing 1 μM PQ. As shown in Figure S3.1A, when 100 μM of metal ions or 10 μM of electroactive molecules was present in the detected solution, almost no effect on the detection of PQ was observed. It was found that Cu^{2+}, HQ, CC, *p*-AP and *p*-NP had no anodic current peaks in the detected potential window of paraquat and the voltammetric peak of Cd^{2+} was around −0.77 V, which is far from that of paraquat (−0.58 V), indicating the good anti-interference ability of VMSF/3DG-CNT/GCE. In addition, the repeatability of the VMSF/3DG-CNT/GCE electrode was evaluated. VMSF/3DG-CNT/GCE was used to repeatedly detect 1 μM PQ, and the anodic peak currents obtained from five measurements were almost same (Figure S3.2), showing the excellent repeatability of the proposed sensor. After 5 days of storage, our VMSF/3DG-CNT/GCE sensor displayed good stability (Figure S3.3).

3.5. Real Sample Analysis

The anti-fouling ability of the VMSF/3DG-CNT/GCE is very important for the analysis of real samples. Surfactants (sodium dodecyl sulfate, SDS), protein (bovine serum albumin, BSA), polysaccharide (starch) and macromolecular substances (humic acid, HA) commonly exist in complex samples and may produce severe surface fouling of an electrode. These were used to verify the anti-fouling ability of the VMSF/3DG-CNT/GCE. We compared the anodic peak currents of PQ on the VMSF/3DG-CNT/GCE and 3DG-CNT/GCE with (I) and without (I_0) fouling substances. As exhibited in Figure 6, the presence of fouling substances could generate surface fouling of the 3DG-CNT/GCE and passivate the sensor, leading to remarkably decreased peak currents (only 20~40% of the initial values) and much wider current peaks. However, 95% of the initial values still remained for the VMSF/3DG-CNT/GCE, indicating the excellent anti-fouling capacity of the VMSF/3DG-CNT/GCE and the great potential for the detection of PQ in complex samples.

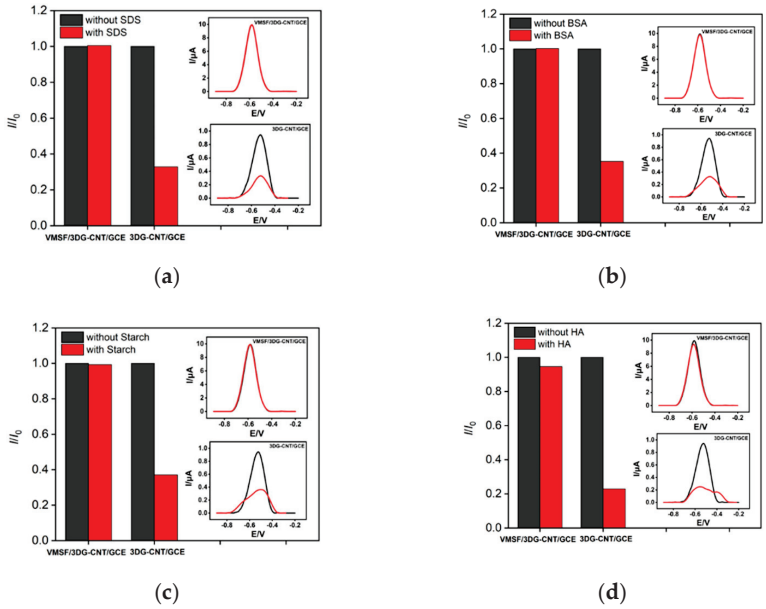

(**a**) (**b**) (**c**) (**d**)

Figure 6. Normalized oxidation peak current ratio of the VMSF/3DG-CNT/GCE and 3DG-CNT/GCE towards PQ (1 μM). I and I_0 represent the currents obtained in the present and absence of 20 μg/mL of SDS (**a**), BSA (**b**), starch (**c**) or HA (**d**) in 0.1 M PBS (pH = 6). The insets are the corresponding DPV curves obtained for the 3DG-CNT/GCE and VMSF/3DG-CNT/GCE in the absence and presence of the fouling species.

Environmental water samples including pond water and a soil leaching solution were used to examine the applicability of the proposed VMSF/3DG-CNT/GCE. Pond water was diluted 10-fold with 0.1 M PBS (pH = 6). Moreover, 0.05 g of soil was added to 50 mL of PBS (pH = 6) to obtain a soil dispersion and the supernatant was directly used as a soil leaching solution for analysis of a real sample. The detection samples were first spiked with several known concentrations of PQ and examined by our VMSF/3DG-CNT/GCE sensor. By comparing the ratio of the concentration detected and the known concentration (recovery), we found that the recoveries achieved are 94.5–109% and the relative standard deviations (RSD) were within 2.3% (Table 2), suggesting the good accuracy and reliability of the VMSF/3DG-CNT/GCE for the determination of PQ in environmental water samples.

Table 2. Determination of PQ in pond water and soil leaching solution samples.

Sample	Spiked (μM)	Found (μM)	RSD (%, n = 3)	Recovery (%)
Pond water	0.0500	0.0499	1.8	99.8
	0.100	0.109	1.8	109
	0.200	0.199	2.3	99.5
Soil leaching solution	0.100	0.100	2.3	100
	0.200	0.189	3.3	94.5
	0.300	0.313	3.3	104

4. Conclusions

In summary, VMSF/3DG-CNT were prepared on the GCE's surface by using a simple and controllable electrochemical method. The obtained VMSF/3DG-CNT/GCE sensor had several advantages. Firstly, the 3DG-CNT nanocarbon composite with a 3D network structure, good conductivity and oxygen-containing functional groups not only displayed a high electroactive area and excellent electrocatalytic ability, but also provided a suitable microenvironment for the stable growth of VMSF. Second, the electrocatalytic capacity of the inner 3DG-CNT layer and the electrostatic enrichment ability of VMSF were combined, showing superior analytical performance regarding PQ in terms of a low LOD and a wide linear range. Thirdly, given the inherent anti-fouling ability of VMSF, the VMSF/3DG-CNT/GCE was successfully applied for the detection of PQ in environmental water samples. Lastly, the fabrication of VMSF/3DG-CNT/GCE sensors is easy, economic and controllable, and could be extended to detect other varieties of analytes by simple functionalization of the 3DG-CNT or VMSF.

Supplementary Materials: The following supporting information can be downloaded at https://www.mdpi.com/article/10.3390/nano12203632/s1. Figure S1: CV curves of bare GCE and VMSF/3DG-CNT/GCE in deoxygenated PBS; Figure S2.1: Optimization of electrodeposition time of 3DG-CNT; Figure S2.2: Optimization of growth time of VMSF; Figure S2.3: Optimization of pH of supporting electrolyte. Figure S2.4: Optimization of concentration of supporting electrolyte; Figure S2.5: Optimization of preconcentration time. Figure S3.1: Anti-interference ability of VMSF/3DG-CNT/GCE; Figure S3.2: Repeatability of VMSF/3DG-CNT/GCE; Figure S3.3: Stability of VMSF/3DG-CNT/GCE.

Author Contributions: Data curation, R.S., G.Y. and L.L.; writing—original draft preparation, W.Z.; writing—review and editing, F.Y. All authors have read and agreed to the published version of the manuscript.

Funding: This work was supported by the National Natural Science Foundation of China (21904117) and Zhejiang Provincial Natural Science Foundation of China (LY21B050003).

Data Availability Statement: The data presented in this study are available on request from the corresponding author.

Conflicts of Interest: The authors declare no conflict of interest.

References

1. Chuntib, P.; Themsirimongkon, S.; Saipanya, S.; Jakmunee, J. Sequential injection differential pulse voltammetric method based on screen printed carbon electrode modified with carbon nanotube/Nafion for sensitive determination of paraquat. *Talanta* **2017**, *170*, 1–8. [CrossRef] [PubMed]
2. Taguchi, V.Y.; Jenkins, S.W.; Crozier, P.W.; Wang, D.T. Determination of diquat and paraquat in water by liquid chromatography-(electrospray ionization) mass spectrometry. *J. Am. Soc. Mass Spectrom.* **1998**, *9*, 830–839. [CrossRef]
3. Zhang, J.; Lin, Z.; Qin, Y.; Li, Y.; Liu, X.; Li, Q.; Huang, H. Fabricated Electrochemical Sensory Platform Based on the Boron Nitride Ternary Nanocomposite Film Electrode for Paraquat Detection. *ACS Omega* **2019**, *4*, 18398–18404. [CrossRef] [PubMed]
4. De Figueiredo-Filho, L.C.S.; Baccarin, M.; Janegitz, B.C.; Fatibello-Filho, O. A disposable and inexpensive bismuth film minisensor for a voltammetric determination of diquat and paraquat pesticides in natural water samples. *Sens. Actuators B Chem.* **2017**, *240*, 749–756. [CrossRef]
5. Valera, E.; García-Febrero, R.; Pividori, I.; Sánchez-Baeza, F.; Marco, M.P. Coulombimetric immunosensor for paraquat based on electrochemical nanoprobes. *Sens. Actuators B Chem.* **2014**, *194*, 353–360. [CrossRef]
6. Podder, B.; Kim, Y.-S.; Zerin, T.; Song, H.-Y. Antioxidant effect of silymarin on paraquat-induced human lung adenocarcinoma A549 cell line. *Food Chem. Toxicol.* **2012**, *50*, 3206–3214. [CrossRef]
7. Li, M.; Wang, X.; Zhu, Y.; Jia, X.; Zhang, S.; Wang, H.; Li, Y.; Hu, G. Fe_2O_3-decorated boron/nitrogen-co-doped carbon nanosheets as an electrochemical sensing platform for ultrasensitive determination of paraquat in natural water. *Chin. Chem. Lett.* **2022**. [CrossRef]
8. Konthonbut, P.; Kongtip, P.; Nankongnab, N.; Tipayamongkholgul, M.; Yoosook, W.; Woskie, S. Paraquat Exposure of Pregnant Women and Neonates in Agricultural Areas in Thailand. *Int. J. Environ. Res. Public Health* **2018**, *15*, 1163. [CrossRef]
9. Rai, M.K.; Das, J.V.; Gupta, V.K. A sensitive determination of paraquat by spectrophotometry. *Talanta* **1997**, *45*, 343–348. [CrossRef]
10. Qin, L.; Zhang, X.; Wu, J.; Zhang, W.; Lu, X.; Sun, H.; Zhang, J.; Guo, L.; Xie, J. Quantification and toxicokinetics of paraquat in mouse plasma and lung tissues by internal standard surface-enhanced Raman spectroscopy. *Anal. Bioanal. Chem.* **2022**, *414*, 2371–2383. [CrossRef]
11. Wachholz, D., Jr.; Deroco, P.B.; Kubota, L.T. A copper-based metal-organic framework/reduced graphene oxide-modified electrode for electrochemical detection of paraquat. *Microchim. Acta* **2022**, *189*, 278. [CrossRef] [PubMed]
12. Traiwatcharanon, P.; Siriwatcharapiboon, W.; Jongprateep, O.; Wongchoosuk, C. Electrochemical paraquat sensor based on lead oxide nanoparticles. *RSC Adv.* **2022**, *12*, 16079–16092. [CrossRef] [PubMed]
13. Jiang, Y.; Li, Q.; Yao, J.; Guo, X.; Ying, Y.; Liu, X.; Wen, Y.; Yang, H.; Wu, Y. Advanced photoelectrochemical detection of paraquat based on plasmonic metal modified photocathode material. *Appl. Surf. Sci.* **2022**, *581*, 151903. [CrossRef]
14. Walcarius, A. Mesoporous materials and electrochemistry. *Chem. Soc. Rev.* **2013**, *42*, 4098–4140. [CrossRef] [PubMed]
15. Xu, Y.; Song, Y.; Xu, F. TEMPO oxidized cellulose nanofibers-based heterogenous membrane employed for concentration-gradient-driven energy harvesting. *Nano Energy* **2021**, *79*, 105468. [CrossRef]
16. Cheng, P.; Chen, S.; Li, X.; Xu, Y.; Xu, F.; Ragauskas, A.J. Tree-inspired lignin microrods-based composite heterogeneous nanochannels for ion transport and osmotic energy harvesting. *Energy Convers. Manag.* **2022**, *255*, 115321. [CrossRef]
17. Gong, J.; Tang, H.; Wang, M.; Lin, X.; Wang, K.; Liu, J. Novel three-dimensional graphene nanomesh prepared by facile electro-etching for improved electroanalytical performance for small biomolecules. *Mater. Des.* **2022**, *215*, 110506. [CrossRef]
18. Zhou, H.; Dong, G.; Sailjoi, A.; Liu, J. Facile Pretreatment of Three-Dimensional Graphene through Electrochemical Polarization for Improved Electrocatalytic Performance and Simultaneous Electrochemical Detection of Catechol and Hydroquinone. *Nanomaterials* **2022**, *12*, 65. [CrossRef]
19. Liang, R.; Jiang, J.; Zheng, Y.; Sailjoi, A.; Chen, J.; Liu, J.; Li, H. Vertically oriented mesoporous silica film modified fluorine-doped tin oxide electrode for enhanced electrochemiluminescence detection of lidocaine in serum. *RSC Adv.* **2021**, *11*, 34669–34675. [CrossRef]
20. Wei, X.; Luo, X.; Xu, S.; Xi, F.; Zhao, T. A Flexible Electrochemiluminescence Sensor Equipped With Vertically Ordered Mesoporous Silica Nanochannel Film for Sensitive Detection of Clindamycin. *Front. Chem.* **2022**, *10*, 872582. [CrossRef]
21. Liu, Q.; Zhong, H.; Chen, M.; Zhao, C.; Liu, Y.; Xi, F.; Luo, T. Functional nanostructure-loaded three-dimensional graphene foam as a non-enzymatic electrochemical sensor for reagentless glucose detection. *RSC Adv.* **2020**, *10*, 33739–33746. [CrossRef] [PubMed]
22. Cui, Y.; Duan, W.; Jin, Y.; Wo, F.; Xi, F.; Wu, J. Ratiometric Fluorescent Nanohybrid for Noninvasive and Visual Monitoring of Sweat Glucose. *ACS Sens.* **2020**, *5*, 2096–2105. [CrossRef] [PubMed]
23. Zhang, J.; Yang, L.; Pei, J.; Tian, Y.; Liu, J. A reagentless electrochemical immunosensor for sensitive detection of carcinoembryonic antigen based on the interface with redox probe-modified electron transfer wires and effectively immobilized antibody. *Front. Chem.* **2022**, *10*, 939736. [CrossRef]
24. Liu, X.; Chen, Z.; Wang, T.; Jiang, X.; Qu, X.; Duan, W.; Xi, F.; He, Z.; Wu, J. Tissue Imprinting on 2D Nanoflakes-Capped Silicon Nanowires for Lipidomic Mass Spectrometry Imaging and Cancer Diagnosis. *ACS Nano* **2022**, *16*, 6916–6928. [CrossRef]
25. Serrano, M.B.; Despas, C.; Herzog, G.; Walcarius, A. Mesoporous silica thin films for molecular sieving and electrode surface protection against biofouling. *Electrochem. Commun.* **2015**, *52*, 34–36. [CrossRef]

26. Ma, K.; Yang, L.; Liu, J.; Liu, J. Electrochemical Sensor Nanoarchitectonics for Sensitive Detection of Uric Acid in Human Whole Blood Based on Screen-Printed Carbon Electrode Equipped with Vertically-Ordered Mesoporous Silica-Nanochannel Film. *Nanomaterials* **2022**, *12*, 1157. [CrossRef]
27. Yan, F.; Luo, T.; Jin, Q.; Zhou, H.; Sailjoi, A.; Dong, G.; Liu, J.; Tang, W. Tailoring molecular permeability of vertically-ordered mesoporous silica-nanochannel films on graphene for selectively enhanced determination of dihydroxybenzene isomers in environmental water samples. *J. Hazard. Mater.* **2021**, *410*, 124636. [CrossRef]
28. Wang, K.; Yang, L.; Huang, H.; Lv, N.; Liu, J.; Liu, Y. Nanochannel Array on Electrochemically Polarized Screen Printed Carbon Electrode for Rapid and Sensitive Electrochemical Determination of Clozapine in Human Whole Blood. *Molecules* **2022**, *27*, 2739. [CrossRef]
29. Zhou, P.; Yao, L.; Chen, K.; Su, B. Silica Nanochannel Membranes for Electrochemical Analysis and Molecular Sieving: A Comprehensive Review. *Crit. Rev. Anal. Chem.* **2020**, *50*, 424–444. [CrossRef]
30. Gong, J.; Zhang, T.; Chen, P.; Yan, F.; Liu, J. Bipolar silica nanochannel array for dual-mode electrochemiluminescence and electrochemical immunosensing platform. *Sens. Actuators B Chem.* **2022**, *368*, 132086. [CrossRef]
31. Gong, J.; Zhang, T.; Luo, T.; Luo, X.; Yan, F.; Tang, W.; Liu, J. Bipolar silica nanochannel array confined electrochemiluminescence for ultrasensitive detection of SARS-CoV-2 antibody. *Biosens. Bioelectron.* **2022**, *215*, 114563. [CrossRef] [PubMed]
32. Teng, Z.; Zheng, G.; Dou, Y.; Li, W.; Mou, C.-Y.; Zhang, X.; Asiri, A.M.; Zhao, D. Highly Ordered Mesoporous Silica Films with Perpendicular Mesochannels by a Simple Stöber-Solution Growth Approach. *Angew. Chem. Int. Ed.* **2012**, *51*, 2173–2177. [CrossRef] [PubMed]
33. Walcarius, A.; Sibottier, E.; Etienne, M.; Ghanbaja, J. Electrochemically assisted self-assembly of mesoporous silica thin films. *Nat. Mater.* **2007**, *6*, 602–608. [CrossRef] [PubMed]
34. Ma, K.; Zheng, Y.; An, L.; Liu, J. Ultrasensitive Immunosensor for Prostate-Specific Antigen Based on Enhanced Electrochemiluminescence by Vertically Ordered Mesoporous Silica-Nanochannel Film. *Front. Chem.* **2022**, *10*, 851178. [CrossRef] [PubMed]
35. Walcarius, A. Electroinduced Surfactant Self-Assembly Driven to Vertical Growth of Oriented Mesoporous Films. *Acc. Chem. Res.* **2021**, *54*, 3563–3575. [CrossRef]
36. Yan, F.; Chen, J.; Jin, Q.; Zhou, H.; Sailjoi, A.; Liu, J.; Tang, W. Fast one-step fabrication of a vertically-ordered mesoporous silica-nanochannel film on graphene for direct and sensitive detection of doxorubicin in human whole blood. *J. Mater. Chem. C* **2020**, *8*, 7113–7119. [CrossRef]
37. Lu, L.; Zhou, L.; Chen, J.; Yan, F.; Liu, J.; Dong, X.; Xi, F.; Chen, P. Nanochannel-Confined Graphene Quantum Dots for Ultrasensitive Electrochemical Analysis of Complex Samples. *ACS Nano* **2018**, *12*, 12673–12681. [CrossRef]
38. Zhou, L.; Ding, H.; Yan, F.; Guo, W.; Su, B. Electrochemical detection of Alzheimer's disease related substances in biofluids by silica nanochannel membrane modified glassy carbon electrodes. *Analyst* **2018**, *143*, 4756–4763. [CrossRef]
39. Gong, J.; Tang, H.; Luo, X.; Zhou, H.; Lin, X.; Wang, K.; Fei, Y.; Xi, F.; Liu, J. Vertically Ordered Mesoporous Silica-Nanochannel Film-Equipped Three-Dimensional Macroporous Graphene as Sensitive Electrochemiluminescence Platform. *Front. Chem.* **2021**, *9*, 770512. [CrossRef]
40. Xi, F.; Xuan, L.; Lu, L.; Huang, J.; Yan, F.; Liu, J.; Dong, X.; Chen, P. Improved adhesion and performance of vertically-aligned mesoporous silica-nanochannel film on reduced graphene oxide for direct electrochemical analysis of human serum. *Sens. Actuators B Chem.* **2019**, *288*, 133–140. [CrossRef]
41. Xuan, L.; Liao, W.; Wang, M.; Zhou, H.; Ding, Y.; Yan, F.; Liu, J.; Tang, H.; Xi, F. Integration of vertically-ordered mesoporous silica-nanochannel film with electro-activated glassy carbon electrode for improved electroanalysis in complex samples. *Talanta* **2021**, *225*, 122066. [CrossRef] [PubMed]
42. Zhu, X.; Xuan, L.; Gong, J.; Liu, J.; Wang, X.; Xi, F.; Chen, J. Three-dimensional macroscopic graphene supported vertically-ordered mesoporous silica-nanochannel film for direct and ultrasensitive detection of uric acid in serum. *Talanta* **2022**, *238*, 123027. [CrossRef] [PubMed]
43. Zhou, H.; Ma, X.; Sailjoi, A.; Zou, Y.; Lin, X.; Yan, F.; Su, B.; Liu, J. Vertical silica nanochannels supported by nanocarbon composite for simultaneous detection of serotonin and melatonin in biological fluids. *Sens. Actuators B Chem.* **2022**, *353*, 131101. [CrossRef]
44. Zou, Y.; Zhou, X.; Xie, L.; Tang, H.; Yan, F. Vertically-Ordered Mesoporous Silica Films Grown on Boron Nitride-Graphene Composite Modified Electrodes for Rapid and Sensitive Detection of Carbendazim in Real Samples. *Front. Chem.* **2022**, *10*, 939510. [CrossRef]
45. Asadian, E.; Shahrokhian, S.; Iraji Zad, A.; Ghorbani-Bidkorbeh, F. Glassy carbon electrode modified with 3D graphene–carbon nanotube network for sensitive electrochemical determination of methotrexate. *Sens. Actuators B Chem.* **2017**, *239*, 617–627. [CrossRef]
46. Luo, X.; Zhang, T.; Tang, H.; Liu, J. Novel electrochemical and electrochemiluminescence dual-modality sensing platform for sensitive determination of antimicrobial peptides based on probe encapsulated liposome and nanochannel array electrode. *Front. Nutr.* **2022**, *9*, 962736. [CrossRef]
47. Alam, A.U.; Deen, M.J. Bisphenol A Electrochemical Sensor Using Graphene Oxide and β-Cyclodextrin-Functionalized Multi-Walled Carbon Nanotubes. *Anal. Chem.* **2020**, *92*, 5532–5539. [CrossRef]
48. Nasir, T.; Herzog, G.; Hebrant, M.; Despas, C.; Liu, L.; Walcarius, A. Mesoporous silica thin films for improved electrochemical detection of paraquat. *ACS Sens.* **2018**, *3*, 484–493. [CrossRef]

49. Rajaram, R.; Gurusamy, T.; Ramanujam, K.; Neelakantan, L. Electrochemical Determination of Paraquat Using Gold Nanoparticle Incorporated Multiwalled Carbon Nanotubes. *J. Electrochem. Soc.* **2022**, *169*, 47522. [CrossRef]
50. de Souza, D.C.; Orzari, L.O.; de Oliveira, P.R.; Kalinke, C.; Bonacin, J.A.; Malaspina, O.; Nocelli, R.C.F.; Janegitz, B.C. Electrochemical Sensor Based on Beeswax and Carbon Black Thin Biofilms for Determination of Paraquat in Apis mellifera Honey. *Food Anal. Methods* **2020**, *14*, 606–615. [CrossRef]
51. Li, J.; Lei, W.; Xu, Y.; Zhang, Y.; Xia, M.; Wang, F. Fabrication of polypyrrole-grafted nitrogen-doped graphene and its application for electrochemical detection of paraquat. *Electrochim. Acta* **2015**, *174*, 464–471. [CrossRef]
52. Ye, X.; Gu, Y.; Wang, C. Fabrication of the Cu2O/polyvinyl pyrrolidone-graphene modified glassy carbon-rotating disk electrode and its application for sensitive detection of herbicide paraquat. *Sens. Actuators B Chem.* **2012**, *173*, 530–539. [CrossRef]

nanomaterials

MDPI

Article

A Novel Fabrication of Single Electron Transistor from Patterned Gold Nanoparticle Array Template-Prepared by Polystyrene Nanospheres

Jingyue Fang [1], Xinxing Li [2], Wenke Xie [1] and Kehui Sun [1,*]

[1] School of Physics and Electronics, Central South University, Changsha 410073, China
[2] Key Laboratory of Nanodevices, Suzhou Institute of Nano-Tech and Nano-Bionics, CAS, Suzhou 215213, China
* Correspondence: kehui@csu.edu.cn; Tel.: +86-0731-88836457

Abstract: In this paper, polystyrene microspheres were firstly prepared by seeded emulsion polymerization, and the uniform monolayer of polystyrene microspheres was prepared on the substrate by the dipping method. Then, polystyrene monolayer film was used as a mask and a low dimensional array structure of gold was prepared by bottom-up self-assembly process. After that, the method of solution etching and annealing was used, and the gold nanoparticle array was post-processed. As a result, gold nanoparticles were recrystallized, with an average diameter of about 50 nm. Subsequently, the semiconductor process was adopted, with focused ion beams induced deposition and electron beam evaporation, and single electron transistors were fabricated, based on self-assembled gold nanoparticles. Finally, the devices were fixed in a liquid helium cryostat and Coulomb blockade was observed at 320 mK. It is a novel fabrication of a single electron transistor based on gold nanoparticle array template and prepared with polystyrene nanospheres.

Keywords: single electron transistor; gold nanoparticle; self-assemble; Coulomb blockade

1. Introduction

As early as 1951, Cornellis Gorter, who is a member of the Kamerlingh Onnes laboratory in the Netherlands, reported Coulomb blocking, studying the single electron phenomenon [1]. Nanoparticles have long been prepared by physical or chemical methods. These nanoparticles served as a Coulomb Island and a single-electron transistor could be prepared by this bottom-up method, to study the single electron phenomenon. In 1995, Chen et al. prepared AuPd nanoparticles with dimensions of 2–3 nm. The single electron transistor constructed exhibited a significant Coulomb blocking effect at 77 K and nonvolatile voltammetry features even at room temperature [2]. In 1996, David L. Klein et al. used a size~5.8 nm Au nanoparticle and CdSe nanoparticles to construct a single electron transistor, and a clear Coulomb step curve was observed at a temperature of 77 K [3]. In 1997, Toshihiko Sato et al. used the molecular self-assembly method to locate Au quantum dots with a diameter of ~10 nm on silicon substrates and prepared a single electron transistor. Coulomb steps and Coulomb oscillations were observed at 4.2 K [4]. In 2010, Hidehiro Yamaguchi et al. used an oligothiophene pentamer to assemble Au quantum dots between nanoelectrodes and measured the differential conductance image at 12 K, the image showed a typical Coulomb diamond, indicating that the device was a single electron transistor [5].

There are three key technical problems in the preparation of existing single-electron transistors: controllable preparation of a small-sized Coulomb Island; controlled positioning assembly of the Coulomb Island; precise control of the size of tunneling barrier between the Coulomb Island and electrode. This is related to the device's operating temperature and its performance consistency. Therefore, researchers have long been eager to develop a

method that can precisely control the size and location of the Coulomb Island, and control the size of the barrier between the Coulomb Island and the electrode to greatly facilitate the preparation and application of single-electron transistors. For example, by fabricating a narrow gap between the source and drain electrodes, the access resistance is reduced and the number of dots involved in the SET operation also diminishes [6]. Willing S. et al. adopted the method of self-assembly of colloidal metal nanoparticle strips, and, since the size of metal nanoparticles and the tunnel barrier width are adjustable, the transistor showed controllable characteristics [7]. In this paper, we propose a method for preparing single electron transistors. The size of Au particles can be controlled by controlling the particle size in a PS microsphere template, the coating time, wet etching and annealing. The thickness of the barrier layer can be precisely controlled by controllable thin film preparation methods, such as double beam deposition or atomic layer deposition. In the double beam system, the in-situ device preparation and the assembly and positioning of the Coulomb island and electrode for the regular periodically arranged Au particle array also becomes simpler. The electron tunneling characteristics of single electron transistors with quantum dots as the core structure have been the frontier and hotspot of the research. Based on this characteristic, it is possible to develop highly sensitive single photon detection devices.

2. Materials and Methods

2.1. Preparation of Polystyrene Microspheres

Monodispersed polystyrene (PS) microspheres were prepared by seed emulsion polymerization. First, the styrene was washed with sodium hydroxide, dried with anhydrous calcium chloride, and then heated to about 50 to 60 °C in a vacuum distillation apparatus to complete the purification of the reagent. Then, the preparation of monodispersed PS microspheres started. Nitrogen gas was introduced into a three-necked round bottom flask in the presence of a reflux device and equipped with a mechanical stirrer. Then, deionized water and alcohol were added, the mixture was stirred and rapidly added to the styrene, reacting for 8 h to obtain a seed emulsion. The effect of the temperature and the stability of the stirring speed were relatively large. Alternatively, it could be stirred for a while, and the initiator reaction added after the system stabilized.

2.2. Preparation of Polystyrene Microspheres Monolayer

After preparation of the PS microsphere emulsion, the substrate was subjected to hydrophilic treatment, and then the PS microsphere template was prepared by the pulling assembly [8,9]. PS microsphere mixed liquor was applied to the washed and dried quartz substrate, and it was observed that the white mixed liquor spread evenly on the substrate. A certain amount of distilled water was then trickled into the culture dish and the substrate sank slowly into the water. The white nanosphere suspension spread evenly on the liquid surface and formed a large area of the film floating on the liquid surface. After a period of time, 2% of the sodium dodecyl sulfate solution was dropped on the liquid surface to change the surface tension of the liquid surface. The liquid surface dropped from the center to the surrounding sudden diffusion so that the film was more closely arranged. When the liquid surface was stable, the substrate fixed on the moving rail was moved down at a certain speed from the blank surface until the substrate sunk into the water. A small amount of sodium dodecyl sulfate solution was added dropwise to "drive" the selected film onto the substrate until the liquid level was stabilized and pulled at a uniform and slow rate to transfer the film onto the substrate completely dry. Then the PS microsphere monolayer film template, shown in Figure 1a, was obtained.

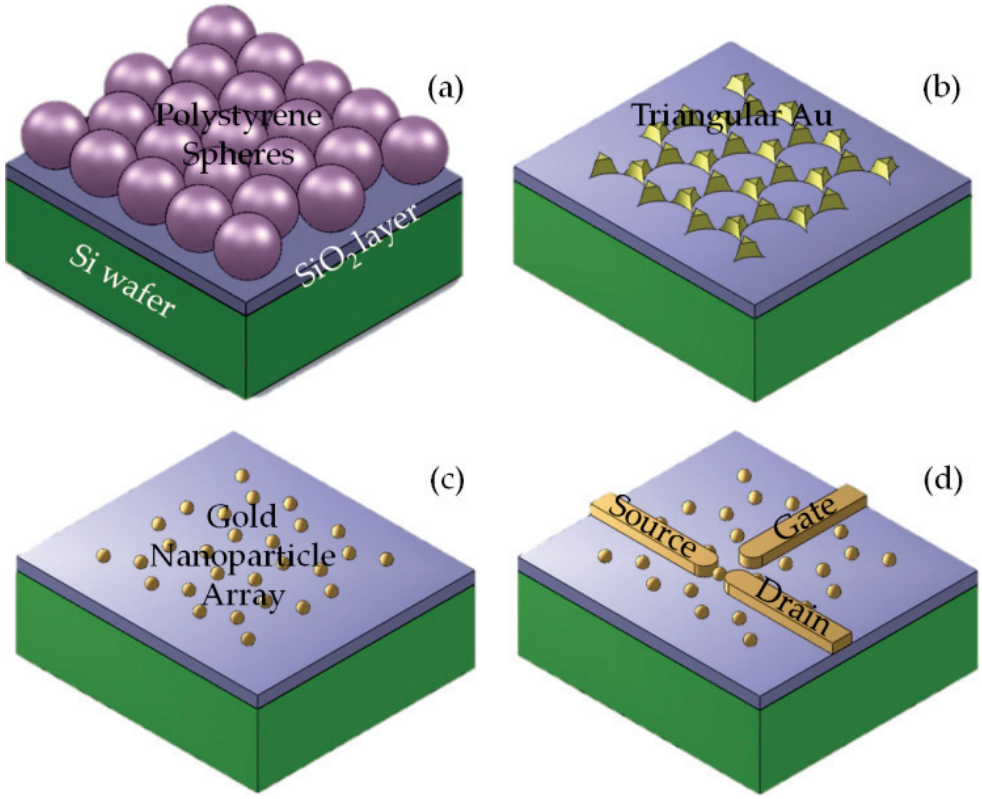

Figure 1. Schematic diagram of the process for SET preparation. (**a**) The PS microsphere monolayer was prepared on Si wafer; (**b**) Triangular gold array was prepared by the PS microsphere template; (**c**) Gold nanoparticle array was prepared by means of solution etching and annealing; (**d**) After 6 nm-thick-SiO_2 was deposited on the gold nanoparticle array, typical electrodes were prepared.

2.3. Preparation of Gold Nanoparticle Arrays

Furthermore, we used monolayer polystyrene microsphere templates as masks to prepare gold nanoparticle arrays [10]. The metal was deposited on the substrate on which the PS microsphere template was assembled by means of electron beam evaporation coating. After deposition, the mixture was ultrasonically cleaned in an anhydrous ethanol and chloroform mixed solution (volume ratio 1:10) for 5 min to wash away the mask plate, then the metal nano-array structure, shown in Figure 1b, was obtained. The metal nanostructure was post-treated by solution etching or annealing to obtain a recrystallized nanoparticle array (Figure 1c). The temperature was 800 °C, the atmosphere was Ar:H_2 = 2:1 (volume ratio), the flow rate was Ar/H_2, 500/250 sccm, the temperature control process was 60 min uniform from room temperature to 800 °C, and then constant temperature for 1 h, and then natural cool down.

2.4. Preparation of Single Electron Transistors Based on Gold Nanoparticles

On the samples of gold nanoparticle arrays that were obtained, a gold nanoparticle was selected as the Coulomb Island, and SiO_2 was deposited with a focused ion beam to a thickness of 6.0 nm in a dual beam system (FEI Helios Nanolab 600i). The ion beam source voltage and current were set at 30 kV and 40 pA, respectively. It could also be achieved by using ALD. Then, using the Coulomb Island as the center, deposition of platinum for the preparation of electrodes was induced. The organ metallic precursor $(CH_3)_3Pt(CpCH_3)$ resulted in platinum incorporated carbon-rich samples. To remove the C and Ga elements in the sediments, the platinum metal content was increased. The samples were placed in H_2O_2:H_2SO_4 = 1:1 solution for 60 s to remove the C and other substances. Then the samples were rinsed with deionized water and dried with N_2. The samples were then allowed to stand in a high-temperature combustion tube furnace at a rate of 20 °C/min and annealed

at 500 °C for 30 min under an O_2 atmosphere (flux 30 sccm) [11]. Finally, the device was bonded to get the single-electron transistor device (Figure 1d).

3. Results and Discussion

3.1. Template of PS Microsphere Monolayer

After the preparation of the PS microsphere emulsion, we first carried out the hydrophilic treatment of the substrate, and then prepared the PS microsphere template by the pulling assembly method. Then, electrons were deposited on the PS microsphere template by electron beam evaporation coating, and the results are shown in Figure 2a. The mask of coated PS spheres was lifted off with a mixed solution of absolute ethanol and chloroform to obtain a gold nanoparticle array structure, as shown in the illustration of Figure 2a. The nanoparticle array obtained was in the form of a hexagonal array of triangular structures with side lengths of 90 mm. We further controlled the shape and size of the gold nanoparticles by means of post-treatment, such as wet etching and annealing. According to the geometrical relationship (inset of Figure 2a), many triangular spaces implanted among the six-angle dense pile. The circles in the triangular spaces touched the neighboring polystyrene spheres. The relationship between the radius of the circles and the polystyrene spheres could be written as $\sqrt{3}(r + R)/2 = R$. So, the radius of the circle r was equal to 30.9 nm when the radius of the polystyrene sphere R was 200 nm. If we wanted to get gold nanoparticles with a size less than 10 nm, the diameter of the polystyrene sphere would need to be less than 65 nm. As shown in Figure 2b, after 800 °C annealing, the triangular nano gold was converted into granular form. Since the gold nanoparticles were annealed at high temperatures, the particles could release stress to recrystallize and, thus, became spherical.

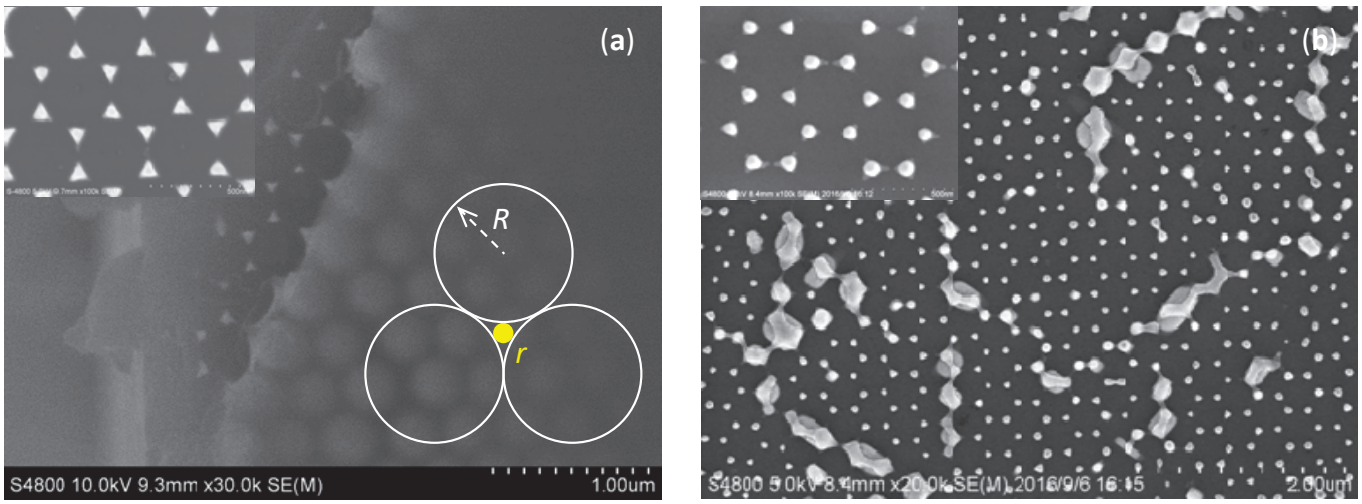

Figure 2. SEM images of (**a**) polystyrene sphere mono-film covered with a 300 nm-thick gold film, and (**b**) gold nanoparticle array after post treatment. The left up inset of (**a**) shows triangular gold array. The right down inset of (**a**) shows the geometrical relationship of polystyrene sphere and gold nanoparticle. The inset of (**b**) shows that the gold nanoparticle formed after annealing is well crystallized with a diameter of about 60 nm.

In the preparation of PS template, we obtained the monolayer template. However, in some local areas there were also cases of bilayer films. As shown in Figure 3, the shape and geometry of the gold nanoparticles array fabricated by the bilayer PS microsphere array template were quite different. The gold nanoparticle array template prepared by monolayer PS microsphere array template had a triangular honeycomb layout (Figure 3c). In contrast, the gold nanoparticle array template prepared by bilayer PS microsphere array template had a point array triangle layout (Figure 3e).

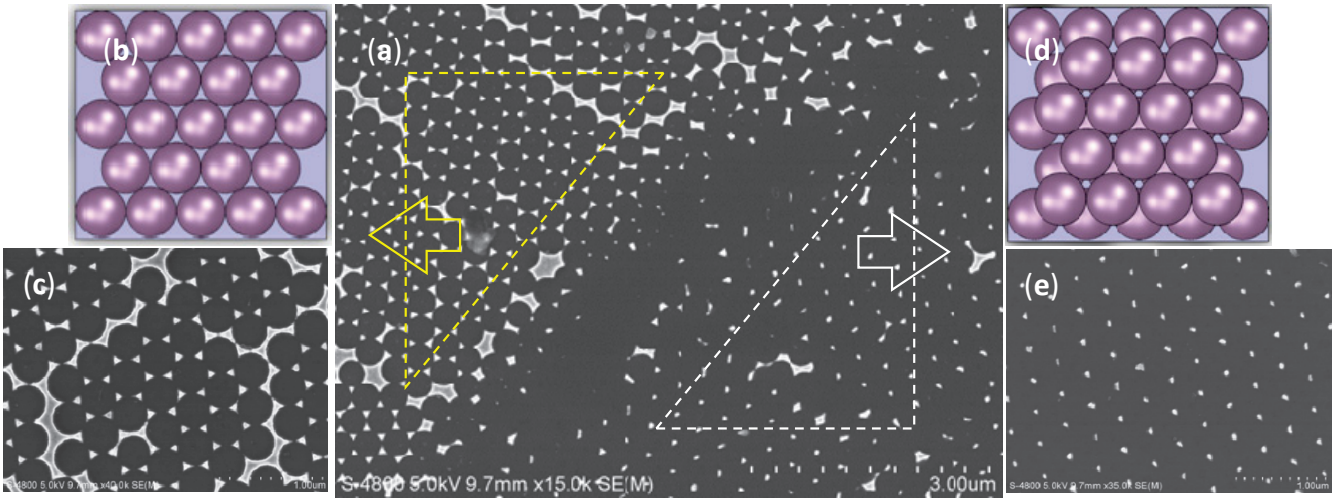

Figure 3. (**a**) SEM image of gold nanoparticles arrays template-fabricated by monolayer and bilayer PS microspheres array template on the same substrate; (**b**) Monolayer PS microspheres array template; (**c**) Gold nanoparticles arrays fabricated by the template as (**b**); (**d**) Bilayer PS microspheres array template; (**e**) Gold nanoparticles arrays fabricated by the template as (**d**).

3.2. Device Preparation

As shown in Figure 4a, there was an insulating layer of silicon oxide on gold nanoparticles, which was deposited by focused ion beams induced deposition (FIBID). Successively, platinum was deposited for electrodes preparation by the method of focused electron beam induced deposition (FEBID) and FIBID. Then, taking post-processing measures, such as annealing, to complete the preparation of the device, a single electron transistor device was the result, as shown in Figure 4c. The compositional changes of the wet etching and thermally annealed FIBID and FEBID materials were investigated before in [11]. EDX results are shown in Table 1. The results implied that the wet etching method was not effective. However, the platinum purity of the calcined sample was higher. It was possible that carbon and gallium reacted with oxygen during the annealing, and carbon dioxide molecules escaped with the gas flow. Therefore, the platinum content would be relatively increased and the conductivity would be enhanced. In addition, the annealing treatment was an alternative method to avoid current leakage.

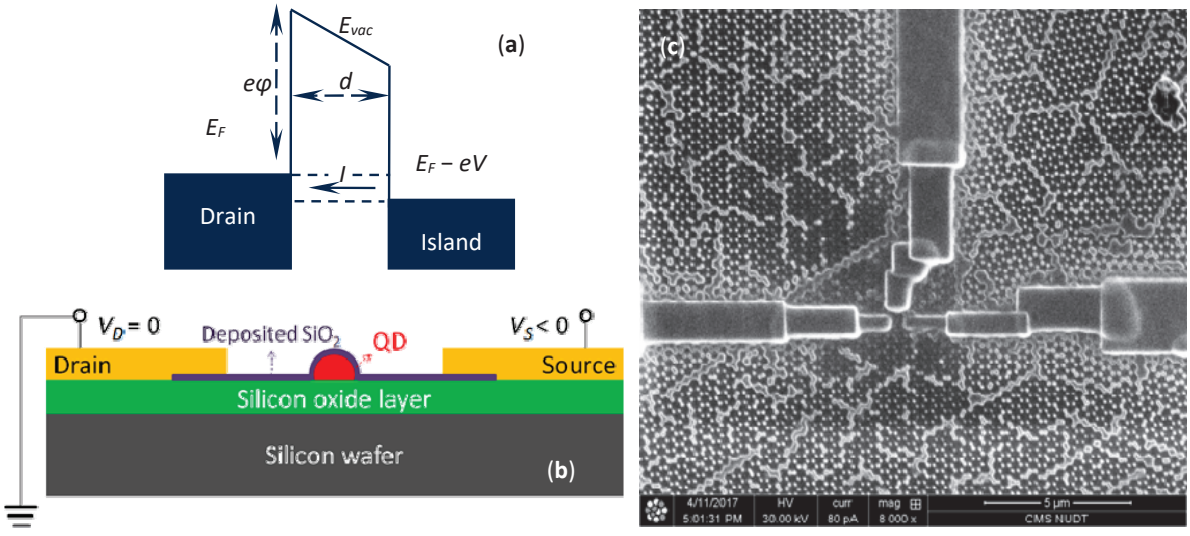

Figure 4. (**a**) Band diagram of electrode-dielectric-gold nanoparticle junction; (**b**) Schematic diagram of the side view of the SET device; (**c**) SEM image of the top view of the SET device.

Table 1. The atomic concentrations of the dual beam-induced resultants.

Element	FIBID			FEBID		
	Deposition	Wet Etching	Calcination	Deposition	Wet Etching	Calcination
C (K)	73.74	70.72	24.23	91.68	90.76	/
O (K)	/	/	34.70	/	/	75.90
Ga (L)	10.16	9.39	14.61	3.73	2.15	/
Pt (M)	16.10	19.88	26.46	4.59	7.09	24.10

The tunneling resistance if electrons go from the drain to the gold nanoparticle can be calculated. The corresponding band diagram of electrode–dielectric–gold nanoparticle junction under a bias V is shown in Figure 4b, where d is the channel length, $e\varphi$ is the work function, E_F is the Fermi energy and E_{vac} is the vacuum level. When a battery lowers the energy levels in the gold nanoparticle with respect to the drain contact, and maintains them at distinct electrochemical potentials separated by eV, the numbers of electrons can be given by different Fermi functions: $f(E, E_F - eV, T)$ and $f(E, E_F, T)$. Supposing that the tunneling probability of electrons inflow from the drain to the gold nanoparticle is the same as the one of electrons outflow in the opposite direction, we can write the current through this junction as follows [12]:

$$\begin{aligned} I &= -\frac{2e}{\hbar}\sum_{n=1}^{N}\int_{-\infty}^{+\infty}\left(f(E,E_F-eV,T)-f(E,E_F,T)\right)T_n(E)dE \\ &= \frac{2e^2V}{\hbar k_BT}\sum_{n=1}^{N}\int_{0}^{E_F}\frac{\exp\left(\frac{E-E_F}{k_BT}\right)}{\left(1+\exp\left(\frac{E-E_F}{k_BT}\right)\right)^2}\exp\left(-\frac{4\sqrt{2m}}{3e\varepsilon\hbar}(e\varphi-(E-E_F))^{\frac{3}{2}}\right)dE \end{aligned} \quad (1)$$

where e and m are the electron charge and mass, respectively; h is the Planck constant ($\hbar = h/2\pi$); N is the total number of sub-bands below Fermi energy; E is the electron energy; k_B is the Boltzmann constant; T is the Kelvin temperature and ε is the electric field intensity. T_n is the tunneling probability of electrons in the energy level of n, in the form of Fowler-Nordheim tunneling formulation.

The resistance of the channel determines the current that flows between the drain and the gold nanoparticle when a voltage V_{ds} is applied. According to Equation (1), an equivalent tunneling resistance R with varying thicknesses of potential barrier length d could be calculated. As Table 2 shows, the tunneling resistance between the metallica electrode and a gold nanoparticle at 320 mK and 2 K were calculated. The following parameters were used in the calculations: Fermi energy E_F = 5.51 eV (gold); modified work function $e\varphi$ = 4.1 eV (interface of gold-SiO_2); cross section dimension of the drain 50×50 nm^2. The results showed that when the thickness of the silicon oxide layer was in a thickness range of 3.0–6.5 nm, the magnitude of the tunneling resistance was in the range of 10^4–10^{13} Ω. This was a proper value for the electron tunneling, while larger resistance would lead to much lower tunneling probability and feebler tunneling current.

Table 2. Equivalent resistance of barrier with different thickness.

d (nm)		3.0	3.5	4.0	4.5	5.0	5.5	6.0	6.5
R (100 kΩ)	@2 K	0.64	10.89	185.23	3.15×10^3	5.36×10^4	9.13×10^5	1.55×10^7	2.64×10^8
	@320 mK	0.10	1.74	29.64	5.04×10^2	8.58×10^3	1.46×10^5	2.49×10^6	4.23×10^7

3.3. Device Test

Coulomb blockade oscillations can be seen clearly in the electrical characteristics of the SET measured at 320 mK. The dependence of the Coulomb blockade on V_{ds} and V_{g} was investigated. Differential conductance versus V_{g} and V_{ds} is shown in Figure 5a. The blue diamond indicated that the electrons had a Coulomb blockade and the number of electrons on the gold nanoparticle island kept constant. However, the red region indicated that single

electron tunneling occurred, which is a typical characteristic of a single electron transistor. The slopes of the two bevel edges of the prismatic when gate voltage was equal to −16 V were $k_s = k_d = 7.2 \times 10^{-3}$, respectively. The Coulomb diamond had symmetry along the $V_{ds} = 0$ direction, which indicated that the source and drain tunneling junctions of the single electron transistor were symmetrical, and if the junction capacitance of the source and drain was different, the Coulomb diamond would tilt. Figure 5b shows the source–drain current curve and its corresponding differential conductance when gate voltage was set at −16 V. The Coulomb blockade effect could be clearly seen, both in the I_{ds}-V_{ds} and G_{ds}-V_{ds} curves. The length of the low conductive region ΔV_{ds} was about 29.25 mV and the charging energy of the Coulomb Island was estimated to be 29.25 meV, which was much larger than the thermal energy of 138.1×10^{-4} meV at 320 mK. The capacitance C_d of 2.74 aF was achieved with a zero-biased resistance of ~1.05 GΩ. The corresponding thickness of the silicon oxide barrier was calculated to be about 6.3 nm. It was in agreement with the device preparation, as before. There was also a capacitance between the Coulomb Island and the gate, and the source of either. According to the relationships $k_s = C_g/(C_g + C_s)$ and $k_d = C_g/C_d$, $C_g = 0.02$ aF and $C_s = 2.72$ aF, the total capacitance was $C_\Sigma = C_s + C_d + C_g = 5.48$ aF. If we assumed that the capacitance of a spherical Coulomb Island with a radius r was given by $C_\Sigma = 4\pi\varepsilon_r\varepsilon_0 r$, the dot diameter was calculated to be 24.6 nm with the dielectric constant of SiO_2 $\varepsilon_r = 4$. It was consistent with the range of island diameter observed in the SEM image of GNPs.

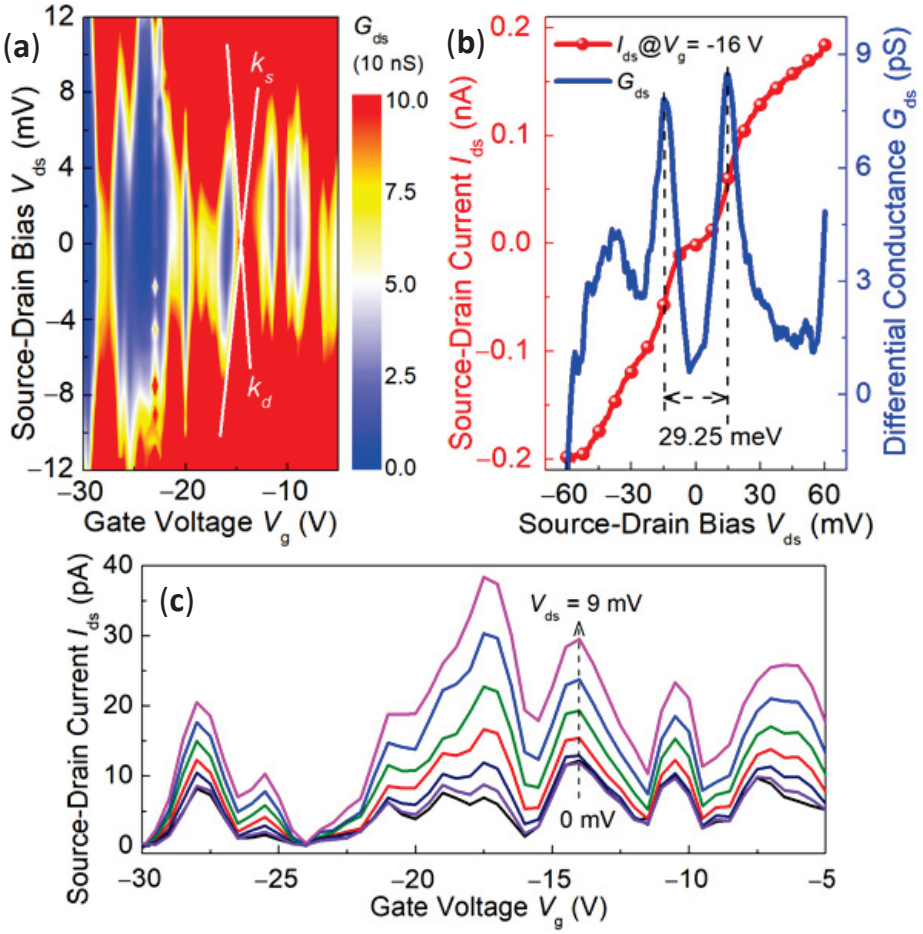

Figure 5. (**a**) Source–drain differential conductance as a function of source drain bias V_{ds} and gate bias V_g at $T = 320$ mK; (**b**) The measured source–drain current curve and its corresponding differential conductance when gate voltage was set at −16 V; (**c**) The measured source-drain current curve as a function of gate bias V_g, when source drain bias V_{ds} was set at different valuea, from bottom to top of 0 mV to 9 mV.

When the source drain voltage did not change, the source leakage current changed with the change of the gate voltage, which is called the Coulomb oscillation effect. As shown in Figure 5c, with increase of the source drain voltage, the values of the Coulomb oscillation peaks increased. This was because, as the source drain voltage increased, the number of levels that fell into the source drain potential window increased, and each time the number of electrons tunneling through the source–island–drain increased; thus. the tunneling current became larger.

Considering the double quantum dot systems in series, their electrochemical potential was independently controlled by their respective side gate electrodes. When there was a capacitance coupling between the quantum dots, adding an electron to one of the quantum dots changed the electrostatic energy of the other quantum dot. Moreover, the gate pressure of the quantum dots was generally capacitive coupled to the quantum dots. The charge stability diagram shows a hexagonal honeycomb. Figure 6a shows a local part of the honeycomb lattice. The point of the honeycomb lattice is called the triple point. At a triple point, the energy of different charge states is degenerate. The distance between the triple points is determined by the coupling strength between the quantum dots. When the coupling between the two quantum dots was very strong, as shown in Figure 6b, the separation of the three state points reached the maximum, and the behavior of the double quantum dots became like that of only one quantum dot.

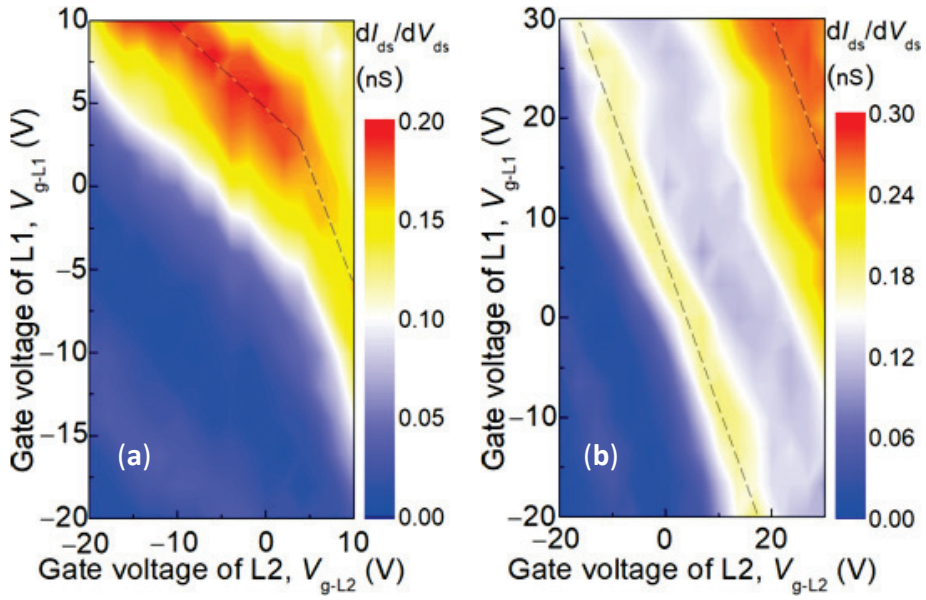

Figure 6. Double quantum dot systems are controlled by gate pressure with different coupling intensities. (**a**) There is capacitive coupling between quantum dots, one electron on one quantum dot changes the electrostatic energy of the other quantum dot; (**b**) The coupling capacitance evolves to the main capacitance, and the separation of the triple point reaches the maximum.

4. Conclusions

In this paper, we used the seed emulsion method to prepare polystyrene microspheres of specific size, and then, by using the dip coating method, a PS microsphere monolayer film was prepared, and it was used as a template for metal evaporation. After removing the template of PS microspheres, the periodic array of gold nanoparticles was obtained. The size of the gold nanoparticles could be controlled and the crystallinity of the particles improved by the method of solution etching and annealing, helping to improve its electrical performance. Based on this, 6 nm thick silicon oxide was deposited on the gold nanoparticles using double beam equipment, and deposition of the source, drain and gate, subsequently. Due to the presence of impurities, such as C and Ga, in the material obtained by the focused ion beam induced deposition, it was necessary to improve the conductivity

of the material by high temperature annealing in an oxygen atmosphere. Finally, the differential conductance test was carried out using the liquid helium cryostat. While changing the gate voltage and sweeping the source drain voltage, under the interaction effect of the Coulomb step effect and the Coulomb oscillation effect, the Coulomb diamond of the single electron transistor conductance was observed. A single electron transistor was made by a novel bottom-up self-assembly method. On the basis of the platform, single electron phenomena, such as single photon assisted tunneling, can be further studied.

Author Contributions: Conceptualization and methodology, J.F.; device preparation and data test, X.L. and J.F.; review and suggestions, W.X. and K.S. All authors have read and agreed to the published version of the manuscript.

Funding: This work was supported by the Natural Science Foundation of Hunan Province (Grant 2022JJ30717).

Data Availability Statement: All data, models, and code generated or used during the study appear in the submitted article. They are available from the corresponding author by request (J.F.).

Conflicts of Interest: The authors declare no conflict of interest.

References

1. Gorter, C.J. A possible explanation of the increase of the electric resistance of thin metal films at low temperature and small field strength. *Physica* **1951**, *15*, 777–780. [CrossRef]
2. Chen, W.; Ahmed, H.; Nakazoto, K. Coulomb blockade at 77 K in nanoscale metallic islands in a lateral nanostructure. *Appl. Phys. Lett.* **1995**, *66*, 3383–3884. [CrossRef]
3. Klein, D.L.; McEuen, P.L.; Katari, J.E.B.; Roth, R.; Alivisatos, A.P. An approach to electrical studies of single nanocrystals. *Appl. Phys. Lett.* **1996**, *68*, 2574–2576. [CrossRef]
4. Sato, T.; Ahmed, H.; Brown, D.; Johnson, B.F.G. Single electron transistor using a molecularly linked gold colloidal particle chain. *J. Appl. Phys.* **1997**, *82*, 696–701. [CrossRef]
5. Yamaguchi, H.; Terui, T.; Noguchi, Y.; Ueda, R.; Nasu, K.; Otomo, A.; Matsuda, K. A photoresponsive single electron transistor prepared from oligothiophene molecules and gold nanoparticles in a nanogap electrode. *Appl. Phys. Lett.* **2010**, *96*, 103117–103119. [CrossRef]
6. Iwata, Y.; Nishimura, T.; Singh, A.; Satoh, H.; Inokawa, H. High-frequency rectifying characteristics of metallic single-electron transistor with niobium nanodots. *Jpn. J. Appl. Phys.* **2022**, *61*, SC1063–SC1069. [CrossRef]
7. Willing, S.; Lehmann, H.; Volkmann, M.; Klinke, C. Metal nanoparticle film–based room temperature Coulomb transistor. *Sci. Adv.* **2017**, *3*, e1603191–e1603200. [CrossRef] [PubMed]
8. Wu, Y.Z.; Zhang, C.; Yuan, Y.; Wang, Z.W.; Shao, W.J.; Wang, H.J.; Xu, X.L. Fabrication of Wafer-Size Monolayer Close-Packed Colloidal Crystals via Slope Self-Assembly and Thermal Treatment. *Langmuir* **2013**, *29*, 14017–14023. [CrossRef] [PubMed]
9. Rybczynski, J.; Ebels, U.; Giersig, M. Large-scale, 2D arrays of magnetic nanoparticles. *Colloids Surf. A Physicochem. Eng. Aspects* **2003**, *219*, 1–6. [CrossRef]
10. Gonçalves, M.R.; Makaryan, T.; Enderle, F.; Wiedemann, S.; Plettl, A.; Marti, O.; Ziemann, P. Plasmonic nanostructures fabricated using nanosphere-lithography, soft-lithography and plasma etching. *Beilstein J. Nanotechnol.* **2011**, *2*, 448–458. [CrossRef] [PubMed]
11. Fang, J.Y.; Qin, S.Q.; Zhang, X.A.; Liu, D.Q.; Chang, S.L. Annealing effect of platinum-incorporated nanowires created by focused ion/electron-beam-induced deposition. *Chin. Phys. B* **2014**, *23*, 088111–088115. [CrossRef]
12. Datta, S. *Quantum Transport: Atom to Transistor*, 1st ed.; Cambridge University Press: Cambridges, UK, 2005; pp. 232–235.

nanomaterials

MDPI

Article

A Novel Crossbeam Structure with Graphene Sensing Element for N/MEMS Mechanical Sensors

Junqiang Wang [1,2,*], Zehua Zhu [1,2], Yue Qi [1,2] and Mengwei Li [1,2,*]

[1] National Key Laboratory of Instrumentation Science & Dynamic Measurement, North University of China, Taiyuan 030051, China; zehua_zhu@163.com (Z.Z.); qiyuenuc@163.com (Y.Q.)
[2] Academy for Advanced Interdisciplinary Research, North University of China, Taiyuan 030051, China
* Correspondence: wangjq210@nuc.edu.cn (J.W.); lmwnuc@163.com (M.L.); Tel.: +86-158-1133-8056 (J.W.); +86-139-3424-8366 (M.L.)

Abstract: A graphene membrane acts as a highly sensitive element in a nano/micro–electro–mechanical system (N/MEMS) due to its unique physical and chemical properties. Here, a novel crossbeam structure with a graphene varistor protected by Si_3N_4 is presented for N/MEMS mechanical sensors. It substantially overcomes the poor reliability of previous sensors with suspended graphene and exhibits excellent mechanoelectrical coupling performance, as graphene is placed on the root of the crossbeam. By performing basic mechanical electrical measurements, a preferable gauge factor of ~1.35 is obtained. The sensitivity of the graphene pressure sensor based on the crossbeam structure chip is 33.13 mV/V/MPa in a wide range of 0~20 MPa. Other static specifications, including hysteresis error, nonlinear error, and repeatability error, are 2.0119%, 3.3622%, and 4.0271%, respectively. We conclude that a crossbeam structure with a graphene sensing element can be an application for the N/MEMS mechanical sensor.

Keywords: graphene; N/MEMS; displacement sensor; pressure sensor

1. Introduction

Graphene, a two–dimensional material, has excellent mechanical, thermal, optical, and electrical properties. With its Young's modulus of up to 1 TPa [1], thermal conductivity reaching 5×10^3 W/m·K [2], light transmittance as high as 97.7% [3], and an ultrahigh carrier mobility of 200,000 $cm^2 \cdot V^{-1} \cdot s^{-1}$ [4], it has become the preferred material for the sensing element in various sensors. Moreover, graphene will be suitable for MEMS and NMES mechanical sensors in the future due to two primary factors: the piezoresistive effect because of graphene microstructure changing under external stress and high compatibility between graphene transferring patterning and micro–nano process technology [5,6].

In previous research, graphene sensors have been used to detect multiple different mechanical parameters, such as pressure [7,8], acceleration, and strain [9–12]. The first typical graphene pressure sensor was proposed by Smith et al. [13,14]. A monolayer graphene membrane was suspended on a cavity in SiO_2/Si substrate, and a sensitivity of 3.95 μV/V/mmHg was obtained as pressure ranged from 200 to 1000 mbar. There is also an unfavorable phenomenon where liquid remains in the square cavity during the graphene wet transferring process. Subsequently, the electrical property of graphene is inevitably affected, which leads to poor stability of the suspended graphene pressure sensor. A new type of graphene pressure sensor was developed by Zhu et al. [15]. A folded graphene ribbon was placed on the maximum strain region of a suspended square Si_3N_4 film, and sensitivity reached up to 8.5 mV/bar with pressure ranging from 0 to 700 mbar. In addition, a more sensitive graphene pressure sensor was developed by Wang et al. [8]. Suspended Si_3N_4 for supporting graphene was etched to form substantial numbers of through hole arrays. Owing to the increased strain on the graphene membrane, the pressure sensor showed a sensitivity of 2.8×10^{-5} $mbar^{-1}$ under a pressure of 0~400 mbar.

Although residual liquid in the cavity can be resolved by the suspended Si_3N_4 approach, the measurement range is below 1 MPa due to the process limitations of the suspended Si_3N_4 structure. In the past few years, some researchers have also made great progress in graphene based accelerometers. A suspended graphene high–g accelerometer made by Hurst et al. has a high repeatable response to a wide range of 1000~3000 g [16]. Another NMES accelerometer with a suspended double layer graphene ribbon with attached silicon proof mass was fabricated by Fan et al. and could measure an effective acceleration of 20~30 g [10]. These suspended graphene mechanical sensors are simple in structure and exhibit excellent electrical performance. Structural stability and reliability, however, require further improvement. For example, suspended graphene is prone to collapse and rupture [17], and an ultra–thin graphene beam has high processing difficulty and low natural frequency. A crossbeam structure, with its excellent mechanical properties, is commonly used in large impact and high–load environments [18,19]. In addition, the sensitivity of graphene mechanical sensors is related to the effect of stress or strain on the sensing element. Compared with the ordinary ribbon of graphene, the fold pattern can capture multiple responses and improve the detection capability of a sensor.

As the core element of a pressure sensor, the quality of graphene directly affects the piezoresistive performance of the device. Improper operation during the graphene transferring process can easily introduce some defects and residues, such as wrinkling, cracking, and photoresistance [20]. This can cause a risk of Dirac point shift and lead to poor resistivity stability [21–23]. Combined annealing for van der Waals force enhancement and water bath heating for cleaning, the performance of graphene can be effectively improved. Another concern is that covering suspended graphene with a passivation layer becomes more difficult. When graphene is exposed to air during fabrication or employment, it is easily contaminated by gas adsorption (e.g., N_2, O_2, CO_2, H_2O, etc.) or other impurities, causing n–/p–type doping in graphene [24,25]. As a result, graphene resistance sharply changes, sensor reliability shows large decreases, and serving life noticeably shortens [26]. Generally, materials with a strong affinity, such as polymer, h–BN, Al_2O_3, and Si_3N_4, are used to protect the graphene sensing element and can improve the electrical properties and long–term stability of sensors [27–32]. Compared with Al_2O_3, depositing and etching Si_3N_4 are relatively convenient methods [33,34], and Si_3N_4 processing is also highly compatible with N/MEMS technology, avoiding risk of oxidation under high temperature [35–37]. Additionally, it is beneficial for covering Si_3N_4, rather than organic polymer or h–BN, on graphene to reduce organic residue pollution in subsequent processing. In this paper, a novel crossbeam structure with a graphene sensing element is presented for N/MEMS mechanical sensors. The core graphene varistors are encapsulated with Si_3N_4 film to achieve highly sensitive pressure detection.

2. Materials and Methods

2.1. Fabrication of N/MEMS Crossbeam Structure

The fabrication process is shown in Figure 1. A passivation layer of Si_3N_4 with a thickness of 200 nm was first deposited on 2″ Si wafer by plasma enhanced chemical vapor deposition (PECVD). The electrode, 15 nm/25 nm thick Cr/Au, was followed by magnetron sputtering [Figure 1a]. A square 900 × 900 μm cavity was then created on the back of the wafer by deep reactive ion etching (DRIE) [Figure 1b]. Subsequently, the Si wafer was diced into small 17 × 17 mm dies, and the CVD–grown monolayer graphene (TTG, ACS Material, LLC, Pasadena, CA, USA) was transferred and patterned by PMMA assistance and oxygen plasma etching, respectively [Figure 1c]. A thin 150 nm thick Si_3N_4 film was also deposited by PECVD to protect the graphene from undesired doping and pollution in the ambient environment. Reactive ion etching (RIE) was used to remove Si_3N_4 on the Pad, and Cr/Au with a thickness of 25/100 nm was sputtered on the Pad [Figure 1d]. Finally, four square cavities with dimensions of 350 × 350 μm were etched by DRIE to create a crossbeam with a length of 900 μm, width of 200 μm, and thickness of 40 μm [Figure 1e].

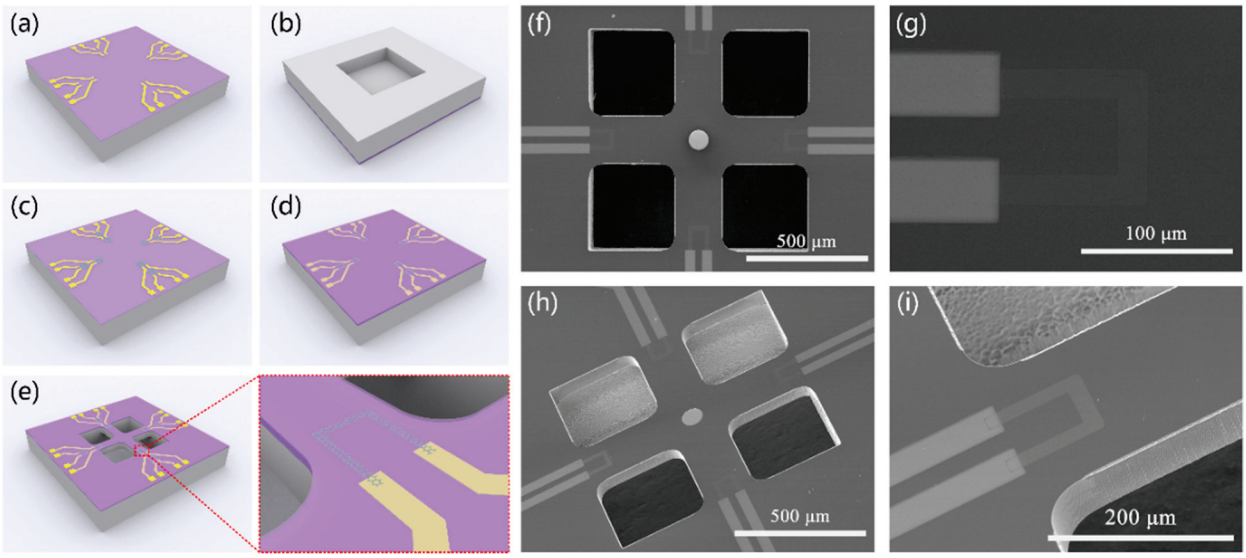

Figure 1. Fabrication process and SEM images of crossbeam structure with graphene sensing element. (**a**) Sputtering Cr/Au electrode. (**b**) Etching deep square cavity on the back of wafer. (**c**) Transferring and patterning monolayer graphene. (**d**) Depositing protective layer of Si_3N_4 and etching Si_3N_4 to leak out the Pad and sputtering Cr/Au on it. (**e**) Release crossbeam structure. (**f**) Top view of whole chip. (**g**) Top view of single graphene element. (**h**) Tilt observation of whole chip. (**i**) Tilt observation of single graphene element.

The crossbeam structure with the graphene sensing element was firstly measured using a scanning electron microscope (Quanta 250, FEI, Inc., Hillsboro, OR, USA). Figure 1f,g shows the top view of the whole chip and single graphene element, respectively. Four identical graphene piezoresistors were arranged at the root of crossbeam. Measurement results of the crossbeam, 900 μm in length and 200 μm in width, confirmed the consistency with the design. The size of the folded graphene ribbon was determined as 30 μm long and 10 μm wide. As shown in Figure 1h,i, the crossbeam structure was also inspected using a SEM with a tilt angle. It is clear that the crossbeam thickness at the root was thicker than that in the middle because of the universal feature of the DRIE process. Nevertheless, it had almost no influence on the mechanical properties of crossbeam.

2.2. Schematic of Transfer Process of Graphene Layer

Single–layer graphene (Gra) was grown on a Cu substrate. After being cropped into a 1.5 × 1.5 cm sample, we coated the graphene on Cu foil with polymethyl methacrylate (PMMA) using a spin coater at speeds of 600 rpm/5 s and 4000 rpm/30 s. The PMMA/Gra/Cu/Gra sample was placed on a hot plate at 130 °C for 20 min. Then, the backside graphene of the sample was etched by O_2 plasma, and the Cu substrate of supporting Gra was etched with 40% $FeCl_3$ solution for about 6 h. After, the PMMA/Gra sample was transferred to the target substrate and heated on a hot plate at 85 °C for 30 min. The PMMA layer was dissolved in acetone (CP) solution at 50 °C for 10 min, and the target was cleaned with alcohol (EA) solution and deionized (DI) water. Finally, photolithography technology and O_2 plasma etching were used for patterning graphene. The parameters of the O_2 plasma etching were as follows: the power was 60 W, gas flow rate was 30 sccm, and etching time was 3 min. The schematic of transferring the graphene layer to the target substrate is shown in Figure 2.

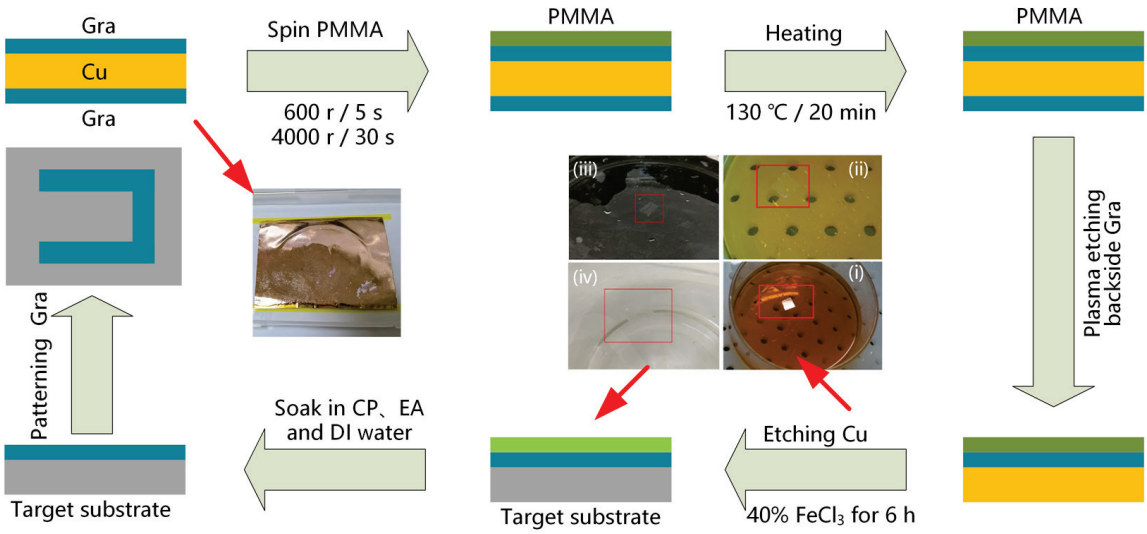

Figure 2. Schematic of transferring graphene layer to target substrate (including patterning graphene).

3. Results and Discussion

3.1. Physical and Electrical Characteristics of the N/MEMS Graphene Units

Raman spectra (HR–800, Horiba Scientific, Inc., Paris, France) were used to analyze the stacking and defects of graphene before and after depositing Si_3N_4. As shown in Figure 3a, the characteristic G and 2D peaks, as well as a weak D peak (defect-related), originating from the CVD–grown monolayer graphene were clearly visible. After depositing the Si_3N_4–protected layer, the intensity of the D peak rapidly increased; meanwhile, the intensity ratio of the 2D peak to the G peak (I_{2D}/I_G) decreased immensely from 3.08 to 0.60. Moreover, a slight shift in the G and 2D peaks was also observed [38,39]. The main explanation for the above phenomena is that the introduction of external atoms disrupts the lattice structure of graphene. Current–voltage (I–V) characteristics were precisely demonstrated by a probing station united with a semiconductor parameter analyzer (B1500A, Keysight, Inc., Santa Rosa, CA, USA). The measurement results are shown in Figure 3b. Compared with the resistance of the open face graphene sensing element from 497.5 to 502.4 $\Omega \cdot sq^{-1}$, Si_3N_4−encapsulated graphene resistance ranged from 566.1 to 570.8 $\Omega \cdot sq^{-1}$. This indicated that graphene can retain high quality and consistency after overlaying a Si_3N_4 protective layer.

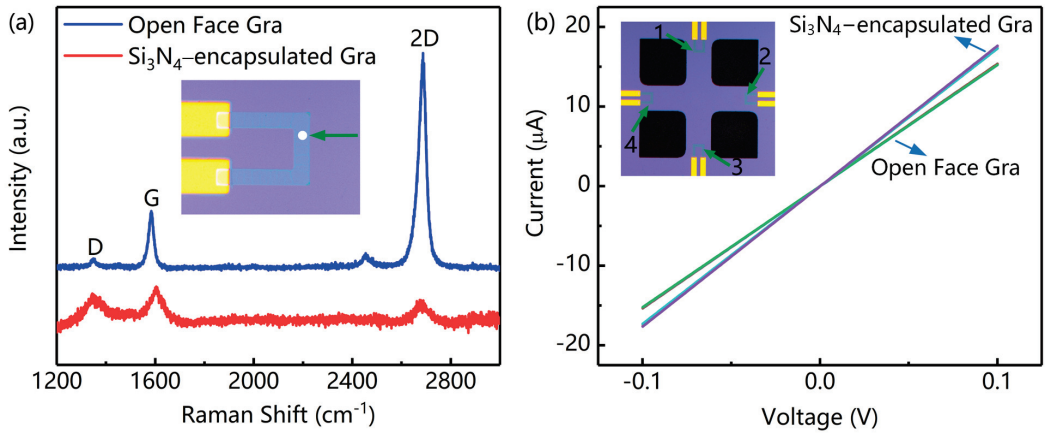

Figure 3. Physical and electrical characteristics of graphene sensing element. (**a**) Raman spectra of graphene sensing element before and after depositing Si_3N_4. (**b**) I−V curve of graphene sensing element with open face and Si_3N_4 protective layer.

To further investigate the effect of a Si_3N_4 layer on the stability of the graphene sensing element, samples with and without the top Si_3N_4 layer were placed in ambient air (20~25 °C and relative humidity 40~60%). From Figure 4a, after 7 days, the graphene resistance without top Si_3N_4 increased by $\Delta R/R_0$ = 25.8%, where R_0 is the initial resistance. In contrast, the relative resistance protected with a Si_3N_4 layer was almost unchanged, showing higher stability. The main reason is that Si_3N_4 can effectively isolate graphene and avoid water or air doping [38]. After 35 days, the unprotected graphene resistance continued to increase, while the protected one remained only slightly increased, as shown in Figure 4b. The corresponding changes in resistance were 7.4% and 46.3%, respectively. We confirmed that the stable performance of graphene resistance is well preserved due to the Si_3N_4 protecting graphene from serious environmental pollution or doping [36].

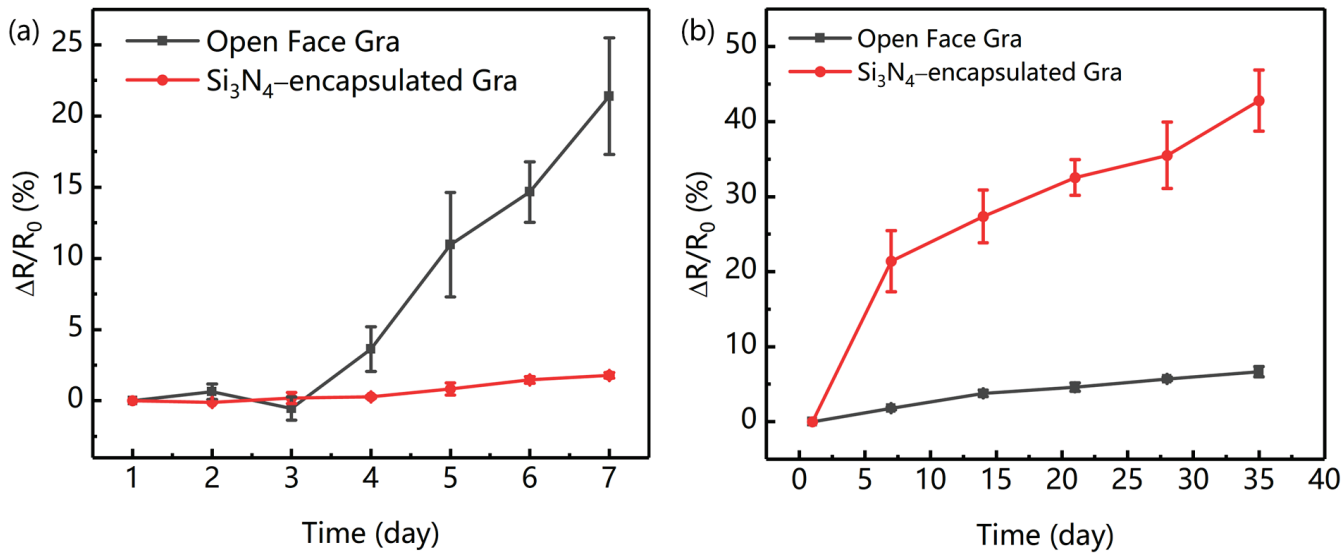

Figure 4. Stability of graphene sensing element with and without the top Si_3N_4 layer: (**a**) 7 and (**b**) 35 days later.

3.2. Mechanical and Electrical Characteristics of Displacement Sensor

Tests of the piezoresistive effect for the graphene sensing element on the crossbeam structure were then performed in an uncomplicated experiment. The setup schematic is shown in Figure 5a. There were eight independent sensing units of the same size, distributed on the surface of chip. Four of them were arranged outside the crossbeam as references and did not sense mechanical signals such as strain, on which electrical tests were mainly performed during fabricating to judge the compatibility and reliability of the process. Other graphene sensing units were located at the root of the crossbeam and were utilized to detect the beam strain signal. A piezo actuator with subnanometer resolution (P–841, Physik Instrumente, Inc., Karlsruhe, Germany) was then used to compress the center of the crossbeam. As the actuator simulated external force to produce a tiny displacement, the bend deformation of the crossbeam correspondingly occurred; meanwhile, the graphene sensing element was affected by stress and strain. The resistances of the four graphene varistors were recorded through a digital multimeter (34461A, Keysight Technologies, Inc., Santa Rosa, CA, USA). Measurement results are shown in Figure 5b. After three cycles of the load–unload experiment, with displacement ranging from 0 to 4.5 μm, the changes in resistance and displacement exhibited an apparent positive linear correlation. Moreover, the output results of the four detection units had high consistency, which further verified that the strain generated at the root of the crossbeam remained the same as when the pressure was applied at the center. The piezoresistive effect of graphene is independent of random crystal orientation and multigrain graphene flake [13].

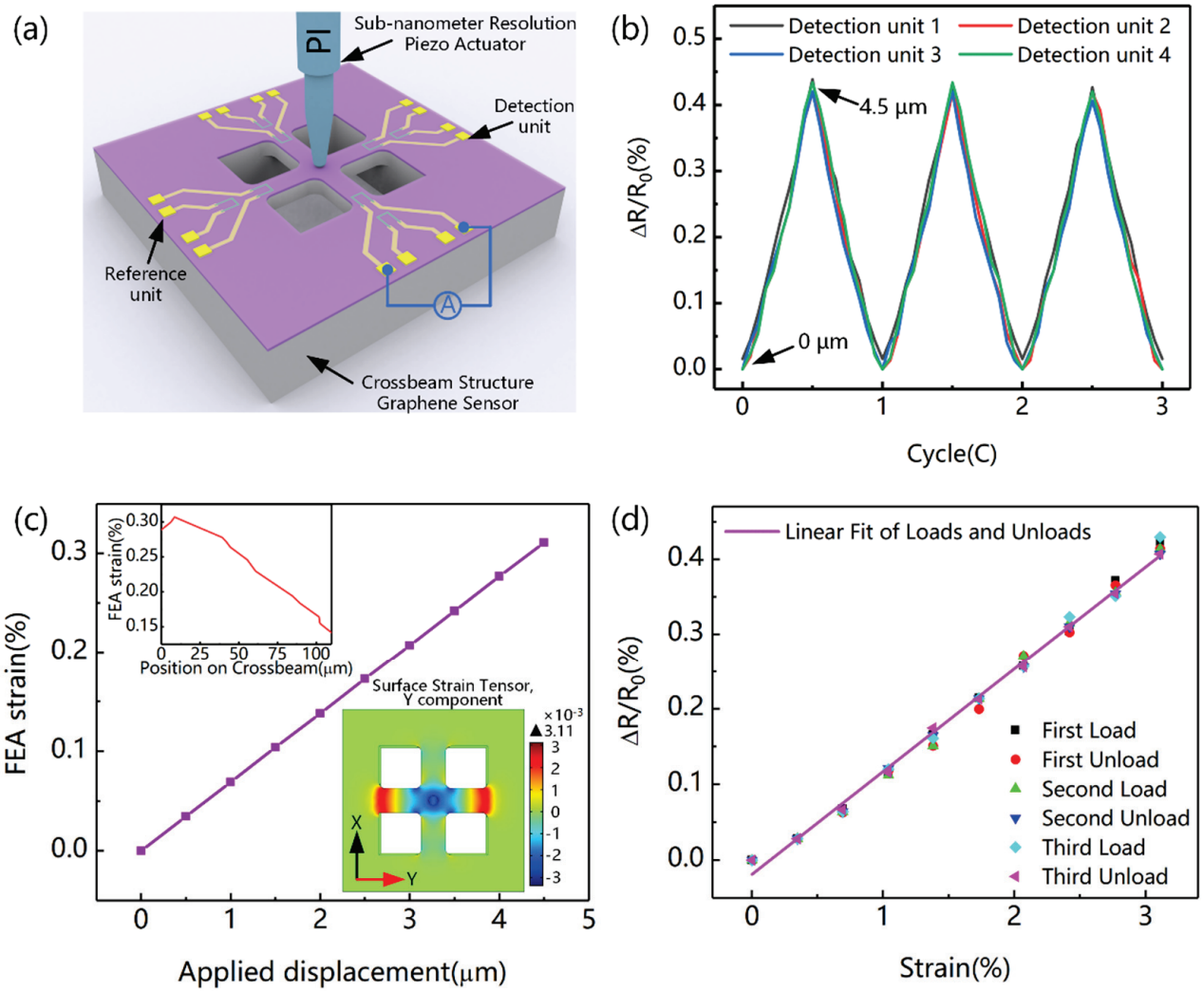

Figure 5. Experimental characterization of crossbeam structure with graphene sensing element. (**a**) Schematic of experimental setup. (**b**) Measurement results of displacement resistance. (**c**) Strain–displacement diagram of crossbeam root by FEA. (**d**) Strain--resistance results of the detection unit 1.

The piezoresistive effect of the graphene sensing element, through the strain−induced resistance change, was further investigated by finite element analysis (FEA). During FEA simulation, differential displacement load, ranged from 0 to 4.5 μm with a step of 0.5 μm, was applied on the center of the crossbeam structure. Although the maximum displacement was located at the center of the crossbeam, the maximum stress (i.e., strain) appeared at the root of the crossbeam. As shown in Figure 5c, the typical surface maximum strain distribution at the root of a single beam was extracted under different displacements. The internal illustrations showed the strain distribution within the range of 110 μm at the root and the Y component of the surface strain tensor under the applied displacement of 4.5 μm. The X component of the tensor was the same as that of the Y component, and they were perpendicular to one another. We found that the effective strain region was located within 110 μm of the root of the crossbeam. In our work, the graphene sensing element was arranged within 15 μm, which included the position of maximum strain. Because strain was the main factor causing the piezoresistive effect of graphene, the maximum strain parameter was used instead of the displacement parameter. Because the output characteristics of the four detection units were basically similar, only one of them was analyzed in detail. The corresponding result of strain–resistance is shown in Figure 5d. The gauge factor (G) of the graphene piezoresistor was defined as the rate of resistance change to strain ($\Delta R/R_0/\varepsilon$). Finally, G = 1.35 was obtained in this work, which is similar to the

G = 1.6 for CVD graphene obtained in previous research [15]. This also demonstrates the feasibility of arrangement of the graphene sensing element.

3.3. Mechanical and Electrical Characteristics of Pressure Sensor

A new type of graphene pressure sensor was developed by stacking an elastic diaphragm, crossbeam chip, and substrate through bonding technology. Figure 6a shows a schematic diagram of the pressure sensor packaging and actual sensor chip. Furthermore, the chip was assembled on the shell, and the signal was led out by wire bonding. In addition, a wheatstone bridge with a constant current supply was used to detect the electrical conductivity changes in a graphene nanofilm caused by external pressure, as shown in Figure 6b. The pressure sensor was then tested by using a self–made oil pressure calibration machine. Figure 6c shows the voltage output results of 10 cycles in the range of 0~20 MPa, with an interval of 1MPa. The graphene sensing element was not only directly covered by Si_3N_4, but also isolated from the environment by multistack bonding. Double protection for graphene can greatly improve the repeatability and stability of a sensor. The results of three reciprocating cycles were extracted, as shown in Figure 6d. The calculated sensitivity of the sensor was 33.13 mV/V/MPa. Correspondingly, the hysteresis error, nonlinear error, and repeatability error reached 2.0119%, 3.3622%, and 4.0271%, respectively.

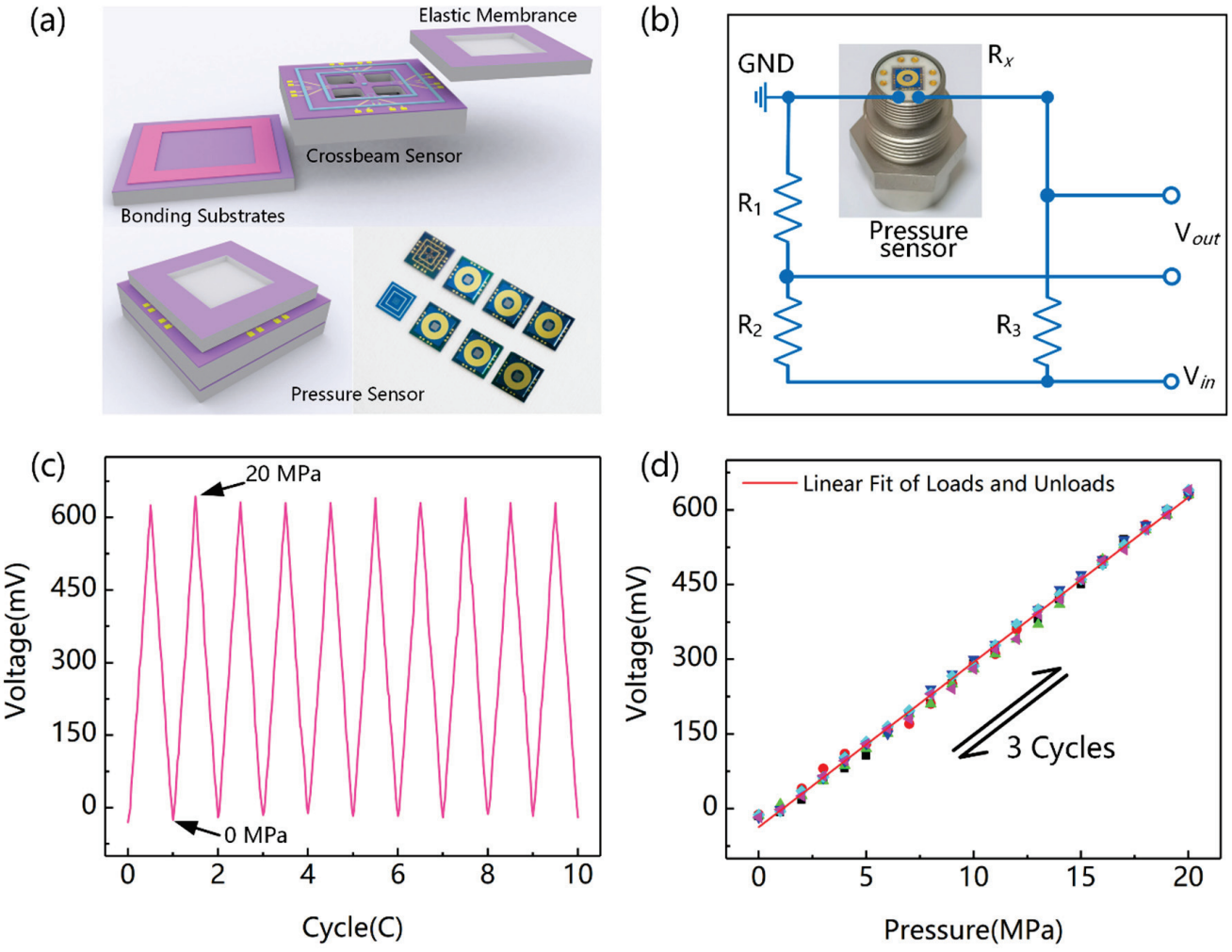

Figure 6. Packaging and testing of graphene pressure sensor based on crossbeam. (**a**) Packaging schematic and actual chip of sensor. (**b**) Shell assembling and electrical connection of sensor. (**c**) Test results of 10 load–unload cycles in full–range condition. (**d**) Test results of 3 reciprocating cycles.

4. Conclusions

In conclusion, a novel crossbeam structure was employed for graphene N/MEMS mechanical sensors in this work, which significantly overcomes some disadvantages in the performance stability and fabrication process of a suspended structure. Defect free structure and high–quality graphene was demonstrated by a SEM inspection, Raman analysis, and I–V measurement. The results of stability tests further confirmed that Si_3N_4 protection can prolong the working life of graphene devices. The piezoresistive effect of the graphene sensing element was gradually confirmed through displacement resistance measurements and strain–resistance analysis. In the end, a gauge factor of 1.35, near to that of CVD graphene, was reached. Based on the crossbeam structure chip, the sensitivity of the graphene pressure sensor was as high as 33.13 mV/V/MPa under a wide range of conditions. Other static specifications also demonstrated high repeatability and reliability. This indicates that the crossbeam structure is an extremely useful application for graphene N/MEMS mechanical sensors.

Author Contributions: J.W.: conceptualization, methodology, writing—original draft preparation, and project administration; Z.Z.: software and data curation; Y.Q.: validation; M.L.: supervision and funding acquisition. All authors have read and agreed to the published version of the manuscript.

Funding: This research was funded by the "173" Projects of China, grant numbers 2020JCJQZD043, 2021JCJQJJ0172 and 2017JCJQZD006.

Data Availability Statement: Not applicable.

Acknowledgments: The authors are thankful for the facility assistance from the Suzhou Institute of Nano–Tech and Nano–Bionics, Chinese Academy of Sciences.

Conflicts of Interest: The authors declare no conflict of interest.

References

1. Lee, C.; Wei, X.; Kysar, J.W.; Hone, J. Measurement of the elastic properties and intrinsic strength of monolayer graphene. *Science* **2008**, *321*, 385–388. [CrossRef] [PubMed]
2. Balandin, A.A.; Ghosh, S.; Bao, W.; Calizo, I.; Teweldebrhan, D.; Miao, F.; Lau, C.N. Superior Thermal Conductivity of Single-Layer Graphene. *Nano Lett.* **2008**, *8*, 902–907. [CrossRef] [PubMed]
3. Nair, R.R.; Blake, P.; Grigorenko, A.N.; Novoselov, K.S.; Booth, T.J.; Stauber, T.; Peres, N.M.R.; Geim, A.K. Fine Structure Constant Defines Visual Transparency of Graphene. *Science* **2008**, *320*, 1308. [CrossRef] [PubMed]
4. Du, X.; Skachko, I.; Barker, A.; Andrei, E.Y. Approaching ballistic transport in suspended graphene. *Nat. Nanotechnol.* **2008**, *3*, 491–495. [CrossRef]
5. Ni, Z.; Yu, T.; Lu, Y.H.; Wang, Y.Y.; Feng, Y.P.; Shen, Z.X. Uniaxial Strain on Graphene: Raman Spectroscopy Study and Band-Gap Opening. *ACS Nano* **2008**, *2*, 2301–2305. [CrossRef]
6. Koenig, S.; Boddeti, N.; Dunn, M.; Bunch, J.S. Ultrastrong adhesion of graphene membranes. *Nat. Nanotechnol.* **2011**, *6*, 543–546. [CrossRef]
7. Davidovikj, D.; Scheepers, P.H.; Van Der Zant, H.S.J.; Steeneken, P.G.; Davidovikj, D.; Scheepers, P.H.; Van Der Zant, H.S.J.; Steeneken, P.G.; Davidovikj, D.; Scheepers, P.H.; et al. Static Capacitive Pressure Sensing Using a Single Graphene Drum. *ACS Appl. Mater. Interfaces* **2017**, *9*, 43205–43210. [CrossRef]
8. Wang, Q.; Hong, W.; Dong, L. Graphene "microdrums" on a freestanding perforated thin membrane for high sensitivity MEMS pressure sensors. *Nanoscale* **2016**, *8*, 7663–7671. [CrossRef]
9. Chen, H.; Lv, L.; Zhang, J.; Zhang, S.; Xu, P.; Li, C.; Zhang, Z.; Li, Y.; Xu, Y.; Wang, J. Enhanced Stretchable and Sensitive Strain Sensor via Controlled Strain Distribution. *Nanomaterials* **2020**, *10*, 218. [CrossRef]
10. Fan, X.; Forsberg, F.; Smith, A.D.; Schröder, S.; Wagner, S.; Östling, M.; Lemme, M.C.; Niklaus, F. Suspended Graphene Membranes with Attached Silicon Proof Masses as Piezoresistive Nanoelectromechanical Systems Accelerometers. *Nano Lett.* **2019**, *19*, 6788–6799. [CrossRef]
11. Wu, S.; Peng, S.; Han, Z.J.; Zhu, H.; Wang, C.H. Ultrasensitive and Stretchable Strain Sensors Based on Mazelike Vertical Graphene Network. *ACS Appl. Mater. Interfaces* **2018**, *10*, 36312–36322. [CrossRef] [PubMed]
12. Bae, S.-H.; Lee, Y.; Sharma, B.K.; Lee, H.-J.; Kim, J.-H.; Ahn, J.-H. Graphene-based transparent strain sensor. *Carbon* **2013**, *51*, 236–242. [CrossRef]
13. Smith, A.D.; Niklaus, F.; Paussa, A.; Vaziri, S.; Fischer, A.C.; Sterner, M.; Forsberg, F.; Delin, A.; Esseni, D.; Palestri, P.; et al. Electromechanical Piezoresistive Sensing in Suspended Graphene Membranes. *Nano Lett.* **2013**, *13*, 3237–3242. [CrossRef] [PubMed]

14. Smith, A.; Vaziri, S.; Niklaus, F.; Fischer, A.; Sterner, M.; Delin, A.; Östling, M.; Lemme, M. Pressure sensors based on suspended graphene membranes. *Solid-State Electron.* **2013**, *88*, 89–94. [CrossRef]
15. Zhu, S.-E.; Ghatkesar, M.K.; Zhang, C.; Janssen, G.C.A.M. Graphene based piezoresistive pressure sensor. *Appl. Phys. Lett.* **2013**, *102*, 161904. [CrossRef]
16. Hurst, A.M.; Lee, S.; Cha, W.; Hone, J. A graphene accelerometer. In Proceedings of the 2015 28th IEEE International Conference on Micro Electro Mechanical Systems (MEMS), Estoril, Portugal, 18–22 January 2015; pp. 865–868. [CrossRef]
17. Fan, X.; Smith, A.D.; Forsberg, F.; Wagner, S.; Schröder, S.; Akbari, S.S.A.; Fischer, A.C.; Villanueva, L.G.; Östling, M.; Lemme, M.C.; et al. Manufacture and characterization of graphene membranes with suspended silicon proof masses for MEMS and NEMS applications. *Microsyst. Nanoeng.* **2020**, *6*, 17. [CrossRef]
18. Park, W.-T.; Kotlanka, R.K.; Lou, L.; Hamidullah, M.; Lee, C. MEMS tri-axial force sensor with an integrated mechanical stopper for guidewire applications. *Microsyst. Technol.* **2012**, *19*, 1005–1015. [CrossRef]
19. Chun, S.; Choi, Y.; Park, W. All-graphene strain sensor on soft substrate. *Carbon* **2017**, *116*, 753–759. [CrossRef]
20. Zhang, Z.; Du, J.; Zhang, D.; Sun, H.; Yin, L.; Ma, L.; Chen, J.; Ma, D.; Cheng, H.-M.; Ren, W. Rosin-enabled ultraclean and damage-free transfer of graphene for large-area flexible organic light-emitting diodes. *Nat. Commun.* **2017**, *8*, 14560. [CrossRef]
21. Liang, X.; Sperling, B.A.; Calizo, I.; Cheng, G.; Hacker, C.; Zhang, Q.; Obeng, Y.; Yan, K.; Peng, H.; Li, Q.; et al. Toward Clean and Crackless Transfer of Graphene. *ACS Nano* **2011**, *5*, 9144–9153. [CrossRef]
22. Suk, J.W.; Lee, W.H.; Lee, J.; Chou, H.; Piner, R.D.; Hao, Y.; Akinwande, D.; Ruoff, R.S. Enhancement of the Electrical Properties of Graphene Grown by Chemical Vapor Deposition via Controlling the Effects of Polymer Residue. *Nano Lett.* **2013**, *13*, 1462–1467. [CrossRef] [PubMed]
23. Ahn, Y.; Kim, H.; Kim, Y.-H.; Yi, Y.; Kim, S.-I. Procedure of removing polymer residues and its influences on electronic and structural characteristics of graphene. *Appl. Phys. Lett.* **2013**, *102*, 091602. [CrossRef]
24. Piazza, A.; Giannazzo, F.; Buscarino, G.; Fisichella, G.; La Magna, A.; Roccaforte, F.; Cannas, M.; Gelardi, F.; Agnello, S. Graphene p-Type Doping and Stability by Thermal Treatments in Molecular Oxygen Controlled Atmosphere. *J. Phys. Chem. C* **2015**, *119*, 22718–22723. [CrossRef]
25. Russo, S.; Craciun, M.; Yamamoto, M.; Morpurgo, A.; Tarucha, S. Contact resistance in graphene-based devices. *Phys. E Low-Dimens. Syst. Nanostruct.* **2009**, *42*, 677–679. [CrossRef]
26. Li, M.; Wu, C.; Zhao, S.; Deng, T.; Wang, J.; Liu, Z.; Wang, L.; Wang, G. Pressure sensing element based on the BN–graphene–BN heterostructure. *Appl. Phys. Lett.* **2018**, *112*, 143502. [CrossRef]
27. Al-Mumen, H.; Dong, L.; Li, W. SU-8 doped and encapsulated n-type graphene nanomesh with high air stability. *Appl. Phys. Lett.* **2013**, *103*, 232113. [CrossRef]
28. Seo, H.-K.; Park, M.-H.; Kim, Y.-H.; Kwon, S.-J.; Jeong, S.-H.; Lee, T.-W. Laminated Graphene Films for Flexible Transparent Thin Film Encapsulation. *ACS Appl. Mater. Interfaces* **2016**, *8*, 14725–14731. [CrossRef]
29. Jee, H.-G.; Han, J.-H.; Hwang, H.-N.; Kim, B.; Kim, H.-S.; Kim, Y.D.; Hwang, C.-C. Pentacene as protection layers of graphene on SiC surfaces. *Appl. Phys. Lett.* **2009**, *95*, 093107. [CrossRef]
30. Alexandrou, K.; Petrone, N.; Hone, J.; Kymissis, I. Encapsulated graphene field-effect transistors for air stable operation. *Appl. Phys. Lett.* **2015**, *106*, 113104. [CrossRef]
31. Wang, H.; Taychatanapat, T.; Hsu, A.; Watanabe, K.; Taniguchi, T.; Jarillo-Herrero, P.; Palacios, T. BN/Graphene/BN Transistors for RF Applications. *IEEE Electron. Device Lett.* **2011**, *32*, 1209–1211. [CrossRef]
32. Jain, N.; Durcan, C.A.; Jacobs-Gedrim, R.; Xu, Y.; Yu, B. Graphene interconnects fully encapsulated in layered insulator hexagonal boron nitride. *Nanotechnology* **2013**, *24*, 355202. [CrossRef] [PubMed]
33. Yang, M.; Zhang, C.; Wang, S.; Feng, Y. Ariando Graphene on β-Si_3N_4: An ideal system for graphene-based electronics. *AIP Adv.* **2011**, *1*, 032111. [CrossRef]
34. Fan, Y.; Jiang, W.; Kawasaki, A. Highly Conductive Few-Layer Graphene/Al_2O_3Nanocomposites with Tunable Charge Carrier Type. *Adv. Funct. Mater.* **2012**, *22*, 3882–3889. [CrossRef]
35. Lee, J.; Tao, L.; Parrish, K.N.; Hao, Y.; Ruoff, R.S.; Akinwande, D. Multi-finger flexible graphene field effect transistors with high bendability. *Appl. Phys. Lett.* **2012**, *101*, 252109. [CrossRef]
36. Yap, R.C.C.; Li, H.; Chow, W.L.; Lu, C.X.; Tay, B.K.; Teo, H.T.E. Identifying the mechanisms of p-to-n conversion in unipolar graphene field-effect transistors. *Nanotechnology* **2013**, *24*, 195202. [CrossRef]
37. Wang, Z.; Li, P.; Chen, Y.; Liu, J.; Qi, F.; Tian, H.; Zheng, B.; Zhou, J. Air-stable n-type doping of graphene from overlying Si3N4 film. *Appl. Surf. Sci.* **2014**, *307*, 712–715. [CrossRef]
38. Geng, D.; Yang, S.; Zhang, Y.; Yang, J.; Liu, J.; Li, R.; Sham, T.-K.; Sun, X.; Ye, S.; Knights, S. Nitrogen doping effects on the structure of graphene. *Appl. Surf. Sci.* **2011**, *257*, 9193–9198. [CrossRef]
39. Su, F.; Zhang, Z.; Li, S.; Li, P.; Deng, T. Long-term stability of photodetectors based on graphene field-effect transistors encapsulated with Si_3N_4 layers. *Appl. Surf. Sci.* **2018**, *459*, 164–170. [CrossRef]

MDPI AG
Grosspeteranlage 5
4052 Basel
Switzerland
Tel.: +41 61 683 77 34

Nanomaterials Editorial Office
E-mail: nanomaterials@mdpi.com
www.mdpi.com/journal/nanomaterials

Academic Open
Access Publishing

mdpi.com

ISBN 978-3-7258-4504-0